Single-Walled Carbon Nanotubes as Charge Extraction Layer for Perovskite Solar Cells



Severin N. Habisreutinger

St Cross College

University of Oxford

A thesis submitted for the degree of
Doctor of Philosophy

Trinity, 2016

Single-Walled Carbon Nanotubes as Charge Extraction Layer for Perovskite Solar Cells

Severin N. Habisreutinger, St Cross College, University of Oxford

Thesis submitted for the degree of Doctor of Philosophy at the University of Oxford.
Trinity Term, 2016

Abstract

This thesis describes the development of a charge-extraction layer for perovskite solar cells based on a network of polymer-functionalized single-walled carbon nanotubes (SWNTs). The starting point is the addition of SWNTs as additives to improve the charge transport characteristics of a solid-state hole-transporting material - *2,2,7,7-tetrakis-(N,N-di-p-methoxyphenylamine)9,9-spirobifluorene* (spiro-OMeTAD). In a double-layer structure this is shown to perform comparably well to devices in which the charge transport of spiro-OMeTAD is enhanced by conventional doping. By means of photo-induced absorption spectroscopy, it could be shown that a significant fraction of photogenerated charges are transferred to the SWNTs. This finding demonstrates that the nanotubes act as charge selective contacts in their own right without requiring the presence of dedicated hole transporter material. Instead, they can be embedded in a matrix of an inert polymer, which can be chosen according to characteristics related to stability rather than their electronic properties. Such a SWNT-PMMA composite structure is shown to outperform conventional hole-transporter systems during and after thermal stressing cycles. Finally, the issue of hysteresis is addressed. The additive 4-*tert*-butylpyridine (tBP) is shown to significantly improve the steady-state performance of devices with the SWNT-PMMA composite structure. In order to understand the mechanism and underlying interactions of the additive, the possible interaction interfaces are investigated one by one, leading to the conclusion that a direct interaction between tBP and the perovskite absorber must be responsible for the observed effect. The work in this thesis opens the avenue for SWNT-based hole transporter systems which provide a chemically stable and mechanically resilient charge-selective contact, and show particular promise for improving the overall stability of perovskite devices.

To my Parents

for their unending love, support and encouragement

Acknowledgements

I would like to thank my supervisor professor Robin Nicholas for all his invaluable advice, guidance and constant support. I would also like to thank professor Henry Snaith for his encouragement, his contagious enthusiasm and extraordinary ideas.

My gratitude goes out to all my the current and former members of the Nicholas group and the Snaith group, which have made my countless hours spent in the lab so much more enjoyable. In particular, I want to thank Tomas Leijtens and Samuel Stranks, which have helped me tremendously in my efforts. A very special thanks also belongs to Giles Eperon for all his ideas, assistance and friendship.

I want to thank my collaborators, in particular Yujiro Tazawa in Prof Andrew Watt's group, and Jeffrey Blackburn, at the National Renewable Energy Laboratory, with whom I many countless invaluable discussions.

I also want to especially thank Nakita Noel for all her advice, patience and love, who has made my life so much brighter and happier.

I would like to acknowledge the partial support by the Engineering and Physical Sciences Research Counci and the International Collaborative Energy Technology R&D Program of the Korean Institute of Energy Technology Evaluation and Planning (KETEP); as well as the St Cross College Travel and Research Fund, which has supported my participation at the international conference HOPV15 in Rome.

I also want to say thank you to all the interesting people I got to meet and all the new wonderful friends I have found during my time in Oxford - you have made my experience here unforgettable.

Finally, I would like to wholeheartedly thank my family, my parents Julei and Klaus, and my sister Lilith, for all their unwavering loving support and all their encouragement.

Contents

1 Introduction **1**

1.1 The climate change challenge 1

1.2 Solar power 3

1.3 Carbon nanotubes 6

1.4 Structure of this thesis 6

2 Theory of solar cells **9**

2.1 Photovoltaic devices 9

2.1.1 Definition 9

2.1.2 Light absorption and charge carrier generation 10

2.1.3 Charge carrier separation and extraction 15

2.1.4 Semiconductor junctions and contacts 16

2.1.5 Polymer heterojunctions 25

2.1.6 Dye-sensitized junctions 26

2.2 Solar cell characterization 29

2.3 Perovskite solar cells 33

2.3.1 Structure and stability 33

2.3.2 Device architectures and performance 40

2.4 Summary 44

3 Single-Walled Carbon Nanotubes **45**

3.1 Definition and synthesis 45

3.2 Characterization 46

3.2.1 Real space 46

3.2.2 Reciprocal space 49

3.3 Band structure 52

3.3.1 Band structure of graphene 52

3.3.2 Band structure of carbon nanotubes . . . 57
3.3.3 Density of states . . . 61
3.4 Electronic charge transport . . . 63
3.4.1 Carbon nanotube networks . . . 64
3.5 Polymer functionalization . . . 66
3.6 Applications in solar cells . . . 71
3.6.1 Organic solar cells . . . 71
3.6.2 Inorganic solar cells . . . 75
3.6.3 Metal halide perovskite solar cells . . . 78
3.7 Summary . . . 84

4 Materials and methods **86**
4.1 Materials . . . 86
4.1.1 Single-wall carbon nanotubes . . . 86
4.1.2 Polymers . . . 88
4.1.3 SWNT functionalization . . . 89
4.1.4 Solar cell fabrication . . . 89
4.2 Solar cell characterization . . . 91
4.3 Absorption spectroscopy . . . 91
4.4 Photoinduced absorption spectroscopy . . . 91
4.4.1 Setup . . . 91
4.4.2 Technique . . . 92
4.5 Transient lifetime measurements . . . 93
4.5.1 Setup . . . 93
4.5.2 Transient photovoltage decay . . . 93
4.5.3 Transient photocurrent decay . . . 94
4.6 Kelvin probe measurements . . . 95
4.6.1 Setup . . . 95
4.6.2 Technique . . . 95

5 Enhanced charge extraction through carbon nanotubes in perovskite solar cells **98**
5.1 Hole extraction in perovskite solar cells . . . 98
5.2 SWNTs as hole-transporter additives . . . 100
5.3 Photoinduced absorption spectroscopy . . . 108

5.4 Transient decay measurements . . . 111
5.5 Summary . . . 112

6 Carbon nanotube/polymer composite as a highly stable charge collection layer in perovskite solar cells 113

6.1 Stability of hole-transporting materials . . . 113
6.2 SWNT-based hole-transporting structure . . . 120
6.2.1 PMMA layer thickness . . . 122
6.2.2 SWNT type . . . 124
6.3 Different protective matrices . . . 129
6.4 Thermal stressing . . . 131
6.5 Operation at elevated temperatures . . . 132
6.6 Direct water exposure . . . 136
6.7 Summary . . . 138

7 Investigating the role of 4-*tert* butylpyridine in perovskite solar cells 140

7.1 The steady-state performance challenge . . . 140
7.2 4-*tert*-butylpyridine (tBP) . . . 144
7.3 Effect on hole-transporting materials . . . 145
7.4 Effect on the SWNT-PMMA system . . . 148
7.5 Identifying the tBP interaction interface . . . 152
7.5.1 tBP and the inert polymer matrix . . . 152
7.5.2 tBP and TiO_2 . . . 154
7.6 Probing the mechanism . . . 158
7.7 Summary . . . 161

8 Conclusion and Outlook 162

8.1 Key findings . . . 162
8.2 Outlook . . . 164

A Poster presentations 166

Bibliography 169

List of Figures

1.1 Global temperature rise 1
1.2 Life-cycle assessment of perovskite solar cells 2
1.3 Global energy consumption by source 3
1.4 Life-cycle assessment of perovskite solar cells 5

2.1 Excitation and relaxation pathways of electrons in an absorber 11
2.2 Solar photon flux and power-conversion efficiency dependence on band gap width 12
2.3 Charge recombination pathways 13
2.4 Metal-semiconductor Schottky junction 18
2.5 Metal-semiconductor Schottky junction - in the dark 19
2.6 Metal-semiconductor Schottky junction - under illumination 20
2.7 Metal-semiconductor Schottky junction - p-type semiconductor 21
2.8 Metal-semiconductor junction - Ohmic contact 22
2.9 Semiconductor-semiconductor junction - pn-junction 24
2.10 Operational principle of organic solar cells 26
2.11 Structure of a dye-sensitized solar cells (DSSC) 27
2.12 Operational principle of a DSSC 28
2.13 Current-voltage characteristics of a solar cell 31
2.14 Parasitic resistances 32
2.15 Perovskite crystal structure 33
2.16 Hydration process of methylammonium lead iodide 36
2.17 Perovskite A-site cations 38
2.18 Methylammonium lead iodide absorption 40
2.19 Meso-superstructured solar cell 41
2.20 Planar heterojunction 42

3.1 Graphene lattice vectors 47

3.2 Single-walled carbon nanotube chirality 48
3.3 Brillouin zone of graphene 50
3.4 Allowed $k_\perp$ vectors of single-walled carbon nanotubes 51
3.5 Brillouin zone of single-walled carbon nanotubes 52
3.6 Molecular orbitals of graphene 53
3.7 Graphene lattice - tight binding basis 55
3.8 Graphene bands in 3D 57
3.9 Single-walled carbon nanotube BZ - TB approximation 58
3.10 Carbon nanotube bands - (9,0) chirality 59
3.11 Carbon nanotube bands - (10,0) chirality 60
3.12 Density of states of single-walled carbon nanotubes 63
3.13 Band bending at the P3HT-SWNT interface 68
3.14 Hole transfer from P3HT to SWNTs 69
3.15 Operational principle of an organic solar cell 72
3.16 Comparison of electron and hole transfer from P3HT to SWNTs 74
3.17 Band alignment of SWNTs and silicon 76
3.18 Band alignment between doped SWNTs and silicon 77
3.19 Energy level diagram of SWNTs on perovskite 83

4.1 Absorption spectrum of CG200 SWNTs 86
4.2 Absorption spectrum of SG65i SWNTs 87
4.3 Absorption spectrum of HiPco SWNTs 87
4.4 Molecular structure of P3HT 88
4.5 Molecular structure of PMMA 88
4.6 Molecular structure of PC 88
4.7 Photoinduced absorption spectroscopy Setup 92
4.8 Transient photovoltage decay 94
4.9 Kelvin probe - contact potential difference 95
4.10 Kelvin probe setup 96
4.11 Kelvin probe signal 97

5.1 Energy scheme of a perovskite solar cell with P3HT/SWNTs as HTL 100
5.2 Schematic and cross section of a device containing SWNTs as HTL 101
5.3 Current-voltage curve of a device without hole-selective contact 102
5.4 Current-voltage curve of a device with doped spiro-OMeTAD 103

5.5 Current-voltage curve of a device with a SWNT-spiro-OMeTAD blend 104
5.6 Current-voltage curve of a device with a SWNT-spiro-OMeTAD double layer 105
5.7 Stabilized-power output 107
5.8 Photoinduced absorption spectra 108
5.9 Photoinduced exciton bleaching 109
5.10 Absorption spectrum of chemically p-doped P3HT/SWNTs 110
5.11 Transient photocurrent decay measurements 111

6.1 Thermal degradation of methylammonium lead iodide 114
6.2 Thermal stressing in dry atmosphere 115
6.3 Thermal stressing of various hole-transporters 117
6.4 Absorption spectra and X-ray patterns after thermal stressing 118
6.5 Impact of Li-TFSI on perovskite degradation 119
6.6 Thermal stressing of a PMMA layer 120
6.7 Thermal stressing of a SWNT/PMMA double-layer 121
6.8 Schematic and cross section of a device with SWNT/PMMA as HTL 123
6.9 Performance dependence on PMMA concentration 124
6.10 Performance comparison between several SWNT types 125
6.11 Performance comparison between several SWNT types 2 126
6.12 Performance of devices containing the SWNT/PMMA double layer 127
6.13 Performance of devices with other polymer matrices 129
6.14 Thermal stressing of devices with PMMA and PC 131
6.15 Operation at elevated temperatures 132
6.16 Comparative operation at elevated temperatures - normalized PCEs 133
6.17 Current-voltage characteristics after thermal stressing 134
6.18 Direct water exposure 136
6.19 Water exposure of a PMMA/SWNT device 137

7.1 Hysteresis and SPO of a device without tBP 141
7.2 Hysteresis and SPO of a device with tBP 142
7.3 Device distribution of devices without tBP 143
7.4 Scanned performance parameters of spiro-OMeTAD 145
7.5 Stabilized performance parameters of spiro-OMeTAD 146
7.6 Scanned performance parameters of partially pre-oxidized spiro-OMeTAD . . 147
7.7 Stabilized performance parameters of partially pre-oxdidized spiro-OMeTAD 147

7.8 tBP concentration dependence - scanned performance 148
7.9 tBP concentration dependence - steady-state performance 149
7.10 Performance statistics of devices with and without tBP 150
7.11 Best-performing device containing tBP 151
7.12 Performance dependence on PMMA thickness with tBP 153
7.13 Polycarbonate with tBP - scanned performance 153
7.14 Polycarbonate with tBP - steady-state performance 154
7.15 Cross section of a device with tBP containing PMMA 155
7.16 tBP premodification - steady-state performance 155
7.17 Devices without charge-selective TiO_2 compact layer 156
7.18 Current-voltage characteristics of devices without charge-selective layers . . . 159
7.19 Workfunction shift after tBP treatment 159
7.20 Schematic illustration of the tBP-perovskite interaction 160

A.1 SSSC14 - Poster 167
A.2 HOPV15 - Poster 168

List of Tables

5.1 Scanned performance parameters 106
5.2 Stabilized performance parameters 107

6.1 Scanned performance parameters of a device with the SWNT/PMMA double layer as HTL 128
6.2 Physical properties of matrix polymers 130
6.3 Scanned performance parameters after thermal stressing 135

7.1 Scan-dependent performance parameters of a device without tBP 141
7.2 Scan-dependent performance parameters of a device with doped spiro-OMeTAD as HTL 142
7.3 Performance parameters for PMMA thickness dependence 152

Publications

Samuel D. Stranks, Severin N. Habisreutinger, Beate Dirks, Robin J. Nicholas, Novel Carbon Nanotube-Conjugated Polymer Nanohybrids Produced By Multiple Polymer Processing, *Advanced Materials*, 25 (2013) 4365-4371.

Severin N. Habisreutinger, Tomas Leijtens, Giles E. Eperon, Samuel D. Stranks, Robin J. Nicholas & Henry J. Snaith, Enhanced Hole Extraction in Perovskite Solar Cells Through Carbon Nanotubes, *The Journal of Physical Chemistry Letters*, 5 (2014) 42074212.

Severin N. Habisreutinger, Tomas Leijtens, Giles E. Eperon, Samuel D. Stranks, Robin J. Nicholas & Henry J. Snaith, Carbon Nanotube/Polymer Composites as a Highly Stable Hole Collection Layer in Perovskite Solar Cells, *Nano Letters*, 14, 10, (2014) 5561-5568.

Giles E. Eperon, Severin N. Habisreutinger, Tomas Leijtens, Bardo, J. Bruijnaers, Jacobus J. van Franeker, Dane W. DeQuilettes, Sandeep Pathak, Rebecca J. Sutton, Giulia Grancini, David S. Ginger, Rene A. J. Janssen, Annamaria Petrozza, Henry J. Snaith, The Importance of Moisture in Hybrid Lead Halide Perovskite Thin Film Fabrication *ACS Nano* 9, (2015), 9380

Tomas Leijtens, Giles E. Eperon, Nakita K. Noel, Severin N. Habisreutinger, Annamaria Petrozza, Henry J. Snaith, Stability of Metal Halide Perovskite Solar Cells *Advanced Energy Materials* 5, (2015), 1500963

Manuscripts in preparation

Severin N. Habisreutinger, Nakita K. Noel, Henry J. Snaith, Robin J. Nicholas, Investigating the role of 4-tert butylpyridine in n-i-p perovskite solar cells, *accepted, Advanced Energy Materials.*

Severin N. Habisreutinger, Henry J. Snaith, Robin J. Nicholas, Carbon nanotubes in perovskite solar cells, *accepted, Advanced Energy Materials.*

Severin N. Habisreutinger, David P. McMeekin, Henry J. Snaith, Robin J. Nicholas, Improving the stability of perovskite solar cells, *accepted, APL Materials.*

Oral presentations

Functionalized Single-Walled Carbon Nanotubes as p-Type Charge Extraction Layer in Perovskite Solar Cells, *Materials Research Society (MRS) Spring Meeting, San Francisco, USA, 2014*

Highly Stable Hole-transporting Layers for Perovskite Solar Cells Based on Functionalized Single-Walled Carbon Nanotubes, *The 6th World Conference on Photovoltaic Energy Conversion, Kyoto, Japan, 2014*

Investigating the Role of 4-tert Butylpyridine (tBP) in a CNT-based Hole Transporter, *Materials Research Society (MRS) Fall Meeting, Boston, USA, 2015*

Chapter 1

Introduction

> "Over billions of years, on a unique sphere, chance has painted a thin covering of life – complex, improbable, wonderful and fragile. Suddenly we humans (a recently arrived species no longer subject to the checks and balances inherent in nature), have grown in population, technology, and intelligence to a position of terrible power: we now wield the paintbrush." Paul MacCready [1].

1.1 The climate change challenge

Never in human history has a paradigm shift been more imperative than today [2]. Anthropogenic climate change caused by greenhouse gas emission from fossil fuel combustion, agriculture and cement production, is in the process of fundamentally changing the climatic conditions on Earth [2]. This threatens the current biosphere as a whole, but most pressingly will imperil the very existence of humankind [2]. At the same time, the global population has undergone an unprecedented surge [3] alongside an increase in energy consumption per person, resulting in a rising overall energy demand of the human population [4] (figure 1.1, figure 1.2).

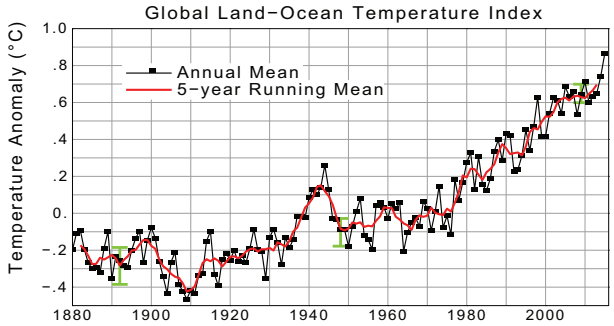

Figure 1.1: Line plot of global mean land-ocean temperature index, 1880 to present. The dotted black line is the annual mean and the solid red line is the five-year mean. (NASA Goddard Institute for Space Studies. Dataset accessed 2016-04-06 [5, 6])

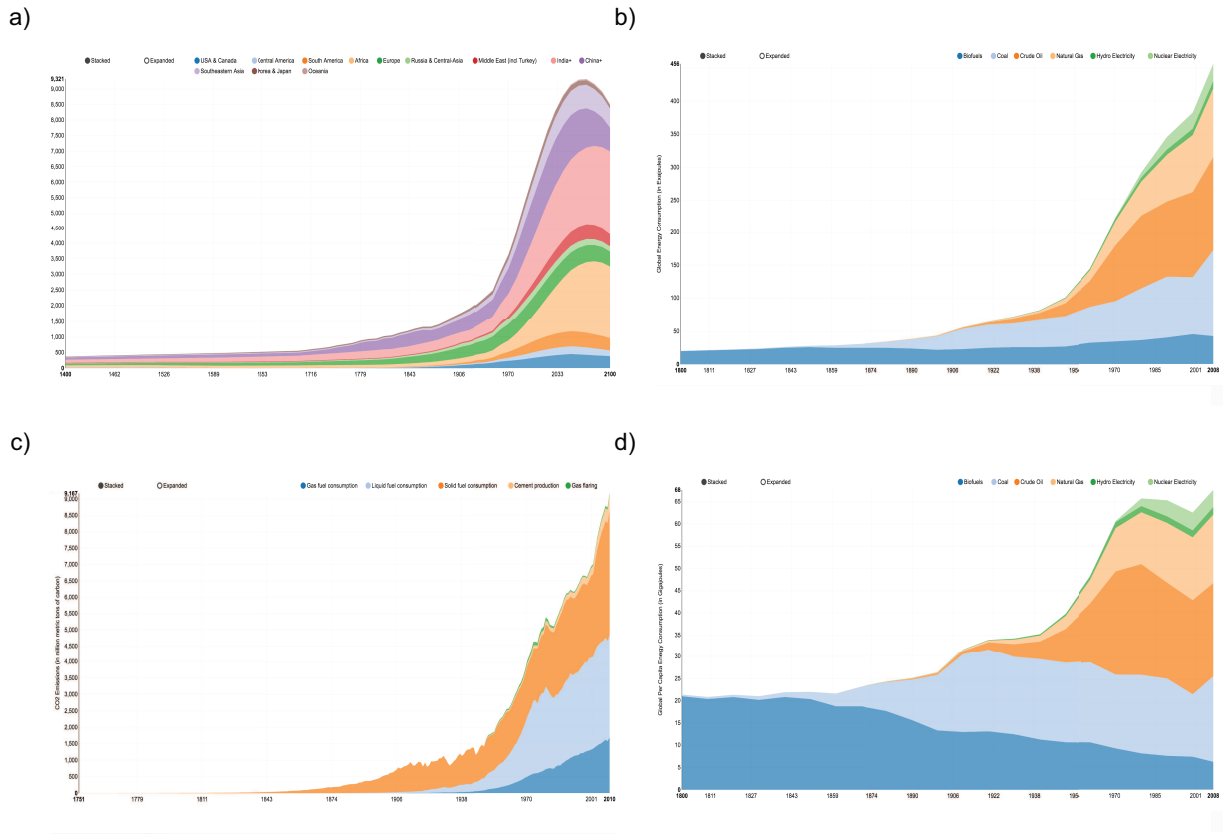

Figure 1.2: a) Global population over time from 1400 projected until 2100; b) Global energy consumption in (EJ) over time from 1800 until 2008; c) CO_2 emissions (in million tons of carbon) over time from 1751 until 2010; d) Global energy consumption per capita (in GJ) over time from 1800 until 2008 (Copyright - Max Roser. Published online at OurWorldInData.org. Individual sources: a) [7]; b) [8]; c) [9]; d) [8])

Climate change and the associated increase of global temperatures will inexorably happen, considering the vast amount of emitted excess greenhouse gases in the atmosphere, however, by shifting towards energy sources with no or very little additional CO_2 emission, the consequences could possibly be mitigated to some extent [10]. Any mitigation will only be possibly if it occurs within the very immediate future, otherwise feedback mechanisms and thermal momentum will dominate the evolution of the future global climate to the very detriment of the human species [2, 10].

The Intergovernmental Panel on Climate Change (IPCC) has outlined and assessed strategies for climate change mitigation in the Working Group III contribution to the IPCCs Fifth Assessment Report [10]. In this report the authors state that *decarbonizing (i.e. reducing the carbon intensity of) electricity generation is a key component of cost-effective mitigation strategies in achieving low-stabilization levels (430-530 ppm CO_2).* In other words, it is essential to remove the generation of additional CO_2 from electricity generation.

1.2 Solar power

The energy production means which do not contribute directly to any further greenhouse gas emissions are typically renewable sources, which are not based on open-cycle combustion processes. To date the contribution of renewable energy to the total global energy market is very small. The estimates of the marketshare vary between 9.3% (primary fuel consumption in 2014 estimated by British Petroleum [4]) and 19.1% (renewable energy share of the global final energy consumption by the Renewable Energy Policy Network [11]) in contrast to 78-86% of fossil fuels. The renewable energy category is comprised of solar sources, namely

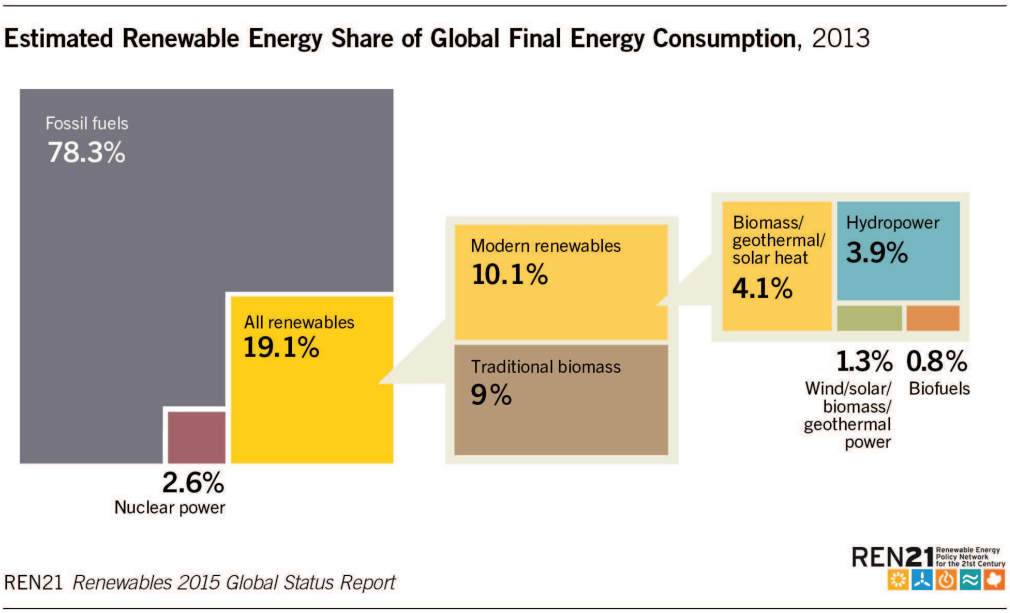

Figure 1.3: Estimated global energy consumption for 2013 by source, data collated by the Renewable Energy Policy Network (REN21). (Reproduced with permission from REN21, 2016, Renewables 2015 Global Status Report, Paris, REN21 Secretariat)

photothermal and photovoltaic, as well as biofuels, geothermal, wind and tidal sources. For the latter, the total amount of energy which could maximally extracted from those sources combined is estimated to amount to roughly 20 TW [12]. In contrast, converting the incident solar energy incident on 1% of the Earth's surface at a power-conversion efficiency of 10% would already provide 105 TW, exceeding the global demand projected for the year 2050

by a factor of ten [13]. Solar power has therefore comparatively limitless possibilities for expansion. However, according to the latest reports, photovoltaic solar energy conversion has only just reached the global threshold of 1.0% of energy production, now accounting for a cumulative capacity of 178 GW [14].

A major hurdle for deeper market penetration is the higher cost of solar power per Watt produced compared to fossil fuel sources [15]. Despite the continuous decrease in prices for solar modules, the levelized cost of electricity (LCOE) of solar power is still much higher than that of comparable energy sources [15]. To become fully competitive and achieve moderate penetration of the electrical grid, solar power needs to reach a target of less than half its current LCOE, which would be 0.06 \$/kWh or 0.04 £/kWh [16]. In the breakdown of cost for solar power, major contributors are the photovoltaic modules themselves accounting for 30-60% of the cost, but a significant part also comes from additional system costs which are often described with the umbrella term *balance of systems* (BoS), consisting of installation systems, labor, land, racking, and developmental costs among others. The overall cost for solar power can therefore be reduced by a two-pronged approach, by reducing the module cost but also by lowering the costs of the BoS. Both can potentially be done by pursuing cheaper and lighter materials, thus reducing the module cost itself but also allowing the development of new racking and installation techniques.

Another important aspect to consider with regards to both cost and sustainability of solar power provided by conventional photovoltaic solar cells, is that they rely on a range of scarce materials, such as Gallium, Indium and Selenium [17]. Finally, from the point of sustainability, the overall energy expenditure and the associated CO_2 emission of the manufacturing process of a photovoltaic module has to be taken into consideration. These values are part of comprehensive life-cycle assessment analyses. This includes two important metrics: the *energy payback time* (EPBT), which is the period required for a renewable energy system to generate the same amount of energy that was used to produce the system itself; and the *greenhouse gas (GHG) emissions* associated with the fabrication and the operation of the system [18]. For the most commonly employed conventional mono-crystalline silicon cell the EPBT is around 1.7 years (under irradiation of 1700 kWh/m^2·yr) [18]. More than two-thirds of the initial energy expenditure is related to the production of the feedstock and material processing for the module. Additionally, the GHG emissions, while orders of magnitude lower compared to combustion-based energy sources, is not completely negligible amounting to 30-37 g_{CO_2eq}/kWh. For context, the GHG emissions for wind power with 12-20

g_{CO_2eq}/kWh and nuclear power with 16-45 g_{CO_2eq}/kWh are still lower [19].

Further innovation in the field of photovoltaic solar cells is therefore needed to become a competitive, carbon-neutral, effective and sustainable energy technology. This requires therefore the development of new active materials which have to be earth-abundant and cheap themselves; and their production and processing needs to have a low energy expenditure and GHG emissions.

In recent years various new ambitious photovoltaic technologies have been pioneered, including organic polymer solar cells [20], quantum-dot solar cells [21] and dye-sensitized solar cells [22, 23], which meet most of the above outlined criteria. The most promising candidate is the perovskite solar cell which is an offshoot and the next step in the evolution of the dye-sensitized solar cell. After its conception in 2009 [24] and reliable realization in 2012 [25], it has shown unrivalled potential for large-scale energy production due to its high-efficiencies paired with low-impact material and manufacturing costs [26].

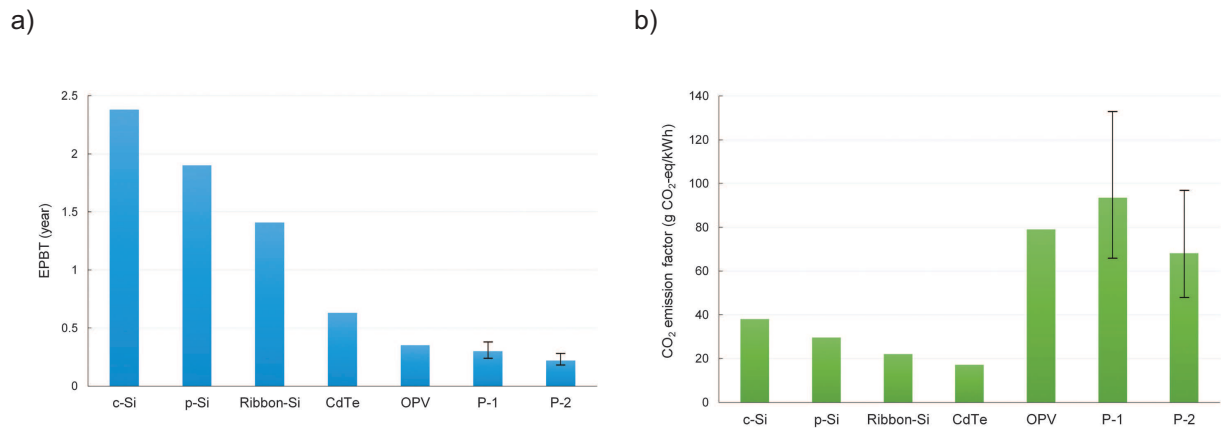

Figure 1.4: Comparison of two perovskite modules P-1 (TiO_2) and P-2 (ZnO) to other types of photovoltaic modules with respect to a) Energy payback time and b) the CO_2 emission factor. (Reproduced with permission from J. Gong *et al*, Energy Environ. Sci. (2015), 8, 1953. Copyright 2015 Royal Society of Chemistry.)

While it is early to fully assess the life-cycle of a perovskite solar cell as a module, the first analysis by Gong *et al.*, pinpoints which aspects of the device fabrication need additional concerted effort for developing new or improved strategies [26]. This study includes the comparison of seven different photovoltaic technologies showing that perovskite solar cells have, in fact, the shortest EPBT with 0.22 years. However, in terms of GHG emissions, with close to 100 g_{CO_2eq}/kWh, perovskite solar cells are associated with by far the most CO_2 emissions per unit of energy produced [26]. The biggest reason for the high "CO_2 cost" is

the relatively short estimated lifetime due to the inherent instability of the material. The authors conclude that perovskite solar modules have enormous potential to become a major photovoltaic technology provided the CO_2 cost is reduced by enhancing the overall stability of the devices.

In this thesis, the stability of perovskite solar cells is investigated by examining the use single-walled carbon nanotubes as charge extraction layer.

1.3 Carbon nanotubes

Single-walled carbon nanotubes (SWNTs) are tubular structures of monolayers of carbon with a diameter of few nanometers and a length of several micrometers. Their mechanical and chemical resilience, combined with extraordinary optoelectronic properties make SWNTs highly interesting components for electronic and optoelectronic devices [27]. However, despite their very beneficial properties, the application of SWNTs in optoelectronic devices, particularly in solar cells, has been difficult because SWNTs come with their own unique challenges such as their electronic heterogeneity and averseness to being individually dispersed in solvents. Furthermore, ambiguity has remained for a long time with regards to the polarity of the charge to be extracted more favorably by SWNTs in solar cells.

In this thesis, a strategy is investigated which employs conjugated polymers as functionalization agents, which facilitate the individualization and dispersion of SWNTs in common solvents. Once dispersed, a method of depositing the polymer-wrapped SWNTs from solution by spincoating has been developed such that the resulting film is a dense interconnected network of nanotubes which effectively can extract photogenerated charges from a perovskite absorber.

1.4 Structure of this thesis

This thesis details the development of a single-walled nanotube based charge-extraction layer for perovskite solar cells, which has a dual-function as active component for charge collection and as passive component as encapsulation layer, improving the stability of a device while maintaining a high power conversion efficiency.

After having introduced and motivated the subject of this thesis in the first chapter, in

the second chapter, the fundamental requirements and concepts of photovoltaic devices are described. This includes a broadly framed discussion of the necessary sequential processes involving photoabsorption, charge generation and charge recombination, and charge separation and extraction. The latter part is addressed more deeply by describing several types of junctions which are used for creating a built-in asymmetry in a device that will provide the driving force to extract photogenerated charges of opposite polarity. This discussion is followed by a brief overview of the performance parameters typically used to quantify the efficiency of a solar cell.

The next section of this chapter introduces the perovskite absorber material, focussing initially on its structure and how that relates to its stability and vulnerability, and strategies on how combat potential degradation of its chemical and structural integrity, when employed in devices. Following, is a short account of the history of the perovskite solar cell including the major developments and evolution steps.

The third chapter gives a theoretical background of single-walled carbon nanotubes (SWNTs). The chapter starts with the definition and some synthesis routes of SWNTs, followed by a theoretical description of their band structure and cause for the intrinsic electronic heterogeneity. This is done by briefly deriving the graphene band structure using the tight-binding approximation and applying it to SWNTs. Next, the charge transport characteristics of individual nanotubes and networks of SWNTs are described from a more macroscopic point of view.

In order to process SWNTs, in particular out of suspension, they require some type of functionalization agent to attach to their outer surface in order to curb intertube attraction caused by van-der-Waals forces and to make them dispersible in solvents. A range of strategies are discussed, with the focus on the strategy used in this thesis, namely polymer functionalization or polymer wrapping.

This chapter is concluded by a brief overview of employing SWNTs in particular, but carbon nanotubes in general, in different types of solar cells, from organic polymer solar cells, to inorganic silicon based solar cells, to finally perovskite solar cells.

The next chapter contains the materials and methods used throughout this thesis.

Chapter five details the first employment of polymer-wrapped SWNTs as additives to the hole-transporting layer. Further, the development of a double-layer structure of sequentially

deposited layers of SWNTs and hole-transporter is described. This approach is shown to achieve device performances comparable to conventional designs. In spectroscopic studies it is revealed that a significant fraction of photogenerated holes transfers from the perovskite absorber to the SWNTs.

This motivates the research outlined in chapter six, which explores the ability of SWNTs to act as a charge-selective contact without the aid of a dedicated hole-transporter. Being independent of a functional, electronically active material, it is shown that the SWNTs can also be encapsulated by inert polymer matrices, which have the advantage of providing a much better barrier against moisture ingress. The latter is shown to be the major cause for the degradation of the perovskite absorber. Finally, the direct comparison to other hole-transporting materials demonstrates a significant enhancement in thermal resilience of operational perovskite devices during and after thermal cycling, as well as direct water exposure.

The seventh chapter addresses the issue of hysteresis. This phenomenon is characteristic for perovskite solar cells, and expressed in a discrepancy of the current-voltage scans depending on the scan rate and direction. The underlying causes are transient processes in the perovskite absorber most likely attributable to ionic motion. To avoid ambiguity, steady-state performance metrics are used to quantify the efficiency of a perovskite solar cell. An additive, 4-*tert*-butylpyridine (tBP), to the conventional hole-transporter is shown to also improve the steady-state performance of devices containing the SWNT-based charge-extraction layer. This chapter teases apart the possible interactions of tBP with all relevant interfaces of a perovskite solar cell, revealing that a direct chemical interaction with the perovskite itself must be responsible for the observed improvement in steady-state performance. This is the first time, that this interaction has been demonstrated, and the findings indicate that the interaction results in interfacial p-doping of the perovskite generating a homojunction in the device. This may have wide implications for the general design of n-i-p perovskite devices and the future development of new hole-transporting materials.

This thesis is concluded with a brief summary of the key findings and an outlook of important and interesting future work which can be based on the findings presented in this thesis.

Chapter 2

Theory of solar cells

This is a chapter gives a very short introduction into the fundamental concepts and processes in photovoltaic devices, and is largely based on *The Physics of Solar cells* by Jenny Nelson, 2003, Imperial College Press [28] and *Physics of Solar Cells* by Peter Würfel, 2005, Wiley [29]. A particular focus has been put on aspects relevant to this thesis.

2.1 Photovoltaic devices

2.1.1 Definition

A photovoltaic device can convert light into electric power. Electromagnetic energy is absorbed by the active material of the device thus increasing the electrochemical potential energy of the electrons. The energy of the absorbed photon allows an electron to transition into an excited state of higher energy. In order to be able to harness this gained potential energy, the excited electronic state has to be separated from the ground state by an energy gap, which does not contain any electronic states and which is much larger than thermal energy k_BT ($\sim$25 meV). The requirement of this gap lies in the relaxation kinetics of the excited electrons. The transition from an excited state to the ground state occurs orders of magnitude more slowly, than the thermal relaxation. The electrons remain therefore sufficiently long in the excited state to be extracted.

In equilibrium, the probability of an electron occupying an energetic state is governed by the Fermi distribution with the Fermi level as its chemical potential. When light disturbs the equilibrium, the electron population in the excited state relaxes into a local, transient thermal equilibrium whose chemical potential is the quasi Fermi level. The difference in the chemical potentials - or quasi Fermi levels - between the occupied excited states and unoccupied ground states, is the maximum potential difference ($\Delta\mu$) of a photovoltaic device. When the device is in open-circuit, i.e. when no current flows between the two terminals, this potential

difference is maximized and referred to as open-circuit voltage (V_{oc}). In order to make the photochemical potential energy of the excited electrons accessible, these charge carriers must be extracted into an external circuit in which they can do work. The first step of the charge extraction relies on separating the charges of different polarities. This is achieved with a built-in asymmetry in the device, which spatially separates excited electrons from the concomitantly created positive counterparts, holes, thus preventing a recombination of the charge pair. This spatial asymmetry can be achieved by selective contacts which prevent the collection of the charge carrier of the opposite polarity, or which make the extraction of one of the charge carriers energetically preferential over the other. The extracted charges can then enter into the external circuit and perform work on a load in the circuit driven by the potential difference of their respective Fermi levels. In order to understand the limiting aspects of a photovoltaic device, the sequence of the three main steps of the conversion process from radiation energy into electric work will be examined in greater detail.

2.1.2 Light absorption and charge carrier generation

A light absorber is characterized by two energy levels separated by an energy gap that is significantly larger than thermal excitation (k_BT). The second requirement for an effective absorber is that its ground state is fully occupied initially whereas the excited state is unoccupied. Individual molecules that fulfill this condition with an energy gap in the visible range are dye molecules. In the case of bulk materials this class of solids is named semiconductor, distinguishing it from metals with practically no band gap ($E_g \leq k_BT$), and insulators with a band gap larger than 4 eV. The latter definition is based on the fact that the gap in states between the occupied valence band and the unoccupied conduction band is so large, electrons could not overcome it by absorbing thermal, visible or low UV radiation. From this follows that all the states of the valence band are filled at all times, not allowing for electrons to move, preventing the flow of electrical current and giving insulators their characteristic property. In semiconductors, in contrast, thermal excitations are enough to promote a small fraction of valence band electrons into the conduction band.

In order for light absorption to occur, the energy of a photon must be equal or larger than the band gap of the energy levels (E_g). A photon with an energy smaller than the band gap $E < E_g$ cannot photoexcite an electron because the additional photoenergy would promote the electron into a state which would be located inside the band gap. In defect-free materials, however, there are no states available within the band gap. A photon with an energy larger

than the band gap, $E > E_g$ can be absorbed by an electron in the ground state, which can then occupy an excited state in the higher energy level (figure 2.1). An excited electron in a state above the band edge will quickly relax through intraband transitions down to the lowest state of the conduction band, losing all its excess energy to the thermal vibrations of the local lattice. The thermalization of electrons to the lowest state in the conduction band occurs within a time-frame of femtoseconds due to the abundance of available states at lower energies. In contrast, the lifetime of excited electrons prior to their interband relaxation to the ground state is of the order of microseconds. This lifetime is long enough for the charges to be extracted at the energies of the band edges. This means, however, that the photon energy in excess of the band gap is lost and cannot be used. Conversely, a very large band gap material can establish a large potential difference between the photogenerated charges, however, it will be limited to a small fraction of the photoenergy range that it can absorb. The maximum efficiency can therefore be obtained for a band gap where the product of voltage and current is maximized.

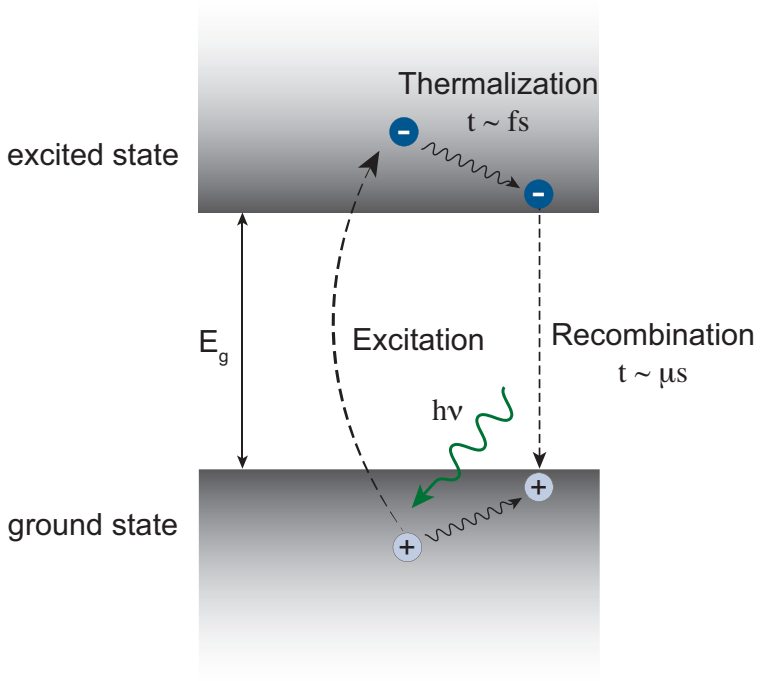

Figure 2.1: An absorber with a ground state and an excited state. Photons with an energy $E \geq E_g$ can excite electrons from the ground state into the excited state. Electrons which are excited beyond the band edge of the excited state, undergo intraband transition within femtoseconds down to the lowest-energy state in this band, losing all their excess energy in scattering events with the lattice and other electrons. Interband transitions i.e. radiative recombination, in contrast, occurs several orders of magnitude more slowly, enabling the extraction of excited electrons.

From this follows that the incident photon flux rather than the energy density of the incoming photons determines the generation of excited charges (figure 2.2 a)). The overall power that can be extracted from an absorber system is therefore tied to the width of the band gap. A narrow band gap will allow the absorption of more photons thus increasing the total number of excited charges which can be extracted. However, the power generated by a photovoltaic device is also dependent on the generated photovoltage in order to drive the current through a load in the external circuit. This voltage, in turn, is determined by the chemical potential difference of the respective quasi-Fermi levels of the excited electrons and their corresponding unoccupied states, which are considered quasi-particles with a positive charge and referred to as "holes".

While a material with a narrow band gap can absorb a large fraction of photons from the visible spectrum, most will lose most of their energy by thermalization, and settle in states at the respective band edges. While the number of extractable charges is large, which will yield a large photocurrent, their potential difference is fairly low, which means the photovoltage will be small. The power such a device can generate is therefore limited by the voltage.

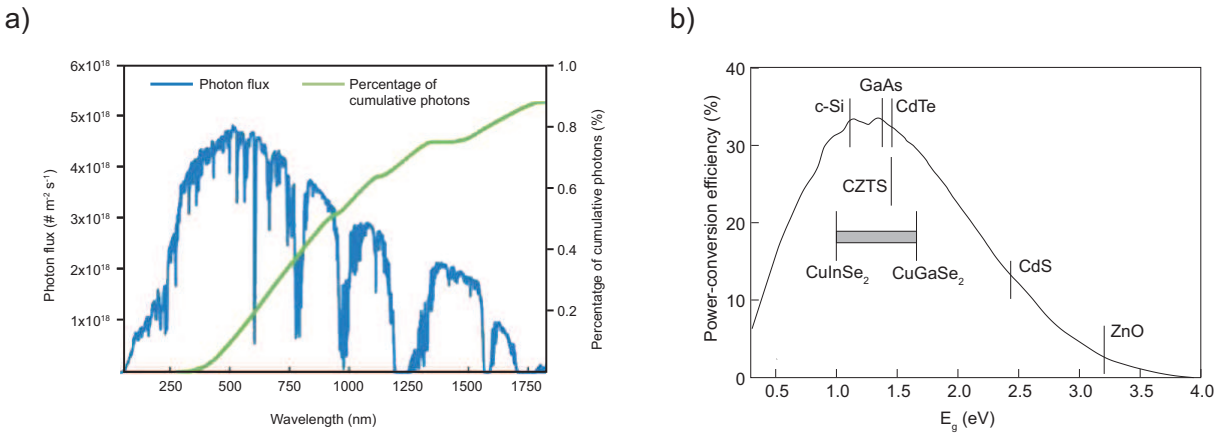

Figure 2.2: a) The AM 1.5 global photon flux spectrum and the percentage of the cumulative photon flux, showing that the majority of photons fall within the range from 300 - 1500 nm (Reproduced with permission from [30]. Copyright 2010 The Royal Society of Chemistry). b) Maximum theoretical power-conversion efficiency (Shockley-Queisser limit) for different solar cell materials with different band gaps under AM1.5 illumination. The band gaps of absorber materials (c-Si, CdTe, CIGS, CZTS) and window materials (CdS, ZnO) are shown for comparison. In the case of the CIGS system, by controlling the In/Ga ratio the band gap width can be tuned [31].

The maximum conversion of solar light into electricity is consequently dependent on the width of the band gap. The theoretical maximum can be calculated under consideration

of the solar photon flux (figure 2.2 a)). The detailed analysis by Shockley and Queisser shows that a maximum conversion efficiency of 33.7% can be achieved for an absorber with a band gap of 1.34 eV [32] (figure 2.2 b)). This maximum efficiency is now known as the *Shockley-Queisser limit*. In figure 2.2 b) the band gap width is plotted against the maximum efficiency, including the band gap values of a range of absorber materials. With a band gap of 1.39 eV the III-V compound semiconductor gallium arsenide (GaAs) comes closest to the ideal band gap. The highest certified efficiency achieved with a single-junction GaAs solar cell is to date at 29.1% [33]. The most commonly used photovoltaic material remains silicon, while its band gap with 1.1 eV is less ideal, its abundance and comparatively low costs, make it commercially more attractive than III-V compounds.

For an absorber material with an appropriate band gap, the absorption can in principle be maximized by increasing the thickness of the absorber layer. Almost perfect absorption can be achieved with layers of several tens or hundreds of micrometers thickness. However, a very thick absorber layer must exhibit excellent charge transport properties, high mobility and long diffusion lengths, in order to be able to extract photogenerated charges i.e. allow charges to diffuse to the interfaces where they can enter the external circuit, before they recombine. Effectively, the thickness of an absorber needs to be optimized for being maximally absorbent while being thin enough to extract the charges.

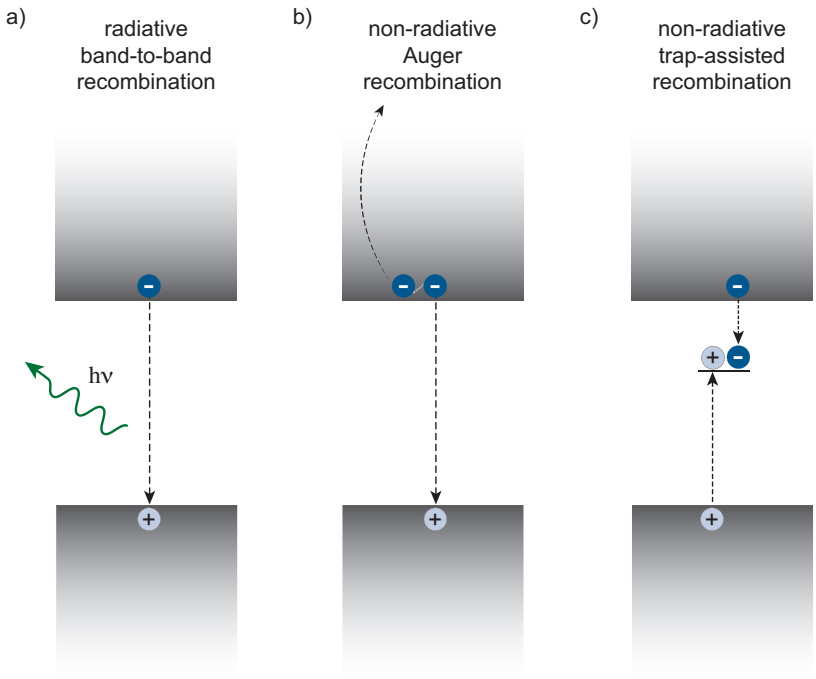

Figure 2.3: a) radiative band-to-band recombination b) non-radiative Auger recombination c) non-radiative trap-assisted recombination

In the context of charge generation, the opposing loss mechanism, namely recombination, has to be addressed. There are several different recombination pathways in a photovoltaic device through which photogenerated charges are lost and thus cannot be extracted into the circuit. One of the most fundamental processes in this context is the spontaneous recombination or radiative recombination, which is a material-specific intrinsic property and is unavoidable. It arises from excited electrons in the conduction band recombining with holes in the valence band and thereby releasing their excitation energy in form of an emitted photon (figure 2.3 a)). This loss mechanism sets a fundamental limit to the overall efficiency for a near-perfect photovoltaic material.

In a spontaneous emission event, the excess energy of the excited electron is released by emitting a photon. This energy can, however, also be transferred to another electron in the conduction band in a collision event resulting in the decay of one electron into a valence-band state and the other electron gaining kinetic energy of the magnitude of the band gap. Eventually, this additional energy will be lost through scattering of the excited electron when it thermalizes down to the lowest available state in the conduction band releasing the energy as heat. This constitutes another built-in loss mechanism, which is, however, non-radiative. It is referred to as *Auger recombination* (figure 2.3 b)). This loss mechanism becomes particularly important in semiconductors with a very high charge carrier density due to much more frequent carrier-carrier collisions.

In practical applications the most important loss mechanism is caused by defects and impurities in the absorber. An excited charge carrier can be captured by a localized state inside the band gap. If this state is relatively close to the nearest band edge of either the conduction or the valence band, it is referred to as shallow trap, and the captured carrier may escape through thermal activation. The loss process occurs when a charge carrier of the opposite polarity relaxes into the same trap state recombining with the captured carrier. This happens in particular for deeper traps from which the captured charges cannot be thermally released. These states are therefore also referred to as recombination centers. They arise due to imperfections, impurities and defects in materials, but are particularly prevalent on surfaces. Surface states often have different energetics for example due to different chemical coordinations or extrinsic impurities. This recombination process loses the excitation energy non-radiatively in form of heat and is the most dominant loss mechanism in real materials.

2.1.3 Charge carrier separation and extraction

After an incident photon is absorbed, it transfers its energy to an electron thus promoting it to the conduction band and generating a concomitant hole in the valence band. Depending on the dielectric environment of the material, the electrostatic Coulomb attraction between the two charge carriers can significantly exceed the thermal energy preventing spontaneous separation. Such a pair of bound charge carriers can also be considered a quasi-particle and is named exciton. Those quasi-particles play an important role in organic semiconductors in which the binding energy between the photogenerated electron and holes is relatively high. As long as the two charges are forming a bound pair, they can not be extracted into the circuit to do work. Additionally, the electron and hole of an exciton will have the tendency to recombine, if they are not separated soon after their generation.

The fundamental mechanism by which electrons and holes are separated in a photovoltaic is a built-in asymmetry which is responsible for driving electrons and holes into different directions. This driving force can be a gradient in the charge density of the two charge carriers. This can also be represented as the conductivity being selectively more favorable to one of the two charge carriers at one of the interfaces.

This driving force can be established by a gradient in the electronic environment. The driving force will result in a net current by removing charges from the absorber. Fundamentally two different types of currents can arise: a drift current due to an electric field in the absorber or a diffusion current due to a difference in charge carrier density or a selective removal of one of the two charges.

An electric field can be established at the interface of two materials with different work function, it if persists in equilibrium, this is commonly referred to as a *built-in* field. Furthermore, differences in electron affinity, band gap and density of states can also give rise to an electric field which, in turn, is named *effective* field. Electric fields can effectively separate photogenerated electrons from their holes by driving the two charges into opposite directions, thus generating drift currents

Diffusion currents, in contrast, are the result of asymmetry in the device introduced by charge selective contacts removing only one type of charge. Such a charge-selective contact is characterized by low resistance for the preferential charge carrier and a high resistance for its counterpart of opposite charge. By exclusively allowing, for example, holes to leave

the system on one interface, a density gradient will be established, being high far away from the interface and low near it. This hole density gradient will drive a hole diffusion current towards this interface, which will effectively act as a hole-sink. If the other contact has a similar selective preference for electrons, the same density gradient will arise for the photogenerated electrons driving an electron diffusion current in the opposite direction of the hole-collecting contact. The overall diffusion current in this device is the sum of the hole and electron diffusion current.

2.1.4 Semiconductor junctions and contacts

In the discussion of how photogenerated charges are separated and extracted in a photovoltaic device, it has become evident that the contacts to the absorber play a fundamental role for a working photovoltaic device by either establishing an field that drives charges towards the contacts or by producing a gradient in the charge density thus inducing diffusion currents. The dominating mechanism depends on the material properties of the absorber and the contacts, and the type of junction they form.

Semiconductors have been introduced conceptually in a previous section, being characterized as solids with two bands which have different charge carrier populations and are separated by a band gap which has the energy range of visible light. The equilibrium distribution of electrons throughout a semiconductor is governed by the Fermi-Dirac distribution, which provides a probability for an electron to occupy an electronic state with energy E at temperature T

$$f(E,T) = \frac{1}{\exp\left(\frac{E-E_\mathrm{F}}{k_\mathrm{B}T}\right)+1} \tag{2.1}$$

At $T = 0\ K$, electrons have no kinetic energy, they will therefore occupy the allowed states of lowest energy, filling all the states up to the *Fermi energy* E_F. In an intrinsic semiconductor, this energy will be located in the middle of the conduction band. Its position can also be quantified with respect to the vacuum energy level by the *work function* Φ, which is a material specific property

$$\Phi = E_\mathrm{vac} - E_\mathrm{F} \tag{2.2}$$

In metals the work function is equal to the *electron affinity* χ, which is the energy gained by moving an electron from the vacuum level to the conduction band edge. The work

function of semiconductors can be modified by doping. Introducing foreign species to the semiconductor lattice can add additional occupied states above the intrinsic Fermi level thus n-doping the material, or additional unoccupied states below the intrinsic Fermi level thus p-doping it. Upon doping the Fermi level will move to a new position, therefore n-doping results in a decrease in the work function and p-doping leads to an increase in the work function $\Phi_n < \Phi_i < \Phi_p$.

When two materials with different work functions are brought in contact, the Fermi levels of the two will equilibrate and form one constant energy level. This gives rise to an electrostatic field across the junction because the vacuum levels now have a gradient i.e. there is now a difference in electrostatic potential across the junction (figure 2.4 and 2.9).

When the two materials that form the junction are the same semiconductor at two different doping levels, this is referred to as *homojunction*. When two different semiconductors or a semiconductor and a metal are forming the junction, this is called a *heterojunction*.

A metal-semiconductor junction is shown in figure 2.4. The semiconductor is n-doped and has smaller workfunction than the metal $\Phi_{\text{sc}} < \Phi_m$. The lower lying Fermi level of the metal implies that when the two materials are brought into contact, electrons from the semiconductor will flow to the energetically lower lying states in the metal. Because the two materials were charge-neutral prior to contact, when electrons move from the semiconductor to the metal, they leave behind positive ions which are immobile and hence form space-charge. Simultaneously, negative charges accumulate in the metal. When the built-up charge gradient is strong enough to counteract the charge exchange, thermal equilibrium between the semiconductor and the metal is reached.

Near the interface, the difference in the vacuum level energies between the two materials gives rise to a gradient in the electrostatic potential. Because of the higher dielectric constant of the semiconductor, i.e. the higher capacity for storing charge, most of the potential difference is dropped across the semiconductor. Further away from the junction, the vacuum level reaches its value prior to the contact and stops varying. Here, the electric field goes to zero. The region across which this field extends into the semiconductor is referred to as *space charge region* because mobile charges have been drained into the metal, leaving behind uncompensated immobile charges, namely ionized atoms, this is why it is also called *depletion region*. As band gap and electron affinity are intrinsic properties of a material, they remain the same after contact. Conduction band and valence band therefore bend

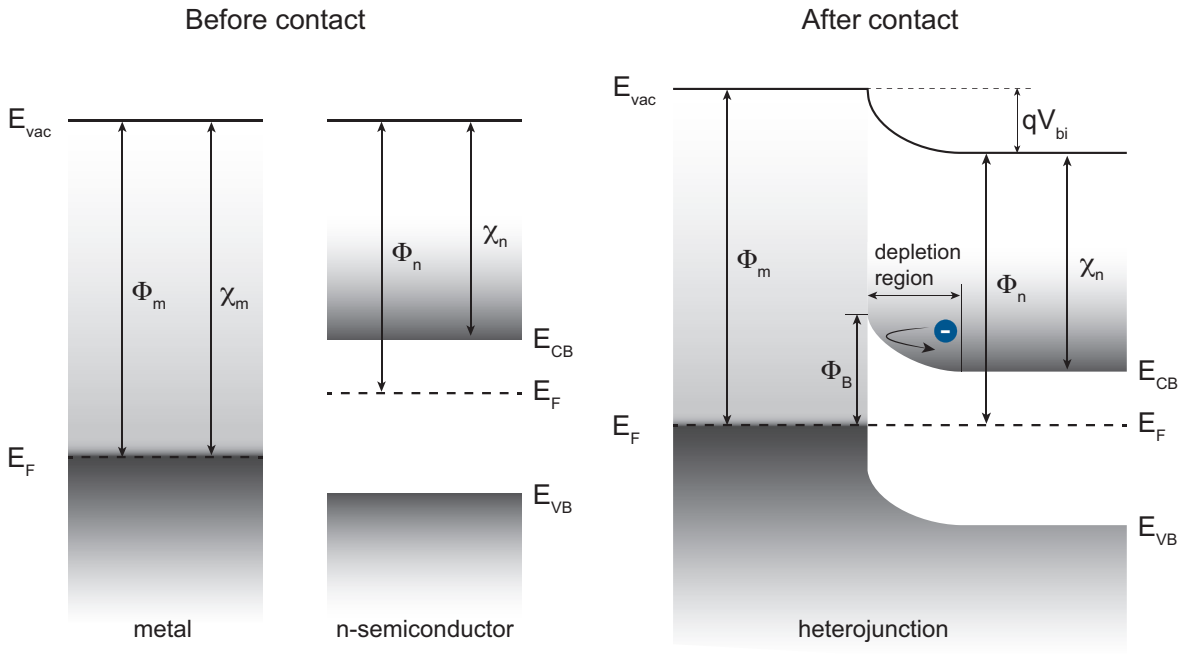

Figure 2.4: A metal with a workfunction Φ_m is brought in contact with an n-type semiconductor with the workfunction Φ_n are brought into contact. Because the semiconductor workfunction is smaller than that of the metal $\Phi_n < \Phi_m$, electron will flow from the semiconductor to the metal, leaving a positively charge depletion region behind. The Fermi level of the metal-semiconductor junction must be constant, but electron affinity and band gap are fixed material properties, which brings about a difference in the vacuum levels of the two materials giving rise to an electrostatic field near the interface. Conduction and valence band bend corresponding to the vacuum level. The conduction band bends such that an energetic barrier (Φ_B) for electrons forms preventing their transfer from the semiconductor to the metal. In contrast, the band bending of the valence band makes this transfer of the minority carriers, the holes, energetically favorable.

corresponding to the bending of the vacuum level. The magnitude of this band bending is given by qV_{bi} with V_{bi} being the built-in potential. The conduction band bends such that an energetic barrier (Φ_B) for electrons forms preventing their transfer from the semiconductor to the metal. In contrast, the band bending of the valence band makes this transfer of the minority carriers, the holes, energetically favorable. The potential barrier with the height Φ_B is also referred to as *Schottky barrier*.

This junction between an n-type semiconductor and a metal now has a built-in electric field at the interface that will drive electrons into the semiconductor and holes towards the metal, thus providing a mechanism for separating charges. This contact is a high-resistance contact for electrons. It is called a *Schottky junction* and can be employed as photovoltaic device.

The asymmetric behavior of this junction can be understood by observing its current-voltage characteristics in the dark (figure 2.5). In an n-type semiconductor conduction is

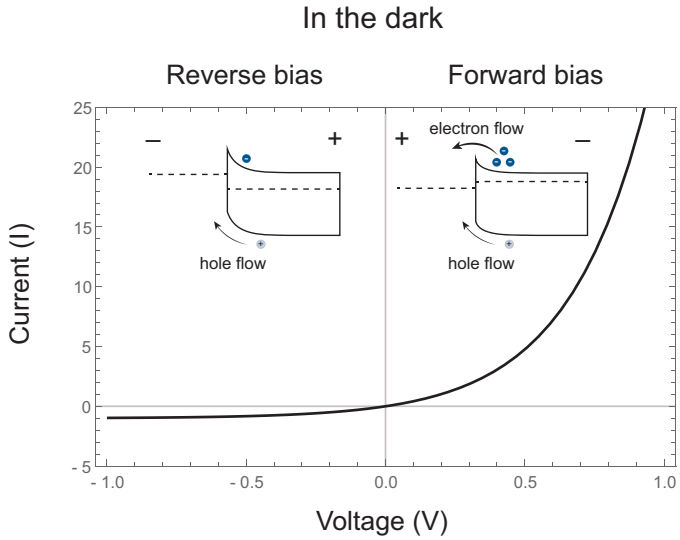

Figure 2.5: Dark current-voltage characteristics of a Schottky juntion between an n-type semiconductor and a metal, as sketched in figure 2.4. For negative or *reverse* bias, the potential barrier Φ_B increases. As a consequence, the diffusion of electrons from the semiconductor, which are the majority carriers in this device, is suppressed. A low current persists in this regime, which is the drift current of holes from the semiconductor to the metal. This current is small because it is limited by the small density of holes. In contrast, when a positive bias is applied, electrons are pushed into the depletion region reducing the Schottky barrier. As a result the electrons can flow across the junction, generating a diffusion current which increases exponentially with the external bias. The asymmetric current-voltage characteristic of the junction is referred to as rectifying or diode behavior.

reliant on the flow of electrons. The Schottky barrier at the interface, however, blocks the transfer of electrons. Only a small fraction of electrons have enough kinetic energy to surmount the barrier. At equilibrium, this diffusion current is balanced by a drift current of holes which are driven from the semiconductor to the metal.

Applying a forward bias, i.e. when a negative bias is applied to the n-terminal, in this case the semiconductor, electrons are pushed into the depletion region, compensating for the positive space charge and thus reducing the potential difference. As a consequence, the barrier height is decreased and more electrons can be thermally activated to overcome it, constituting a diffusion current to the metal. This current is referred to as forward current and increases exponentially with the decrease of the barrier height and the increase of the external bias.

In contrast, applying a reverse bias, the potential barrier increases in height, further reducing the number of electrons that can transfer to the metal thus suppressing any diffusion current. What remains is the small drift current of holes, which is limited by the low density of holes. This current is also referred to as *leakage current*.

This characteristic that current can flow for forward bias but not for reverse bias is referred to as *rectifying behavior* and constitutes the charge separation property of the junction. The difference in the work function of the metal and the semiconductor determine the magnitude of the band bending and thus the asymmetry between forward and reverse current. This property is exploited under illumination to extract photogenerated charges (shown in figure 2.6).

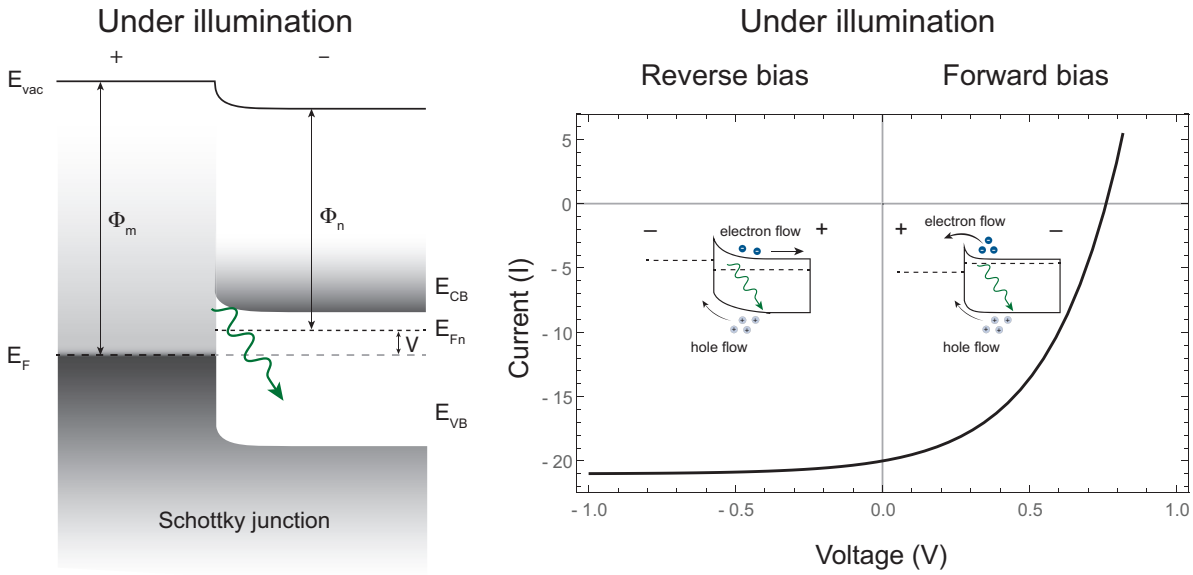

Figure 2.6: Current-voltage characteristics under illumination of a Schottky junction between an n-type semiconductor and a metal.

Under illumination, photons with an energy larger than E_g will promote electrons into the conduction band of the semiconductor. The electric field will drive concomitantly created holes to the metal, resulting in an accumulation of electrons in the semiconductor. This accumulation of negative charge will counteract the positive space charge in the semiconductor and thus reduce the potential difference across the interface. The photoexcitation of electrons therefore disturbs the thermal equilibrium in which the occupancy of all electronic states is governed by the Fermi distribution (1.1). As long as the change in the charge carrier distribution is small and relatively slow, the distribution of electrons and holes can be approximated by describing them individually with a quasi-equilibrium distribution around their own respective quasi-Fermi levels. The quasi-Fermi level of the electrons will be higher than the Fermi level of the junction due to a population increase of electrons in the conduction band. This difference between the Fermi levels, the quasi-Fermi level of electrons in the semiconductor and the Fermi level in the metal, thus establishes a *photovoltage* V which is

essential for photovoltaic energy conversion (figure 2.6 a)).

The photovoltage acts in the forward direction i.e. the accumulation of photogenerated electrons on the n-side of the junction reduce the potential barrier similar to applying an external forward bias. The photovoltage is largest when the two terminals are not connected. In this configuration, there is no net current flow because the diffusion current from the electrons matches the drift current of photogenerated holes. In the current-voltage characteristics, this configuration can be identified as the crossing of the curve with the current axis (marked by a the red circle in figure 2.6 b)). When the two terminals are connected without a load, the two chemical potentials of the semiconductor and the metal equilibrate. There is no potential difference throughout the device and hence no photovoltage. In this configuration (marked with a green circle in 2.6 b)), a large photocurrent flows through the junction. This current is the reverse drift current composed of photogenerated holes. In between these two configurations, a load can be introduced into the circuit. The photovoltage will drive the photocurrent through the load thus performing work, or in other words, the junction generates power (more details in chapter 2.2).

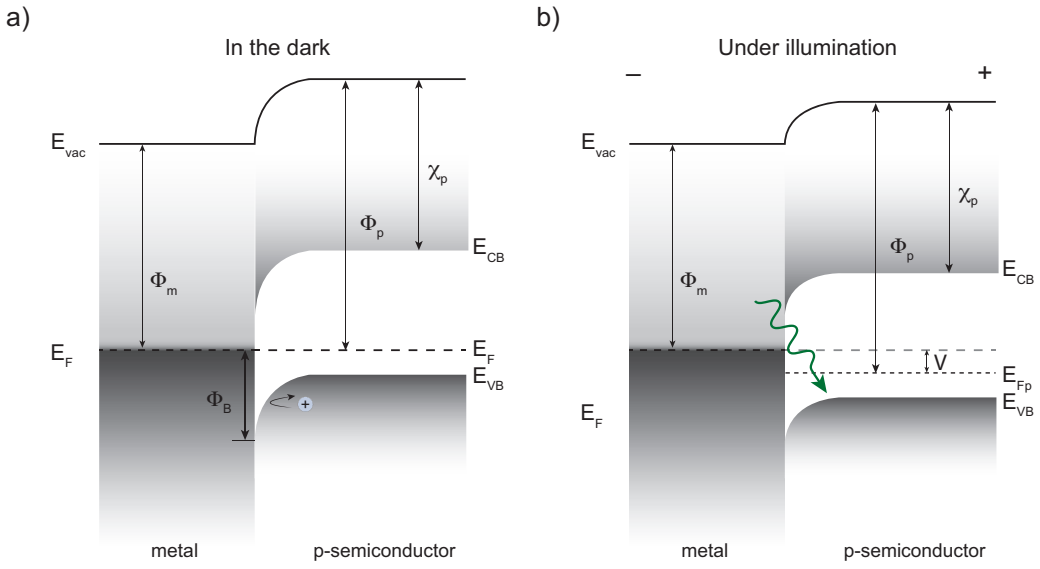

Figure 2.7: a) Contact between an p-type semiconductor and a metal whose workfunction is smaller than that of the semiconductor $\Phi_m < \Phi_p$. The band bending is therefore unfavorable for holes which constitute the majority carriers, thus blocking their flow into the metal in equilibrium. b) Under illumination and at open circuit, the accumulation of holes results in a lowering of the quasi-Fermi level in the semiconductor reducing the height of the Schottky barrier allowing thermally activated holes to transfer into the metal. At open-circuit, this hole diffusion current is equal to the drift current of the electrons, there is no net current flowing through the junction.

Analogous to the described configuration with an n-type semiconductor, in the case of p-type junction, a Schottky junction arises when $\Phi_m < \Phi_p$. The majority carriers in this junction are the holes of the p-semiconductor. The arising Schottky barrier bends downwards and thus blocks the hole flow from the semiconductor into the metal (figure 2.7). In the equilibration of the Fermi levels upon contact, holes flow from the semiconductor into the metal leaving behind negative space charge. Electrons are the minority carrier due to their low density and are driven across the junction by the electric field, constituting the leakage current of the junction. At equilibrium, this current is balanced by thermally activated holes, so that there is no net current flowing through the junction. Under illumination, the photogenerated electrons generate a drift current from the semiconductor into the metal while the holes diffuse away from the junction into the semiconductor. This junction exhibits the same rectifying behavior as the n-type junction, except for having the opposite polarity.

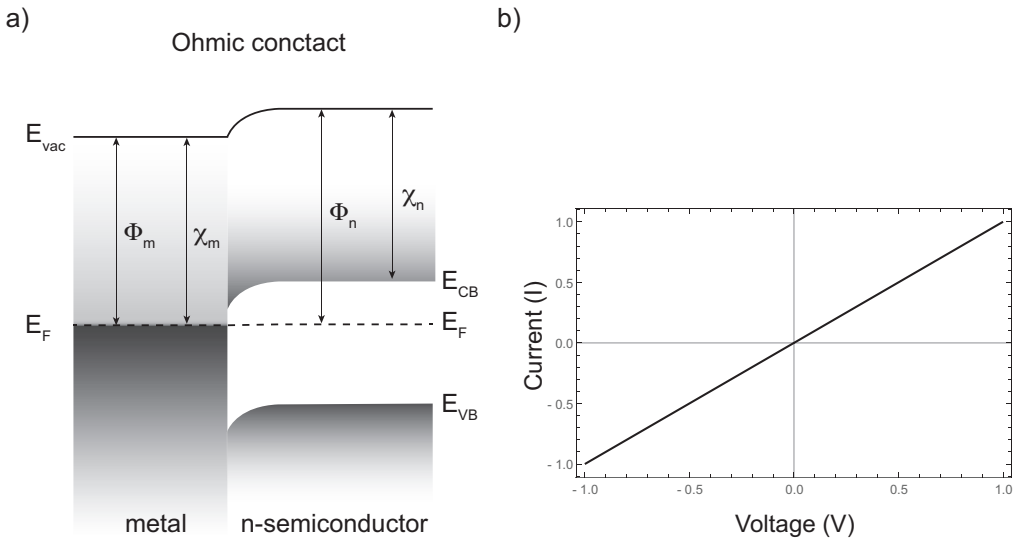

Figure 2.8: Contact between an n-type semiconductor and a metal whose workfunction is smaller than that of the semiconductor $\Phi_m < \Phi_n$. The band bending is therefore favorable for electrons which constitute the majority carriers, thus allowing them to flow in both directions of the junction.

Metal-semiconductor junctions are not necessarily always Schottky junctions. When the work function of the n-type semiconductor is larger than that of the metal $\Phi_\mathrm{n} > \Phi_m$ the bands bend in the other direction and therefore facilitate the transfer of electrons, the majority carriers, from the semiconductor to the metal, and inhibit the same transfer path for holes, the minority carrier (figure 2.8 a)). The potential difference leads to an accumulation of the majority carriers in the junction, making it carrier rich. The downward bending conduction band allows the electrons to readily flow across the junction in both directions, making it a

low-resistance contact, referred to as *Ohmic contact*. Under illumination no photovoltage is established because both charges can move across the junction, so that there is no process which selectively removes the minority carriers, which is the underlying mechanism for it. Without rectifying behavior the current can flow in both directions, linearly following the applied bias (figure 2.8 b)).

The description so far is largely based on the approximation that the energy states on the surface behave similar to the states inside the bulk of the solid. This approximation is known as the *Schottky-Mott* approximation, which stipulates that the Schottky barrier height can be derived in the case of an n-type junction from the difference between the metal work function and the electron affinity of the semiconductor, i.e. the difference between the Fermi level of the metal and the interfacial conduction band edge. In reality, however, semiconductor observe this rule to a varying degree [34]. The underlying cause is a phenomenon referred to as *Fermi-level pinning*, which makes the band bending almost independent of the work function of the metal. This disconnect between the height of the Schottky barrier and the properties of the metal arises due to interfacial states inside the semiconductor band gap. These states can be induced by the metal itself or they can be free surface states whose position can differ significantly from those of the bulk [35]. Upon contact with the metal, most of the charges flowing from the metal to the semiconductor are absorbed by those states, thus shielding the band structure of the bulk from the charges from the metal.

Aside from metal induced band gap states, there are further limitations to a Schottky junction as a photovoltaic device. The photovoltage of the junction is dependent on the height of the barrier. Which can only maintain a photovoltage up to a height approaching half of the width of the band gap. For larger barrier heights, the minority carrier will start to dominate the charge flow thus reducing the potential difference. Highly doped semiconductors can lead to the formation of very abrupt barriers, which are thin enough for the majority carriers to tunnel through them and therefore reducing the effectiveness of the barrier.

These limitations can be overcome by junctions between a p-type and an n-type semiconductor. Such a *pn-junction* can be formed both as a homojunction or a heterojunction. Most commonly, it is a homojunction, in which the same semiconductor is heavily p-doped on one side, and heavily n-doped on the other side. The smaller work function of the n-doped side implies a lower electrostatic potential compared to the p-doped side, giving rise to an electric field across the junction. The physical process establishing the field occurs when the

two sides are put in contact. As a consequence, the Fermi levels of the two differently doped sides will equilibrate. In this process the mobile majority carriers, electrons on the n-side and holes on the p-side, will diffuse into the other side where they recombine. The mobile carriers leave behind ionized immobile donor and acceptor atoms, which lacking their mobile counterparts to neutralize them, constitute space charge of opposite polarity to the doping type.

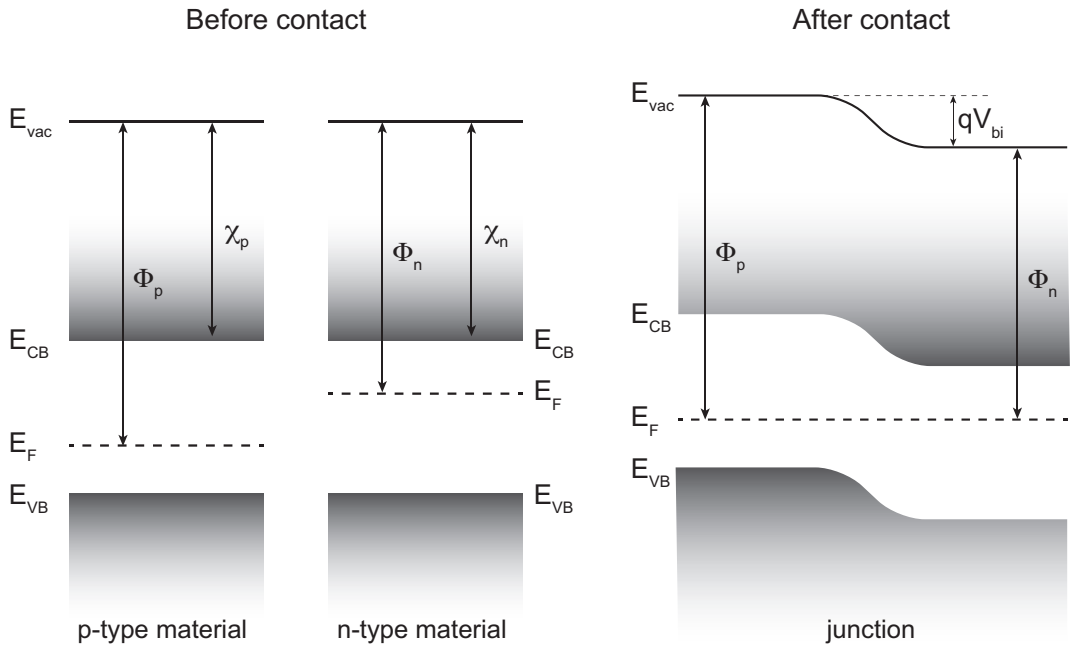

Figure 2.9: Two semiconductors with different work functions (i.e. different Fermi level positions with respect to the vacuum level) are brought into contact. Because the Fermi level has to be constant in equilibrium, the vacuum levels now have a gradient which is equivalent to a difference in electrostatic potential thus giving rise to an electrostatic field across the junction.

The electrostatic field will drive minority carriers across the junction giving rise to drift currents, while diffusion drives a current in the opposite direction. At equilibrium, both currents are balanced so there is no net current flowing across the junction. The drift current is limited by the number of minority charge carriers. The diffusion current is limited by the high-resistance imposed by the potential barrier for both electrons and holes. Under illumination charges are generated throughout the p- and n-layer, once they diffuse into the depletion zone, they are driven across the junction by the electric field as drift current.

The current-voltage characteristics of a pn-junction are very similar to those of a Schottky-junction. However, in a solar cell a pn-junction has several advantages. As mentioned, the thermal deposition of a metal onto the semiconductor can introduce defect states. A pn-junction can also achieve much higher built-in voltages without giving rise to an inversion

layer in which the minority carrier start to outnumber the majority carriers

2.1.5 Polymer heterojunctions

The concept of Schottky or pn-junctions is very useful for inorganic solid-state semiconductors such as silicon and gallium arsenide because the dielectric environment, i.e. a relatively large dielectric permittivity, allows for direct dissociation of electron-hole pairs. These pairs of photogenerated charges, referred to as excitons, are bound by electrostatic Coulombic attraction. Their binding energy therefore scales inversely with the dielectric permittivity $E_b \propto 1/\varepsilon_0$. In silicon, which has a dielectric permittivity of 11.4, the binding energy of the photogenerated excitons is merely ~ 15 meV [36]. This binding energy is therefore smaller than the thermal energy $k_\mathrm{B}T \sim 25$ meV at room temperature, and the dissociation of these excitons can occur spontaneously.

In contrast, for conjugated polymers, which have a similar band structure to inorganic semiconductors, the dielectric permittivity is much lower [37] resulting in a binding energy of the geminate electron-hole pairs exceeding the thermal energy by more than an order of magnitude [38]. The electrostatic fields in these materials are unable to separate the excitons into free carriers, which are needed to generate photocurrent. Instead, an additional driving force is required to split the excitons. This can be provided by an interface of two materials with strongly differing electron affinities, so that the potential drop at this interface is larger than the exciton binding energy [39]. In order to extract free charges, excitons must reach this interface before they have a change to recombine. The exciton diffusion length in these materials is only on the orders of tens of nanometers [40]. Significant optical absorption, however, requires the absorber to be rather on the order of hundreds of nanometers. These two conflicting requirements can both be met by distributed interfaces in a blend structure (figure 2.10 a)). The two interfacial materials of such a *bulk heterojunction* are the *donor*, typically a low-band gap polymer which absorbs across a wide range of the solar spectrum, and the *acceptor*, typically a fullerene derivative with a very high ionization energy i.e. a low lying valence band equivalent. The large difference in electron affinities between the donor and the acceptor material gives rise to strong electrostatic fields in the immediate vicinity of their interface. These fields are therefore able to dissociate excitons which reach this interface by transferring the electron into the acceptor material while the hole remains in the donor material. As free charges or *polarons*, hole and electron can now diffuse through their respective media to the collecting electrode.

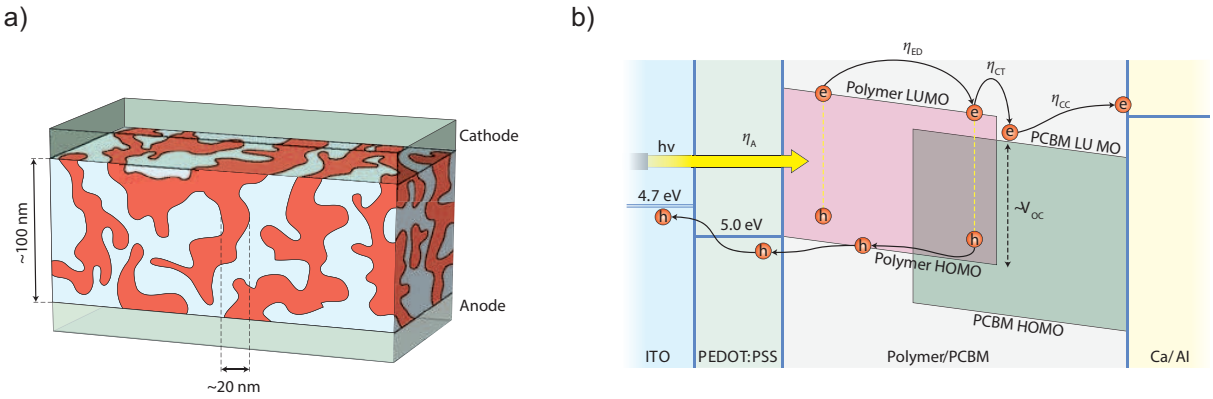

Figure 2.10: a) Conceptual morphology model with bicontinuous interpenetration network of the polymer and the acceptor b) The conceptual operating mechanism of an organic polymer solar cell. the photon absorption in the donor material generates excitons which are then separated into free charges at the interface with the acceptor material. This exciton dissociation occurs when the electron is transferred to the acceptor while the hole remains in the donor. Once separated the charges can diffuse to their respective electrodes. The photovoltage of such a device is determined by the potential difference between the acceptor energy level (LUMO) of the electron population and the donor energy level (HOMO) of the holes. (Reproduced with permission from Li *et al.*, Nat. Photonics 2012, 6, 153 [39]. Copyright 2012 Nature Publishing Group.)

A blend structure, such as the one shown in figure 2.10 a), consists of a bicontinuous interpenetration network of donor and acceptor material. There the individual domains provide interfaces within reach of the exciton diffusion while the overall absorber structure can be hundreds of nanometers thick and thus have sufficient optical depth. Selective charge collection is facilitated by the built-in asymmetry of the different workfunctions of the contacts (figure 2.10 b)).

2.1.6 Dye-sensitized junctions

Dye-sensitized junctions are based on a very similar principle, with the difference, that light absorption does not occur in the electron donor but instead in a sensitizer at the interface between an electron and a hole accepting material. The sensitizer is typically anchored to the electron accepting material, which will have a larger electron affinity than the sensitizing dye molecules, giving rise to the junction which splits the excitons.

In a typical device structure with a dye-sensitized junction, the photoactive material consists of a dye-sensitized mesoporous layer of TiO_2 particles which have been sintered together in order to facilitate the electron transport within the layer. This mesoporous layer

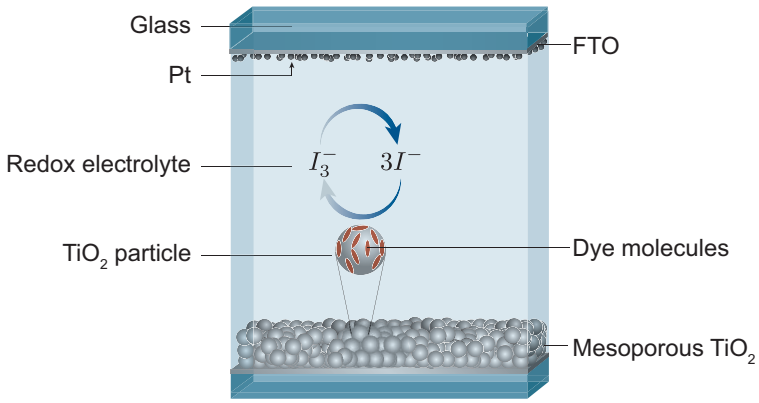

Figure 2.11: Scheme of a dye-sensitized solar cell. At the bottom a tens of micrometer thick layer of mesoporous TiO_2 forms the n-type contact. This layer consists of nanometer size TiO_2 particles which are sensitized with an absorber dye. The p-type contact of the junction is an electrolyte which contains a redox couple, typically iodide-triiodide. The p-type charge transfer occurs by re-reduction of triiodide to iodide at the platinum electrode at the top.

can have a thickness of several micrometers, the individual nanoparticles, it is composed of, typically have a diameter of 10-30 nm. The sensitizer commonly has a functional group that specifically anchors to TiO_2 enabling the formation of a monolayer of dye on top of the mesoporous layer. The mesoporosity of the TiO_2 layer mimics the distributed, interpenetrating interfacial network of the organic bulk heterojunction by maximizing the interface between the dye and the electron acceptor. The hole-accepting material in these devices consist of an electrolyte with a redox couple which infiltrates the mesoporous structure of the sensitized electron acceptor. A redox couple contains two ionic species which each have a different oxidation state. In dye-sensitized solar cells (DSSCs) this redox couple is typically iodide/triiodide [41]. This redox couple has one partner with a more positive charge, the oxidized species in this case triiodide, and one partner with a more negative charge, the reduced species, here, this is iodide. These two species are able to exchange an electron which is how they transfer charge.

The working principle of a DSSC can be described as six consecutive electron transfer steps, which are illustrated in figure 2.12. Upon photoexcitation an electron from the ground state of the dye is promoted into its excited state. The energetically lower position of the TiO_2 conduction band allows the system to minimize its free energy by injection of the excited electron into the conduction band of the oxide. After the electron donation, the dye molecules are in an oxidized state from which they are restored via electron transfers from an electrolyte redox couple (6). The dye-regenerating electron transfer transforms iodide molecules into triiodide molecules which subsequently diffuse through the electrolyte to the

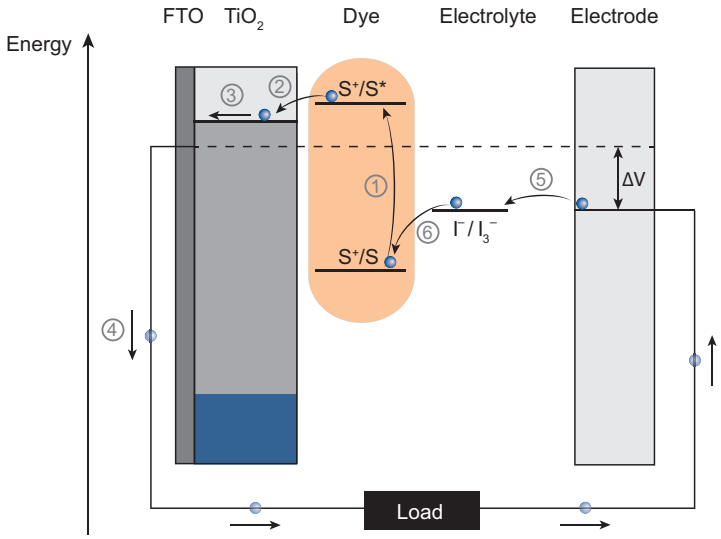

Figure 2.12: Energy scheme of a dye-sensitized solar cell. The working principle is illustrated by the consecutive electron transfers (1-6), neglecting, however, back-electron transfers. In step (1), an electron is promoted by photon absorption into the excited state of the dye. It is then in step (2) rapidly transferred into the conduction band of the TiO_2 layer. In step (3) it migrates through the mesoporous TiO_2 layer and is extracted into the circuit, where it can do work (4). In step (5), an electron transfer from the platinum reduces tri-iodide (I_3^-) to iodide (I^-). In step (6), iodide reduces the oxidized dye molecule by donating an electron.

cathode. At the platinum coated cathode the triiodide molecules are re-reduced to iodide molecules through an electron transfer from the cathode (5). This constitutes one half of the electronic circuit of the device.

The other half of the circuit involves the photogenerated electrons which upon excitation in the dye molecules are injected into the conduction band of the TiO_2 particles (2) which make up the mesoporous layer. The electrons can migrate through the interconnected mesoporous network until they reach the transparend electron-collecting electrode (3). There the electrons are introduced into the electric circuit (4) where they can do work on their way to the cathode where the triiodide molecules are reduced and thus completing the circuit. This is schematically illustrated in figure 2.12.

After the seminal discovery by Grätzel and O'Regan in 1991 [42], within a few years the power-conversion efficiency rapidly rose to 10% but experienced merely incremental improvements up to 11.9% to date [33]. A big limitation of this device design is the liquid electrolyte, in particular with respect to stability and practicability.

A consequential development was the discovery by Bach *et al.* that the liquid electrolyte can be replaced by solid-state organic hole transport material, namely 2,2,7,7-tetrakis-(N,N-di-p-methoxyphenylamine)9,9-spirobifluorene (spiro-OMeTAD), thus bringing about

the solid-state dye-sensitized solar cell [23]. While the solid-state incarnation of the DSSC never exceeded the efficiency of its liquid counterpart, it was an essential step on the way of the evolution of the perovskite solar cell.

The important property of all discussed junctions is the built-in asymmetry which is the key for selective charge collection by driving photogenerated electrons and holes into different directions. In inorganic solid-state junctions this asymmetry is based on a difference in electronic properties of two interfacial materials, such as work function, electron affinity, band gap or density of states. Upon contact these spatial variations in electronic properties give give rise to electrostatic fields which can drive the charge separation and collection. The photovoltage of a junction is determined by the maximum charge separation.

2.2 Solar cell characterization

The objective of a solar cell is to perform work on a load. The output of a solar cell is measured as work done per unit of time i.e. electrical power, which is defined by the product of current and voltage

$$P = \frac{Q \cdot V}{t} = I \cdot V \tag{2.3}$$

A solar cell must therefore generate both current and voltage. As outlined in the previous sections, the property of a device to do that is a two-level absorber system in combination with a built-in asymmetry to separate the photogenerated charges. This asymmetry commonly results in rectifying behavior which will allow significantly larger current flow under forward bias than under reverse bias. The physical principle underlying this phenomenon is explained in detail in 2.1.4.

When the two terminals of a solar cells are connected without any load, the device operates at short-circuit and the generated photocurrent is referred to as *short-circuit current* (commonly given as current density J_{sc}). It is dependent on the size of the band gap and the intensity of the incident light.

When a load is present in the circuit this results in a potential difference between the two terminals. The arising electric field will induce a current which flows in the opposite direction of the photocurrent. This reverse current is independent of illumination and also flows in the dark, it is therefore referred to as *dark current*. This current describes the

rectifying diode behavior of small reverse current (drift current) and large forward current (diffusion current). For an ideal diode, this current is dependent on the applied bias

$$J_{\text{dark}}(V) = J_0 \left[\exp\left(\frac{qV}{k_{\text{B}}T} \right) - 1 \right] \tag{2.4}$$

The constant J_0 is the reverse saturation current. It is a junction and material specific property which is dependent on the minority carrier concentration and is largely independent of the bias. The net current-voltage characteristics of junction can - in approximation - be described by the short-circuit current minus the dark current in the *ideal diode equation*

$$J(V) = J_{\text{sc}} - J_0 \left[\exp\left(\frac{qV}{k_{\text{B}}T} \right) - 1 \right] \tag{2.5}$$

When the two electrodes are not connected, the potential difference between them has its maximum value, the *open-circuit voltage* (V_{oc}). This configuration corresponds to a load in the circuit at which the dark current matches the photocurrent and there is no net current flowing through the device $J(V) = 0$

$$V_{\text{oc}} = \frac{k_{\text{B}}T}{q} \ln\left(\frac{J_{\text{sc}}}{J_0} + 1 \right) \tag{2.6}$$

Since the current in an ideal diode is proportional to the light intensity, the photovoltage depends logarithmically on the light intensity. The photovoltage is defined in the forward bias region.

A solar cell therefore operates in the regime from 0 to V_{oc}, in which the product of its photocurrent and photovoltage are positive, and the device produces power $P_A = J \cdot V > 0$. The maximum-power point (MPP), when the product of current and voltage reaches its maximum value, defines the operating point of a solar cell (figure 2.13). The ratio of the product of the maximum-power point current J_{MPP} and voltage V_{MPP} to the product of the the maximum current J_{sc} and the maximum voltage of the device V_{oc} defines the fill factor (FF).

$$FF = \frac{J_{\text{MPP}} \cdot V_{\text{MPP}}}{J_{\text{sc}} \cdot V_{\text{oc}}} \tag{2.7}$$

The fill factor is a measure of the "squareness" of the current-voltage curve, i.e. it describes the fraction of generated power output compared to an idealized maximum power output in a case of no internal losses.

The *power-conversion efficiency* (PCE) is defined as the fraction of generated maximum power density P_{MPP} compared to the power density coming from the incident light P_{light}

$$\text{PCE} = \frac{P_{\text{MPP}}}{P_{\text{light}}} = \frac{J_{\text{MPP}} \cdot V_{\text{MPP}}}{P_{\text{light}}} = \frac{J_{\text{sc}} \cdot V_{\text{oc}} \cdot FF}{P_{\text{light}}} \tag{2.8}$$

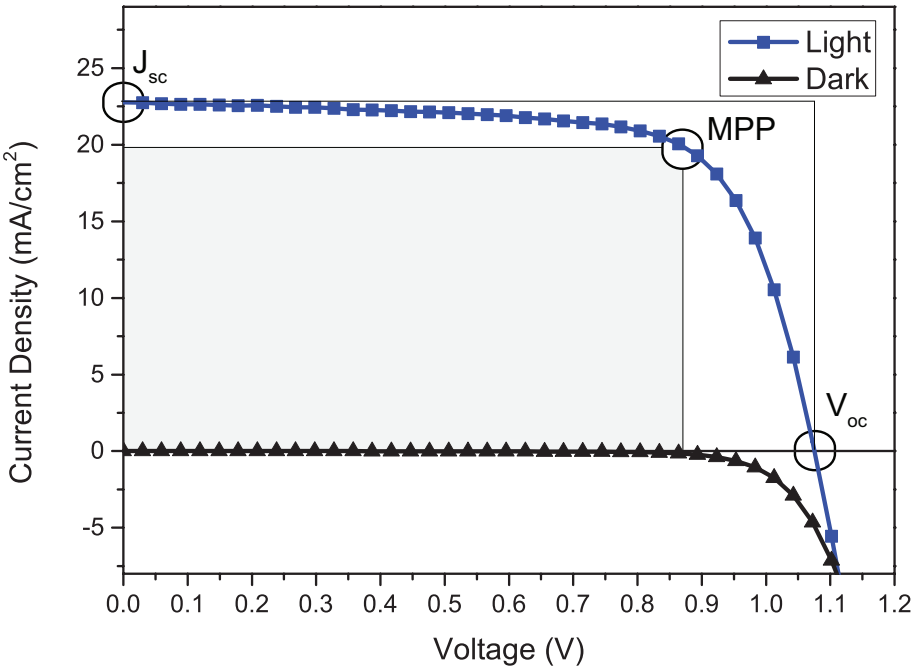

Figure 2.13: Current-voltage characteristics of a solar cell both in the dark and under illumination. The characteristic performance parameters have been highlighted. At short-circuit, when there is no load present in the circuit i.e. V = 0 V, the photocurrent reaches its maximum value, the short-circuit current J_{sc}. When the dark current turns on and matches the value of the photocurrent, the maximum photovoltage of the device, the open-circuit voltage V_{oc} is achieved and there is no net current flowing through the junction. The final performance parameter, the fill factor, is a metric for the "squareness" of the curent-voltage curve. It incorporates several intrinsic properties of the device including the series resistance, shunt resistance and homogeneity of the semiconductor. The fill factor is defined as the fraction of the rectangle defined by the product of the maximum power-point (MPP) voltage and current (shaded in light gray) to the product of the V_{oc} and the J_{sc} (no shading).

In order to allow for direct comparison of efficiencies, the measuring conditions need to be standardized. For solar cells, the standard test conditions (STC) include the Air Mass 1.5 spectrum, an incident power density of 1000 W m^{-2} (i.e. 100 mW cm^{-2}), and a temperature of 25°C.

There are two major resistances in a real device through which generated power is lost. The first one is the summation of all contact resistances through the device, referred to as *series resistance* (R_s). In particular, the contacts of the absorber contribute to this resistance. It impacts the JV-curve by reducing the steepness of the slope beyond the maximum power point (figure 2.14).

The second one arises due to leakage current i.e. ohmic diffusion currents through the diode in the rectification regime and through direct contact of contacts of different polarity. It particularly impedes the performance of poorly rectifying devices. These leakage currents

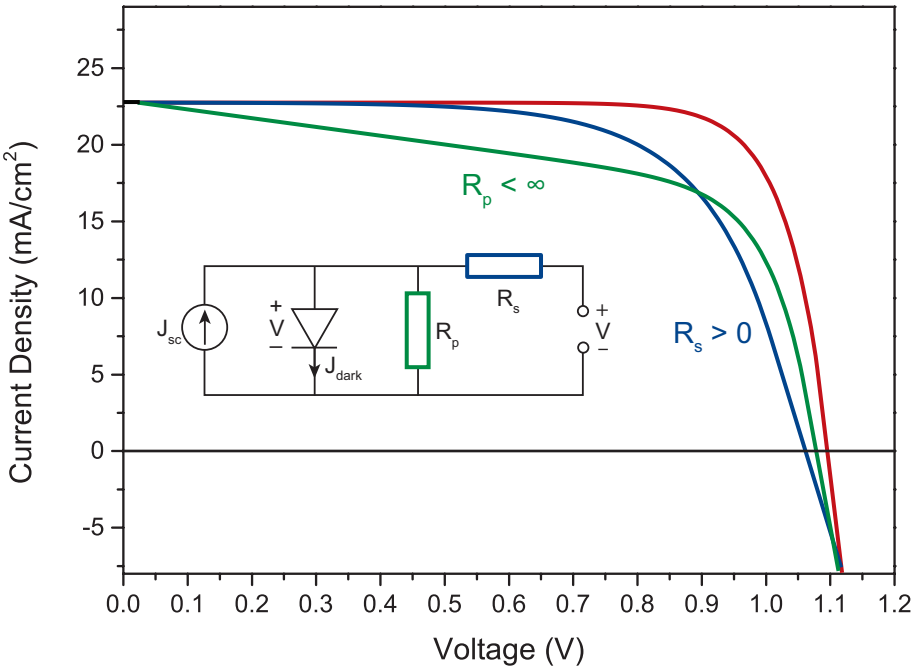

Figure 2.14: Current-voltage characteristics illustrating parasitic resistance losses. The JV-curve in red follows the ideal diode equation with $R_p \to \infty$ and $R_s = 0$. The JV-curve in blue shows the effect of $R_s > 0$, where the slope of the curve beyond V_{MPP} is reduced in steepness. The JV-curve in green has a reduced shunt resistance $R_p < \infty$, which is why its slope between zero and V_{MPP} is slanted and not horizontal. This is caused by leakage paths through the diode connecting the two electrodes, opening up an additional circuit with an non-infinite resistance as illustrated in the equivalent electrical circuit. This allows for linear ohmic diffusion currents to flow even in the rectifying voltage regime of the diode.

reduce the *shunt resistance* or *parallel resistance* (R_p) which in an ideal device would be infinitely large. The higher the shunt resistance, the more horizontal is the JV curve from zero to V_{MPP} (figure 2.14).

Both resistances impact the fill factor. A good fill factor requires the series resistance to be as low as possible, while the shunt resistance is a high as possible. Including these two so called parasitic resistances into the diode equation (2.5), it becomes

$$J(V) = J_{sc} - J_0 \left[\exp\left(\frac{q(V + J \cdot AR_s)}{k_B T} \right) - 1 \right] - \frac{V + J \cdot AR_s}{R_p} \tag{2.9}$$

A high efficiency can therefore only be attained for a device which has the following properties: the absorber layer absorbs photons broadly across the visible range and suffers from very few non-radiative decay losses, thus providing a large photocurrent and photovoltage; and the charge-selective contacts have very high charge carrier mobilities thus minimizing the series resistance, while also being very charge selective to prevent recombination losses and leakage currents, thus maximizing the shunt resistance.

2.3 Perovskite solar cells

2.3.1 Structure and stability

Perovskite solar cells contain as active layer a material which has an ABX_3 perovskite crystal structure (figure 2.15). This material is composed of a monovalent cation at the A site, a divalent metal cation at the B site and halogen anion at the X site. This specific configuration of a three-dimensional perovskite can only be formed by a certain combination of ions, determined by their respective size, which can be predicted by the Goldschmidt tolerance factor t

$$t = \frac{R_X + R_A}{\sqrt{2}(R_X + R_B)} \tag{2.10}$$

where R_X is the radius of the X^- anion, R_A is the radius of the monovalent cation, R_B is the radius of the divalent metal ion.

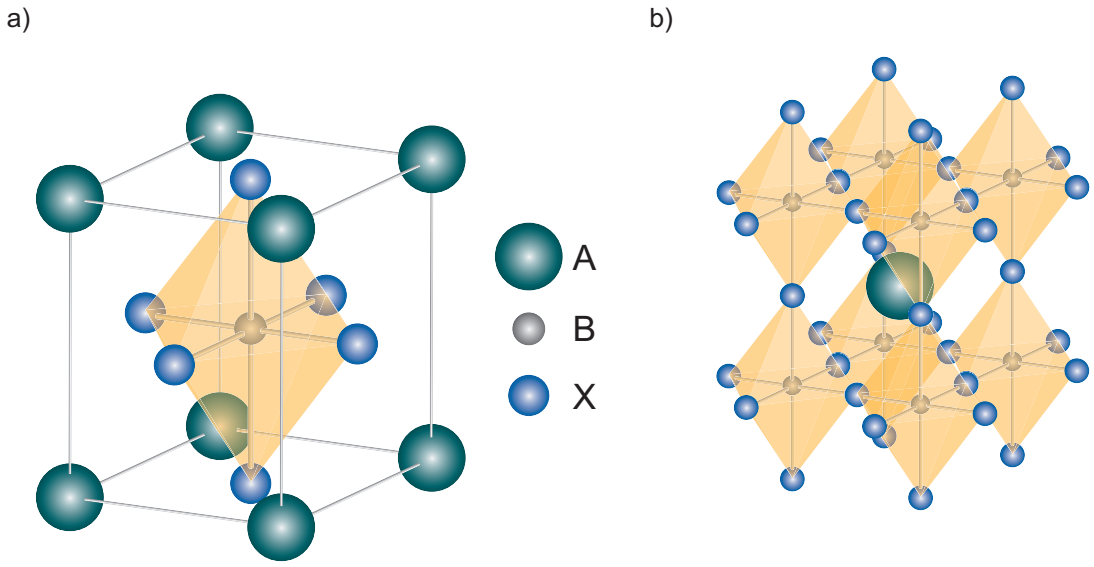

Figure 2.15: a) The ABX_3 unit cell characteristic for the perovskite crystal structure. Cations, which can occupy the A site include the inorganic Cs^+, and the organic methylammonium (MA, $CH_3NH_3^+$) and formamidinium (FA, $CH(NH_2)_2^+$). The metal cation at the B site can be occupied by any divalent metal ion such as Pb, Sn and Ge. The X site can in principal be occupied by any halide anion. b) In the perovskite bulk, ionically bound metal-halide octahedra which form a cage around the A site cation.

For a perfectly cubic perovskite structure $t = 1$. In practice, however, a three-dimensional cubic perovskite structure can be formed by ions if t is in the range $0.9 \leq t \leq 1$. For $0.7 \leq t \leq 0.9$ lower symmetry structures such as tetragonal, rhombohedral, hexagonal or orthorhombic can be formed [43].

Cations for the A site which have the appropriate size include the inorganic Cs, and the organic methylammonium (MA, $CH_3NH_3^+$) and formamidinium (FA, $CH(NH_2)_2^+$) [44]. The metal cation at the B site can be occupied by any divalent metal ion such as Pb, Sn and Ge, which have been demonstrated to possess beneficial optoelectronic properties in the perovskite configuration [25, 24, 45, 46, 47, 48].

Finally, the X site can in principal be occupied by any halide anion, however, most studies have thus far focused on iodide, bromide and chloride [45].

A three-dimensional perovskite structure can be obtained with practically any combination of these materials. However, two aspects govern the applicability of such a material for photovoltaic devices: it must have the right, beneficial optoelectronic properties such as wide-range absorption and high charge-carrier mobilities, on one hand, and sufficient structural and chemical stability for implementation in real-world applications, on the other hand. As the international standards for the stability of a photovoltaic device set the stipulate device integrity over a period of 25 years, both structural and chemical stability are of crucial importance in the development of new materials.

Structural stability relates to the property of a material to remain in one single crystalline phase over a relatively wide temperature range. This means that any new material must be inherently stable enough to meet the standard set by the International Electrotechnical Commission (IEC), which requires solar cells to undergo 200 thermal cycles between -40°C and +85°C without a deviation of the photocurrent larger than ±2% in current measured at peak power above 25°C [49]. Chemical stability, in turn, refers to the ability of the material be impervious to reactive species such as oxygen and water.

The prototypical material is methylammonium lead iodide $CH_3NH_3PbI_3$, in whose unit cell, the organic cation (MA^+) sits on the A site of the perovskite, lead cation (Pb^{2+}) occupies the B site and the anion iodide (I^-) the X site (figure 2.15 a)). In the crystal structure, the organic cation $CH_3NH_3^+$ forms hydrogen bonds to the surrounding PbI_6 octahedra (figure 2.15 b)).

Films have been fabricated via various methods such as spin coating [25, 24, 50] vapour deposition [51, 52], sequential deposition [53], and combinations thereof. In single-step spin-coating, a solution of the precursors is deposited onto a substrate, which is then heated to 100°C until the perovskite has fully crystallized.

The structural stability of this perovskite is largely governed by phase changes, which impact its optoelectronic properties such as band gap, absorption cross section, carrier mobilities, which in turn are relevant to the performance of photovoltaic devices. However, in depth studies have shown that materials of the $MAPbX_3$ class are quite crystallographically stable over a wide range of temperatures [25, 50, 54]. This suggests that the material has a high degree of structural stability. However, due the relatively low melting point of the methylammonium halides, the $MAPbX_3$ perovskites start to degrade after 30 minutes at 150°C [44].

Chemical stability, however, poses a significantly bigger challenge mainly due to the hygroscopic nature of the organic component. This hygroscopicity of methylammonium iodide translates into rapid degradation of the perovskite when the material is in contact with moisture and - in general - with all polar solvents [55]. The reason is structure specific. While the lead cation and the iodide anion form strong ionic bonds, the methylammonium is bound by comparatively weak hydrogen bonds in the perovskite structure [56]. Water molecules can readily infiltrate the perovskite crystal and bind more strongly to the organic cation. Even at a relative humidity of merely 10% every unit cell of a thin perovskite film can be occupied by a water molecule [56]. While at low relative humidity, moisture ingress can have beneficial effects on device performance [57], however, as the relative humidity is increased, the perovskite undergoes a chemical transformation into its hydrated phases. This process is reversible to a certain degree, however upon prolonged exposure, this hydration inexorably leads to the disintegration of the perovskite material [58]. The first hydration step involves the ingress of individual water molecules into the perovskite unit cell, forming the mono-hydrate phase $CH_3NH_3PbI_3{\cdot}H_2O$, which is in equilibrium with a small amount of the dihydrate phase, depending on the time and intensity of the moisture exposure [58]. Further exposure to moisture results in the formation of the crystalline dihydrate phase $(CH_3NH_3)_4PbI_6{\cdot}H_2O$.

Irreversible degradation of the perovskite is thought to occur when the dihydrate phase is further exposed to moisture leading to the dissolution of the organic cation $CH_3NH_3^+$ in the excess water following this reaction scheme

$$(CH_3NH_3)_4\ PbI_6 \cdot 2\ H_2O \xrightarrow{H_2O} 4\ CH_3NH_3I\textit{(aq)} + PbI_2\textit{(s)} + 2H_2O \tag{2.11}$$

The formation of the dihydrate phase is also observed by Christians et al. when exposing perovskite films to humid air in the dark and at room temperature [59]. This hydration

process is largely characterized by a change in crystal structure and a decrease in absorption across the visible range. However, the transient absorption measurements indicate that the hydrate phase does not have an effect on the charge carrier dynamics at short times (<1.5 ns). It is speculated that water permeates the perovskite crystal along the grain boundaries, leaving individual domains intact [58, 59]. The cause for the breakdown of the perovskite crystal structure lies with the hydrogen bonding of the $CH_3NH_3^+$ cation to the PbI_6 octahedra. When hydrated, H_2O bonds more strongly to the organic cation. This is particularly true when under light and heat, when the hydrogen bonding is weakened due to thermal strain.

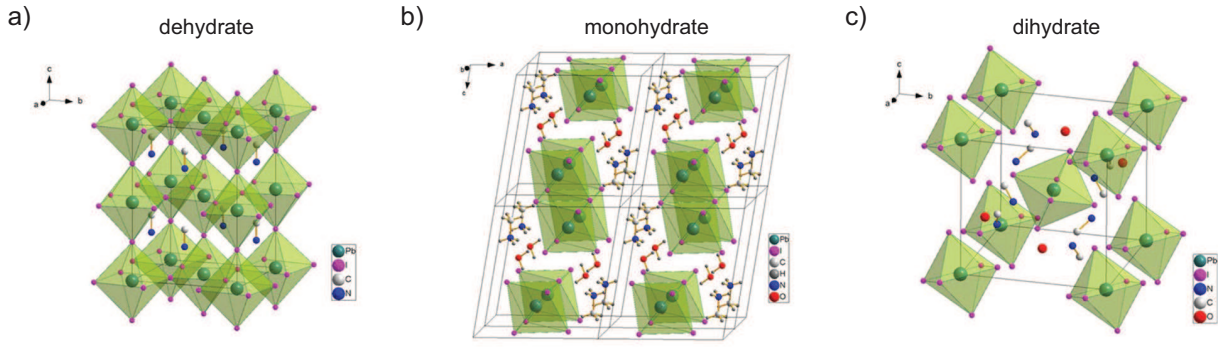

Figure 2.16: The crystal structure of $CH_3NH_3PbI_3$ is shown in d) together with the two hydration phases: e) monohydrate $CH_3NH_3PbI_3{\cdot}H_2O$ and f) dihydrate $(CH_3NH_3)_4PbI_6{\cdot}H_2O$ (Adapted with permission from A. Leguy *et al.*, Chem. Mater. 2015, 27, 3397-3407 [58]. Copyright (2015) American Chemical Society)

The structural changes induced by the hydration process are shown in figure 2.16. In a) the dehyrate phase in its cubic configuration is shown. When the perovskite transitions into the monohydrate phase, water intercalates into the perovskite breaking up the three-dimensional structure. Instead, the unit cell is now composed of one-dimensional, isolated $(PbI_3)^-$ double-chains, in which each $(PbI_6)^{4-}$ octahedron is connected to two neighboring octahedra by a common corner, and thus forming a two-octahedra-wide band. The charge-neutrality is maintained by the intercalated methylammonium cations which balance the negative $(PbI_3)^-$ chains. Further structural stability is provided by the H_2O molecules, which are inserted between $(PbI_3)^-$ chains, by forming hydrogen bonds between the hydrogen atoms of the water molecules and the nitrogen atom of the methylammonium [58].

Initially every single unit cell will first saturate with one water molecule, forming the mono-hydrate phase. Further hydration, will result in the dihydrate phase, in which every unit cell will contain two molecules of water. Structurally this phase which can be described as a zero-dimensional network of $(PbI_6)^{4-}$ octahera, which are charge-balanced by the sur-

rounding $CH_3NH_3^+$ cations (figure 2.16 c)) [58].

Limited exposure to humidity will not inexorably result in the disintegration of the perovskite $CH_3NH_3PbI_3$ into its organic and inorganic components, CH_3NH_3I and PbI_2, instead the initial hydration can be reversible when the hydration is discontinued before the methylammonium iodide is removed from the system and and the intercalated H_2O is driven out of the system by drying [58, 59, 60]. The final breakdown of $CH_3NH_3PbI_3$ occurs principally under two conditions: either an external force such as heat, light or an applied bias, breaks the weakened hydrogen bonds between the inorganic Pb-I cage and the organic methylammonium cation and allowing for these volatile molecules to be released from the crystal; or water is present in liquid form or condensed excess and is thus able to dissolve the methylammonium ions directly and to remove them thusly [58].

In their study, Leguy et al. report that the hydration of the absorber material is accompanied by a rapid decline in solar cell performance [58]. In fact, the decline in performance preceeds the structural breakdown of the perovskite which is characterized by the loss of absorption features, indicating that the moisture ingress into the devices is likely to initially deteriorate the charge transfer between the perovskite absorber and the hole-selective material, thus effectively reducing charge extraction [58].

The vulnerability to moisture is therefore the biggest stability issue for perovskite solar cells. The two strategies which can potentially mitigate this weakness and increase the chemical stability of the perovskite absorber include compositional changes to the perovskite itself or moisture-blocking contacts which prevent interactions between the perovskite and external ambient humidity.

A significant increase in thermal stability can be achieved by substituting the volatile methylammonium cation for the much more thermally stable formamidinium (FA) [44]. While the thermal stability of $FAPbI_3$ is higher compared to $MAPbI_3$, this perovskite is structurally unstable because it undergoes a phase transition at 55°C [61] and therefore exists as two polymorphs within the operating range of a solar cells [47]. The black polymorph, which is the desired trigonal phase for a wide-range absorption, exhibits a significant degree of stability at high temperatures (> 160°C), but tends to revert into its hexagonal phase, the wide-band gap yellow polymorph, at temperatures below 60°C in the presence of moisture [62]. Increased phase-stability of the black trigonal phase of $FAPbI_3$ can be achieved in mixed cation-perovskites, specifically in which methylammonium is the minor cation at

concentrations < 20% [63]. Further stabilization of the structure is attained by integrating a mixture of both bromide and iodide [64]. The further addition of small amounts of cesium as third A-site cation were shown to effectively suppress hexagonal phase impurities of MA/FAPb(I/Br)$_3$ [65]. The hygroscopic nature and thermal volatility of methylammonium may, however, still pose a potential risk for instability. As cesium has also been shown to suppress the formation of the undesired hexagonal phase, the most stable perovskite composition to date is based on a cationic FA/Cs mixture at the perovskite A site, lead at the B site, and a mixture of I and Br at the X site [66].

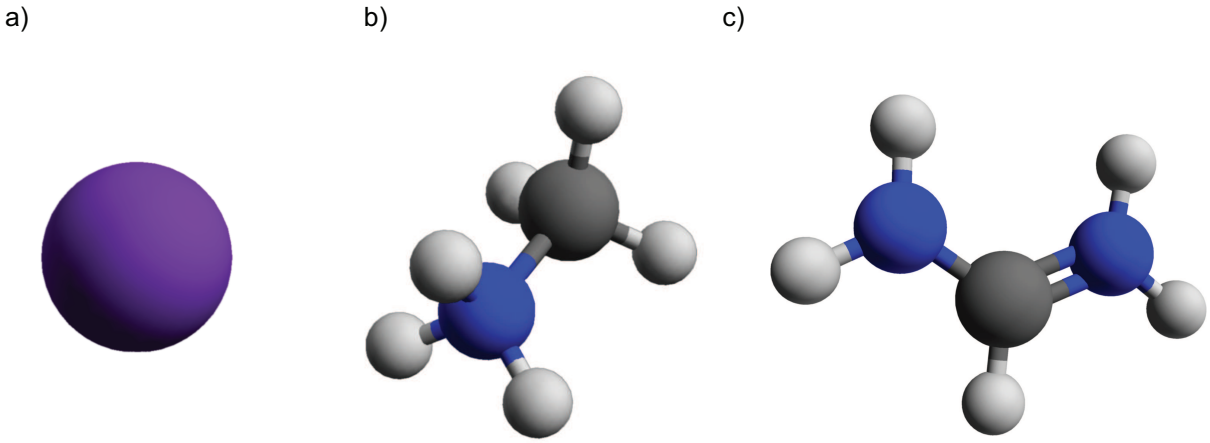

Figure 2.17: A-site cations: a) cesium b) methylammonium c) formamidinium

Aside from modifying the compositional stability of the perovskite absorber itself, the second strategy to preserve the integrity of the perovskite in devices, seeks to engineer multi-functional contacts which act as charge collectors while also blocking moisture ingress and "sealing in" the volatile organic component, preventing it from leaving the perovskite structure.

The most common device architecture is the n-i-p structure, in which electrons are collected by the transparent electrode at the bottom and the top-layer is a hole-collecting layer extracting the p-type charges. The extreme vulnerability of $MAPbI_3$ to moisture has spurred efforts to use the hole-collector, which forms the top layer of a device, as the first line of defense against moisture ingress. Several approaches have been investigated: the employment of a thin blocking layer between the perovskite and the hole-transporting material (HTM), such as Al_2O_3 [67, 68, 69, 70], moisture-blocking hole transporters [71, 72, 73, 74, 75, 76, 77, 78, 79, 80, 81, 82, 83, 84, 85] and hydrophobic carbon electrodes [86, 87, 88, 89, 90, 91].

A focal point of many studies has been the relatively poor barrier property by the most common hole-transporting materials, namely 2,2,7,7-tetrakis-(N,N-di-p-methoxyphenylamine)9,9-spirobifluorene (spiro-OMeTAD), poly(triarylamine) (PTAA) and poly(3-hexylthiophene) (P3HT), to effectively prevent moisture ingress. The combination of heat, light and moisture generally results in rapid degradation of the perovskite layers underneath the hole-transporters, which occurs even more rapidly when the HTMs are doped with a hygroscopic dopant such as bis(trifluoromethane)sulfonimide lithium salt (Li-TFSI) [60, 71, 77]. Based on this observations many efforts have been undertaken to completely remove the need for such a dopant [72, 92, 93, 85, 91] or replacing the reactive dopant with inert additives to improve the charge transport characteristics of the undoped hole-transport material [82]. At the same time, synthesizing new polymeric hole transporters that have hydrophobic properties has been proposed as an avenue to prevent moisture ingress [71, 72, 73].

Very thin layer of an insulating layer between the perovskite absorber and the hole-transporter can also be used to halt the moisture ingress and improve stability in a non-dry environment [94, 68, 95]. Using atomic layer deposition (ALD) as a technique to deposit an ultrathin layer of Al_2O_3 between the perovskite and spiro-OMeTAD, the stability of a device kept at RH 50% without illumination for 24 days, could be improved and its performance was reported to still be at 90% of the initial value [94].

Interestingly, a thick carbon cathode can be used as a protective element to increase the stability of a perovskite solar cell [86, 87, 88, 89, 90]. In some architectures, these devices do not even require a selective p-type contact [86, 87, 88, 90]. Most remarkable is a triple-layer structure composed of mesoporous TiO_2 and mesoporous ZrO_2, which are then infiltrated with $CH_3NH_3PbI_3$ and contacted by a thick carbon layer [86]. In the initial report, stable performance under full sunlight illumination, unencapsulated in ambient air for a period of more than 1000h was reported [86]. The stability of this architecture has been further demonstrated since with a range of stress-tests including outdoor testing [90]. An encapsulated device is reported to show remarkably stable performance when aged outdoors for seven consecutive days in Jeddah, Saudi Arabia. Further, stable performance was observed when an encapsulated device was thermally stress-tested by keeping it 80-85°C for 90 days, in the dark. Photostability of the perovskite devices was also demonstrated by continuously monitoring the power-output of an unencapsulated device in argon atmosphere at 45°C and at maximum power-point tracking conditions. However, not the full sunlight spectrum was used in this experiment, instead an LED array served as light source, emitting only in the

visible range without including contributions from the UV region.

The inherent vulnerability to moisture and subsequent degradation of $CH_3NH_3PbI_3$ makes it essential to develop strategies to protect the absorber as well as possible without sacrificing performance on the path to commercialization. In this thesis, the degradation under ambient humidity conditions and elevated temperatures will be discussed, along with how functionalized single-walled carbon nanotubes can be implemented in structures that are capable of suppressing that degradation.

2.3.2 Device architectures and performance

One of the most compelling reasons to utilize perovskite, in particular, methlyammonium lead iodide, $CH_3NH_3PbI_3$, as an absorber material in solar cells is its very wide absorption across the visible spectrum. The material exhibits a very sharp absorption edge at around 760 nm, and extends its absorption across the shorter wavelength range (figure 2.18). In addition, the characteristic absorption spectrum does not exhibit sharp excitonic peaks which would indicate strongly bound electron-hole pairs.

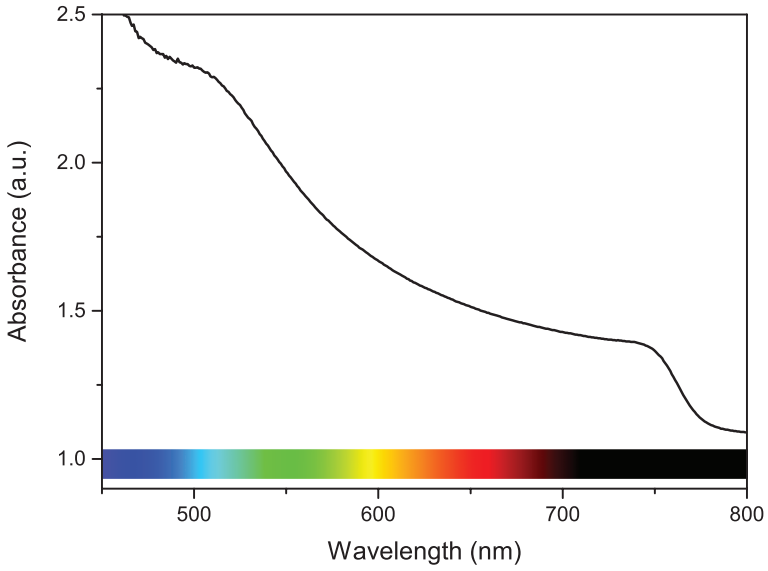

Figure 2.18: Characteristic absorption for $CH_3NH_3PbI_3$ extending across a wide range of the visible spectrum

The first utilization of two perovskite absorbers $CH_3NH_3PbI_3$ and $CH_3NH_3PbBr_3$ in solar cells was reported by Kojima *et al.* in 2009, employing the perovskites as sensitizers in liquid electrolyte DSSCs [24]. The devices were fabricated in the typical DSSC architecture, with the perovskite replacing the typical dyes as sensitizers anchored to a mesoporous TiO_2 layer

(figure 2.11). These devices delivered an efficiency of up to 3.8%, however, suffered from rapid degradation. Similarly, Im *et al.* prepared devices in a similar fashion and were able to improve the efficiency to 6.5% but also observed dissolution of the perovskite absorbers within minutes in the electrolyte [96].

The breakthrough discovery for perovskite solar cells was made in 2012, when the hybrid material was introduced into the concept of solid-state DSSCs replacing the dye as sensitizer [25, 50]. The important difference to liquid DSSC devices is that the p-type side of the junction, the liquid electrolyte, is substituted by the solid-state hole-transporter spiro-OMeTAD, thus avoiding the rapid dissolution of the perovskite due to interaction with the electrolyte. The n-type side of the junction of a ss-DSSC still consists of a sensitized mesoporous TiO_2 layer, into which photoexcited electrons are injected. Such a device was shown to yield a power-conversion efficiency of 7.6% [25]. The true breakthrough, however, was the observation that the mesoporous TiO_2 n-type layer can be replaced by an electronically inert alumina scaffold, yielding an even higher efficiency of 10.9% [25].

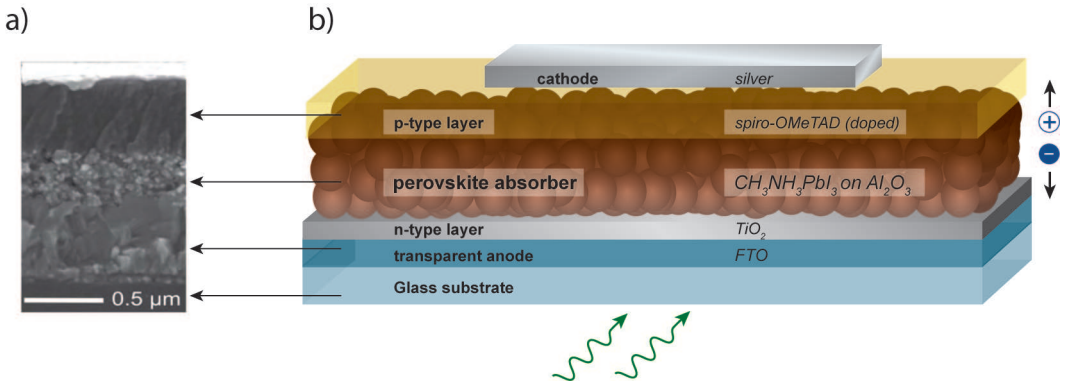

Figure 2.19: a) Scanning-electron microscope image of the cross section of a meso-superstructured solar cell in which the perovskite is coated onto an alumina scaffold. b) shows a typical schematic of the meso-superstructured architecture, in which electrons are collected at the transparent electrode. (a) has been adapted and reproduced with permission from Ball *et al.*, Energy Environ. Sci. 2013, 6, 1739. [97]. Copyright 2013 The Royal Society of Chemistry)

The implication of this finding is that the role of the perovskite extends beyond that of a mere sensitizer but is capable of long-range charge transport comparable to traditional inorganic semiconductors. This was confirmed by Stranks *et al.*, by measuring electron-diffusion lengths exceeding 1000 nm in $CH_3NH_3PbI_3$ [98]. Aside from the broad absorption, the perovskite evidently has also excellent charge transport properties. However, this study could not clearly determine whether the measured charge carriers were free charges or bound-electron hole pairs. A later study then revealed that excitons in the perovskite have a

binding energy of merely 16 meV which is evidence that excitonic charge-pairs spontaneously dissociate and transport in this material is dominated by free charges [99].

These excellent charge carrier properties were translated into devices by demonstrating the fabrication of high-performance planar heterojunction devices through optimization of the deposition procedure [100, 51].

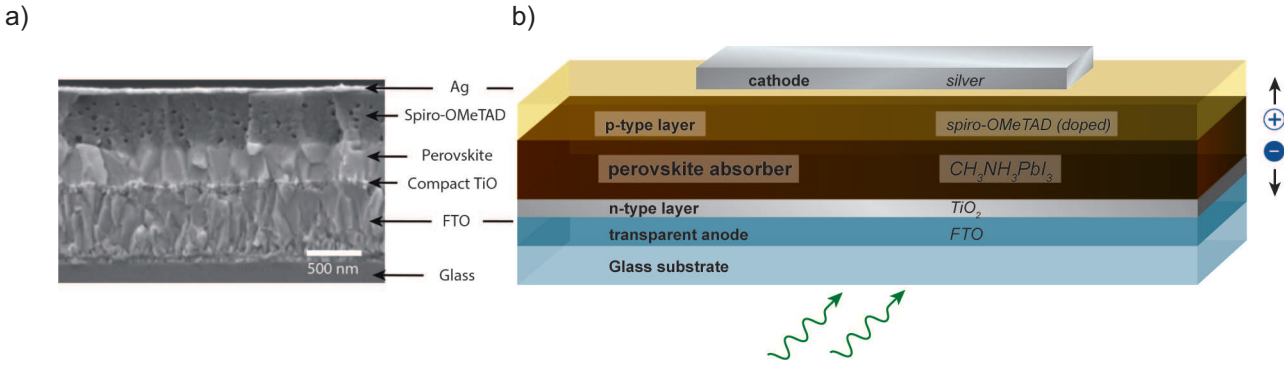

Figure 2.20: a) Scanning-electron microscope image of the cross section of a planar n-i-p heterojunction perovskite solar cell. b) shows a typical schematic of the n-i-p planar architecture, in which electrons are collected at the transparent electrode. (a) has been adapted and reproduced with permission from Liu *et al.*, Nature 2013, 501, 395 [51]. Copyright 2013 Nature Publishing Group)

The device structure now differs fundamentally from dye-sensitized solar cells. Light absorption, charge generation and charge transport occur in the $CH_3NH_3PbI_3$ absorber. The built-in asymmetry of the device facilitating charge selective carrier extraction is provided by the two contacts on both sides of the perovskite. Initially these two contacts were a thin compact layer of TiO_2 exclusively accepting electrons, on one side, and spiro-OMeTAD on the p-type side. In this architecture FTO acts as electron-collecting anode at the bottom of the cell, while silver or gold are used as cathode on top of the device. This device structure can therefore be referred to as *n-i-p* architecture.

This architecture can also be inverted to form a *p-i-n* junction by employing a transparent p-type charge collection layer on top of the FTO electrode, and collecting electrons on top of the device [101, 95].

In the past four years a variety of deposition methods have been reported, ranging from single-solution deposition [25, 50], to single-source vapor deposition [51, 52], to two-step sequential deposition by both solution and evaporation processing [53], as well as combinations of solution and evaporation processing [102, 103]. This demonstrates the flexibility of the material with respect to its processing which will allow the development of large-scale

processes necessary for industrial scale device output. Furthermore, continuous refinement of the deposition methods led to a progressive improvement in material quality, which, combined with compositional tuning of the perovskite, resulted in a steep rise in efficiencies, yielding a certified value of 22.1% (March, 2016) [33].

2.4 Summary

In this chapter fundamental aspects and mechanisms of a photovotlaic solar solar cell were briefly discussed. Starting at a two-level absorber system, which is required for photoabsorption, photoabsorption and charge generation process was described taking into account the effects of the badgap width on the photocarrier generation, on the one hand, and establishing a large photovoltage, on the other hand. After the photogeneration of charges, they can be lost through several decay and recombination pathways, some of which are unvoidable whereas others depend on the quality of the absorber material and its charge collecting interfaces.

Another essential requirement for a photovoltaic device is a built-in asymmetry which drives the charges of opposing polarity in different directions. This asymmetry is commonly established by junctions of two materials with different electron properties, constituting a low-resistance pathway for one of the two charge carrier types, and a high-resistance path for the other. Several such junctions were discussed including junctions with inorganic semiconductors, organic polymers and inorganic-organic materials.

The current-voltage characteristics of such a junction is commonly used to assess the conversion efficiency of incident solar power into electric power. The relevant performance parameters were discussed in conjunction with possible limitations commonly encountered in a real solar cell.

In the next section, the fundamental structural properties of perovskite absorbers were highlighted, with particular focus on stability. The structural and chemical weaknesses of the most common perovskite absorber, methylammonium lead iodide, were discussed showing that this material is highly vulnerable to degradation due to interactions with water. Subsequently, strategies were review which have been employed to protect the perovskite absorber. These are either based on changing the composition of the perovskite itself by replacing the A site cation, or on integrating the perovskite in device structures deliberately designed to prevent moisture ingress.

Finally, this chapter is concluded by a brief overview over the most essential aspects of the evolution of the perovskite solar cell and its different architectures..

Chapter 3

Single-Walled Carbon Nanotubes

In this chapter the fundamental properties of single-walled nanotubes are described and discussed. Furthermore, the process of polymer functionalization is discussed and followed by a brief overview of single-walled carbon nanotubes being integrated into different types of solar cells.

3.1 Definition and synthesis

A carbon nanotube (CNT) is a cylindrical carbon allotrope which can be imagined as a rolled up graphite sheet. The number of layers in the graphite sheet determines the number of walls of the CNT. A single-walled carbon nanotube (SWNT) is therefore formed when the rolled up graphite layer consist of only a single, monoatomic layer which is known as graphene.

There exist several synthesis methods for SWNTs. In this work, the focus rests on two commercially available SWNT types synthesized using two gas-flow methods employing different catalysts. Both processes rely on the Boudouard reaction, which describes the disproportionation of CO to CO_2 and C at high temperatures. The first one is referred to HiPco process due to the use of a continuous flow of high-pressure carbon monoxide. In this method, the SWNT formation is catalyzed by an unsupported iron catalyst ($Fe(CO)_5$), whose decomposition products act as nuclei for the SWNT growth [104]. The resulting SWNTs have a Gaussian diameter distribution with a mean around 1.0 nm and a total diameter range from 0.8-1.2 nm [105]. The chiral angles are evenly distributed within this diameter range.

The CoMoCAT synthesis process employs a silica-supported catalyst composite of Cobalt and Molybdenum [106]. The advantage of this method is a very high selectivity towards SWNTs, meaning very few other carbon allotropes such as multi-walled carbon nanotubes,

other fullerenes or amorphous carbon are formed during the synthesis process [106]. The specific CoMoCAT SWNTs used in this work have the product name CG200. They have a diameter range of 0.7-1.4 nm, with a mean aspect ratio of 1000. What sets these SWNTs apart is that they have a slightly higher concentration of metallic-type SWNTs in the range of around 48% compared to typically 33-37% [107]. The origin and implications of this difference in intrinsic electronic properties will be discussed in the following sections and chapters of this thesis.

3.2 Characterization

3.2.1 Real space

A single-walled carbon nanotube can be considered to be a rolled up sheet of graphene. From this follows that graphene can be used as a starting point for the characterization of its electronic properties and band structure. In figure 3.1, a graphene sheet is illustrated with its two basic lattice vectors $\mathbf{a}_1$ and $\mathbf{a}_2$ which span the graphene unit cell (shaded in blue) These two vectors are defined in Cartesian coordinates as

$$\mathbf{a}_1 = \left(\frac{\sqrt{3}}{2}, \frac{1}{2}\right) ; \ \mathbf{a}_2 = \left(\frac{\sqrt{3}}{2}, -\frac{1}{2}\right) \tag{3.1}$$

The two vectors have a length $||\mathbf{a}_1|| = ||\mathbf{a}_2|| = a_0 = 2.46$Å and open at an angle of 60°. The unit cell contains two carbon atoms: one at $\frac{1}{3}(\mathbf{a}_1 + \mathbf{a}_2)$ and one at $\frac{2}{3}(\mathbf{a}_1 + \mathbf{a}_2)$ The bond length between two neighboring carbon atoms in the lattice can thus be calculated to be $d_{\text{(C-C)}} = \frac{1}{\sqrt{3}} a_0 = 1.42$ Å.

A unique feature of carbon nanotubes is the fact that there are infinitely many different ways to roll up a graphene sheet into a tubular shape. The way how the graphene sheet is rolled up determines the diameter and the chirality of SWNT. The latter property is important, as shown in detail below, because it underlies the particular electronic property of an SWNT of a specific chirality.

The chirality of a SWNT is defined as the angle of the hexagonal helix around the axis of the tube. Chirality can be expressed in vectorial form with the chirality vector $\mathbf{C}$ which is the vector between the two points of the graphene sheet, which will connect when the graphene sheet is rolled up to form the nanotube. The length of this vector is therefore equal to the circumference of the nanotube. Expressed in terms of the basic lattice vectors

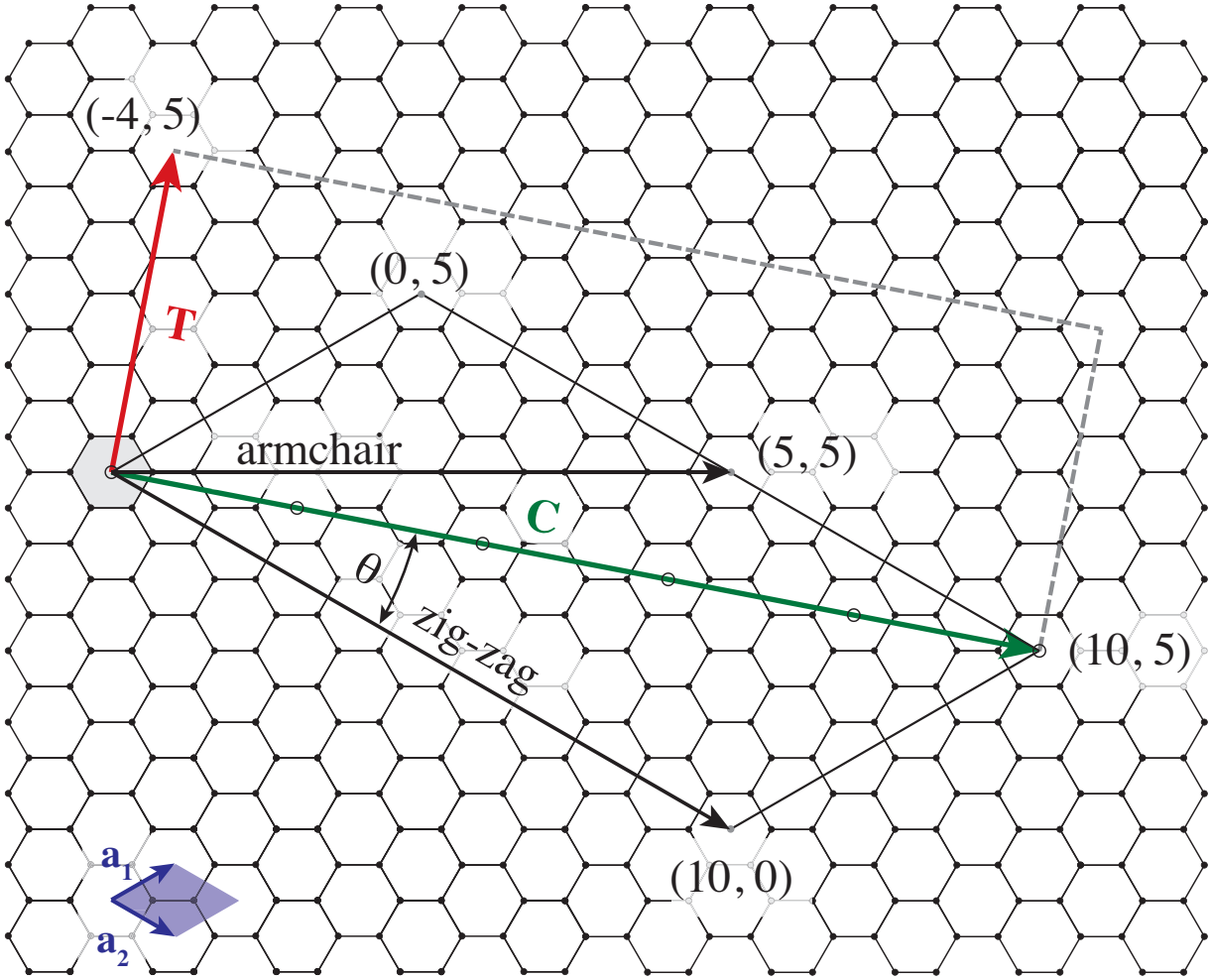

Figure 3.1: Graphene lattice characterized with the two lattice vectors $\mathbf{a}_1$ and $\mathbf{a}_2$. As an example, a chiral vector C of a (10, 5) SWNT is illustrated. The chiral vector can be expressed with the lattice vectors $c = 10\mathbf{a}_1 + 5\mathbf{a}_2$. The length of $|\mathbf{C}|$ is equal to the circumference of the nanotube. The translation vector $\mathbf{T}$ is orthogonal to $\mathbf{C}$ spans together with the chiral vector the unit cell of the nanotube. The chiral angle θ between $\mathbf{a}_2$ and $\mathbf{a}_1$ is a measure of the chirality of the nanotube.

of graphene, this vector becomes $\mathbf{C} = n_1\mathbf{a}_1 + n_2\mathbf{a}_2$. The two integers (n_1, n_2) are referred to as chiral indices. They uniquely define a nanotube and its particular properties such as diameter and electronic band structure. The diameter d of a nanotube can be calculated using its circumference *i.e.* the length of $\mathbf{C}$

$$d = 2R = \frac{|\mathbf{C}|}{\pi} = \frac{a_0}{\pi}\sqrt{n_1^2 + n_2^2 + n_1 n_2} = \frac{a_0}{\pi}\sqrt{N} \tag{3.2}$$

An example is shown in figure 3.1. On a graphene sheet, the chiral vector of a $(10, 5)$ nanotube is illustrated in green. Its chiral angle is the angle θ between $\mathbf{C}$ and $\mathbf{a}_2$ and can be expressed as

$$\theta = \arccos\left(\frac{\mathbf{C}\cdot\mathbf{a}_2}{|\mathbf{C}|\cdot|\mathbf{a}_2|}\right) = \arccos\left(\frac{n_1 + 2n_2}{2N}\right) \tag{3.3}$$

The hexagonal graphene lattice has a six-fold rotational symmetry, which means the range from 0° and 60° describes all tubes with unique chirality. Additionally, for each tube with a chiral angle between 0° and 30°, there exists a tube with equivalent chirality within the range of 30° to 60°, differing only in the handedness of the helix of graphene lattice points around the tube. All unique cases can therefore be discussed within the angle range $0° \leq \theta \leq 30°$ or in terms of chiral indices $n_1 \geq n_2 \geq 0$. There exist two special cases of achiral nanotubes, when the chiral angle $\theta = 0° \Leftrightarrow (n_1, 0)$, this type of nanotube is referred to as "zig-zag" tube; and when the chiral angle $\theta = 30° \Leftrightarrow (n, n)$, this type of nanotube is referred to as "armchair" tube. Both type of nanotubes are illustrated on the graphene sheet in figure 3.1 as well as in tubular form in figure 3.2.

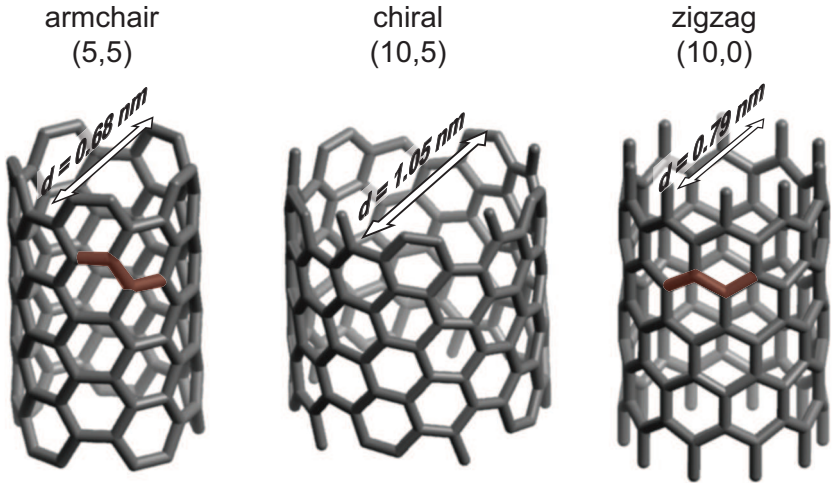

Figure 3.2: Three single-walled carbon nanotubes are shown. A *armchair* nanotube with a chiral angle $\theta = 30°$and the chiral indices (5,5); a *chiral* nanotube with a chiral angle $\theta = 19.1°$and the chiral indices (10,5); and a *zigzag* nanotube with a chiral angle $\theta = 0°$and the chiral indices (10,0);

In order to characterize the unit cell of a carbon nanotube, another vector is needed which is orthogonal to the chiral vector $\mathbf{C}$ *i.e.* parallel to the tube axis. The length of this vector is defined by the smallest translational period T, within which the lattice does not repeat. This translational vector $\mathbf{T} = t_1\mathbf{a}_1 + t_2\mathbf{a}_2$ can be calculated from the condition $\mathbf{C} \cdot \mathbf{T} = 0$ which yields

$$\mathbf{T} = -\frac{2n_2 + n_1}{m_R}\mathbf{a}_1 + \frac{2n_1 + n_2}{m_R}\mathbf{a}_2 \tag{3.4}$$

$m_R \in \mathbb{N}$ is the greatest common divisor of $2n_2 + n_1$ and $2n_1 + n_2$. The length of the translational vector $|\mathbf{T}| = T$ is the smallest translational period and the length of the unit cell of the carbon nanotube alongside its axis

$$T = |\mathbf{T}| = a_0 \cdot \frac{\sqrt{3(n_1^2 + n_2^2 + n_1 n_2)}}{m_R} = \sqrt{3}a_0 \cdot \frac{\sqrt{N}}{m_R} \tag{3.5}$$

In the example of a $(10, 5)$ nanotube as illustrated in figure 3.1, this vector is $\mathbf{T} = -4\mathbf{a}_1 + 5\mathbf{a}_2$. With the chiral vector $\mathbf{C}$ and the translational vector $\mathbf{T}$, the unit cell of a carbon nanotube is now fully defined by the rectangle that these two vectors span. The area of the unit cell is therefore $A_{\text{CNT uc}} = |\mathbf{C} \times \mathbf{T}| = \sqrt{3}a_0^2 \cdot \frac{N}{m_R}$. The number of carbon atoms per nanotube unit cell can then be calculated by counting the number of graphene unit cells that fit into the area of the unit cell surface of the nanotube.

$$q = \frac{A_{\text{CNT uc}}}{A_{\text{graphene uc}}} = \frac{\sqrt{3}a_0^2 \cdot \frac{N}{m_R}}{\frac{\sqrt{3}}{2}a_0^2} = \frac{2N}{m_R} \tag{3.6}$$

There are q graphene unit cells per nanotube and there are two carbon atoms per graphene unit cell, the total number of carbon atoms per nanotube unit cell is therefore

$$N_{\text{C}} = 2q = \frac{4N}{m_R} \tag{3.7}$$

3.2.2 Reciprocal space

With the nanotube unit cell fully characterized in real space with $\mathbf{C}$ and $\mathbf{T}$, its counterpart in reciprocal space - the first Brillouin zone (BZ) - can now be calculated. The Brillouin zone is an important tool for the description of the band structure of a material as it contains all allowed wave vectors. The reciprocal lattice of a hexagonal honeycomb lattice is again a hexagonal lattice. Starting with the Brillouin zone of graphene, its basic lattice vectors in reciprocal space $\mathbf{k}_1$ and $\mathbf{k}_2$ can be constructed using the real space lattice vectors $\mathbf{a}_1$ and $\mathbf{a}_2$, as defined in (3.1) from the condition $\mathbf{k}_i \cdot \mathbf{a}_j = 2\pi\delta_{i,j}$

$$\mathbf{k}_1 = \frac{4\pi}{\sqrt{3}a_0}\left(\frac{1}{2}, \frac{\sqrt{3}}{2}\right) = k_0 \cdot \left(\frac{1}{2}, \frac{\sqrt{3}}{2}\right) \tag{3.8}$$

$$\mathbf{k}_2 = \frac{4\pi}{\sqrt{3}a_0}\left(\frac{1}{2}, -\frac{\sqrt{3}}{2}\right) = k_0 \cdot \left(\frac{1}{2}, -\frac{\sqrt{3}}{2}\right) \tag{3.9}$$

$$k_0 = \frac{4\pi}{\sqrt{3}a_0} \tag{3.10}$$

Going from the basic lattice vector in reciprocal space of graphene to the ones of the carbon nanotubes, the Brillouin zone can be constructed by converting the vectors that define the nanotube unit cell in real-space - the chiral vector $\mathbf{C}$ and the translational vector $\mathbf{T}$ - into their reciprocal lattice counterparts. The vector corresponding to the translational vector goes parallel to the tubular axis, it is therefore defined as $\mathbf{k}_{\text{T}} \equiv \mathbf{k}_{\parallel}$ with the length $|\mathbf{k}_{\parallel}| = 2\pi/T$. The nanotube can be considered to be infinitely long, meaning there are no

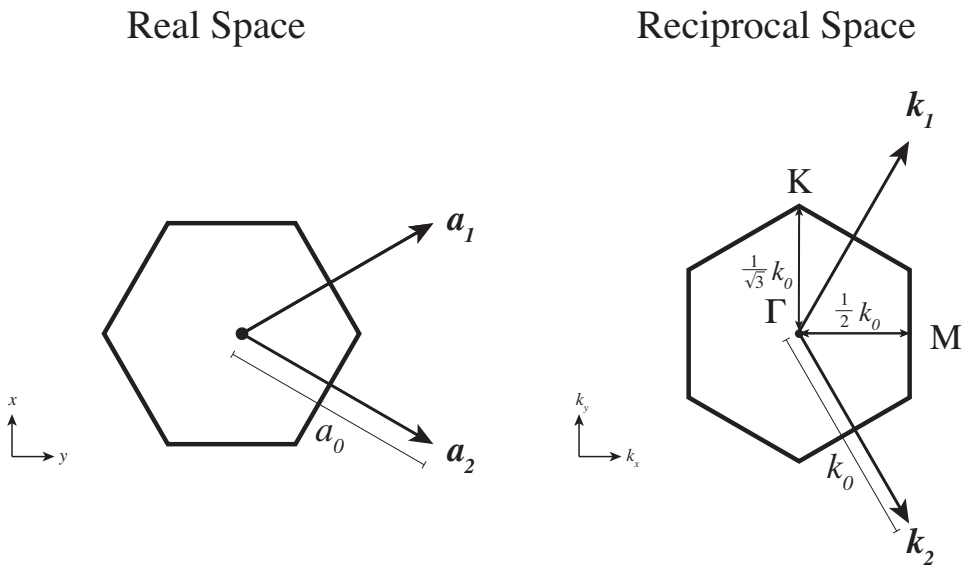

Figure 3.3: The unit cell in real space and the Brillouin cell in reciprocal space of graphene. The basic lattice vectors in real space are $\mathbf{a}_1$ and $\mathbf{a}_2$ with a length a_0, in reciprocal space the equivalents are $\mathbf{k}_1$ and $\mathbf{k}_2$ with a length $k_0 = \frac{4\pi}{\sqrt{3}a_0}$. In reciprocal space, the symmetry points of the Brillouin zone Γ, K and M have also been added

boundary conditions affecting $\mathbf{k}_{\|}$, which is therefore continuous and Brillouin zone alongside the tube axis lies in the interval $(-\pi/T, \pi/T]$.

This is different for the orthogonal wave vector $\mathbf{k}_\mathrm{C} \equiv \mathbf{k}_\perp$, which corresponds to the circumferential real space vector, and is non-continuous. This follows from the boundary condition of a standing wave around the nanotube axis $\phi(x+c) = \phi(x) \Leftrightarrow m \cdot \lambda = |\mathbf{C}| = \pi d$, where m is an integer. This condition arises from the description of quasi-particles and particles - such as electrons or phonons - with a Bloch wavefunction which has to satisfy $\psi(\mathbf{r} + \mathbf{C}) = \mathrm{e}^{i\mathbf{k}\cdot\mathbf{C}} \cdot \psi_\mathbf{k}(\mathbf{r}) = \psi(\mathbf{r})$. The only possible wavefunctions are ones with a phase shift of a multiple of 2π because at all other wavelengths they vanish due to destructive interference. As a consequence only a discrete number of wavelengths $\lambda_m = m \cdot \lambda$ are possible (denoted by the integer m). The same is therefore true for the wave vector $k_\perp$ which is quantized according to

$$m \cdot \lambda = |\mathbf{C}| = \pi \cdot d \Leftrightarrow k_{\perp,m} = \frac{2\pi}{\lambda} = \frac{2}{d} \cdot m \tag{3.11}$$

Accordingly, the wave vector $k_{\perp,m}$ has $2m$ nodes around the circumference. The largest possible wavevector *i.e.* the smallest possible wavelength is dependent on the number of atoms ($2q$) in the unit cell. Projecting the carbon atoms on the circumference of the nanotube, q pairs of equidistant carbon atoms become apparent (figure 3.4).

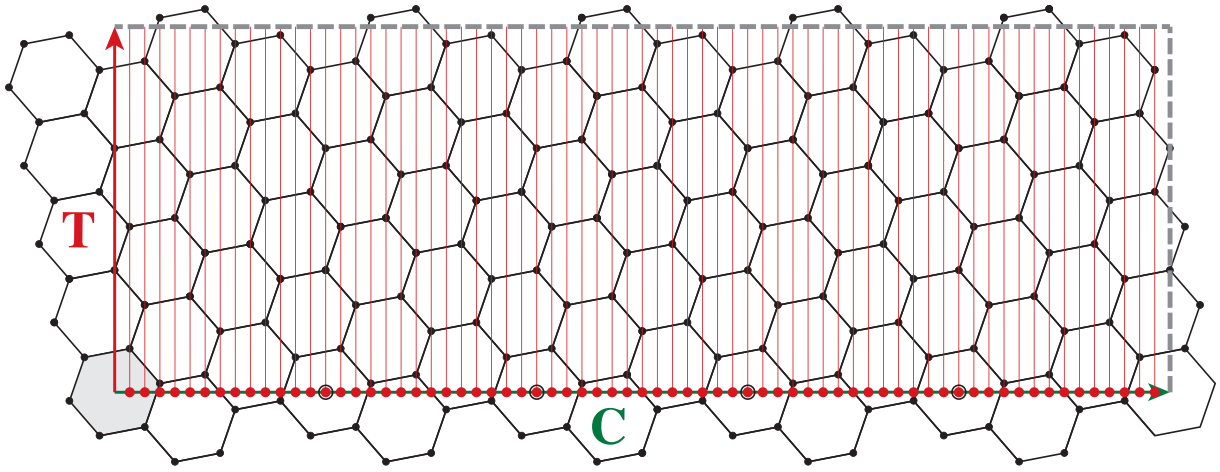

Figure 3.4: From the projection of the carbon atoms onto **C**, it becomes apparent that there are q pairs of carbon atoms at equidistance

Because there are two atoms associated with every intersection, this means that the smallest period involves four atoms, which is therefore the minimum number of atoms necessary for defining one full wavelength. Because the nodes cannot exceed the number of atoms, the condition $|m| \leq q/2$ follows. The quantization number m can therefore take all values in the interval $-q/2+1, -q/2+2, ..., 0, 1, ..., q/2$.

The implication is that wavevectors only exist as discrete lines in $\mathbf{k}_\perp$ direction, with a separation of in $2/d$. They are, however, continuous in $\mathbf{k}_\parallel$ direction. The resulting Brillouin zone is therefore the collection of q lines parallel to the tubular axis with a length of $2\pi/T$ over a distance $2q/d$ in $\mathbf{k}_\perp$ direction. The two basic wavevectors of the nanotube can be calculated from the following conditions

$$\mathbf{k}_\perp \cdot \mathbf{C} = 2\pi \qquad \mathbf{k}_\perp \cdot \mathbf{T} = 0 \tag{3.12}$$

$$\mathbf{k}_\parallel \cdot \mathbf{C} = 0 \qquad \mathbf{k}_\parallel \cdot \mathbf{T} = 2\pi \tag{3.13}$$

The resulting vectors are

$$\mathbf{k}_\perp = \frac{2n_1 + n_2}{q \cdot m_R}\,\mathbf{k}_1 + \frac{n_1 + 2n_2}{q \cdot m_R}\,\mathbf{k}_2 \tag{3.14}$$

$$\mathbf{k}_\parallel = -\frac{n_2}{q}\,\mathbf{k}_1 + \frac{n_1}{q}\,\mathbf{k}_2 \tag{3.15}$$

In figure 3.5 three examples are shown of the Brillouin zone of carbon nanotubes with different chiralities.

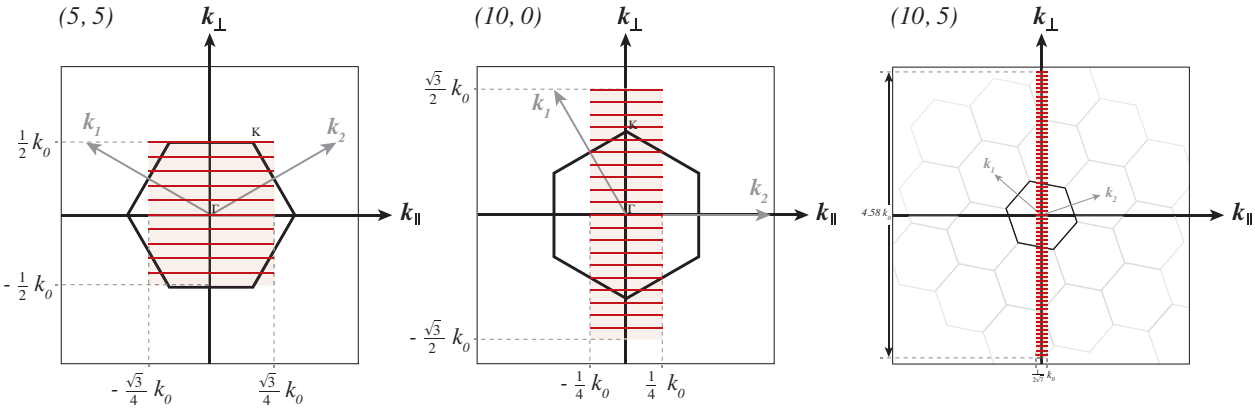

Figure 3.5: Brillouin zone of three carbon nanotubes with different chiralities. The reciprocal vectors of the carbon nanotubes $k_\parallel$ and $k_\perp$ define the orientation of the allowed Bloch momenta with respect to the Brillouin zone of graphene.

3.3 Band structure

A good approximate description of the band structure of carbon nanotubes can be obtained using graphene as starting point and then considering the case of a rolled-up graphene sheet with its previously described boundary condition in the circumferential direction.

3.3.1 Band structure of graphene

The band structure of graphene can be sufficiently well approximated using the *tight-binding model*. The basis for this approximation is given by a strong localization of valence electrons around their atoms due to tight binding. The wavefunction of these electrons in the solid resembles therefore the one of single atoms, allowing for an analytical derivation of band energies.

One carbon atom has eight valence electrons available: $2s$, $2p_x$, $2p_y$ and $2p_z$. In the planar configuration of graphene, the $2s$ orbitals hybridize with the in-plane p orbitals, namely p_x and p_y to form three molecular sp^2 orbitals. The head-on overlap with the hybridized sp^2 orbitals of their neighbors results in the formation of very strong covalent *sigma* (σ) bonds. Due to the electrostatic repulsion of the occupying electrons, the three sp^2 orbitals maximize their relative distance between each other by opening at an angle of 120°. This is the underlying cause for the planar hexagonal lattice structure of graphene. The strength of these σ bonds is responsible for the elastic properties of graphene. The electrons occupying these bands cannot contribute to the electronic properties of graphene and, by

extension, of carbon nanotubes because the σ bands lie energetically too far below the Fermi level (Figure 3.6) [108]. These bands can therefore be largely neglected for semi-empirical calculations of the graphene band structure.

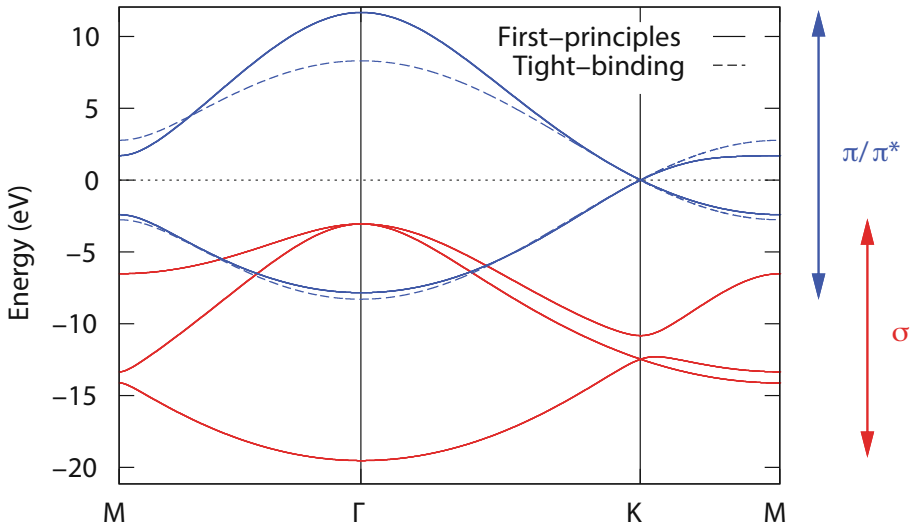

Figure 3.6: Molecular bands of graphene with respect to the Fermi energy $E_F = 0$. The σ bands (in red) are energetically very far away from the Fermi level and do therefore not participate in charge transport. In contrast, the π bands (in blue) are very close to the Fermi energy. In fact, the bonding π band, constituting the highest valence band, and the antibonding π^*, constituting the lowest lying conduction band, cross at the K points of the Brillouin zone, giving graphene metallic properties. The solid lines show the bands which have been derived from *ab initio* calculations, the dashed lines have been calculated using the tight-binding approximation, which will be discussed in more detail further in the text [108].

The remaining p_z orbitals are perpendicular to the bonding plane of graphene and cannot couple with the σ orbitals for reasons of symmetry. The sideways overlap of these orbitals with their neighboring p_z orbitals results in the formation of delocalized *pi* (π) orbitals. In contrast to the σ orbitals, the π orbitals cross the Fermi levels at the high symmetry points of the Brillouin zone (figure 3.6). Hence, the bonding π orbitals form together the highest levels of the valence band and the anti-bonding π^* orbitals give rise to the conduction band. These bands are therefore entirely responsible for the electronic properties of graphene. The electronic properties of graphene can therefore be described by characterizing the p_z orbitals. The sideways overlap of the p_z orbitals leads to much weaker coupling with the neighboring orbitals. They retain therefore to a large degree their atomic orbital characteristics. The tight-binding approximation allows therefore a sufficiently good description of the electronic properties of graphene, certainly at and close to the K point of the Brillouin zone.

A starting point to describe the band structure of a solid is finding solutions to the

time-independent Schröderinger equation.

$$\hat{H}\psi_{\mathbf{k}} = E(\mathbf{k})\psi_{\mathbf{k}} \tag{3.16}$$

The operator $\hat{H}$ is the Hamiltonian acting on the wavefunction $\psi_{\mathbf{k}}$, which is equal to the state $\psi_{\mathbf{k}}$ times the constant energy of that state. The wavefunctions which obey that rule, represent stationary waves or standing waves which correspond to molecular orbitals whose overlap results in the electronic bands of a solid.

For the tight-binding approximation, the starting point are the eigenfunctions ϕ_{at} of the atomic Hamiltonian $\hat{H}_{\text{at}}$, which describes the energy orbitals of an electron when its parent atom is completely isolated. In a solid, the atomic orbitals change due to orbital overlap, thus ϕ_{at} is not an eigenfunction of the crystal Hamiltonian. However, due to the tight-binding assumption, going from the atomic Hamiltonian $\hat{H}$ to the one of the solid $\hat{H}$ requires only a relatively small modification ΔU

$$\hat{H}(\mathbf{r}) = \sum_{\mathbf{R}} \hat{H}_{\text{at}}(\mathbf{r} - \mathbf{R}) + \Delta U(\mathbf{r}) \tag{3.17}$$

In a crystal with a periodic potential landscape, a general solution for (3.16) is a Bloch wavefunction $\psi(\mathbf{r}) = \mathrm{e}^{i\mathbf{k}\cdot\mathbf{r}} \cdot u_{\mathbf{k}}(\mathbf{r})$ because it merely undergoes a phase change under translation within the crystal. To approximate the Bloch wave to the case of a highly localized wave function, it can be expressed as linear combination of atomic orbitals

$$\psi(\mathbf{r}) = \frac{1}{\sqrt{N}} \sum_{\mathbf{R},n} b_n \phi_n(\mathbf{r} - \mathbf{r}_n - \mathbf{R}) \cdot \mathrm{e}^{i\mathbf{k}\cdot\mathbf{R}} \tag{3.18}$$

$\mathbf{R}$ represents all possible lattice vectors and $1/\sqrt{N}$ is the normalization term of the wavefunction to unity $\langle \psi \,|\, \psi \rangle = \mathbb{1}$.

In the specific case of graphene, there are two carbon atoms (A and B) in a unit cell. In a unit cell are accordingly two p_z orbitals represented by ϕ_A and ϕ_B, both are assumed to be well localized at the position of their respective atom. The total function ϕ is a linear combination of the two orbitals

$$\phi(\mathbf{r}) = \sum_{n} b_n \phi_n(\mathbf{r}) = b_A \phi_A(\mathbf{r}) + b_B \phi_B(\mathbf{r}) \tag{3.19}$$

Before applying the Hamiltonian from (3.17) on the wavefunction ψ from (3.18), its effect on the individual wavefunction of the p_z orbital for a single electron is assessed

$$\hat{H}\phi_A(\mathbf{r}) = \hat{H}_{\text{at}}\phi_A(\mathbf{r}) + \Delta U_A \phi_A(\mathbf{r}) = \varepsilon_A \phi_A(\mathbf{r}) + \Delta U_A \phi_A(\mathbf{r}) \tag{3.20}$$

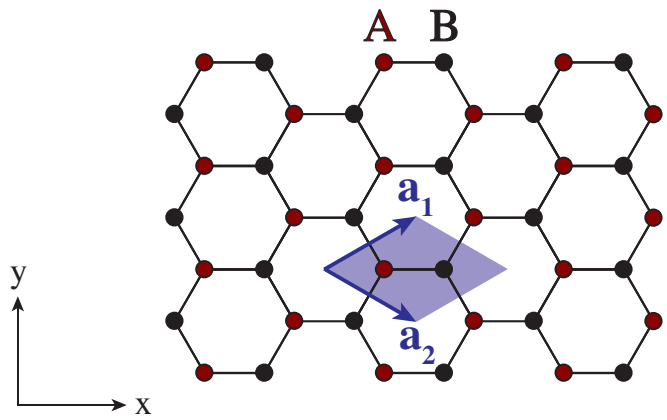

Figure 3.7: In the graphene lattice contains two sub-lattices, the A lattice in red and the B lattice in black. As dictated by the σ bonds resulting from the sp^2 hybridization, each carbon atom has three nearest neighbors, which are in the respectively other sublattice.

The term ε_A is the eigenvalue of the p_z state of carbon atom A. Due to the symmetry of the lattice, atom A and B are equivalent, hence $\varepsilon_A = \varepsilon_B = \varepsilon$. It is convenient to calculate the band energies with respect to ε which can therefore be set to zero. The Hamiltonian applied on both p_z orbitals can thus be simplified to yield

$$\hat{H}\phi_A(\mathbf{r}) = \Delta U_A \phi_A(\mathbf{r}) \Leftrightarrow \hat{H}\phi_B(\mathbf{r}) = \Delta U_B \phi_B(\mathbf{r}) \tag{3.21}$$

The solution for (3.16) can be calculated by applying the Hamiltonian on (3.18). However, in order to generate two equations for the two parameters b_A and b_B, the functions of the two p_z orbitals can be projected onto ψ, respectively.

$$E\,\langle\phi_A\,|\,\psi\rangle = \langle\phi_A\,|\,U_A\,|\,\psi\rangle \tag{3.22}$$

$$E\,\langle\phi_B\,|\,\psi\rangle = \langle\phi_B\,|\,U_B\,|\,\psi\rangle \tag{3.23}$$

The left-hand side parts of these equations can be evaluated separately, knowing that the functions are orthogonal and normalized, and assuming that only the three nearest-neighbor orbitals have non-zero overlap (Figure 3.7).

$$\langle\phi_A\,|\,\psi\rangle = \int \mathrm{d}^3\mathrm{r}\;\phi_A^*(\mathbf{r})\;\psi(\mathbf{r}) = b_A + b_B\left(\int \mathrm{d}^3\mathrm{r}\;\phi_A^*(\mathbf{r})\;\phi_B(\mathbf{r})\right)\left(1 + \mathrm{e}^{-i\mathbf{k}\cdot\mathbf{a_1}} + \mathrm{e}^{-i\mathbf{k}\cdot\mathbf{a_2}}\right) \tag{3.24}$$

$$\langle\phi_B\,|\,\psi\rangle = \int \mathrm{d}^3\mathrm{r}\;\phi_B^*(\mathbf{r})\;\psi(\mathbf{r}) = b_B + b_A\left(\int \mathrm{d}^3\mathrm{r}\;\phi_B^*(\mathbf{r})\;\phi_A(\mathbf{r})\right)\left(1 + \mathrm{e}^{i\mathbf{k}\cdot\mathbf{a_1}} + \mathrm{e}^{i\mathbf{k}\cdot\mathbf{a_2}}\right) \tag{3.25}$$

These terms can be simplified by introducing the abbreviation term $\alpha(\mathbf{k})$ for the exponential

functions and the overlap integral γ_0 between neighboring orbitals.

$$\gamma_0 := \int \mathrm{d}^3\mathrm{r}\ \phi_A^*(\mathbf{r})\ \phi_B(\mathbf{r}) = \int \mathrm{d}^3\mathrm{r}\ \phi_B^*(\mathbf{r})\ \phi_A(\mathbf{r}) \tag{3.26}$$

$$\alpha(\mathbf{k}) := 1 + \mathrm{e}^{i\mathbf{k}\cdot\mathbf{a_1}} + \mathrm{e}^{i\mathbf{k}\cdot\mathbf{a_2}} \tag{3.27}$$

Evaluating the right-hand side of (3.22 and 3.23) similarly

$$\langle \phi_A \,|\, U_A \,|\, \psi \rangle = b_B \cdot \alpha \int \mathrm{d}^3\mathrm{r}\ \phi_A^*\ \Delta U_A\ \phi_B \tag{3.28}$$

$$\langle \phi_B \,|\, U_B \,|\, \psi \rangle = b_A \cdot \alpha \int \mathrm{d}^3\mathrm{r}\ \phi_B^*\ \Delta U_B \phi_A \tag{3.29}$$

Introducing γ_1 as the nearest-neighbor interaction. The value of this overlap integral has been found experimentally to be typically of the order of 2.9 eV [109]

$$\gamma_1 := \int \mathrm{d}^3\mathrm{r}\ \phi_A^*\ \Delta U_A\ \phi_B = \int \mathrm{d}^3\mathrm{r}\ \phi_B^*\ \Delta U_B\ \phi_A \tag{3.30}$$

With that, the equations (3.22) and (3.23) become

$$E(\mathbf{k})(b_A + b_B \cdot \gamma_0\alpha) = b_B \cdot \alpha\gamma_1 \tag{3.31}$$

$$E(\mathbf{k})(b_B + b_A \cdot \gamma_0\alpha) = b_A \cdot \alpha^*\gamma_1 \tag{3.32}$$

Solutions for the Schröderinger equation (3.16) can be obtained by solving the secular equation

$$\begin{vmatrix} E(\mathbf{k}) & \alpha(E(\mathbf{k})\gamma_0 - \gamma_1) \\ \alpha^*(E(\mathbf{k})\gamma_0 - \gamma_1) & E(\mathbf{k}) \end{vmatrix} = 0 \tag{3.33}$$

Because the tight-binding approximation assumes only very little overlap between neighboring orbitals due to the strong localization of the electrons, this entails that $\gamma_0^2 \approx 0$, thus

$$E(\mathbf{k}) = \pm\gamma_1|\alpha| = \pm\gamma_1\ \sqrt{3 + 2\cos(\mathbf{k}\cdot\mathbf{a}_1) + 2\cos(\mathbf{k}\cdot\mathbf{a}_2) + 2\cos[\mathbf{k}(\mathbf{a_1} - \mathbf{a_2})]} \tag{3.34}$$

Expressed in k_x and k_y coordinates this becomes

$$E(k_x, k_y) = \pm\gamma_1 \sqrt{1 + 4\cos\left(\frac{3}{2}\ a_0 k_y\right)\cos\left(\frac{\sqrt{3}}{2}\ a_0 k_x\right) + 4\cos^2\left(\frac{\sqrt{3}}{2}\ a_0 k_x\right)} \tag{3.35}$$

In figure 3.8 the dispersion relation from 3.35 is shown. At the K and K' edge points (Dirac points) of the Brillouin zone, the bonding and the antibonding π bands both have the same value $E(\mathbf{k}) = 0$, which corresponds to the reference energy eigenvalue ε. The two-valence electrons of the graphene unit cell are located in the anti-bonding π band i.e. valence band. The bonding π band - conduction band - is therefore unoccupied. From this follows that the energy at which the bands touch is the Fermi energy of graphene ε_F. Since the lowest states in the conduction band are not separated by a gap from the Fermi energy, graphene exhibits metallic characteristics. Due to a low density of states near the Fermi energy, however, it can also be described as semi-metallic [108].

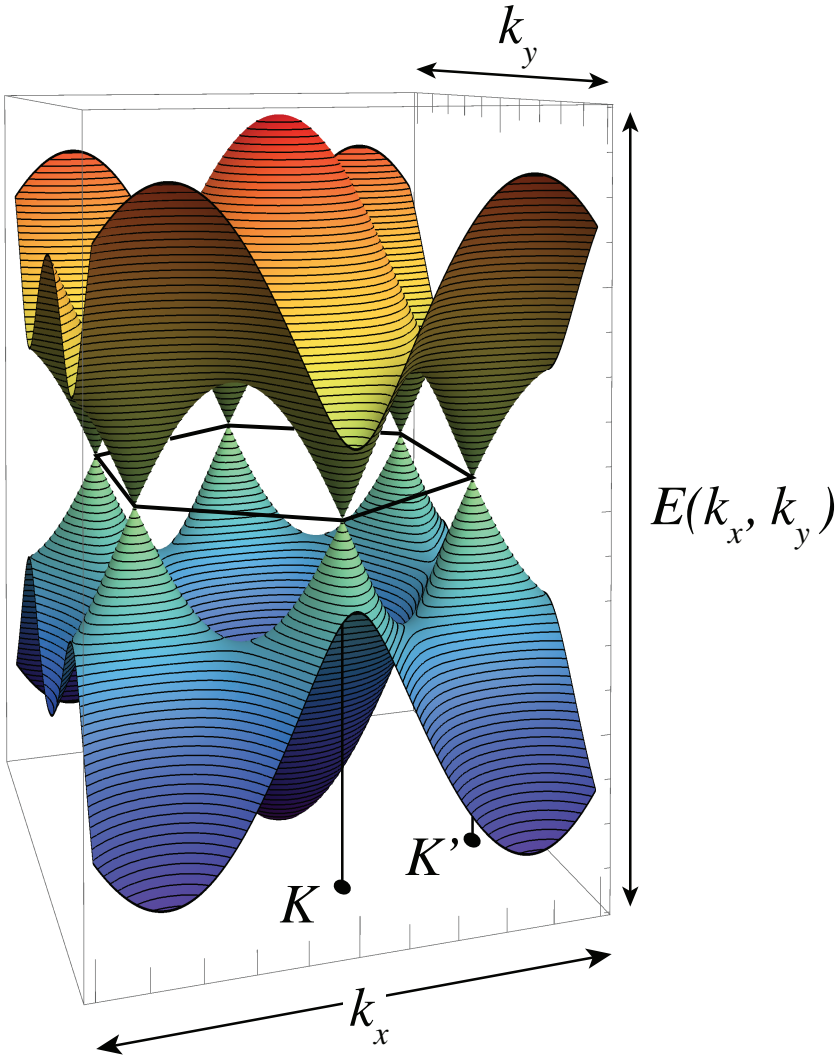

Figure 3.8: Three-dimensional representation of the graphene π bands according to (3.35) derived with the tight-binding approximation. At the K points, the bonding π band and the anti-bonding π^* band cross over, giving graphene a metallic character.

3.3.2 Band structure of carbon nanotubes

The band structure of graphene can now be used as starting point to describe the band structure of single-walled carbon nanotubes in an approach referred to as *zone-folding approximation*. As described in section 3.2.2, while states along the tube axis are continuous; for circumferential states around the carbon nanotube, the allowed values of the momentum space are confined to discrete parallel lines in the Brillouin zone. In the zone-folding approximation, the bands of SWNTs are therefore described by the energies of graphene along these allowed momenta. These discrete k lines are also referred to as *sub-bands*.

Depending on the geometry of the nanotubes i.e. the chiral indices, these subbands

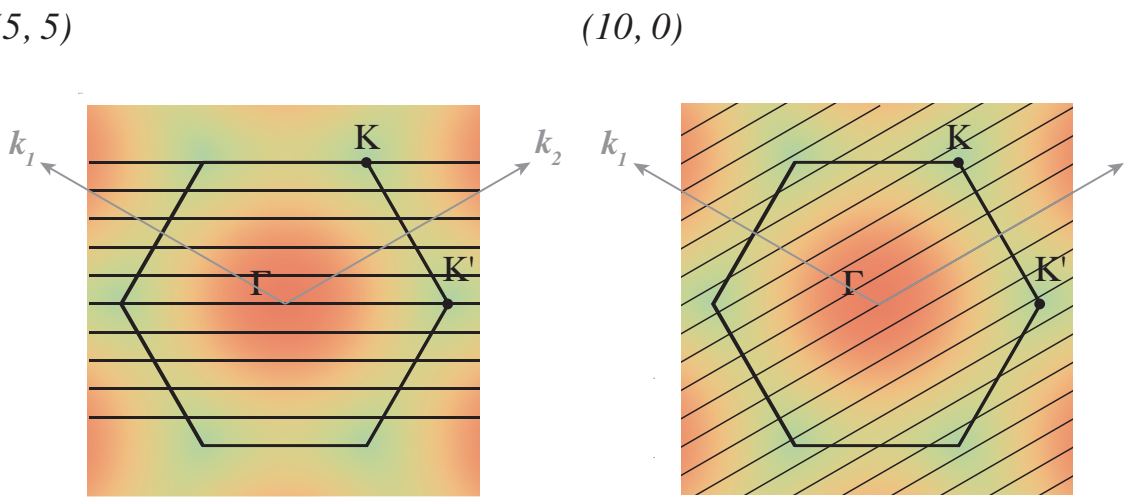

Figure 3.9: Top-view projection of the Brillouin zone of graphene overlaid with the allowed Bloch momenta of two nanotubes with different chiralities. On the left-hand side a nanotube with the chiral indices $(5,\ 5)$, on the right-hand side a nanotube with the chiral indices $(10, 0)$. An important difference between the two is the relative position of the allowed Bloch moment with regards to the K points of graphene.

change in number and orientation. This is an important observation with respect to the electronic properties of SWNTs. If the K point of the graphene Brillouin zone is among the allowed states of the carbon nanotube that means that the valence band and the conduction band cross at this point, as shown in figure 3.8, making the nanotube metallic. For low-energy excitations, a dispersion relation can be obtained by performing a second-order perturbation close to the Fermi energy in the vicinity of the K point [110].

$$E(k) = \pm\frac{3a_0}{2}\ \gamma_1\ |\mathbf{k} - \mathbf{K}| \tag{3.36}$$

The dispersion relation remains linear as for graphene excitations and retains accordingly the metallic characteristic. From (3.36), the Fermi velocity can written as $v_F = \frac{3}{2\hbar}a_0\gamma_1$ and has a value around $v_F \simeq 8 \times 10^5$ m s^{-1}[110].

In all other cases, when the Brillouin K point does not coincide with a subband of the SWNT, there is a gap between the two bands, making the nanotube semiconducting. After low-energy expansion, the dispersion relation for the subbands closest to the K point reads

$$E(k_\parallel) \simeq \pm\frac{3a_0}{2}\ \gamma_1\sqrt{\left(\frac{2\pi}{|\mathbf{C}|}\right)^2\left(q \pm \frac{1}{3}\right)^2 + k_\parallel^2} \tag{3.37}$$

The integer q represents the number of available bands. The wave vector $k_\parallel$ describes the continuum of states within a subband alongside the tube axis. The bandgap at the Fermi

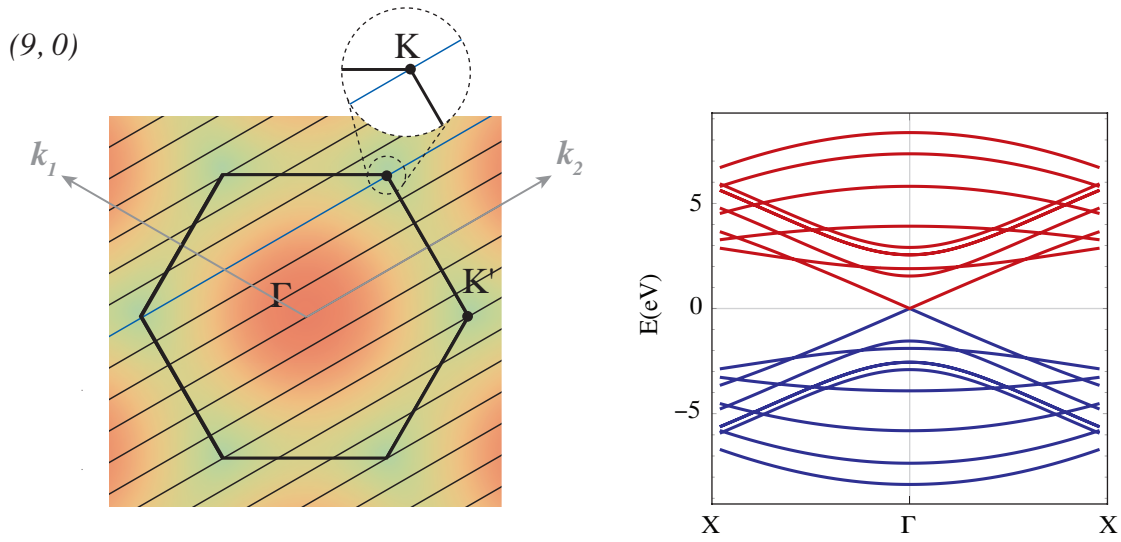

Figure 3.10: In the left panel, the contour plot of the Brillouin zone of graphene is superimposed with the allowed Bloch states of a $(9, 0)$ nanotube. The K point of graphene is magnified to show that it is among the allowed states of the nanotube. As a consequence, the π bands of the nanotube cross at this point. The corresponding band structure of this nanotube, derived by the zone-folding approximation, is shown in the right panel. As can be seen, the lowest π bands cross, making this nanotube metallic.

level i.e. for $k_{\parallel} = 0$ and for $q = 0$ is thus

$$E^{+}(k_{\parallel} = 0) - E^{-}(k_{\parallel} = 0) = \frac{2\pi a_0 \gamma_1}{|\mathbf{C}|} = \Delta E_g \tag{3.38}$$

In this approximation, the bandgap decreases inversely with the diameter ($d_{\mathrm{CNT}} \propto |\mathbf{C}|$) of the nanotube. This holds only the vicinity of the Fermi level where the dispersion relation is linear. Further away, this relation is not linear any more due to *trigonal warping* due to which not only the diameter but also the chiral indices ($n_1,\ n_2$) affect the bandgap [111].

Another important quantity with regards to the transport properties, is the effective mass of the charge carriers, which is dependent on the band curvature at the edges

$$m^* = \frac{1}{\hbar}\left[\frac{\partial^2 E(k)}{\partial k^2}\right]^{-1} = \frac{2\pi\hbar}{3|\mathbf{C}|v_F} \tag{3.39}$$

The inverse dependence of the effective mass on the diameter in (3.39) means that the mass goes to zero for an infinite diameter i.e. the graphene limit.

The ratio of semiconducting to metallic nanotubes can be quantified using the following arguments. The condition that allowed k states must fulfil is $\mathbf{k} \cdot \mathbf{C} = 2\pi \cdot m$ (compare with 3.11 and 3.12). The K point of the graphene Brillouin zone can be described with its coordinate vector $\mathbf{K} = \frac{1}{3}(\mathbf{k}_1 - \mathbf{k}_2)$, thus nanotubes with a metallic character are the ones

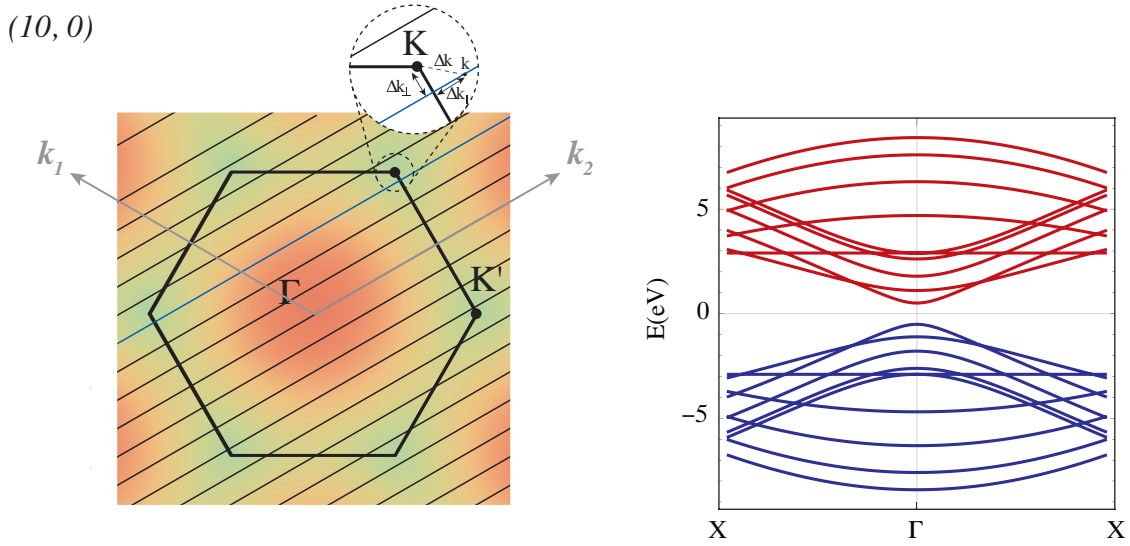

Figure 3.11: In the left panel, the contour plot of the Brillouin zone of graphene is superimposed with the allowed Bloch states of a $(10, 0)$ nanotube. The K point of graphene is magnified to show that it is not among the allowed states of the nanotube and has a distance of $\Delta k_\perp$ to the K point. As a consequence, the π bands of the nanotube do not cross and therefore have a gap. The corresponding band structure of this nanotube, derived by the zone-folding approximation, is shown in the right panel. As can be seen, between the lowest π bands there is a small bandgap, making this nanotube semiconducting.

whose allowed k states coincide with the K point

$$\mathbf{K} \cdot \mathbf{C} = 2\pi \cdot m \qquad m \in \mathbb{N} \tag{3.40}$$

$$\frac{1}{3}(\mathbf{k}_1 - \mathbf{k}_2) \cdot (n_1\mathbf{a}_1 + n_2\mathbf{a}_2) = 2\pi \cdot m \qquad (\mathbf{a}_i \cdot \mathbf{k}_j = 2\pi\delta_{ij}) \tag{3.41}$$

$$n_1 - n_2 = 3m \tag{3.42}$$

This result states that all nanotubes where the difference between there chiral number is a multiple of three are metallic including all armchair (n, n) nanotubes [112, 113].

That means all other nanotubes exhibit semiconducting characteristics.

$$n_1 - n_2 = 3m + p, p = \begin{cases} 0 \text{ metallic SWNT} \\ \\ \pm 1 \text{ semiconducting SWNT} \end{cases} \tag{3.43}$$

From this follows that in a normal distribution of chiralities, one third of nanotubes are metallic, because their band structure slices through the center of the graphene cone at the K points (figure 3.8); the remaining two thirds, for which $p = \pm 1$ are semiconducting. This predicted correlation between chirality and electronic properties of single-walled carbon nanotubes, derived from the approximated band structure of graphene and the boundary conditions of rolling a graphene sheet up into tubular shape with finite circumference, has been directly verified by experiments [114, 115].

Because the character of the nanotube band structure depends strongly on the chirality of the nanotube, nanotubes of similar diameter can therefore have drastically different electronic properties. Currently, all synthesis routes for carbon nanotubes produce a distribution of chiralities and diameters, thus, a distribution of semiconducting and metallic nanotubes, which will significantly affect the charge transport characteristics of a nanotube network.

3.3.3 Density of states

The density of states (DOS) is the number of available states ΔN for a given energy interval ΔE. The shape of the density of states has a strong dependence on the dimensionality of system in question. For a one-dimensional system, such as carbon nanotubes, the DOS diverges as the inverse of a square root of the energy in the vicinity of the band extrema (figure 3.12). A general analytical expression of the DOS for carbon nanotubes was derived by Mintmire et al.[116].

Considering a single one-dimensional, doubly degenerate band $E(k)$, the density of states can be calculated with

$$n(E) = \frac{2}{q \cdot |\mathbf{k}_\parallel|} \sum_j \int dk_\parallel \; \delta(k_\parallel - k_j) \; \left| \frac{\partial E^\pm(k_\perp, k_\parallel)}{\partial k_\parallel} \right|^{-1} \tag{3.44}$$

In this equation k_j is given by $E - E^\pm(k_\perp,\ k_\parallel) = 0$, and the length of the one-dimensional Brillouin zone

$$q \cdot |\mathbf{k}_\parallel| = \frac{4\pi^2 d}{\sqrt{3} a_0^2} \tag{3.45}$$

The density $n(E)$ for a vector k close to the Fermi level i.e. next to the K point can be calculated using the linear approximation from equation (3.36)

$$E(\mathbf{k}) = \pm \frac{3a_0}{2} \; \gamma_1 \; |\mathbf{k} - \mathbf{K}| \tag{3.46}$$

Any allowed wave vector $\mathbf{k}$ has a continuous component $\Delta\mathbf{k}_\parallel$ and a quantized component in the circumferential direction $\Delta\mathbf{k}_\perp$. The distance between $\mathbf{k}$ to the next K point expressed as $|\mathbf{k}-\mathbf{K}|$ can thus be described in terms of these components, this is illustrated in the inset of figure 3.11

$$|\mathbf{k} - \mathbf{K}| = \sqrt{\Delta k_\perp^2 + \Delta k_\parallel^2} \tag{3.47}$$

$\Delta k_\perp$ can be obtained by projecting $\Delta\mathbf{k}$ onto the circumference $\mathbf{C}$ knowing that $\mathbf{k} \cdot \mathbf{C} = 2\pi m$

$$\Delta k_\perp = (\mathbf{k} - \mathbf{K}) \cdot \frac{\mathbf{C}}{|\mathbf{C}|} = \frac{1}{|\mathbf{C}|} \left(2\pi m - \frac{2\pi}{3} n_1 + \frac{2\pi}{3} n_2 \right) = \frac{2}{3d} (3m - n_1 + n_2) \tag{3.48}$$

The contribution of a certain state at k to the total density of states at the energy $E(k)$ is given by

$$\left|\frac{\partial E^{\pm}(k_\perp, k_\parallel)}{\partial k_\parallel}\right|^{-1} = \left|\frac{\sqrt{3}a_0\gamma_1}{2} \cdot \frac{\partial\sqrt{\Delta k_\perp^2 + \Delta k_\parallel^2}}{\partial k_\parallel}\right|^{-1} \tag{3.49}$$

$$= \left(\frac{2}{\sqrt{3}a_0\gamma_1}\right) \frac{|E^{\pm}|}{(\sqrt{E^{\pm})^2 - E_m^2}} \tag{3.50}$$

using the abbreviation

$$E_m = \frac{\sqrt{3}}{2}a_0\gamma_1 \; k_\perp = \frac{a_0\gamma_0}{\sqrt{3}d} \cdot |3m - n_1 + n_2| \tag{3.51}$$

Additionally, each line in the vicinity of the K will have two points located by $\mathbf{K}$ at any given $E(\mathbf{k})$ and two equivalent points at $-\mathbf{K}$ which will also contribute to the density of states at this energy. Together, four additional states have to be taken into account when inserting (3.50) into (3.44), and integrating over $k_\perp$.

$$n(E) = 4 \cdot \frac{a_0}{\pi^2 d\gamma_1} \sum_{m=-\infty}^{\infty} g(E,\; E_m) \tag{3.52}$$

with

$$g(E,\; E_m) = \begin{cases} \frac{|E|}{\sqrt{E^2 - E_m^2}} & \text{for} \;\; |E| > |E_m| \\ 0 & \text{for} \;\; |E| < |E_m| \end{cases} \tag{3.53}$$

At $E = E_m$ the density of states diverges. These singularities are known as *van Hove singularities*. These points where the slope vanishes are given by $E_m = m\; a_0\gamma_1/\sqrt{3}d$ with $m = 0, 3, 6, ...$ for metallic and $m = 1, 2, 4, 5, 7, ...$ for semiconducting nanotubes. As shown before, metallic nanotubes have no bandgap but semiconducting tubes have a small bandgap equal to

$$E_{11}^S = 2E_{m=1} = \frac{2a_0\gamma_1}{\sqrt{3}d} \tag{3.54}$$

In figure 3.12 the density of states for the two cases of a metallic (9, 0) and a semiconducting (10, 0) are shown next to the linearly approximated band structure derived from the tight-binding approximation of graphene. The relevant energy levels for the metallic nanotube E_i^m and the semiconducting nanotube E_i^s, as well as the intraband transitions E_{ii} are labeled.

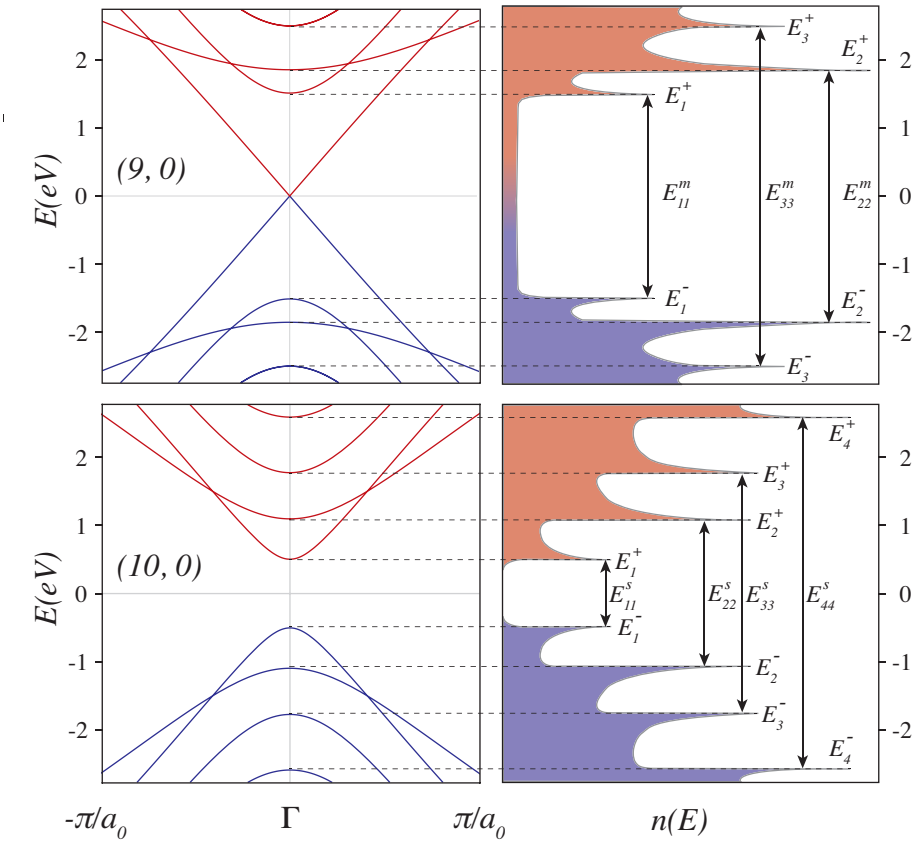

Figure 3.12: Density of states for a (9, 0) nanotube (above) and a (10, 0) nanotube (below) derived from the zone-folding approximation. The density of states are shown next to the linearly approximated bandstructure according to the tight-binding model of graphene (3.37). Band energies and interband transitions are indicated.[110]

3.4 Electronic charge transport

Metallic single-wall carbon nanotubes can be considered one-dimensional quantum wires [117] which have two overlapping bands at the Fermi level constituting the two conduction channels [118], each with a conductance of $G_0 = 2e^2/h = (12.9\ \mathrm{k\Omega})^{-1}$[119]. This property of ballistic charge transport predicted for individual metallic SWNTs has since been confirmed experimentally and experimental values close to the theoretical limit have been reported [120, 121, 122]. This indicates that the mean-free path of an electron i.e. that distance it can travel before being scattered is several microns long [123]. In fact, even in individual semiconducting SWNTs ballistic transport was observed for nanotube lengths of around 300 nm [124]. Consistently, the resistivity of an individual nanotube can be as low as $\rho = 5.1 \times 10^{-6}\ \Omega \cdot \mathrm{cm}$ corresponding to a conductivity $\sigma \approx 200\ 000$ S/cm [114] with an intrinsic electron mobility of more than 100 000 $\mathrm{cm}^2/\mathrm{Vs}$ [125].

3.4.1 Carbon nanotube networks

For applications, in general, mesoscopic networks of SWNTs have to be considered. In films, however, SWNTs exhibit orders of magnitude lower conductivities in the range of 6600 S/m [126] with the mobility decreasing to around $10 - 20$ cm^2/Vs [127, 128]. This discrepancy in the electronic transport properties between individual nanotubes and networks of nanotubes is largely caused by the large resistance at nanotube-nanotube junctions [129, 130, 131, 132, 133, 134].

Several factors affect the magnitude of this inter-tube resistance in a nanotube network. The spatial separation and overlap between two crossing tubes determines the hopping probability i.e. the inter-tubular charge transfer probability [132, 135]. Electronic transfer between nanotubes is further hampered by Schottky barriers which form between semiconducting and metallic SWNTs [129, 136]. The inter-tube resistance can therefore be in the range of 200 kΩ $-$ 20 MΩ [129, 130]. Whereas the resistance along an individual nanotube with a length of around one micrometer is $\sim$ 10 kΩ [131, 137]. Charge transport through a nanotube network is therefore mainly limited by the resistance at these inter-tube junctions rather than by the resistances of the individual tubes [133]. Consequently, networks containing longer nanotubes exhibit lower sheet resistances since charges travelling through the film have to cross fewer inter-tube junctions [138].

The density of the network is another critical factor which determines the sheet resistance as it sets the percolation threshold [131]. In contrast to networks of aligned nanotubes, the ones in which the nanotubes are randomly oriented have a much lower percolation threshold which is - due to their high aspect ratio - typically less than 1% surface coverage or 1wt% in polymer matrices [135, 139]. The additional benefit of random networks is that they are generally easier to fabricate and should not exhibit any electrical anisotropy [140]. Once the percolation threshold is reached, the conductivity of a nanotube network scales with its density and thickness [140].

Aside from network specific parameters such as density, thickness and ensemble orientation, aspects relating to the properties of the nanotubes affect the conductivity of the network. These include bundle size, graphene defect density, nanotube purity, bundle size, number of walls, ratio of semiconducting to metallic nanotubes and doping level [140]. One of the most crucial factors determining the conductivity of a nanotube film is the purity of the carbon nanotubes distribution because the presence of amorphous or sp^3 bonded car-

bon will have a highly detrimental effect on the sheet conductivity. Improvements in the synthesis processes towards purer, defect-free nanotubes are a way to minimize resistances caused by these impurities. Purification processing of the nanotubes can lead to additional elimination of defects or amorphous carbon.

The thickness of the carbon nanotube bundles is another factor which impacts the overall conductivity of a nanotube network [141]. Comparing the conductivity of networks with different average bundle sizes, the one with the thinnest bundle diameter is shown to have the lowest resistance at a fixed transmittance. This can likely be attributed to nanotubes on the inside of the bundle, which may not participate in charge transport but will impact the overall transmittance of the film, meaning that at a fixed transmittance, the total number of charge transporting nanotubes is lower for a network with thicker bundles. For the same reason, networks of multi-wall carbon nanotubes have much higher resistances than the ones with single-wall nanotubes, as the inner-walls do not participate in charge transport.

Highly conductive nanotube films can therefore be achieved when debundled single-wall nanotubes are employed. Also, for films consisting of debundled SWNTs there is an observable dependence of the conductivity on the diameter of the nanotubes [142]. Wider nanotubes form more conductive films than nanotubes with a narrower diameter. The underlying reason is the inverse dependence of the bandgap on the diameter, which results in wider nanotubes having a smaller bandgap. A smaller bandgap, in turn, allows more electrons to be thermally activated and consequently increases the number of mobile charges available for charge transport. For metallic nanotubes, as shown in 3.3.2, the valence and conduction band overlap at the Dirac points which means that mobile charges are always available. A higher content of metallic species in a nanotube network can therefore contribute to higher sheet conductance. A uniform chirality distribution of SWNTs will yield 67% semiconducting nanotubes which will have a much lower conductivity than the remaining 33% of metallic tubes. In addition, the junctions between semiconducting and metallic nanotubes exhibit much higher resistances than junctions of nanotubes with the same electronic characteristics [129].

3.5 Polymer functionalization

An essential step for the use of SWNT networks is the debundling and individualization of single nanotubes. This improves the charge transport characteristics of the network on the one hand, but also facilitates the dispersability of the instrinsically hydrophobic nanotubes for solution processing on the other hand. Van-der-Waals interactions lead to the propensity of carbon nanotubes to form bundles.

The most common post-processing strategy to individualize SWNTs and make them dispersible is to functionalize the nanotube walls. This can be achieved by covalent and by non-covalent interactions between the functionalizing agent and the nanotubes [143]. Covalent sidewall functionalization is a successful strategy only if the electronic properties of the nanotubes are not important for the application because it is based on breaking the π-conjugation of the SWNTs thus disrupting their electronic properties [144, 145].

In contrast, non-covalent functionalization does not hamper the electronic or optical properties of the nanotubes [145]. In one non-covalent strategies, SWNTs can be brought into aqueous suspensions by encapsulating the nanotubes with surfactants such as sodium dodecyl sulfate (SDS) [146]. The process relies on ultrasound treatments of a mixture of the surfactants and the nanotubes which breaks up the bundles and allows the hydrophobic tails of the surfactant molecules to arrange themselves around the nanotube walls while their hydrophilic heads make the nanotubes dispersible in water.

Another approach uses single-stranded DNA (ss-DNA), in which the DNA wraps helically around the SWNTs driven by π-π-stacking between the nucelobases of the DNA and the π-electrons of the SWNT walls [147]. The hydrophilic functional group of the DNA makes the functionalized SWNTs dispersible in water. This strategy has also been shown to be able to differentiate between semiconducting and metallic nanotubes by controlling the interaction between the DNA strands and the SWNTs through changes in the pH of the aqueous environment [148]. Furthermore, by choosing specific DNA sequences, researchers were able to separate individual nanotube chiralities [149]. A drawback of the DNA based approach is that the functionalization can only be done in an aqueous medium. The nanotube dispersion are therefore not compatible with systems which are water-sensitive such as perovskite absorbers.

A class of non-aqueous solvents which is compatible with perovskites are organic solvents, which include amongst others chlorobenzene, toluene and chloroform. A means to disperse SWNTs in those solvents is the use of several conjugated polymers or block-copolymers. The dispersion becomes possible when the conjugated polymer backbone wraps around the nanotube and interacts via π-π stacking with the π-electrons of the nanotube wall. The side chains help to isolate and individualize by creating a steric barrier, and disperse the nanotubes, on the one hand, but can also affect the selectivity and effectivity of the wrapping process itself [150].

Conjugated polymers that have been shown to disperse SWNTs include poly(phenylene-vinylenes)[151], poly(phenyl acetylenes) [152], polycarbazoles [153]. Furthermore, polyfluorenes are able to not only disperse SWNTs but preferentially wrap semiconducting types [154, 155, 156]. The stiff polymer backbone aligns in order to maximize the π-π interaction between the nanotube and the fluorene units, which forces the polymer into a helical conformation around the nanotube. It is argued that due to the relative stiffness of the backbone this wrapping is only effective for a narrow range of large chiral angles. Additionally, the length of the alkyl side chains plays a critical role, such that a shorter alkyl chain makes the polymers less selective and broadens the distribution of wrapped SWNTs [154, 155]. The most effective side chains are octyl chains which interconnect between neigboring polymer chains and then align, through van-der-Waals interactions, on similar zigzag motifs on the SWNT wall [155]. Aside from the π-conjugated polymer backbone and the alkyl-sidechains, the solvent in which the polymer wrapping is induced is a critical parameter for the selectivity of the polymer [155, 157].

Polyfluorenes, however, have wide band gaps which might hinder the charge transfer between nanotubes which are wrapped by these polymers [150]. For optoelectronic applications, of particular interest, is therefore the family of poly(alkyl thiophenes) as wrapping polymers for SWNTs, since they have a much narrower bandgap and the polymer-wrapping might synergistically improve the performance of the SWNTs [158]. In the right solvent environment, one that exhibits a low solubility for SWNTs and is non-polar [157], the polythiophene with twelve-carbon side-chains, poly(3-dodecylthiophene) (P3DDT), can be used to highly selectively wrap semiconducting SWNTs [159, 160].

In chlorinated solvents, in contrast, polythiophenes generally wrap SWNTs of all chiralities [161, 159, 162]. Additionally, analogous to the observed trend for polyfluorene polymers, a reduced length in the side chains also decreases the selectivity of the polymers [159]. A poly-

thiophene, which has been shown to very effectively and non-discriminately wrap SWNTs is accordingly the six-carbon-chain poly(3-hexylthiophene) (P3HT) [163, 164]. The polymer forms a monolayer sheath around the SWNTs allowing for non-wrapping polymer to be removed by purification [164].

Charge transfer from wrapping P3HT to the SWNTs has been studied in great detail [165, 166], showing that charges transfer on an ultrafast time scale between the polymer and the SWNTs [165]. The charge transfer was inferred from time-resolved photoluminescence decay [165]. The flat band diagram of the polymer and the SWNTs would suggest electron transfer from the polymer to the SWNTs (figure 3.16)[167, 168, 169].

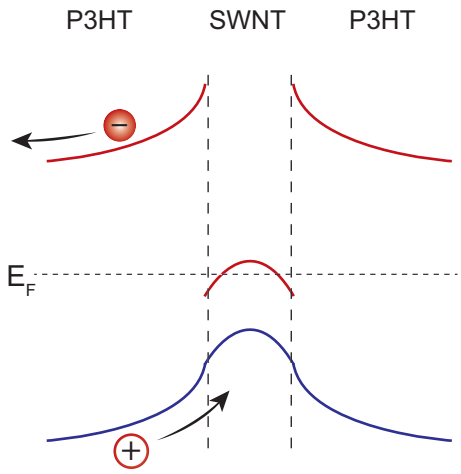

Figure 3.13: Proposed band alignment at the SWNT-P3HT heterojunction by Lan *et al.* [170]. The upwards band bending of the polymer and the downwards band bending of the SWNT creates a potential barrier for electrons and a driving force for holes towards the SWNTs. This would explain why hole transfer rather than electron transfer from the polymer to the nanotubes is observed.

Interestingly, measurements of the surface potential using a Kelvin probe force microscope (KPFM) at the junction between P3HT and SWNTs suggested that at the polymer-nanotube interface holes are transferred to the SWNTs rather than electrons [170]. The authors of this study built a device that could extract one type of charge carrier to the ground, allowing the P3HT-SWNT heterojunction to be dominated by either electron or hole transfer. Measuring the changes in surface potential (SP) in the dark and in the light of P3HT and the SWNTs at the polymer interface, it could be demonstrated that in an electron dominated environment no changes in the SP of the SWNTs could be measured [170]. However, when the electrons were extracted to the ground, resulting in an accumulation of holes and thus making the SWNT-polymer interface hole dominated, the SP of the SWNTs would shift

due to illumination [170]. This finding indicates that photogenerated holes transfer form the polymer to the SWNTs thus changing their potential.

To explain this behavior the authors speculate that the Fermi level alignment between the SWNTs and P3HT results in an upward band bending of P3HT and a downward band bending of the SWNTs (figure 3.13). The LUMO of the polymer would thus form a potential barrier for electrons, whereas the bending of the HOMO would create a driving force for hole transfer from the polymer to the SWNTs [170].

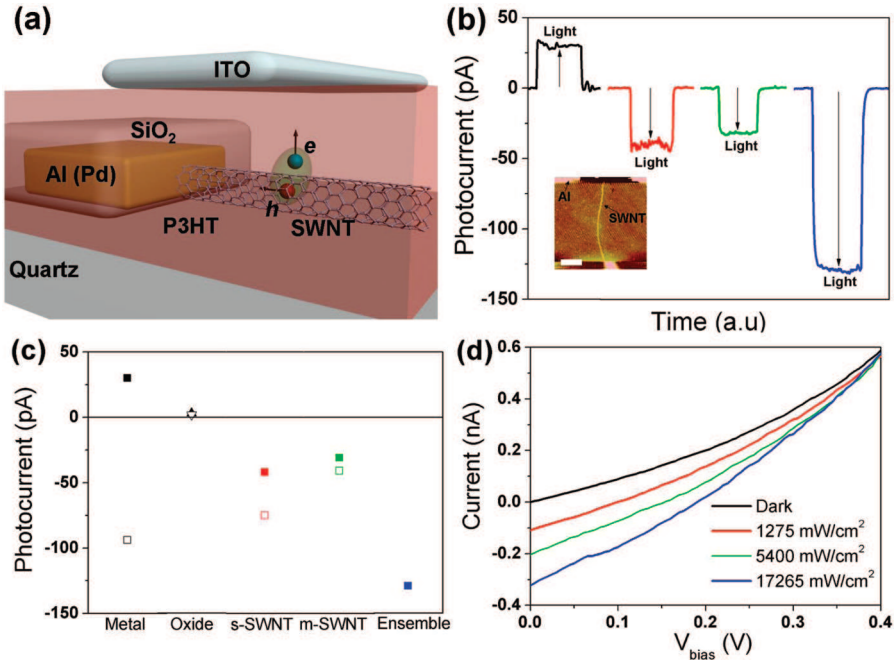

Figure 3.14: a) Schematic of the heterojunction between an individual SWNT and a P3HT matrix. Photogenerated excitons dissociate at the heterojunction, followed by holes transfer into the nanotube, and electrons collected by ITO electrode. b) Short circuit photocurrent for an individual semiconducting SWNT/P3HT junction (red line), an individual metallic SWNT/P3HT junction (green line), an ensemble SWNT/P3HT device containing six nanotubes (blue line), and an Al/P3HT reference device (Al area of $\sim 1000\mu m^2$) (black line). The devices are under continuous wave (CW) green laser (532 nm) illumination with intensity of 1275 mW/cm^2, and the current is collected from the ITO electrode. (Inset) AFM image of a single SWNT bridging the metal contacts. Scale bar is 2 µm. c) Short circuit photocurrent of metal/P3HT (black squares), metal/oxide/P3HT (black triangles), single semiconducting SWNT/P3HT (red squares), single metallic SWNT/P3HT (green squares), and ensemble SWNT/P3HT (blue square) junctions. Filled and open symbols correspond to Al and Pd electrodes, respectively. d) Current-voltage characteristics of an Al-contacted ensemble SWNT/P3HT device with six nanotubes under 532 nm CW laser illumination. (Adapted with permission from N. Dissanayake et al. Nano Letters (2011), 11, 286290 [166]. Copyright (2011) American Chemical Society.)

Further evidence for efficient hole transfer from the polymer to the SWNT valence band comes from direct photocurrent collection in hole-only devices with a SWNT-P3HT heterojunction [166]. Individual SWNTs were contacted with an Al (or Pd) electrode and

embedded in a P3HT matrix, which was itself contacted with ITO (figure 3.14 a)). The illumination with a CW laser at 532 nm, leads to the photogeneration of excitons in the P3HT, which dissociate at the heterojunction between the polymer and the SWNT. The measured photocurrent is shown in figure 3.14 b). In the absence of a nanotube, a positive photocurrent is extracted from the Al/P3HT/ITO junction, which corresponds to an electron injection into Al which is in agreement with the relative positions of the work functions of the electrodes, $\phi_{\mathrm{Al}} = \sim 4.3$ eV and $\phi_{\mathrm{ITO}} = \sim 4.7$ eV. In contrast, when an SWNT is contacted, the extracted photocurrent is negative, and therefore the result of hole transfer from the polymer to the nanotubes. When the Al electrode is replaced with Pd, a metal with a much higher work function ($\phi_{\mathrm{Pd}} = \sim 5.1$ eV), the sign of the photocurrent changes for the device without SWNTs, however, it remains the same for the devices with SWNTs (figure 3.14 c)). The preferential charge extraction of holes displayed by the SWNTs occurs therefore independent of the relative workfunction positions of the contacting electrodes.

By back gating the SWNT-polymer heterojunction with a silicon oxide covered doped silicon substrate, the photocurrent could be measured dependent on the gate voltage. The gate voltage dependence of the photocurrent suggests that the exciton dissociation mechanism in this system relies on the workfunction difference between the polymer and the SWNT. The workfunction of the SWNTs is strongly increased by heavy p-doping due to charge exchange between P3HT and the nanotubes when they form a junction. Remarkably, this is not just observed for semiconducting nanotubes but also for metallic nanotubes [166]. The metallic nanotube can therefore function equally well as hole transporter in this system. In an ensemble of electronically mixed SWNTs the extracted photocurrent increases by contribution of all SWNTs independent of the electronic nature (figure 3.14 b) and d)).

Previous density functional theory (DFT) calculations had shown that at the interface of a metallic SWNT and P3HT a strong electrostatic potential drop can be observed, making the polymer much more attractive for negative charges, and thus making the hole transfer from P3HT to the nanotubes more energetically favorable [171]. Additionally, due to the charge transfer between the polymer and metallic nanotubes, the electrostatic interactions are likely to be stronger for metallic nanotubes in a mixed distribution of SWNTs [171].

3.6 Applications in solar cells

The extraordinary charge transport properties of carbon nanotubes, in particular the high charge carrier mobilities combined with the large aspect ratios, has led to a range of studies investigating ways to integrate them into photovoltaic solar cells. Carbon nanotubes have been incorporated in three different ways in solar cells, as transparent electrode, charge selective contact layer and as part of the active layer. The following section will focus on single-walled carbon nanotubes as part of the active layer and their use as charge collection layers.

3.6.1 Organic solar cells

The basic principles of organic polymer solar cells is described in more detail in section 2.1.5. In short, the active layer of an organic or polymer-based solar cell consists of two crucial components, a donor, which is typically a conjugated polymer, and an acceptor, which is often a fullerene derivative [172]. The donor absorbs photons which generate bound electron-hole pairs - excitons. These need to diffuse to the heterojunction, the donor forms with the acceptor which readily accepts electrons thus providing a driving force for the dissociation of the excitons. Due to the low dielectric environment in the polymers, the exciton binding energy is generally large [173], especially compared to the built-in electric fields, which are consequently not able to dissociate the excitons directly [40]. A strong potential drop at the donor-acceptor interface is therefore required to separate the electrons from their holes in order to generate free carriers which can be extracted at their respective electrodes [39]. Because extractable charges can only be generated at the donor-acceptor interface, the donor domains should not be larger than twice the diffusion length of excitons which is around 10 nm [174], so that the excitons can diffuse to the interface before recombining. After the charge-separation at the interface, free electrons and holes must reach their respective electrodes to be extracted into the circuit. This requires a continuous path through the two donor system for the holes and through the acceptor system for the electrons. For charges to be extracted efficiently both charge carrier domains need to form intercalated continuous percolation networks with high mobility for their respective charge carrier.

Carbon nanotubes should therefore be an ideal component for such a heterosystem, since they exhibit extremely high mobilities for electrons (10^5 cm^2 Vs^{-1})[125, 175] and due to their aspect ratio of up to 10^6 [176], they can form interconnected percolation networks at very

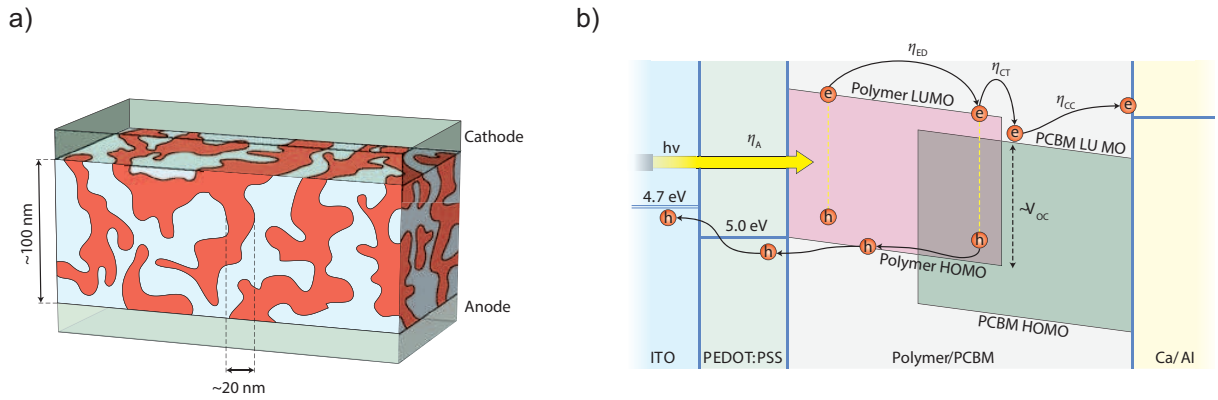

Figure 3.15: a) The operating mechanism of a PSC. b) Conceptual morphology model with bicontinuous interpenetration network of the polymer and the acceptor. (Reproduced with permission from [39] Copyright 2012 Nature Publishing Group.)

low concentrations [135]. The excellent charge transport properties of SWNTs, as individual tubes [124] as well as networks [177] give them a particular advantage over fullerenes, which, although being the established family of acceptors [37], have a relatively poor electron mobility due to hopping-based charge transport, and exhibit a propensity of clustering [178], which is why charge extraction is still a limiting factor for the device performance in fullerene-based heterojunctions. Furthermore, a study suggested that SWNTs have a higher electron affinity than C_{60} and its derivatives [179], and should therefore provide a greater driving force for exciton dissociation. Additionally, several studies have reported that SWNTs can serve as nano-template for the polymer crystallization improving the photophysical properties of the polymer [161, 164, 180].

The band alignment of P3HT and SWNTs depends on the diameter of the SWNTs since the bandgap of an SWNT scales inversely with its diameter $E_g \propto 1/d$. For SWNTs with a diameter exceeding 1 nm, SWNTs form a type I heterojunction with P3HT [164], which may be more prone to energy transfer rather than charge transfer [165]. This is in particularly true when the charges are bound in an exciton whose binding energy is requires a heterojunction in order to dissociate it into free charges. This is in general the case in polymeric environments with a low dielectric permittivity. Lioudakis et al. reported accordingly that they could not observe efficient charge separation at the interface between P3HT and wide-bandgap SWNTs [181].

SWNTs with a diameter $d < 1$ nm, however, should form a type II heterojunction with P3HT [165, 182, 183], where both the lowest unoccupied molecular orbital (LUMO) and the highest occupied molecular orbital (HOMO) of the donor lie energetically above those

of the acceptor [184]. This staggered heterojunction should promote exciton dissociation by facilitating selective electron transfer from the P3HT to the nanotubes. In fact, charge transfer is modelled [169] and observed to occur on a sub-picosecond time scale [165] and results in long-lived free charges in the P3HT [184] (figure 3.16). The polymer-SWNT interface shoulder therefore be able to dissociate excitons into free charges at the polymer-nanotube interface, and facilitate rapid transfer away from the interface thus preventing charge recombination.

The first application of SWNTs as component of the active layer in polymer solar cells with a polythiophene absorber was therefore that of the electron acceptors, replacing the commonly used fullerene-derivative [185, 186, 187, 188, 189, 180, 190]. All studies observed a much higher open-circuit voltage for the polymer-based devices with SWNTs as compared to fullerenes, reaching up to 1.81 V [190]. However, the overall power-conversion efficiency was generally significantly lower than for fullerene-based devices. The highest efficiency for a two-component P3HT-SWNT system was 0.72%, whereas devices with fullerenes as acceptors can perform almost an order of magnitude better with a PCE of close to 5% [191]. It was suggested that this may be due to insufficient interfacial area between the polymer and the SWNTs [188], leading to insufficient and incomplete exciton dissociation. This may be compounded by the fact that low concentrations of SWNTs were used which came close to the lower percolation threshold limit. The reason was that higher concentrations were shown to lead to shunting and increased recombination, which was correlated with the electronic heterogeneity of the SWNTs [176]. Especially the presence of metallic species was identified as cause for the generally poor performances [182, 192, 193].

The findings by Dissanayake *et al.* and Lan *et al.*, in contrast to the previous approaches, suggest that SWNTs act as hole-acceptor rather than as electron-acceptor [166, 170]. This mechanism could provide a justification for the inexplicably high open-circuit voltages previously reported [189, 180, 190]. The open-circuit voltage in organic bulk-heterojunctions is approximately given by the energy offset between the photogenerated electrons and their corresponding holes after exciton dissociation, i.e. between the HOMO of the donor and the LUMO of the acceptor [39]. For the system with P3HT as donor and SWNTs as acceptor, the HOMO of the polymer is at around -5.0 eV and the LUMO (conduction band) of the SWNTs is around -4.0 eV. The open-circuit voltage should therefore not exceed 1.0 eV (figure 3.16 a)). In contrast, when hole transfer from the polymer to the nanotubes is assumed, after exciton dissociation the electron population is in the LUMO of P3HT at -2.8

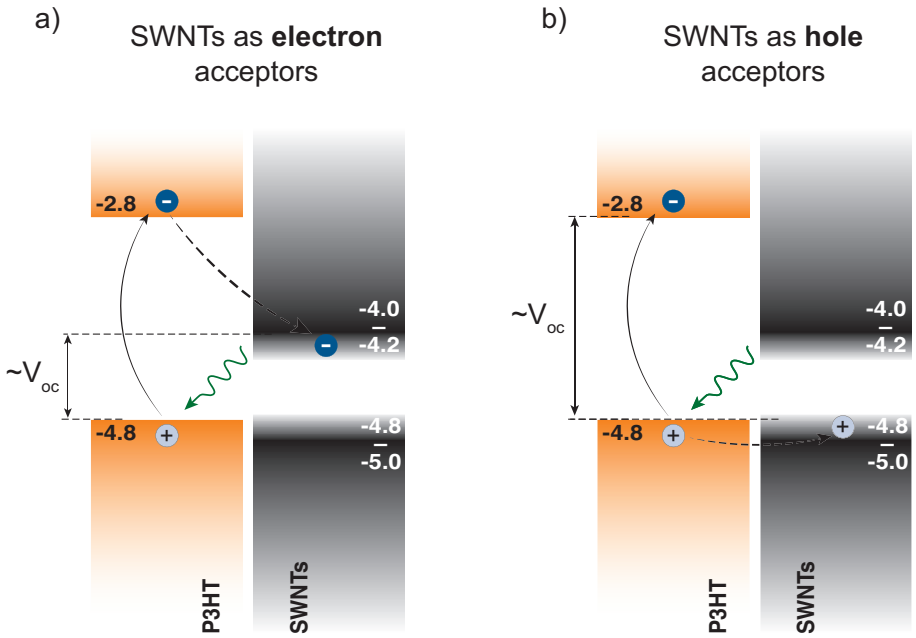

Figure 3.16: Comparison of the two possible charge transfer mechanisms between P3HT and SWNTs. a) Shows the SWNTs as acceptor. After photogeneration of the exciton in the P3HT, it diffuses to the P3HT-SWNT interface where it dissociates by transferring the electron to the SWNT conduction band while the hole remains in the HOMO of the polymer. The possible V_{oc} should be smaller or, ideally, equal to the energy offset between the conduction band of the SWNTs and the HOMO of P3HT, which is around 1.0 eV. b) Shows the SWNTs as hole acceptor. In this scenario, exciton dissociation occurs due to hole transfer from the polymer to the valence band of the SWNTs, while the electron remains in the LUMO of the P3HT. The attainable photovoltage should then be the difference between the nanotube valence band and the LUMO of the polymer, which would be around 2.0 eV. A possible cause for this mechanism is band bending due to Fermi level alignment when polymer and nanotubes form a heterojunction, as proposed by Lan *et al.* [170].

eV while the corresponding holes sit in the valence band of the SWNTs at -4.8 eV. The possible open-circuit voltage would therefore be around 2.0 eV (figure 3.16 b)), which could explain a value around 1.81 eV [190]. As a rationale for hole transfer rather than electron transfer as the dominating charge transfer from the polymer to the nanotubes could be band bending in the polymer due to Fermi level alignment (figure 3.13) [170].

Experimentally, further evidence for hole transport was provided Chaudhary *et al.* [194]. This study investigated the impact of incorporating a layer of SWNTs on all possible interfaces in a P3HT-PCBM device. The results indicate that the nanotubes positively affect the device performance when employed for hole collection. In contrast, put on the electron accepting interface resulted in a zero-field device without any significant power output [194]. Based on this work, Dabera *et al.*, investigated the hole transport characteristics of P3HT-wrapped SWNTs [195]. The interaction between P3HT and the SWNTs was shown to lead to relatively strong p-doping of the SWNTs through charge exchange with the polymer.

Therefore charge transport for holes was measured to be 2-3 orders of magnitude higher than that of electrons in a field effect transistor (FET). After confirming the hole-transporting properties of the P3HT-SWNT nanohybrids, incorporating them into an organic bulk heterojunction was shown to improve the power-conversion efficiency compared to a device without hole-transporting layer yielding a PCE of 7.6% [195].

3.6.2 Inorganic solar cells

With a bandgap of 1.1 eV, silicon is an excellent absorber in the visible range and has become one of the most common commercial solar cell materials to date [196]. As elaborated in the previous chapter, its fundamental mechanism is based on the photovoltaic effect of the p-n junction, which is the heterojunction which arises where strongly n-doped silicon meets strongly p-doped silicon forming a so-called p-n junction [29]. Instead of heavily p-doped silicon, it is also possible to use other p-type materials. Carbon nanotubes fulfil the requirements to be a possible p-type partner in a heterojunction considering their outstanding optoelectronic properties and their inherent p-type characteristic due to ambient oxygen doping [197].

Due to their electronic heterogeneity, carbon nanotubes will form two different types of junctions with silicon. Semiconducting SWNTs will form classic pn-junctions with n-type silicon. Upon contact, for the Fermi levels of the two materials to align, the charge carrier concentration must equilibrate. Thus, holes will be injected from the nanotubes into the silicon, while electrons flow from silicon into the nanotubes. This entails, however, that the previously charge-neutral materials lose their mobile charges with immobile charges of the opposite polarity remaining. These space charges, negative on the SWNT side and positive on the silicon side, will give rise to a built-in electric field which acts in the opposite direction of the charge carrier diffusion, generating a drift current. The charge re-distribution between the materials leads to band bending at the interface, bending the SWNT bands downwards, and the Si bands upwards, resulting in an Ohmic p-type contact but a Schottky potential barrier for the electrons figure 3.17. An equilibrium is reached when the drift current matches the diffusion current, and the total current at the junction is zero. In the case of metallic SWNTs forming a junction with silicon, a so called Schottky junction arises, which leads to similar conditions differing mainly in the magnitude of the reverse saturation current and the switching characteristics [198] (figure 3.17).

Under operation of an SWNT-silicon junction, photons of the visible spectrum are absorbed by the silicon, photoexciting electrons into the conduction band, thus generating concomitantly holes at the previous place in the valence band. This process disturbs the previously obtained thermal equilibrium, shifting the Fermi level of the silicon up. The potential difference between the non-equilibrium Fermi level in the silicon and that of the nanotubes, reestablishes a built-in field which will separate the photogenerated charge carriers, driving the holes towards the SWNTs, where they are extracted into the circuit. The open-circuit of the junction is determined by the workfunction difference of silicon and the nanotubes, while the short-circuit current is mainly dependent on the bandgap of silicon.

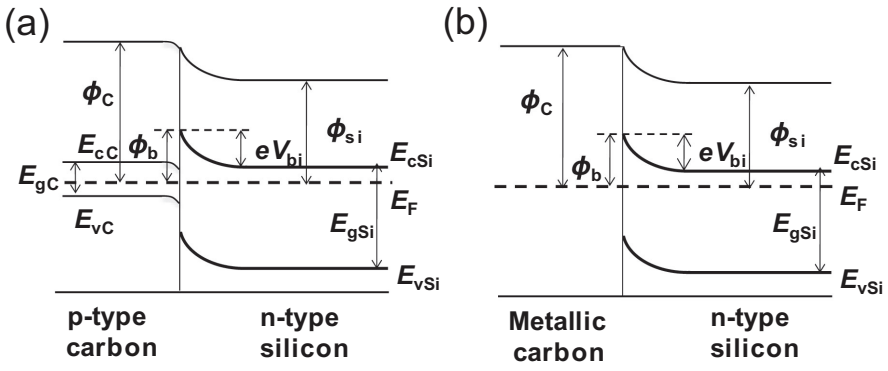

Figure 3.17: Energy-band alignment between a carbon material and silicon, forming a heterojunction. Depending on the electronic properties of the carbon material, two types of heterojunctions can arise: a) a p-n junction i.e. a semiconductor-semiconductor junction and b) a Schottky junction i.e. a metal-semiconductor junction. (Reproduced with permission from Li *et al.*, Adv. Mater. 2015, 27, 6549 [198]. Copyright 2015 WILEY-VCH Verlag GmbH & Co. KGaA)

In pioneering experiments it had been demonstrated, that carbon nanotubes and silicon can form heterojunction with rectifying behavior illustrating that workfunction and bandgaps of the two materials should be able to separate photogenerated carriers [199, 200, 201]. Based on this work, the first solar cell based on a carbon nanotube-silicon heterojunction was reported in 2007, using double-walled carbon nanotubes for both charge generation and transport, and achieving an efficiency of 1.3% [202]. The main limitation of this first incarnation of a nanotube-silicon solar cell were the low photocurrent and poor fill factor, mainly due to the high sheet resistance. Single-walled carbon nanotubes as the p-type component with silicon in an p-n junction started with an efficiency of 2.7% in a pristine state (2009) and above 4.0% when doped with acid (2010) [203, 204]. The limiting factor remained the poor conductivity of the nanotube film caused, in particular, by the nanotube-nanotube

junctions. A range of strategies have been proposed and implemented combating this issue for example by directly growing highly interconnected SWNT networks of high purity onto a n-doped silicon substrate [205, 206, 207, 208, 209, 210]. Due to high-purity, defect-free nanotube networks and without the presence of charge transport hampering surfactants, the resistivity was significantly reduced resulting in an improved device efficiency of more than 10% for pristine nanotubes [209, 210]. In a similar vein, by aligning nanotubes at the Si interface high-density coverage with a lot of direct charge extraction paths were achieved, thus also yielding an efficiency above 10% [211, 212, 213, 214].

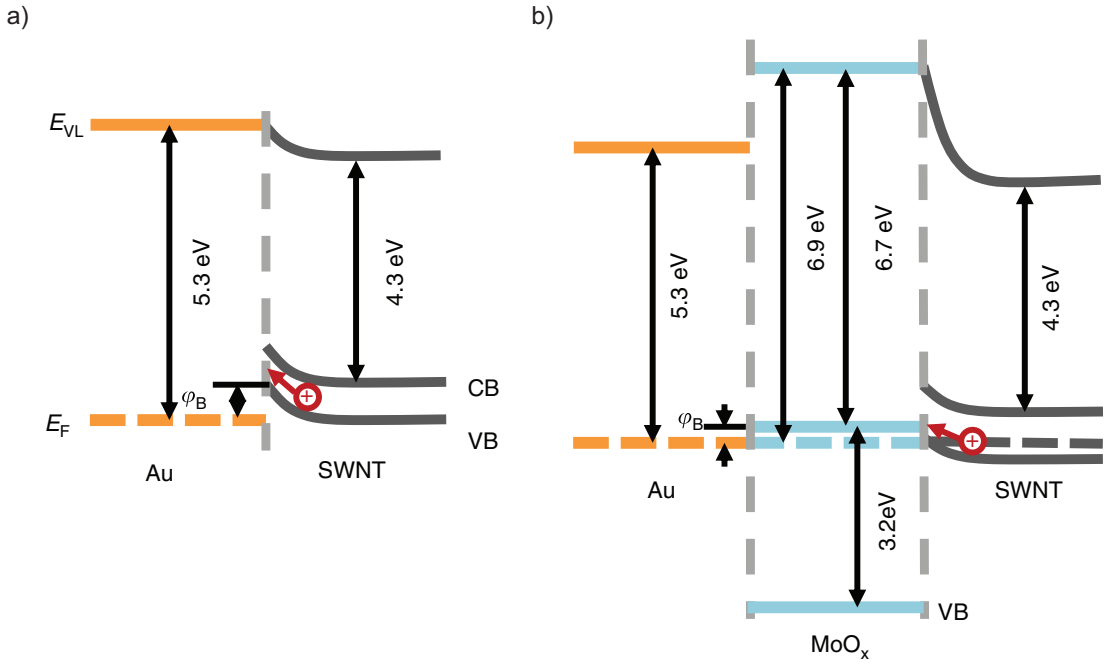

Figure 3.18: a) The work function of the SWNTs is around 4.7eV, the one of the gold electrode is around 5.3 eV, because of the work difference, an interface dipole layer is formed at the SWNT/Au-anode interface until the valence band edge of the SWNTs aligns with the Fermi level of the Au anode; this is accompanied by large band bending. b) The work function of the MoO_x layer is higher than the ionization energy of the SWNTs and is close to the Fermi level of the SWNTs; this facilitates the hole transfer from the SWNTs to the Au anode through the MoO_x layer. The change in the band alignment due to the insertion of the MoO_x layer enhances the photogenerated hole extraction from the SWNTs to the Au anode, leading to a significant increase in the short-circuit current density and a reduction of the net series resistance (R_s) value. Therefore, as an effective hole transport layer, MoO_x enhances the photovoltaic performance by preventing current leakage and consequent counter-diode formation [210]. (Reproduced with permission from Wang *et al.*, Nat. Commun. 2015, 6, 6305 [210]. Copyright 2015 Nature Publishing Group.)

For devices with pristine nanotubes, charge extraction is still limited. The main culprit appears to still be the intertube junctions. Thus improving the junctions between the nanotubes should result in a higher power conversion efficiency. Infiltrating the nanotube network with nitric acid was shown to significantly reduce the sheet resistance by removing

residue on the substrate and p-doping the nanotube [205]. Futhermore, at the interface a photoelectro-chemical cell is formed that enhances the charge separation and transport [205]. The overall efficiency achieved with this configuration was 13.8% [205]. Further improvements were achieved by reducing the reflectance of the devices, which for silicon can reach up to 40% in the visible range. A layer poly(methyl methacrylate) (PMMA) with a refractive index of 1.49 was demonstrated to reduce the reflective losses to less than 10% thus boosting the efficiency of a device with pristine SWNTs from 7.1 to 11.5%, and with the addition of nitric acid to 13.1% [214]. Aside from polymers such as PMMA, metal oxides can function as effective anti-reflection coatings [208, 210]. A film of 70 nm of TiO_2 decreases the reflectance in the visible down to 5% and combined with HNO_3/H_2O_2 doping, an efficiency of 15.1% was reached [208]. A layer of MoO_3 inserted between the SWNTs and the gold electrode was found to enhance the performance in several ways. By acting as anti-reflection coating, on one hand, but also by improving the hole extraction from the SWNTs to the gold electrode, by reducing shunting losses and by effectively p-doping SWNTs (figure 3.18), increasing the overall efficiency to 17.0% which is to date the best device performance for a p-SWNT/n-Si heterojunction solar cell [210].

In conclusion, by forming p-n or Schottky heterojunctions with n-type silicon absorbers, SWNTs have been demonstrated to efficiently separate charges and extract holes. The main limitations of these devices are reflective losses and the charge transport through the SWNT network caused by the intertube junctions. The former can be reduced using polymer or metal oxide layer as anti-reflection coatings, while the latter can be overcome by acid treatments and doping. The state-of-the-art silicon-nanotube device has a power-conversion efficiency of 17.0%.

3.6.3 Metal halide perovskite solar cells

Metal halide perovskite solar cells have been introduced in great detail in the previous chapter 2.15. Their initial architecture was based on a layered structure with the transparent anode at the bottom, the perovskite absorber in the middle, and the hole-collecting metal cathode at the top. An essential part for efficient charge extraction are the charge selective contacts on both sides of the perovskite absorber. The prototypical p-type contact is spiro-OMeTAD. It has essentially two functions, block the transfer of electrons and facilitate the transfer of holes, which can then be extracted into the circuit.

Carbon nanotubes had been shown to be p-type in nature under ambient conditions [197] with a workfunction in the range of 4.7-5.1 eV [215, 216]. Based on this, previous studies have successfully implemented them as p-type contact in organic solar cells [195] and inorganic solar cells [211], they should therefore be able to be an effective hole-transport material or cathode for perovskite solar cells.

In one of the first studies which used carbon nanotubes as a charge transport element in an n-i-p mesostructured perovskite solar cells, a free-standing film of SWNTs and DWNTs was laminated onto the perovskite and used as cathode [217]. Remarkably, the CNT film was shown to fulfill a dual-function as both hole-transporter and electrode, thus eliminating the need for a metal electrode. The comparatively low efficiency of 6.3% may be explained by relatively high resistance of the CNT film and a lack of charge-selectivity. Therefore, incorporating an additional layer of doped spiro-OMeTAD significantly improved the performance yielding a power-conversion efficiency of 9.9% [217].

Multi-walled carbon nanotubes (MWNTs) were used as additional additives by Lee *et al.* to further improve the conductivity of doped spiro-OMeTAD [218]. However, the authors observed a decrease in performance when the nanotubes contacted the perovskite directly, which they attributed to back-electron transfers. By inserting a layer of only doped spiro-OMeTAD at the interface and subsequently depositing a layer of spiro-OMeTAD containing the nanotubes, was therefore employed to ensure the charge-selectivity of the composite hole-transport layer. The loading of 2wt% of MWNTs in the spiro-OMeTAD solution improved the performance from 12.8% to 15.1% [218]. This improvement was attributed to a higher conductivity and reduction in series resistance.

A similar hierarchical composite structure of spiro-OMeTAD and carbon nanotubes had previously been described by Habisreutinger *et al.* [219]. The declared aim of this study was to replace the lithium based dopant in spiro-OMeTAD in order to remove a potentially harmful component which is known to be highly hygroscopic and reactive [220]. In contrast to previous studies, the n-type contact did not incorporate a mesoporous TiO_2 layer instead was composed of a compact TiO_2 layer and an inert alumina scaffold [25]. Charge selectivity was therefore not exclusively reliant on the n-type contact but was enhanced by wrapping the SWNTs in a p-type polymer (P3HT) which was hypothesized to improve the charge selectivity of the SWNT film [219], in accordance to previous findings [166, 195]. The polymer-wrapped SWNTs were directly deposited onto the perovskite and then capped with a subsequently deposited layer of neat spiro-OMeTAD. This double layer structure was shown

to outperform a blend structure in which the SWNTs were randomly dispersed throughout the spiro-OMeTAD matrix. The best-performing device reached a power-conversion efficiency of 15.4%, with a series resistance as low as 1.8 Ω/cm^2. Photoinduced absorption measurements were used to show that a significant fraction of photogenerated holes were transferred from the perovskite to the SWNTs. Comparing the photovoltage decay of two devices, one with just neat spiro-OMeTAD and one with the double layer of SWNTs and spiro-OMeTAD, revealed that the charge extraction was improved by about one order of magnitude [219] (More details in chapter 5).

Based on the finding that a large fraction of photocarriers are directly injected into the SWNTs, in a follow-up study, the neat spiro-OMeTAD layer was replaced altogether by an inert polymer matrix [221]. The polymer-wrapped SWNTs are thus shown to be a highly selective and effective hole-transporter in their own right yielding a scanned power-conversion efficiency of up to 15.3%. A high performance is interestingly contingent on the presence of the polymer matrix, despite it being electronically inert. While its role with regards to the charge extraction of photogenerated holes, is merely passive, the polymer layer appears to be essential by filling structural holes and gaps in the SWNT mesh-like network, thus closing shunting pathways and reducing recombination.

Aside from improving the charge extraction efficiency, the polymer matrix has an important second role, namely improving the device stability by preventing any interaction between any ambient moisture with the perovskite absorber. In fact, this study highlights the extreme vulnerability of the perovskite absorber towards ambient moisture, in particular, in thermal stressing experiments at an increased temperature of 80°C. The double layer hole-transporting structure composed of polymer-wrapped SWNTs and inert polymer matrix is shown to be able to protect the structural integrity of the perovskite while other hole-transporting materials cannot. One of the important finding is that especially the hygroscopic lithium-dopant on which most materials rely to improve their hole conductivity is accelerating moisture ingress and thus accelerating the perovskite degradation.

In this structure, individual SWNTs provide a direct high-speed connection for photogenerated holes from the perovskite to the cathode, with only few transfers required between nanotubes. It is likely that intertube resistances are therefore largely mitigated [221]. (More details in chapter 5).

While the previous study had used P3HT to functionalize SWNTs, Cai *et al.* used carbon

nanotubes to improve the charge transport characteristics of P3HT as the hole-transporting material for perovskite devices [222]. The nanotubes used in this study were a mix of single-walled and multi-walled carbon nanotubes which for structural reasons were dubbed "bamboo-like carbon nanotubes". Adding low concentrations of CNTs in the range from 0-2wt% to the P3HT solution prior to deposition was investigated. The highest-efficiency attained in this study was 8.3% for a CNT-loading of 1wt%. The observed improvement due to the presence of CNTs was ascribed to an improved crystallinity and enhanced morphology of P3HT consistent with the findings by Ren *et al.* [193]. Additionally, the presence of MWNTs was linked to an increase in the conductivity of the HTL by an order of magnitude [223] thus reducing interfacial charge recombination. Higher loadings, however, were shown by impedance measurements to reduce the recombination resistance by opening additional charge recombination pathways [222]. Similar findings had previously been reported by Chen *et al.*, who had observed an improvement in efficiency from 4.1% to 6.5% by dispersing multiwalled carbon nanotubes in P3HT [224]. The authors concluded that this improvement could be attributed to the confluence of improved morphology and enhanced conductivity of the MWNT-P3HT matrix [224]. In contrast, Zheng *et al.* were able to demonstrate that MWNTs dispersed in a very thin P3HT matrix can function as hole-selective cathode for perovskite solar cells with a peak performance of 13.4% [225].

Wei *et al.* followed the approach which had previously demonstrated for carbon black [86], using MWNTs as hole-selective electrode [226]. The MWNT film is deposited prior to the perovskite formation thus embedding the MWNTs into the perovskite and achieving a good perovskite-carbon interface. The comparison with carbon black and graphite flakes reveals that the superior interfacial morphology and higher conductivity of the MWNT film directly correlates with a better performance. Remarkably, in this approach neither another hole-transporting material nor a metal electrode are required for achieving devices with an efficiency of 12.7% and an impressive fill factor of 0.80. Interestingly, the efficient hole-extraction of the MWNT layer results additionally to an almost complete mitigation of the commonly observed current-voltage hysteresis [226]. A similar device structure in which no additional hole-transporter or metal electrode is needed, was chosen by Cao *et al.*, who investigated the SWNT loading of a hole-collecting carbon electrode composed of graphite and carbon black [227]. This study showed that the addition of 0.05wt% SWNTs to the carbon composite can improve the device performance from around 9.9% to up to 14.7%, mainly by improving the photovoltage and the fill factor [227]. Luo *et al.* employed

cross-stacked superaligned carbon nanotubes as a carbon electrode with hole-transporting function in a similar device design [228]. The authors used iodide to dope the nanotube layer which improved the efficiency to a value of up to 10.5%. Furthermore, in this study, the devices were encapsulated with a layer of PMMA resulting in improved stability in ambient conditions [228].

Aitola *et al.* fabricated a hybrid carbon electrode based on single-walled carbon nanotubes and drop-casted spiro-OMeTAD [229]. In contrast, to previous studies which had been done on methlyammonium lead triiodide perovskite, the authors made use of a mixed formamidinium lead iodide-methylammonium lead bromide $(FAPbI_3)_{0.85}(MAPbBr_3)_{0.15}$ perovskite which yields a power-conversion efficiency of up to 18.8% for a spiro-OMeTAD-based device with a gold electrode. The best-performing device with a nanotube-spiro-OMeTAD composite as hole-accepting electrode yielded a scanned efficiency of 15.5%, significantly outperforming a pure SWNT electrode and a non-selective gold electrode [229].

The study by Jeon *et al.* investigated several avenues to integrate single-walled carbon nanotubes as electrode in place of indium-tin oxide (ITO) as transparent cathode in the inverted p-i-n architecture [230]. Moderate performance was achieved with a combination of SWNTs and PEDOT:PSS as electron blocking layer, in contrast, using MoO_x resulted in a very poor device performance. The highest efficiency of 5.4% of an ITO-free flexible device was obtained with nitric acid as p-dopant for the SWNTs and, interestingly, without any additional electron-blocking layer [230]. The limitations of this device compared to a control device with ITO as electrode, were attributed to a mismatch between the energy levels of the SWNTs and the perovskite absorber [230].

Two studies coming out of the National Renewable Energy Laboratory investigated in more detail more fundamental questions regarding the perovskite-nanotube interface [231, 232]. Purified semiconducting SWNTs with a narrow (6,5) chirality were deposited layer-by-layer onto perovskite and probed by photoemission spectroscopy. Schulz *et al.* could thus show that upon contact, electron donation from the perovskite to the nanotubes occurs effectively n-doping the nanotubes, which therefore undergo a significant downwards band bending towards the interface with a magnitude of over 0.5 eV (figure 3.19) [231].

By probing the interface with XPS measurements, the authors could also show that the n-doping results from electron transfer from the methylammine group in the perovskite to the SWNTs.

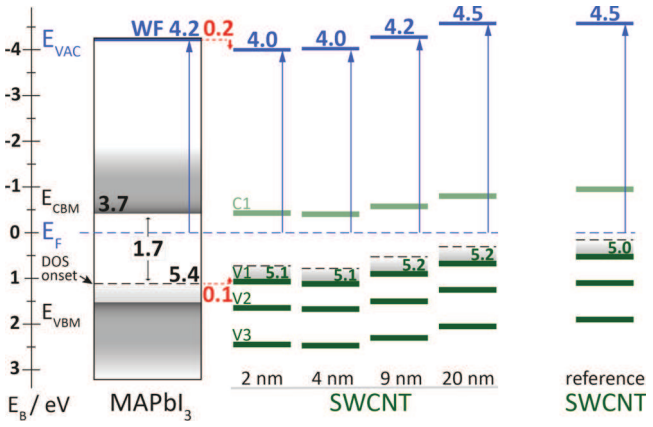

Figure 3.19: Energy level diagram of semiconducting (6,5) SWNTs on $MAPbI_3$ perovskite. The workfunction values are given in blue. The reference SWNT measurements was done by measuring the workfunction of 9 nm of SWNTs on gold. Compared to the reference, the SWNT bands are downshifted as a result of n-doping by the electron injection from the perovskite. With increasing thickness, the SWNT layer becomes intrinsic again thus bending upwards and facilitating one-directional hole extraction. Reproduced with permission from Schulz *et al*, J. Phys. Chem. Lett., 7, 3, 418-425, 2016. Copyright 2016 American Chemical Society

Transient absorption spectroscopy measurements confirmed the beneficial effect of the band bending by showing that holes are extracted by the nanotubes on an even faster time scale than the concomitantly photogenerated electrons are extracted by the TiO_2 which forms the n-type contact [231]. The band bending is credited with facilitating rapid transfer of photogenerated holes away from the interface and hinder back-transfer of holes thus reducing recombination losses.

Ihly *et al.* followed-up on the previous study by carefully probing the charge transfer kinetics between the perovskite and SWNTs using time-resolved spectroscopy over time scales spanning femtoseconds to several hundreds of microseconds [232]. By using a highly purified distribution of semiconducting monochiral SWNTs, the authors are able to unequivocally assign changes in the absorption spectra to the excitonic SWNT transition.

Femtosecond transient-absorption measurements show that charge extraction of photogenerated holes sets in within the first picosecond after generation and is complete after three nanoseconds. The transient absorption dynamics reveal further that neither TiO_2 as n-type contact nor spiro-OMeTAD as p-type contact markedly change the bleach recovery time, in contrast, SWNTs at the interface significantly reduce the bleach recovery time. This shows that the SWNTs are able to remove photogenerated holes faster from perovskite absorber. Once injected into the SWNTs, these holes are also shown to be extremely long-lived, several orders of magnitude longer than in the perovskite, indicating that the previously shown

potential barrier due to band bending prevents back-transfer or recombination of the holes.

In this study, time-resolved microwave conductivity measurements are used to show that the efficient hole extraction improves the extraction of electrons by TiO_2. The authors suggest that the rapid removal of holes inhibits recombination and thus raises the quasi-Fermi level of the electrons in the perovskite, which would increase the driving force for the previously poor electron injection into the TiO_2.

Finally, the enhanced charge extraction of the SWNTs is shown by employing a thin (5 nm) SWNT film as interfacial layer between the perovskite and doped spiro-OMeTAD, and thus improving the power-conversion efficiency from 14.7% to 16.5% [232].

3.7 Summary

This chapter discusses single-walled carbon nanotubes from their synthesis, their theoretical description, their fundamental properties and eventually their application in photovoltaic solar cell. Starting out at the lattice description of graphene sheet, the implications are demonstrated, when this description is applied to single-walled carbon nanoubes, namely the quantization of the circumferential k-vector. Graphene is a zero-bandgap semiconductor with metallic properties due to the crossing of conduction and valence band at the Dirac points. In contrast, because only a set of quantized k vectors are allowed for SWNTs, only the ones with a certain chirality in which the allowed k vectors and the Dirac points overlap, have this metallic characteristic, the remaining SWNTs have a small bandgap and are therefore true semiconductors. This characteristic is demonstrated by approximating the band structure of graphene and SWNTs with the tight-binding approximation.

The next section details the macroscopic charge transport property of SWNTs and SWNT networks. This is followed by a description of functionalization techniques for SWNTs with a focus on the relevant polymer processing, which is employed in the experimental section of this thesis. In particular, P3HT wrapping and its effect on SWNTs was highlighted by reference to two reports which highlight the p-type character of SWNTs when they form a junction with P3HT.

In the final section of this chapter, the application of SWNTs in three classes of photovoltaic devices was reviewed. Starting with organic polymer solar cells, which included the first reports of successful integration of SWNTs in devices. Initially, the SWNTs were

thought to act as electron transport materials similar to fullerenes. However, later studies point out that discrepancies of previous reports could be explained by assuming that the SWNTs rather act as hole-transporters. In inorganic solar cells, SWNTs were right away employed as p-type component of a pn-junctions together with n-type silicon. Several optimization approaches are detailed culminating in the currently best performing device SWNT-Si junction with an efficiency of 17.0%. This chapter is concluded with a detailed review of all available studies to date in which carbon nanotubes are used as charge transporting component in perovskite solar cells.

Chapter 4

Materials and methods

In this chapter, the materials and methods are described, followed by a short overview over the experimental setups that have been employed throughout the experiments of this thesis.

4.1 Materials

4.1.1 Single-wall carbon nanotubes

Several powdered singled- walled carbon nanotubes (SWNTs) were used in this study.

- CG200: diameter range from 0.7-1.4 nm, relative purity of 90% as the percentage of carbon that is present as SWNTs, semiconducting SWNTS $\sim$ 52%. CoMoCAT process, Sigma-Aldrich

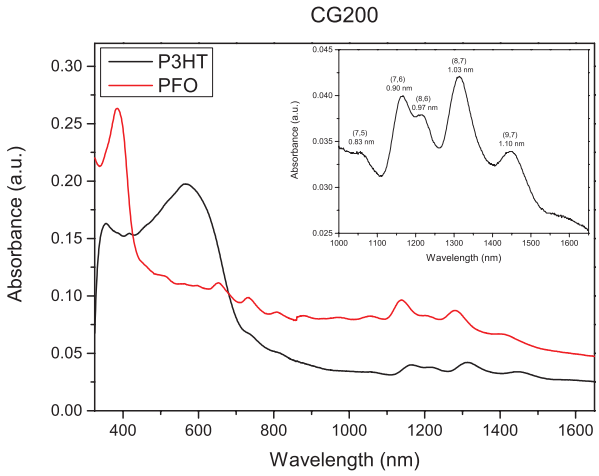

Figure 4.1: Absorption spectrum of CG200 SWNTs

- SG 6,5i: diameter range from 0.7-0.9 nm, relative purity of 93% as the percentage of carbon that is present as SWNTs, semiconducting SWNTS ~ 95%, enriched (6,5) chirality, CoMoCAT process, Sigma-Aldrich

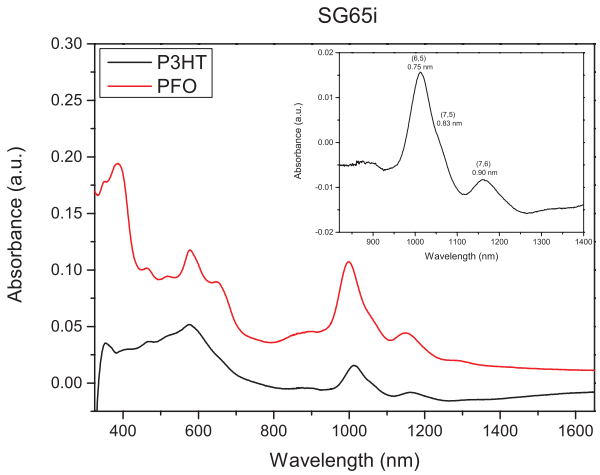

Figure 4.2: Absorption spectrum of SG65i SWNTs

- SG 7,6: diameter range from 0.7-1.1 nm, relative purity of 77% as the percentage of carbon that is present as SWNTs, semiconducting SWNTS ~ 66%, enriched (7,6) chirality, CoMoCAT process, Sigma-Aldrich

- HiPco (purified): produced by the HiPco process were purchased from NanoIntegris with lengths 100-1000 nm and an intermediate diameter distribution of 0.81.2 nm. (<15w% iron catalyst impurities)

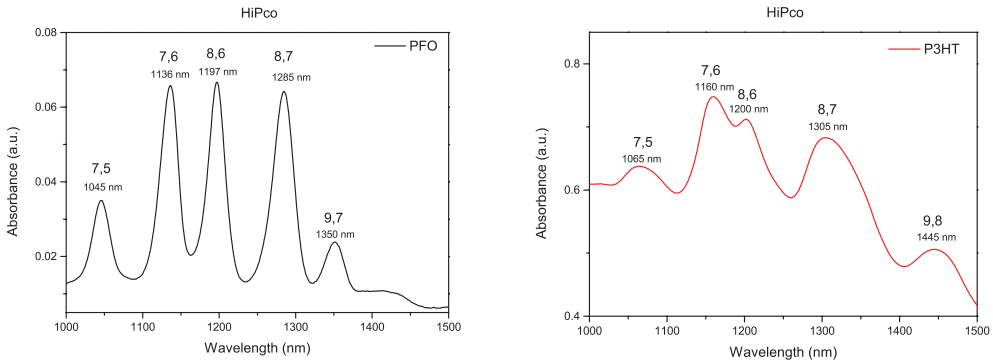

Figure 4.3: Absorption spectrum of HiPco SWNTs

- HiPco (raw): produced by the HiPco process were purchased from NanoIntegris with lengths 100-1000 nm and an intermediate diameter distribution of 0.8-1.2 nm. (~35wt% iron catalyst impurities)

4.1.2 Polymers

- P3HT: poly(3-hexylthiophene), regioregular, average molecular weight, M_w = 50 000 g mol^{-1}, regioregularity = 95%, Rieke Metals Inc.

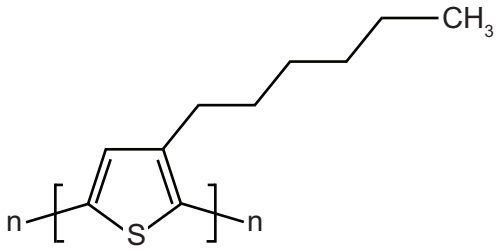

Figure 4.4: Molecular structure of P3HT

- PMMA: poly(methyl methacrylate), average molecular weight M_w = 97 000 g mol^{-1}, Sigma-Aldrich

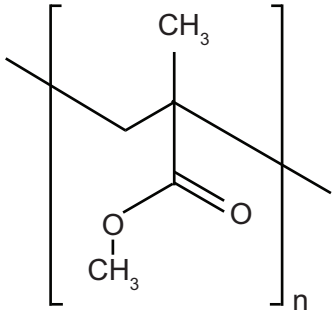

Figure 4.5: Molecular structure of PMMA

- PC: poly(bisphenol A carbonate), average molecular weight M_w = 45 000 g mol^{-1}, Sigma-Aldrich

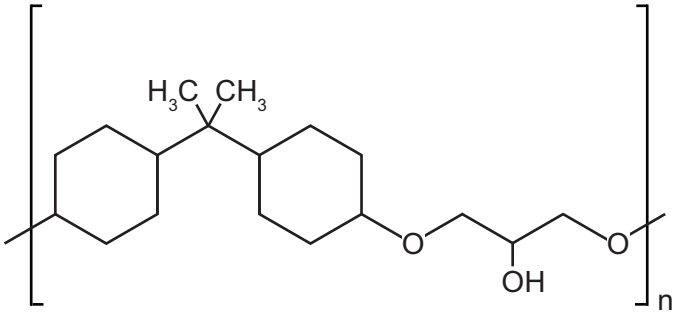

Figure 4.6: Molecular structure of PC

- PS: polystyrene, average molecular weight M_w = 35 000 g mol^{-1}, Sigma-Aldrich

4.1.3 SWNT functionalization

3.0 mg of P3HT are dissolved in 5.00 ml of chlorobenzene and sonicated in an ultrasonic bath sonicator for 60 min. 2.5 mg of SWNTs was added, as purchased, to the dissolved polymer solution and treated with an ultrasonic probe for 10 min. After the sonication treatment 5 ml of chlorobenzene were added to improve the solubility of the polymer-nanotube-hybrids. The mixture was subsequently centrifuged for 8 min at 10 000 g to remove nonfunctionalized SWNTs and other carbonaceous particles. The precipitate was discarded while the supernatant was recovered. In order to remove the excess polymer according to the solvent extraction technique detailed first described by Schuettfort et al.,[164]. 10 ml of toluene was added. The mixture was then mildly heated for 60 min to induce aggregation of the functionalized SWNTs. The aggregates were then removed by centrifugation (4 min at 16 000 g). This time the supernatant containing excess polymer was discarded and the precipitate was recovered and redispersed in 5 mL of toluene. This mixture was then sonicated for 15 min in the ultrasonic bath to fully redisolve nonwrapped polymers. After the sonication, the mixture was mildly heated for 15 min to induce aggregation and then centrifuged for 4 min at 16 000 g. The final pellet consists of 2.0-2.2 mg of polymer-wrapped nanotubes, which are dispersed in 6 ml of chloroform. Immediately prior to spin-coating, the chloroform dispersion was sonicated with an ultrasonic probe for 1 min at low intensity (10% of amplitude) to break up clusters and bundles.

4.1.4 Solar cell fabrication

A glass wafer with a layer of fluorine doped tin oxide (FTO) was first cleaned with detergent and de-ionized water, then with acetone and isopropanol. Thereafter it was treated for 10 min in O_2 plasma. The electron accepting TiO_2 compact layer was spin-coated (2000 rpm for 60 s) from a mildly acidic (after addition of 12 µM HCl) solution of titanium isopropoxide in anhydrous ethanol and sintered at 500°C.

The low-temperature meso-structured scaffold was afterwards deposited by spin-coating (2500 rpm for 60s) from a colloidal dispersion of 20 nm Al_2O_3 nanoparticles in isopropanol followed by drying at 150°C [97].

For the perovskite solution a mixed-halide precursor was prepared, based on methylammonium iodide (MAI) and lead(II) chloride ($PbCl_2$) in a 3:1 molar ratio. For a 0.9

M concentration, 440.7 mg/ml of methylammonium iodide (Dyesol) and 257.0 mg/ml of lead(II) chloride (Sigma-Aldrich) were dissolved in dimethylformamide (Sigma-Aldrich) and stirred at 70°C for 30 min. After having cooled down to room temperature, 6 µl/ml of hypophosphoric acid (Sigma-Aldrich) were added to the solution.

The perovskite solution was the spin-coated onto preheated (70°C) Al_2O_3 substrates. After spin-coating the samples were dried for 10 minutes at room temperature and for 10 minutes at 70°C. After, they were annealed at 100°C for 105 min, followed by 15 min at 120°C.

Following this step, the hole transport layer was deposited by spin-coating. For the two-layer structure of SWNT and polymer, first the SWNT layer was deposited dynamically by drop-by-drop spin-coating 200 µl of solution (3000 rpm for 90 s). The film was blow-dried with an airgun and let dry at room temperature for 15 min. PMMA (65 mg/ml in chlorobenzene or 50 mg/ml in toluene) was subsequently deposited by spin-coating (2000 rpm for 45 s). For the study in chapter 7, 4-*tert*-butylpyridine (Sigma-Aldrich) was added to the PMMA solution in the range of 0-40 µl/ml.

For the spiro-OMeTAD hole-transporter: 96 mg/ml 2,20,7,70-tetrakis-(N,N-di-p-methoxy-phenyl-amine)9,9-spirobifluorene (Borun chemicals) was dissolved in chlorobenzene at 90°C. For doping either pre-oxidized spiro-OMeTAD [233] was added at a concentration of 10wt% or for lithium-doping 32 µl/ml lithium bis(tri-fluoromethanesulfonyl)imide (Sigma-Aldrich) of a 170 mg/ml solution in 1-butanol were added to the spiro-OMeTAD solution For the other polymeric hole-transporters: 15 mg/ml poly(3-hexylthiophene) (P3HT) in dichlorobenzene with added 3.4 µl/ml tBP and 6.8 µl/ml Li-TFSI from 28.3 mg/ml Li-TFSI/acetonitrile; 15 mg/ml poly(triarylamine) (PTAA, M_w= 23 300) in toluene with added 6.8 µl/ml and 13.6 µl/ml Li-TFSI from 28.3 mg/ml Li-TFSI/acetonitrile. Spiro-OMeTAD was spincoated at 2000 rpm for 60s, P3HT and PTAA were spincoated at 3000 rpm for 30 swhich was spincoated at 2000 rpm for 60s.

Finally, 50-100 nm of copper/silver/gold electrodes were thermally evaporated onto the HTL.

4.2 Solar cell characterization

For measuring the performance of the solar cells, simulated AM 1.5 sunlight was generated with a class AAB ABET solar siupmulator calibrated to give siupmulated AM 1.5, of 100.0 mW cm^{-2} equivalent irradiance, using an NREL-calibrated KG5 filtered silicon reference cel . The current-voltage curves were recorded with a sourcemeter (Keithley 2400, USA). The solar cells were masked with a metal aperture defining the active area (0.0919 cm^2) of the solar cells. Additionally, by removing active material between individual cells on the same glass substrate, single-cell contributions were ensured. Measurements were done in a light-tight sample holder to minimize any edge effects and ensure that the reference cell and test cell are located during measurement in the same spot under the solar simulator.

4.3 Absorption spectroscopy

Absorbance measurements for the films were carried out in the wavelength range 250-1500 nm, using a PerkinElmer Lambda 9 Photospectrometer, at room temperature.

4.4 Photoinduced absorption spectroscopy

4.4.1 Setup

Photoinduced absorption (PIA) spectra were obtained from full device structures with varying hole transport layer architectures. A schematic of the setup is shown in figure 4.7. The samples were excited with an Argon ion laser with a wavelength of 515 nm with a maximum fluence of 50 mW cm^{-2} and chopped at a frequency of 23 Hz. The optical probe is in the form of a white light halogen bulb of around 100 mW cm^{-2} intensity. After passing through the sample, the probe beam enters a monochromator (SpectraPro-2300i, Acton Research Corporation) coupled to diode for detection in the visible (PDA10A, Thorlabs) and in the NIR (ID-441-C, Acton Research Corporation). Acquisition is made by a lock-in amplifier locked at the light modulation frequency (SR830, Stanford Research Systems) and a NI USB-6008 (National Instruments) acquisition card. A computer running LabView (National Instruments) controls the setup and record spectra. No further treatment is applied to the data.

4.4.2 Technique

PIA is a quasi steady-state pump-probe technique, which compares the change in absorption between the groundstate and photoexcited state of a sample. The pump laser is a continuous-wave laser which is chopped at a frequency of 23 Hz, thus providing clearly defined pump-on and pump-off intervals. In the pump-on state, pump photons are absorbed by groundstate electrons which are excited into the excited state. The photons from the probing white-light cannot be absorbed by these excited charges. The transmittance of a sample increases therefore during the pump-on interval compared to the transmittance during a pump-off interval. A direct comparison between these two states per wavelength interval reveals a sample's changes in its transmission, and correspondingly, its absorption characteristics due to photoinduced processes.

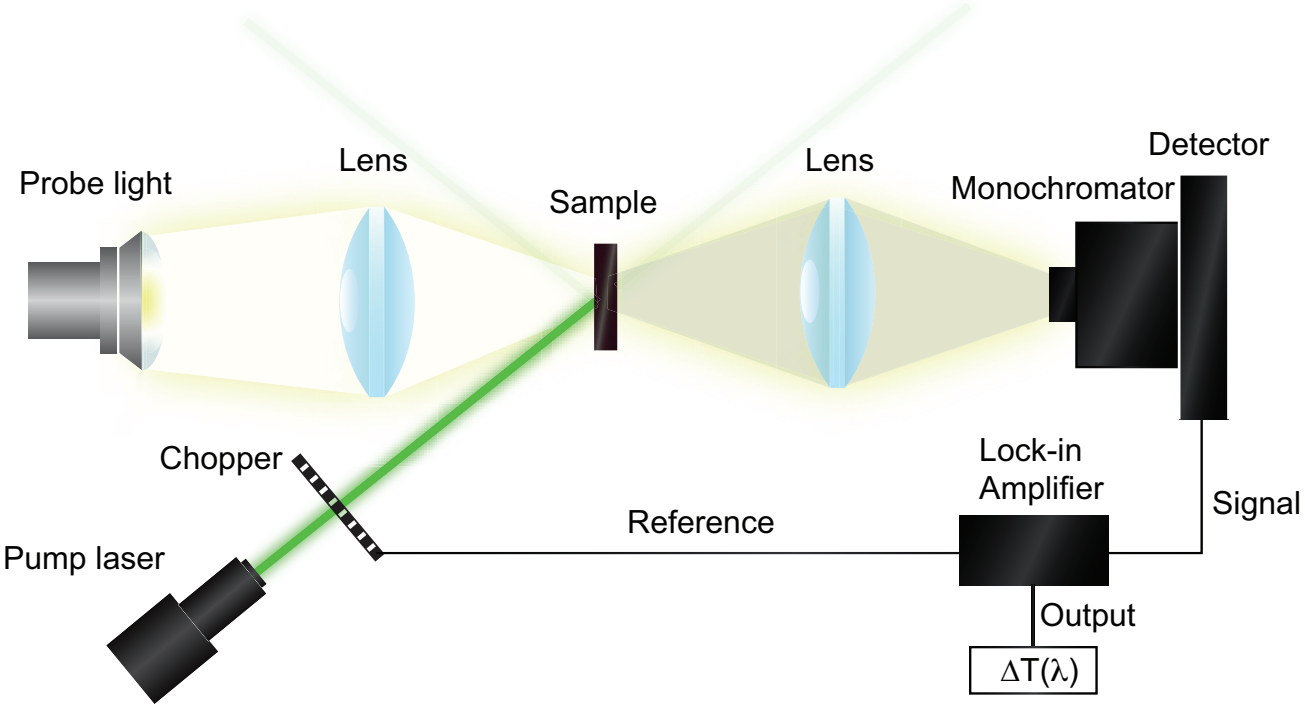

Figure 4.7: Photoinduced absorption setup. The probe light is comes from a white-light source and is focussed onto a sample. The transmitted light is focussed again to be collected by a monochromator. The detector connected to the monochromator monitors the transmittance through the sample per wavelength interval. To test the change in transmittance under quasi steady-state conditions, the sample is pumped with a laser pulse. The laser is chopped at a rate of 23 Hz. The chopper is connected to a lock-in amplifier which uses the chopper frequency as the reference signal. This allows a direct quantification of the change in absorption between the pump-on and the pump-off state induced by the white probe-light. The output signal is the change in transmittance.

4.5 Transient lifetime measurements

4.5.1 Setup

Transient lifetime measurements were performed by a similar method to O'Regan et al. [234]: a white light bias was generated from an array of diodes (Lumiled Model LXHL-NWE8 whitestar) with red-light pulsed diodes (LXHLND98 redstar, 200 μs square pulse width, 100 ns rise and fall time) as the perturbation source, controlled by a fast solid-state switch. The voltage dynamics were measured on a 1 GHz Agilent oscilloscope across the high impedance (1 MΩ) port. The perturbation light source was set to a suitably low level such that the voltage decay kinetics were monoexponential. This enabled the charge recombination rate constants to be obtained directly from the exponential decay rate of the voltage decay. Small perturbation transient photocurrent measurements were performed in a similar manner to the open-circuit voltage decay measurement. However, the signal was recorded directly through a low impedance port (50 Ω) on the oscilloscope, enabling short-circuit conditions. For the voltage decay measurements, a Keithley 2400 sourcemeter was connected in series with the solar cell and parallel with the oscilloscope which was set on the high impedance port.

4.5.2 Transient photovoltage decay

For the transient photovoltage (TPV) measurements, the current is kept constant by a sourcementer so that no extra current is allowed to flow through the device following the light pulse, therefore the photoexcited charges cannot be extracted from the device. Because no charge extraction occurs, the decay of the induced voltage change is entirely governed by the charge recombination within the cell, and therefore provides a time constant for the recombination rate k_{rec}. The perturbation was kept small enough to ensure that the change in the charge carrier distribution Δn and the corresponding change in voltage ΔV decay monoexponentially.

$$\frac{d\Delta V}{dt} \propto \frac{d\Delta n}{dt} = k_{\mathrm{rec}} \cdot \Delta n = \frac{\Delta n}{\tau_{\mathrm{rec}}} \tag{4.1}$$

The time constant τ_{rec} is the electron lifetime before it recombines in the device, and can be obtained by fitting the voltage decay signal to a monoexponential (figure 4.8).

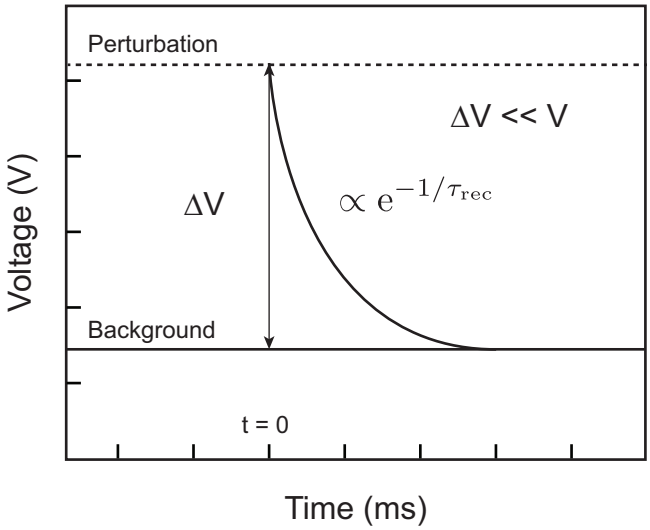

Figure 4.8: Transient photovoltage decay. After the perturbation pulse at t = 0, the voltage change ΔV decays monoexponentially allowing the extraction of the recombination rate of the sample.

4.5.3 Transient photocurrent decay

The transient photocurrent decay measurements are performed under short-circuit conditions, allowing the photogenerated charges to be extracted. The perturbation pulse generates additional charge carriers which generate a photocurrent signal. The decay of this signal has two underlying pathways by which these additional charge carriers are lost: Charges can be extracted from the system depending on their extraction rate k_{extract}. At the same time, these charges also recombine at the recombination rate k_{rec}. The signal decay is therefore the sum of these two loss rates.

$$k_{\text{signal}} = k_{\text{rec}} + k_{\text{extract}} \Leftrightarrow \frac{1}{\tau_{\text{signal}}} = \frac{1}{\tau_{\text{rec}}} + \frac{1}{\tau_{\text{extract}}} \tag{4.2}$$

When the recombination rate is known from TPV measurements, the extraction rate can be calculated.

$$k_{\text{extract}} = k_{\text{signal}} - k_{\text{rec}} \tag{4.3}$$

A useful metric to assess the device architecture is the charge collection efficiency η, which is the ratio of the extraction rate and the signal decay rate. This metric quantifies the fraction of charges which was extracted into the circuit compared to all total number of photogenerated charges

$$\eta_{\text{coll}} = \frac{k_{\text{extr}}}{k_{\text{signal}}} = \frac{k_{\text{extract}}}{k_{\text{extract}} + k_{\text{rec}}} \tag{4.4}$$

4.6 Kelvin probe measurements

4.6.1 Setup

Surface photovoltage measurements were take with a KP Technology Kelvin probe station (KP020 + SPS040). Highly-ordered pyrolytic graphene (HOPG) was used as a reference. The workfunction was determined in the dark and in air.

4.6.2 Technique

Figure displays schematic representation of two metals with different work functions, representing the metal of the Kelvin probe tip and the sample. In a) the two metals do not interact and their Fermi levels align at the vacuum level (E_{vac}) at energies corresponding to the respective work functions Φ_1 and Φ_2. When the two metals are connected, in b), the Fermi levels equilibrate when electrons from the metal with the smaller workfunction flow to the metal with a lower electrochemical potential. Because the two metals were charge neutral before they were connected, the electron flow from the the tip to the sample has charged the sample negatively, while the tip is now positively charged. This gives rise to an electrostatic potential between the two metals. The charge flow stops when the arising electrostatic potential compensates for the potential difference of the workfunctions, which is also referred to as contact potential difference ($\mathrm{V_{CPD}}$). This value can now be measured by gradually applying counter voltage (V_B) until it compensates for the $\mathrm{V_{CPD}}$ and preventing further current flow.

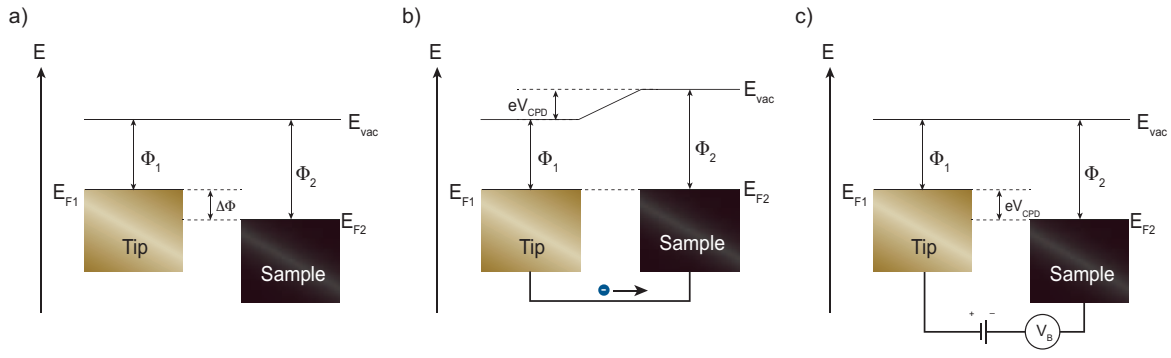

Figure 4.9: Schematic representation of two metals with different work functions, representing the metal of the Kelvin probe tip and the sample.

The Kelvin method makes use of this concept of measuring the contact potential difference, however, it does so without directly connecting the two samples. Instead this method

relies on a periodic modulation of the distance between the two metals thus changing the capacitance between the two which results in current flow through an external circuit. When the two tip is brought close to the sample, only separated by a dielectric, such as air or vacuum, they form a parallel plate capacitor with distance d_0 (figure 4.10) and a capacitance C, defined as

$$C = \varepsilon_0 \varepsilon_r \cdot \frac{A}{d_0} \tag{4.5}$$

with ε_0 being the relative permittivity, ε_r the relative dielectric constant (which is ~ 1 for air) and A the area of the probe tip. At a constant potential V_{CPD} between the two metals, the capacitor charges with the charge Q

$$Q = C \cdot V_{\mathrm{CPD}} \tag{4.6}$$

Because the capacitance changes with the distance between the probe and the sample (4.5), and the amount of charge depends on the capacitance, it follows that a change in the distance between tip and sample leads to a change in charge and thus results in a current flow through the external circuit.

$$I(t) = \frac{\mathrm{d}Q(t)}{\mathrm{d}t} = \frac{\mathrm{d}C(t)}{\mathrm{d}t} \cdot V_{\mathrm{CPD}} = \frac{1}{\frac{\mathrm{d}d(t)}{\mathrm{d}t}} \cdot \varepsilon_0 \varepsilon_r \cdot A \cdot V_{\mathrm{CPD}} \tag{4.7}$$

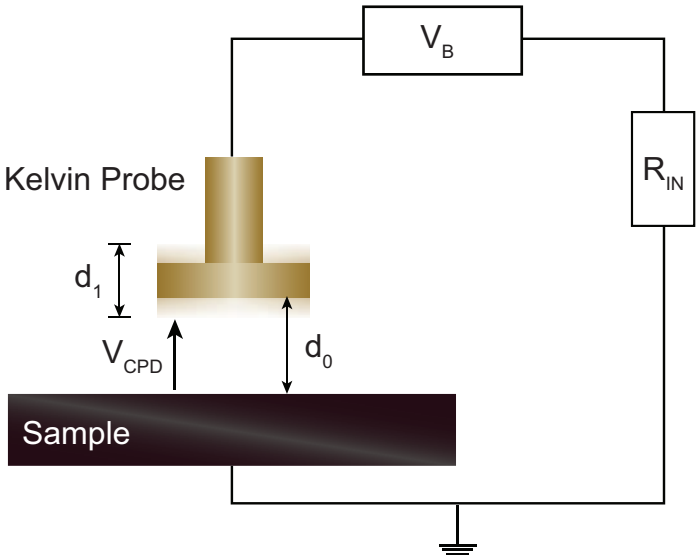

Figure 4.10: .

This current is induced by a sinusoidal oscillation of the probe tip at a mean distance d_0 between the tip and the sample at an amplitude of d_1 with the condition that $d_1 < d_0$ and

a frequency ω

$$d(t) = d_0 + d_1 \cdot \sin(\omega t) \tag{4.8}$$

The amplitude of the current signal is characterized by the ratio of d_1 to d_0 which is defined as the modulation factor $m = d_1/d_0$. The current induced by the oscillating tip is therefore

$$I(t) = \varepsilon_0 \varepsilon_r \cdot A \cdot \frac{m \cdot \omega \cos(\omega t)}{1 + m \cdot \sin(\omega t)^2} \cdot V_{\mathrm{CPD}} \tag{4.9}$$

The resulting current signal can be recorded and will look like figure 4.11.

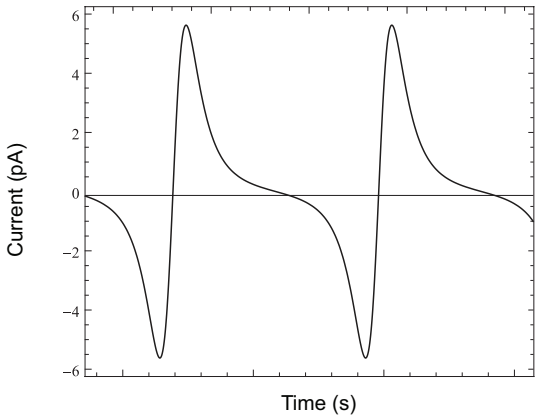

Figure 4.11: Capacitive current signal from an oscillating Kelvin probe according to (4.9).

A backing voltage V_B can now be introduced into the circuit (figure 4.10) so that the current vanishes $I(t) \to 0$.

$$I(t) = \frac{\mathrm{d}C(t)}{\mathrm{d}t} \cdot (V_{\mathrm{CPD}} - V_B) \tag{4.10}$$

When $V_B = V_{\mathrm{CPD}}$ the current goes to zero and the magnitude of the contact potential is known.

Chapter 5

Enhanced charge extraction through carbon nanotubes in perovskite solar cells

The work in this chapter has been reproduced in part and adapted with permission from: Severin N. Habisreutinger, Tomas Leijtens, Giles E. Eperon, Samuel D. Stranks, Robin J. Nicholas & Henry J. Snaith, *The Journal of Physical Chemistry Letters*, 5 (2014) 4207-4212 [219]. Copyright 2014 American Chemical Society.

5.1 Hole extraction in perovskite solar cells

The first incarnations of perovskite solar cells were liquid-state dye-sensitized solar cells, in which the dye had been replaced by methylammonium lead iodide as absorber material. Charge extraction occurred through the mesoporous TiO_2 layer extracting electrons, and a liquid electrolyte extracting the holes [24, 96]. Being immersed in an electrolyte was reported to be immensely detrimental for the durability of the devices, whose perovskite absorber degraded within minutes. Few years before, Bach et al. had demonstrated the concept of a solid-state dye sensitized solar cell in which the liquid electrolyte was replaced by an amorphous solid-state hole conductor, 2,2,7,-7-tetrakis(N,N-di-p-methoxyphenylamine)-9,9-spirobifluorene (spiro-OMeTAD) [23]. For dye-sensitized solar cells this development was regarded as a way to improve the practicality of the technology and stability [101, 235]. Furthermore, the more favorable positions of the energy levels of spiro-OMeTAD, as opposed to the redox potential of the iodidide couple in the electrolyte, should theoretically yield a higher V_{oc} [236]. However, the intrinsic hole mobility of spiro-OMeTAD is too low for efficient charge extraction and requires p-doping [23, 237]. The lithium salt lithium bis(trifluoromethyl-sulfonyl) amine (Li-TFSI) has been shown to be able to increase the hole mobility in spiro-OMeTAD by an order of magnitude [237]. Details of the mechanism re-

sponsible for the improved hole conductivity in of spiro-OMeTAD through the addition of Li-TFSI were elucidated by Abate et al.[220]. Based on the observation that the doping process only occurs in the presence of oxygen, the authors describe the mechanism as a redox reaction in which the presence of lithium cations enable the oxidation of spiro-OMeTAD by consuming O_2^- and forming lithium oxide complexes. At the same time, the oxidized spiro-OMeTAD cation is weakly coupling to the delocalized charge of the TFSI anion. Effectively, this oxidation process generates mobile holes in the organic matrix which contribute to the enhanced hole transport characteristics [220]. The drawback of this method is the consumption of Li^+ which suggests that long-term operation will be compromised once the dopant has been depleted. Furthermore, the process is reliant on atmospheric oxygen, which may have a detrimental effect on the overall device stability [92, 238].

However, in particular the hygroscopicity of the lithium salt may potentially prove detrimental for the structural integrity of the perovskite absorber by accelerating the permeation of water molecules through the organic matrix. The contact with moisture may ostensibly result in solvation of the organic methylammonium cation which is only connected by weakly binding hydrogen bonds to the ionic lattice of lead iodide, and will readily dissolve in polar solvents. Moisture ingress into the device is therefore likely to result in a breakdown of the perovskite structure and compromise the device stability.

5.2 SWNTs as hole-transporter additives

The concerns with regards to the long-term stability of perovskite solar cells in the presence of reactive Li-dopants in spiro-OMeTAD motivated the development of functionalized SWNTs as chemically inert and stable alternative to "dopants".

As described in the previous chapter, P3HT-wrapping was used to make the SWNTs dispersible in solvents which do not degrade the perovskite and - for the purpose of improving the charge transport characteristics of spiro-OMeTAD - can dissolve spiro-OMeTAD so they can be added to the solution [164]. Such supramolecular nanohybrids (P3HT/SWNT) composed of SWNTs and a polymer-coating have been shown in previous studies that they are able to enhance the performance of certain organic solar cells as additives [166, 195]. Because the energy levels of the wrapping sheath of P3HT make the electron transfer from the perovskite to the SWNTs potentially less energetically favorable, the polymer coating could possibly lead to selective hole-transfer to the nanotubes [166].

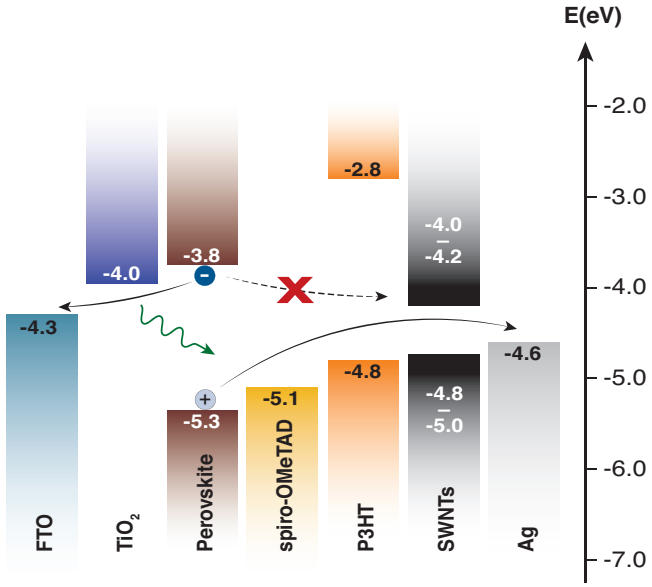

Figure 5.1: Energy levels of the various components of the device, showing energetically favorable pathways for holes and electron transfer to the respective electrodes. The valence and conduction band edges of SWNTs cannot be discretely assigned because the distribution of SWNTs with varying diameters (0.8 – 1.2 nm) leads to varying band edges [219].

The energy levels for each component in the cell is shown in Figure 5.1. The positions of the valence bands and highest occupied molecular orbitals (HOMOs) make it more favorable for the holes to transfer from the perovskite to the hole-accepting electrode through the layers of spiro-OMeTAD and functionalized SWNTs. In contrast, the very low electron affinity of

P3HT make it conceivable that electron transfer from the perovskite to the SWNTs would be limited, so that this junction does not suffer from excessive charge recombination and thus poor charge extraction. The values of the energy levels of the SWNTs functionalized with P3HT depicted in Figure 5.1 are approximate average values for SWNTs within the diameter range 0.8 - 1.2 nm, obtained from literature [164, 239].

The solar cell structure employed in this study is shown schematically in figure 5.2, where sequential layers of compact n-type TiO_2, mesoporous Al_2O_3, perovskite $CH_3NH_3PbI_3$, and SWNT-hole conductor composite are coated on to fluorine doped tin oxide (FTO) glass.

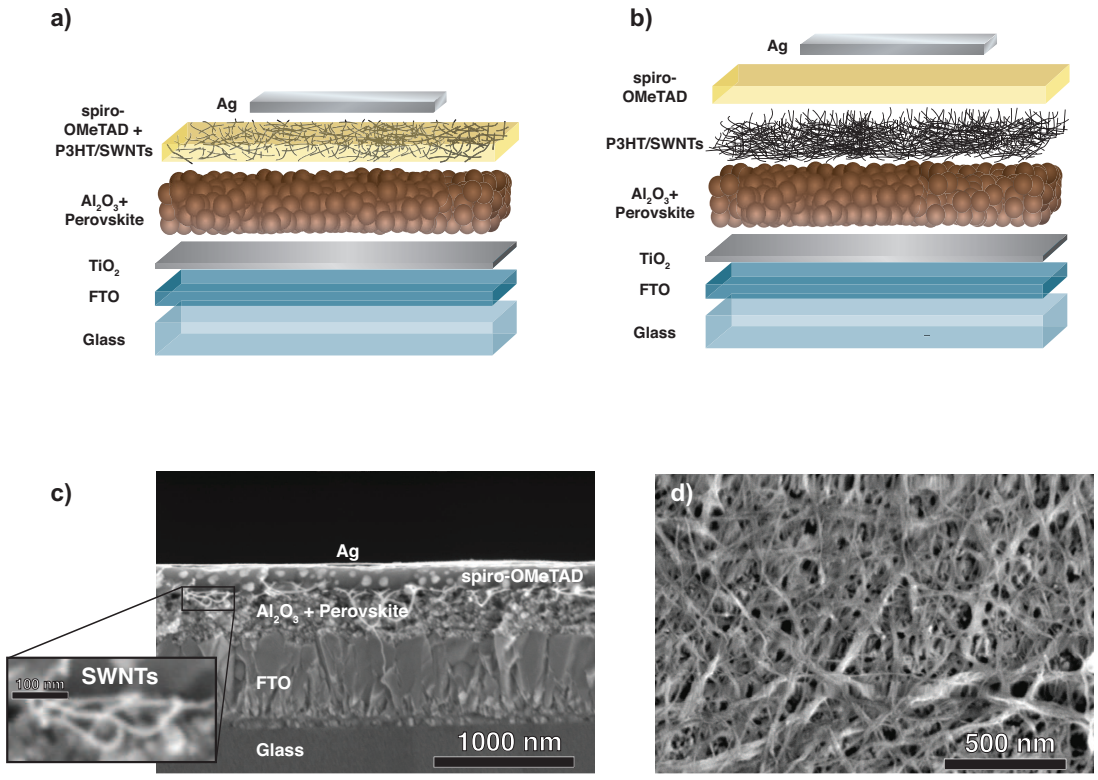

Figure 5.2: Schematic of a device with a blend structure composed of undoped spiro-OMeTAD and P3HT/SWNTs. (b) Schematic architecture of a device with a P3HT/SWNT layer underneath the hole transport material (spiro-OMeTAD) matrix. (c) A cross-sectional scanning electron microscope (SEM) image of a representative device. Individual SWNTs can be seen to protrude from the interface between the alumina and spiro-OMeTAD layers. (d) Top view of a bare SWNT layer showing the thick mesh-like structure of the SWNT layer.

The necessity for a dedicated charge-selective p-type layer i.e. a hole-transporting layer is shown in figure 5.3. The current-voltage characteristics of a device lacking the hole-transporting layer, where the hole-collecting cathode directly contacts the perovskite absorber, exhibits a very poor device performance with an especially low short-circuit pho-

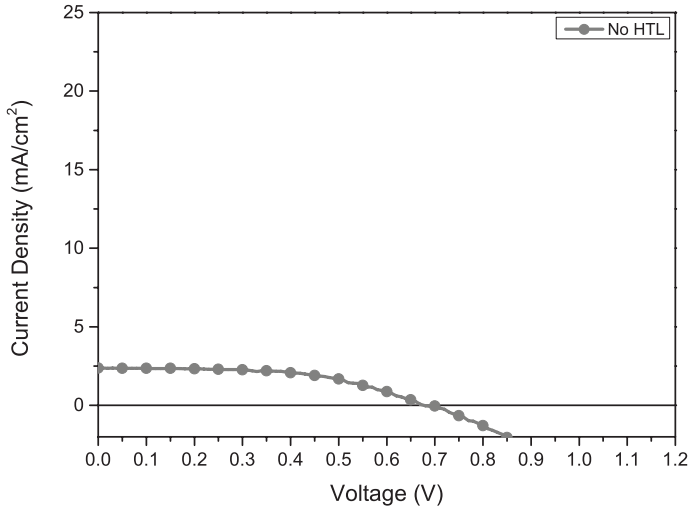

Figure 5.3: Current-voltage characteristics of a device without a hole-transporting layer. In this device, the metal cathode directly contacts the perovskite absorber allowing both photogenerated electrons and holes to transfer to the electrode where they can recombine. Accordingly, the charge extraction efficiency is very low.

tocurrent. This suggests that direct metallic contact to the perovskite absorber when coated on an inert alumina scaffold, where both electrons and holes reside within the perovskite, is not advantageous for selective charge extraction. It has been shown that if the perovskite is coated onto an electron-accepting mesoporous layer of TiO_2, photogenerated holes could be directly collected by a gold electrode [240] because rapid electron transfer to the mesoporous TiO_2 competes more favorably than electron transfer to, and recombination at, the gold electrode, however, the efficiency is significantly lower in this case [241]. Contrastingly, when the perovskite is coated onto an insulating alumina scaffold, as is the case in the architecture used in this study, electrons are not extracted as quickly and remain in the perovskite. Direct electron transfers from the perovskite to the hole-collecting metal electrode are therefore likely to occur, constituting a recombination pathway. The presence of a charge-selective hole contact can therefore reduce the recombination at the electrode by accepting holes and blocking electrons.

Accordingly, a significant improvement in efficiency can be observed when a dedicated hole-transporter is used (figure 5.4). The hole-mobility of neat spiro-OMeTAD is of the order of 10^{-5} $cm^2V^{-1}s^{-1}$ [242], which is relatively low and therefore impacts effective charge extraction and may impact device performance by limiting the series resistance [242]. Even though the charge recombination is significantly suppressed for neat spiro-OMeTAD, compared to device without hole-transporter, as only photogenerated holes can transfer from the perovskite to the spiro-OMeTAD layer. The current-voltage characteristics in figure 5.4 (in

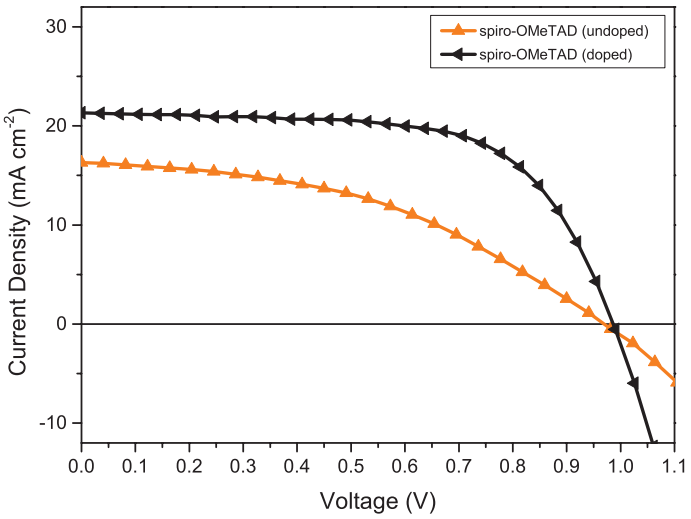

Figure 5.4: Current-voltage characteristics of two devices with spiro-OMeTAD as hole-transporting layer. Without doping with Li-TFSI, the hole-mobility of spiro-OMeTAD is limiting charge extraction. The JV-curve of the device with a doped spiro-OMeTAD layer is shown in black. In comparison, the JV-curve of the device without doping (in orange), exhibits a much higher series resistance and a lower photocurrent.

orange) show that this device yields a performance of 6.8% power-conversion efficiency with a photocurrent of 16.3 mA/cm^2. A device, in which the spiro-OMeTAD layer is doped with an optimized concentration of Li-TFSI, is shown as reference (in black). The comparison of the two device performances illustrates how the poor charge transport characteristics of the neat spiro-OMeTAD layer impacts the device performance. This is evident by the much lower photocurrent and, in particular, by the much higher series resistance which results in a much lower fill factor. By doping spiro-OMeTAD with Li-TFSI the mobility of the holes is increased by an order of magnitude [237], thus reducing the series resistance significantly, which enhances both fill factor and extracted photocurrent, yielding a device with a power-conversion efficiency of 13.5%.

Integrating a network of highly conducting carbon nanotubes into the layer of neat spiro-OMeTAD was thought to be able to reduce the charge transport limitations of the undoped material by increasing the overall conductivity of the layer without introducing a dopant that could undermine the device stability. The first approach was based on previous findings that SWNTs can form complete percolation thresholds at concentrations as low as 1vol% [243]. To this end, the polymer-wrapped SWNTs were dispersed in the spiro-OMeTAD solution, similar to dopants, so that they would form a percolation network throughout the undoped spiro-OMeTAD matrix once deposited by spin-coating.

Blending the P3HT/SWNTs into the neat spiro-OMeTAD film yields in fact a solar cell

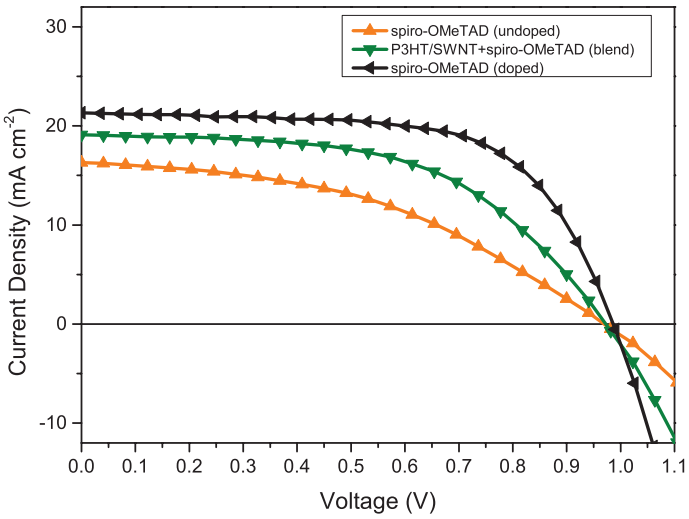

Figure 5.5: The device with the blend structure in which P3HT/SWNTs were dispersed in the neat spiro-OMeTAD solution prior to deposition is shown in green to yield a better performance than the device with undoped spiro-OMeTAD in orange. However, current-voltage characteristic of this device still does not match that of the device with a conventionally doped spiro-OMeTAD layer in black.

with a better performance (shown in green in figure 5.5). The improved performance can be largely attributed to an improved charge extraction due to a decrease in series resistance. The series resistance can be approximated by a linear fit to the current-voltage curve in the forward bias regime. For the neat spiro-OMeTAD device, the series resistance is approximately 16.9 Ω/cm^2, for the blend structure of P3HT/SWNT and spiro-OMeTAD device this resistance is decreased by more than half to 8.8 Ω/cm^2. As a consequence the fill factor is improved, and so is the photocurrent at short-circuit, reaching a value of 19.1 mA/cm^2. The open-circuit voltage remains the same for the neat and the blend spiro-OMeTAD structure, which indicates that the presence of the SWNTs does not result in an increased charge recombination at the interface. This means that the P3HT-wrapped SWNTs do not have a detrimental effect on the charge selectivity of the HTL layer by being charge selective for holes themselves. The power-conversion efficiency of this device reaches now 10.0%, showing a strong improvement in performance in comparison to the undoped device.

However, compared to the performance of a device with a Li-TFSI doped spiro-OMeTAD layer, the randomly interdispersed SWNTs do not sufficiently improve the charge extraction efficiency of the device. The limitations can still be attributed to a poorer charge transport, which results in a higher series resistance i.e. a worse fill factor and a lower photocurrent, as well as a higher recombination rate resulting in a reduced shunt resistance and in a lower open-circuit voltage.

While a percolation network of SWNTs throughout the spiro-OMeTAD layer has been achieved which is evident from the improvement in performance relative to the device without dopants, the nanotube network must still have a lot of internal resistance mainly due to intertube junctions. The nanotubes may also not have enough direct interfacial contact to the perovskite absorber to efficiently transport holes away from the interface, relying on charge transfer from spiro-OMeTAD to the nanotubes.

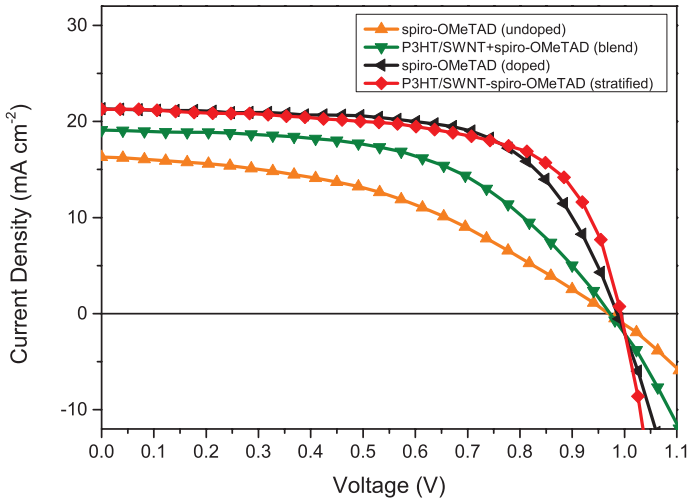

Figure 5.6: Comparison of current-voltage characteristics of two strategies of P3HT/SWNT incorporation into spiro-OMeTAD with two control devices with spiro-OMeTAD. Dispersing P3HT/SWNTs in the spiro-OMeTAD layer improves the JV-characteristics (green circles) compared to undoped spiro-OMeTAD but does not achieve the same performance as doped spiro-OMeTAD. The greatest improvement is achieved by sequential deposition of P3HT/SWNTs and spiro-OMeTAD (red diamonds), which results in a stratified HTL structure, which is comparable to the performance of doped spiro-OMeTAD.

Based on these considerations, a second approach was investigated in which the nanotubes and spiro-OMeTAD are deposited sequentially. The initial deposition of the P3HT/SWNTs alone ensures that the nanotubes form a densely interconnected network with a direct interface with the perovskite layer allowing efficient direct transfer of photogenerated holes from the absorber to the nanotubes. Subsequent coating and infilling with spiro-OMeTAD prevents the evaporated top electrode from directly contacting the perovskite, and forms the hole-conductor contact to the electrode. The nanotube network thus constitutes a highly conductive percolation network within the amorphous hole conductor matrix, with a large interfacial contact to the perovskite absorber.

Figure 5.2 c) shows a scanning electron microscopy (SEM) image of a representative device cross-section. P3HT/SWNT bundles are apparent protruding from the interface between the Al_2O_3-perovskite and spiro-OMeTAD layer. The amorphous spiro-OMeTAD readily in-

filtrates the P3HT/SWNT layer filling the openings and gaps of the mesh-like nanotube layer, due to its excellent pore filling properties [244], and good wettability upon coating this surface. There is clearly stratification, with much higher P3HT/SWNT density near the perovskite surface, which should allow efficient charge transfer away from the interface. In fact, this is evident as a much improved photocurrent in the current-voltage characteristics of a device with such a sequentially coated stratified P3HT/SWNT-spiro-OMeTAD composite layer, shown in figure 5.6. Additionally, an improvement in open-circuit voltage can be observed. This would indicate that the quasi-Fermi level of the perovskite align more favorable with those of the SWNTs rather than with the ones of spiro-OMeTAD, and that less recombination occurs at this interface. Photogenerated holes are probably channeled away from the interface through individual SWNTs fast enough that the recombination rate with concomitantly generated electrons is reduced. This device yields a scanned power-conversion efficiency of 13.6% (table 5.1).

It is clear that the stratified structure with the formation of a dense, interconnected network of P3HT/SWNT hybrids allows photogenerated holes from the perovskite to rapidly move through the horizontal plane to the most efficient vertical pathway to the top electrode. The fact that the devices work so well indicates that direct contact of the P3HT/SWNTs to the perovskite surface does not introduce an undesired electron recombination pathway but instead facilitates selective hole transport.

HTL structure	J_{sc}[mA cm^{-2}]	V_{oc}[V]	FF	PCE[%]	R_s[Ω cm^{-2}]
spiro-OMeTAD (undoped)	16.3	0.97	0.43	6.8	16.9
P3HT/SWNT-spiro-OMeTAD (blend)	19.1	0.97	0.54	10.0	8.8
spiro-OMeTAD (doped)	21.3	0.99	0.65	13.7	4.5
P3HT/SWNT-spiro-OMeTAD (stratified)	21.3	1.00	0.64	13.6	1.6

Table 5.1: Performance parameters of the devices devices shown in figure 5.6. These include two approaches of incorporating P3HT/SWNTs into the spiro-OMeTAD layer and two control structures.

In perovskite devices – in particular on inert scaffolds and in flat heterojunction configurations – current-voltage characteristics exhibit hysteretic behavior [245] (More detailed discussion in section 7.1). The observed current-voltage curves of these devices appear to have a strong dependence on the scanning conditions, introducing ambiguity into the interpretation of the operational performance of a device. It has therefore been proposed to employ the metric of "stabilized power output as a more reliable and unambiguous metric for determining device performance. This measurement is performed by holding the device at a constant voltage in the vicinity of its maximum-power voltage, and letting the photocurrent stabilize. The the product of constant voltage and stable photocurrent will provide an unambiguous steady-state efficiency under which this device is able to operate. In figure 5.7, the stabilized power-output for a device with a P3HT/SWNT-spiro-OMeTAD structure, and a control device with Li-TFSI doped spiro-OMeTAD are shown. The devices stabilize at 0.79 and 0.81 of the scanned efficiencies, respectively.

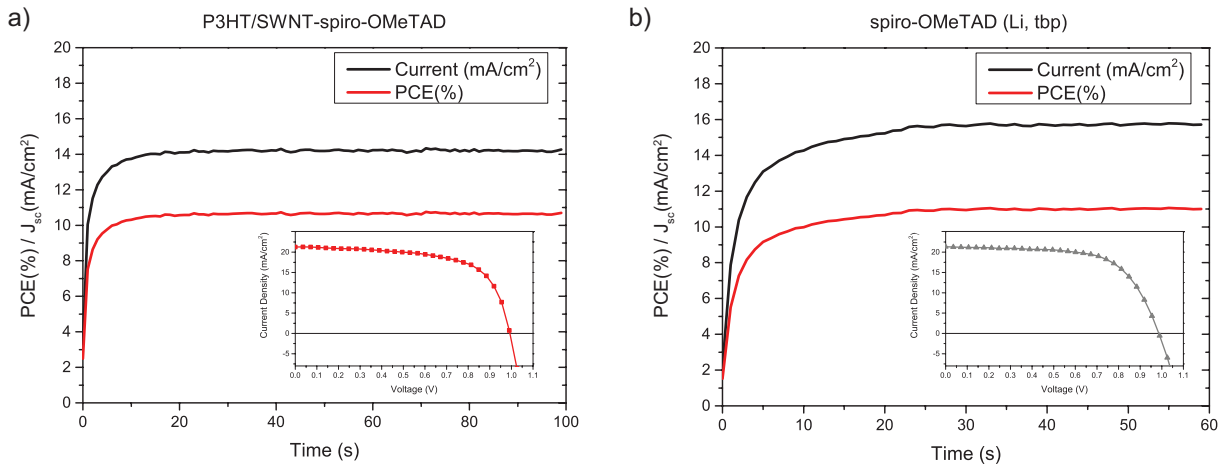

Figure 5.7: Stabilized-power output (SPO) and current-voltage characteristics of a) a device with the stratified P3HT/SWNT-spiro-OMeTAD structure and b) a device with Li-TFSI doped spiro-OMeTAD

HTL structure	J_{sc}[mA cm^{-2}]	V_{oc}[V]	FF	PCE[%]	SPO[%]	SPO/PCE
spiro-OMeTAD (doped)	21.3	0.99	0.64	13.5	11.0	0.81
P3HT/SWNT-spiro-OMeTAD	21.3	1.02	0.65	13.6	10.7	0.79

Table 5.2: Stabilized performance parameters of two representative devices with doped spiro-OMeTAD and the double-layer structure of P3HT/SWNT and neat spiro-OMeTAD.

5.3 Photoinduced absorption spectroscopy

The proposed mechanism of charge extraction was subsequently investigated using photoinduced absorption (PIA) spectroscopy. PIA is a quasi-continuous-wave (CW) technique, which enables probing the optical signature of photogenerated species. Because spiro-OMeTAD and P3HT/SWNTs exhibit different optical signatures when in the oxidized state i.e. when electron-deficient, it can be determined whether the photogenerated holes are residing on either component or both.

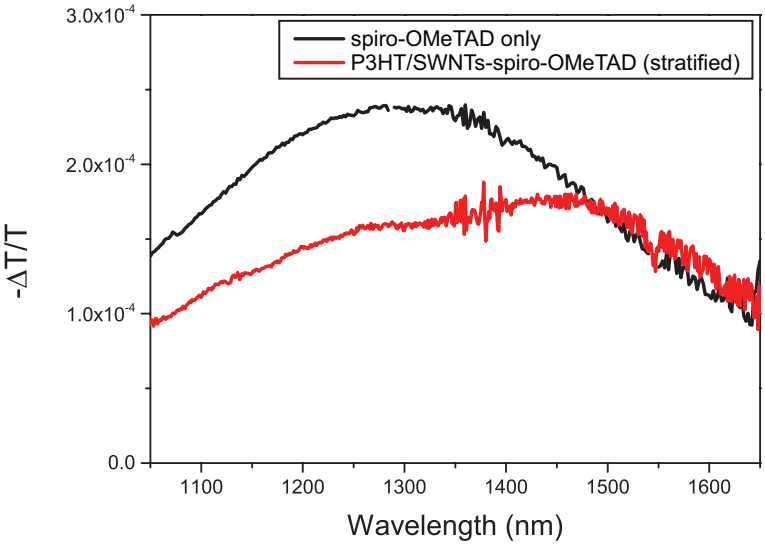

Figure 5.8: Photoinduced-absorption (PIA) spectra of both the neat spiro-OMeTAD and the P3HT/SWNT-spiro-OMeTAD stratified structure on perovskite. The broad absorption feature at 1300 nm is characteristic of the presence of holes in spiro-OMeTAD. In the presence of the P3HT/SWNT interlayer this feature appears to be much weaker and appears to be overlaid with a second, longer wavelength feature centered around 1450 nm

The PIA spectrum of a device with undoped spiro-OMeTAD HTL is shown in figure 5.8. The broad feature at 1300 nm is characteristic of the presence of holes in spiro-OMeTAD (i.e. its oxidized state) [246].

For the stratified P3HT/SWNT-spiro-OMeTAD structure, the broad feature of oxidized spiro-OMeTAD becomes weaker and appears to be overlaid with a second, longer wavelength feature centered around 1450 nm. This suggests a smaller or shorter-lived hole population in the spiro-OMeTAD in the presence of P3HT/SWNTs. To isolate the specific features of P3HT/SWNTs in the PIA spectra, separate PIA measurements were carried out on devices with neat P3HT/SWNT films in place of spiro-OMeTAD. The resulting PIA spectrum is plotted in figure 5.9 together with the absorption spectrum of a P3HT/SWNT film on glass.

The absorption spectrum has the characteristic absorption peaks associated with the E_{11} transitions of s-type P3HT/SWNTs according to their chirality [247].

The PIA spectrum shows a series of photobleaching (PB) features, which coincide with bleaching of the ground state absorption of the P3HT/SWNTs. The PIA absorption feature further into the infrared is presumably absorption of the oxidized P3HT/SWNTs or electrons in the electron-accepting TiO_2 layer on the adjacent side of the perovskite film. The photobleaching features were not observed in PIA measurements on films of P3HT/SWNTs on glass without the active perovskite layer. It can therefore be excluded that the observed PB features are caused by charge transfer between the SWNTs and the encapsulating P3HT sheath.

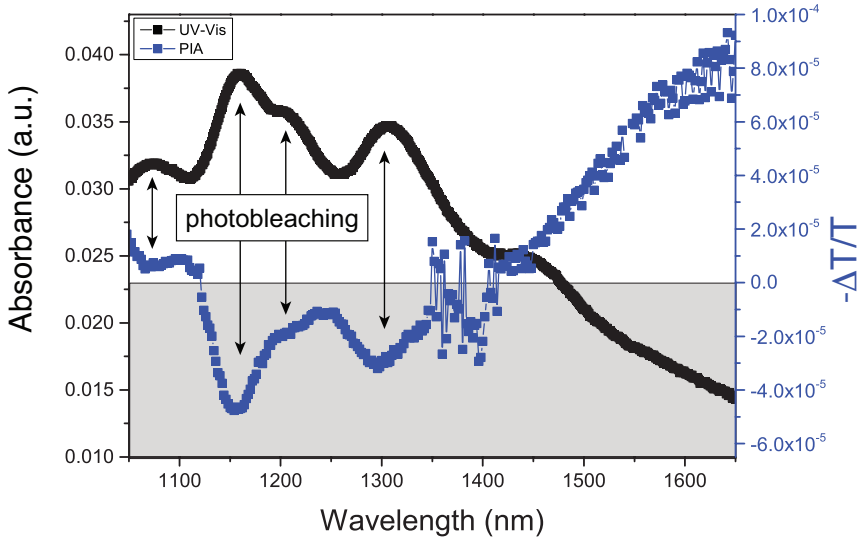

Figure 5.9: The PIA spectrum of a device with a neat P3HT-wrapped SWNT layer as HTL is plotted together with the absorption spectrum of a P3HT/SWNT film on glass. The photobleaching dips correspond well to the exciton absorption peaks of the s-type SWNTs which is evidence for direct hole injection from the perovskite absorber into the P3HT/SWNT valence band.

This result suggests that in fact a significant number of photogenerated holes are transferred from the perovskite to the SWNTs. The photogeneration of a hole in the perovskite presents the opportunity of a valence band electron of the SWNTs to transfer to an energetically more favorable state. The population of electrons in the valence band of the SWNTs is thus reduced when a large number of holes are generated, provided the charge transfer between perovskite and SWNTs is thermodynamically possible and favorable, which this experiment suggests. The effect of the valence band depopulation is a reduction of absorbance of the typical absorption features, as can be observed in figure 5.9.

To confirm that the photobleaching features observed in the PIA measurements are in fact the result of the transfer of photogenerated holes to the SWNTs, chemical p-doping was used to show that valence band depletion would exhibit the observed exciton bleaching. To this end P3HT/SWNTs were chemically p-doped in solution with 2,3,5,6-tetrafluoro-7,7,8,8-tetracyanoquinodimethane (F_4TCNQ) [248].

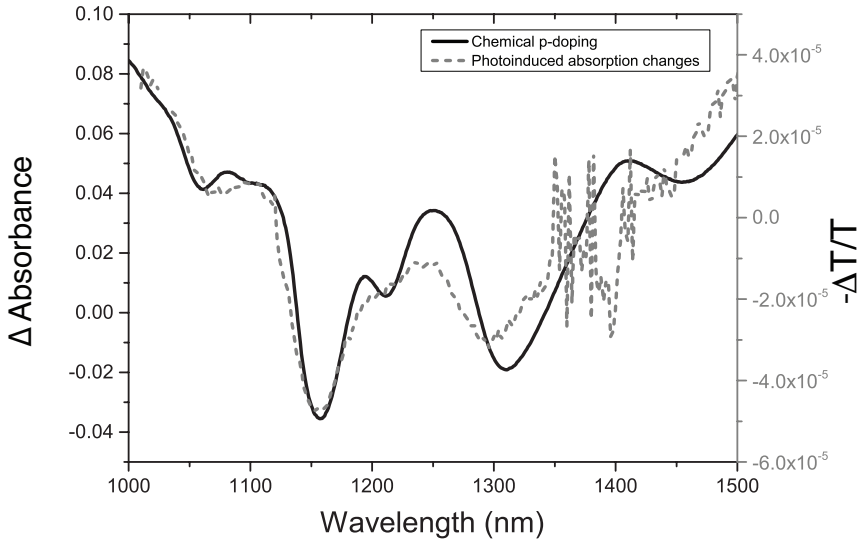

Figure 5.10: The absorption spectrum resulting from subtracting the absorption spectrum of undoped SWNTs and highly p-doped (oxidized) SWNTs in solution, overlaid with the photoinduced absorption spectrum of a P3HT/SWNT film on top of a perovskite absorber (excited at 515 nm)

In the doping process, electrons transfer from the SWNTs to the F_4TCNQ, thus depleting the electron population in the valence band the same way the photogenerated holes from the perovskite would deplete the SWNT valence band states in a device. The change in absorbance between the undoped and the highly p-doped (oxidized) absorption spectrum (figure 5.10) shows a bleaching of the absorption of the ground state transitions (E_{11}) which resembles closely the photobleaching features detected in the PIA measurements from figure 5.9. This indicates that the photobleaching features observed the PIA measurements in figure 5.9 are the result of the depletion of valence band states which can be attributed to the injection of holes photogenerated in the perovskite absorber. These measurements show that significant hole transfer from the perovskite to the P3HT/SWNT nanohybrids must occur.

5.4 Transient decay measurements

To further clarify how direct hole transfer from the perovskite to the nanotubes leads to an increase in efficiency, we performed small perturbation transient decay measurements (details in section 4.5). The results are shown in figure 5.11.

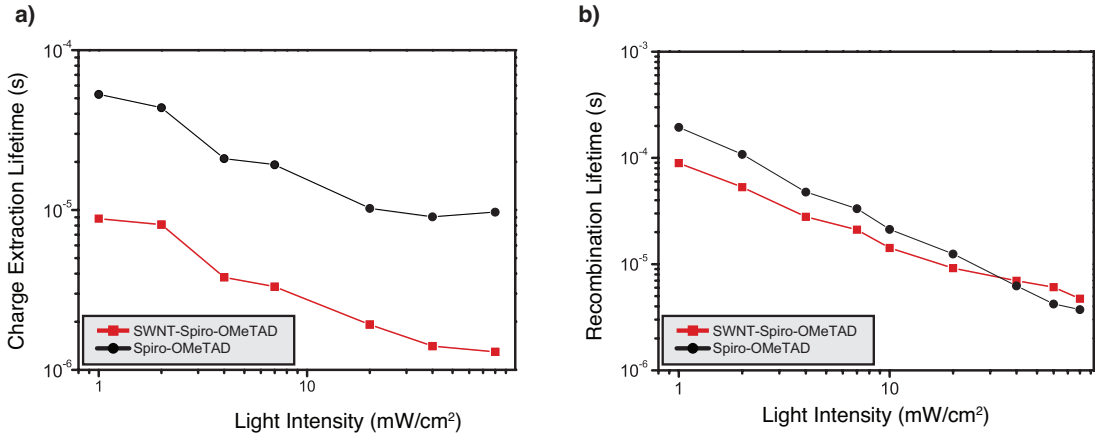

Figure 5.11: The results of the decay measurements of two devices with two different HTLs, one with neat spiro-OMeTAD, one with SWNT-spiro-OMeTAD. The charge extraction lifetime is shown in a). The device with the SWNT interlayer exhibits close to one order of magnitude faster extraction. The recombination lifetime τ_{rec} in b) appears to be quite similar in both devices.

Figure 5.11 a) illustrates the charge extraction time measured under short-circuit conditions plotted against various light intensities for two devices with a hole-transporting layer of either neat spiro-OMeTAD or of the sequentially coated double-layer structure composed of P3HT/SWNT and spiro-OMeTAD. For all light intensities, it can be seen that the charge extraction occurs almost one order of magnitude faster in the presence of the P3HT/SWNT nanohybrids interlayer.

The charge extraction lifetimes – the average time it takes for a photogenerated hole to be extracted – decrease with light intensity for both the neat spiro-OMeTAD layer and the SWNT-spiro-OMeTAD double layer structure. This increase in the charge extraction rate indicates that under low light intensities charge transport through undoped spiro-OMeTAD limits hole transport for both structures, because it has previously been demonstrated that neat spiro-OMeTAD has a strongly charge density dependent mobility [242]. However, more importantly, the extraction rate is almost one order of magnitude higher for all light intensities in the presence of the P3HT/SWNTs as compared to the neat spiro-OMeTAD layer. This is further evidence that a large fraction of holes is extracted through the carbon

nanotubes rather than through neat spiro-OMeTAD, which results in a greatly improved extraction rate.

In figure 5.11 b) the recombination lifetimes τ_{rec} are shown. For both HTL structures these appear to be comparable for all light intensities. That means that the improved device performance can be attributed to faster charge transport through the HTL.

5.5 Summary

In summary, P3HT-wrapped single-walled carbon nanotubes act as highly effective p-type charge transporter component in conjunction with spiro-OMeTAD for perovskite solar cells. The SWNTs are able to fully replace Li-TFSI doping of spiro-OMeTAD which is usually required for comparable efficiencies. Sequentially depositing nanotubes and spiro-OMeTAD is shown to be superior to a blend structure, in which the SWNTs are directly dispersed in the spiro-OMeTAD solution. This is most likely because the nanotubes can form a well-connected percolation network in this configuration with a large interfacial contact to the perovskite absorber and direct contact to the electrode. The photoinduced absorption study and the transient decay measurements both indicate that a significant fraction of charges is transported through the carbon nanotubes

Chapter 6

Carbon nanotube/polymer composite as a highly stable charge collection layer in perovskite solar cells

The work in this chapter has been adapted and reproduced in part with permission from: Severin N. Habisreutinger, Tomas Leijtens, Giles E. Eperon, Saupmuel D. Stranks, Robin J. Nicholas & Henry J. Snaith, *Nano Letters*, 14, 10, (2014) 5561-5568 [221]. Copyright 2014 American Chemical Society.

6.1 Stability of hole-transporting materials

A fundamentally important aspect in the development of new types of photovoltaic devices is their stability and resilience against external and internal stressors such as thermal cycles, atmospheric moisture, UV irradiation and others. For perovskite solar cells the aspect of moisture stability is particularly interesting because its active material is highly sensitivity to moisture. This follows as a consequence of the nature of its organic constituent methylammonium iodide, which - as an amine salt - is highly soluble in polar solvents, above all, water [55].

In devices, the first line of defence is the hole-transporting material which caps the device as the top layer. Before ambient moisture can interact with the perovskite absorber, it has to percolate through this layer. The readiness of this material to permit moisture permeation is thus an important aspect for assessing the overall device stability. Furthermore, any inhibition of moisture ingress has to be maintained by the hole-transporting material also a higher operational temperatures of up to 85°C. In this study, three hole-transporting materials were investigated with regards to their ability to retain the structural and operational integrity of the perovskite absorber by exposing fully-functional perovskite devices to thermal stressing in ambient air.

As a reference for the degradation mechanisms of the perovskite, a bare fully crystallized $CH_3NH_3PbI_3$ film was subjected to 80°C in ambient air. After 24 hours, the perovskite changes color from its characteristic dark brown to a bright yellow, as shown in figure 6.1. The corresponding absorption spectra and X-ray scattering pattern indicate that this color change can be attribtued to a change of the perovskite crystal structure. The diffraction pattern after heating does not exhibit the peaks characteristic for the $CH_3NH_3PbI_3$ perovskite. Instead there remains only one dominating peak at 12.7° which corresponds to a signature feature of a pure lead iodide film. This suggests that the degradation of the perovskite at 80°C is correlated with the loss of methylammonium cations indicating that the composite material reverts to PbI_2 according to the reaction

$$CH_3NH_3Pb_3 \rightleftharpoons CH_3NH_3I + PbI_2 \tag{6.1}$$

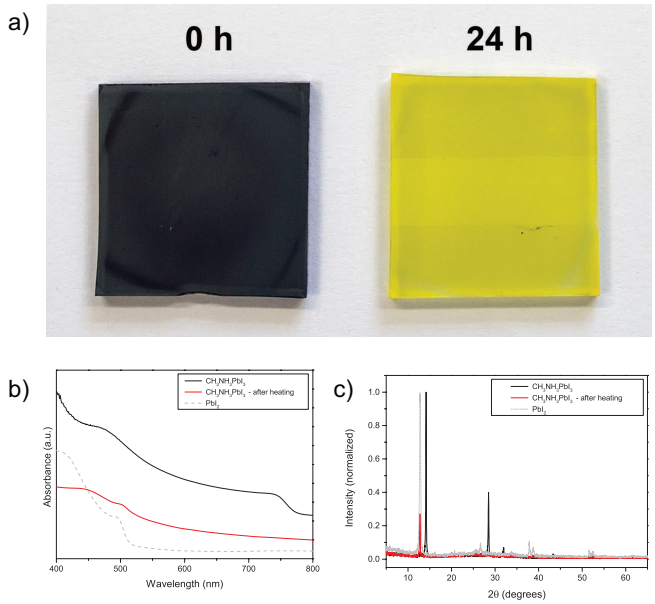

Figure 6.1: : a) photograph of perovskite devices without hole transporting before and after 24 h exposed to 80° C. b) Absorption spectrum of the perovskite before and after heat exposure. The typical perovskite absorption across the visible range vanishes. c) XRD spectra of the perovskite before and after 24 h of heating, compared to a layer of pure lead iodide. The most pronounced features of the perovskite crystal structure at 14.2° and 28.5° disappear fully and are replaced by a single peak at 12.7° which is associated with a film of pure lead iodide. That would also account for the yellow coloration of the degraded perovskite film.

Being exposed to 80°C in ambient conditions clearly leads to a breakdown of the perovskite. The question remains what is the driving degradation mechanism. There are two possible forces that could act upon the perovskite leading to its degradation: elevated temperature or atmospheric moisture. To test this, a bare perovskite layer on glass was kept at 80°C for 96 h in a completely dry atmosphere.

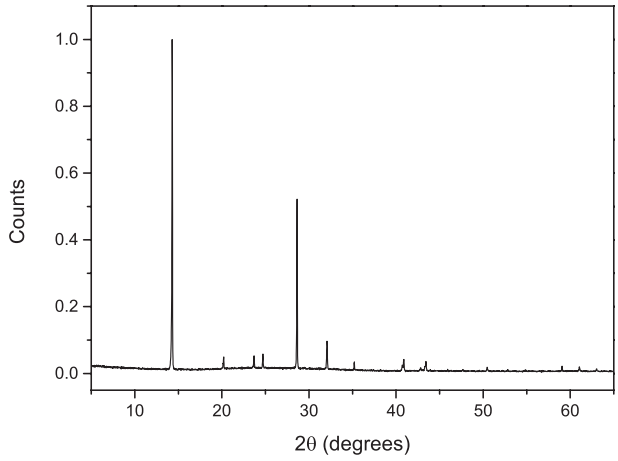

Figure 6.2: X-ray diffraction pattern of a perovskite film after 96 h at 80°C in a completely dry atmosphere. The characteristic features of the perovskite crystal structure at 14.2° and 28.5° appear to be completely unchanged. The feature peak of PbI_2 at 12.7° can not be observed, indicating in the absence of moisture, no degradation occurs at this temperature.

The X-ray diffraction pattern of the perovskite film after 96 h at 80°C in a dry atmosphere remains unchanged (figure 6.2). The typical indicator of the degradation onset is the peak characteristic for PbI_2 at 12.7°, however, no such feature can be observed in figure 6.2. This shows that in the absence of moisture, the perovskite does not suffer any degradation. The previously observed transformation to PbI_2 can therefore be attributed to the presence of moisture, which is likely to initialize the breakdown of the perovskite.

In follow up studies, the interaction between water and $CH_3NH_3PbI_3$ was studied in more detail using several methods such as absorption spectroscopy, X-ray diffraction and ellipsometry, showing there are at least two intermediate hydrate phases of the perovskite before it decomposes [58, 59, 60]. The observations are summarized in section 2.3.1, in short, water molecules readily infiltrate into the perovskite structure, where they hydrate the perovskite. Because the organic methylammonium ion is connected by comparatively weak hydrogen bonds to the surrounding Pb-I cage, external stresses such as heat can break them through thermal strain. The polar water molecule inside the perovskite unit cell will bind to the organic cation and possibly remove it. This results in the disintegration of the perovskite structure and a loss of its beneficial optoelectronic properties. The rate of degradation was found to be strongly linked to the layer placed on top of the perovskite, likely correlated with the hydrophobicity of the material [60].

It is conceivable that the hole-transporting layer, which forms the outermost layer in a typical perovskite solar cell, could have a protective effect on the perovskite structure

by shielding it from the ingress of atmospheric moisture thus preventing the weakening of the perovskite crystal structure, and by "sealing in" the volatile perovskite components preventing the thermally induced loss of the organic molecules. The extent of this protection will consequently depend on the hydrophobicity, permeability, and density of the hole-transporting material. These additional properties of the hole-transporter, which are largely unconnected to its electronic characteristics, may therefore have a strong impact on the overall solar cell stability.

The selected hole-transporting materials which were investigated under these aspects were chosen based on the prevalence in the field of perovskite solar cells and the high efficiencies associated with them. As elaborated in 5.1, spiro-OMeTAD, has become standard p-type material in the field and is therefore found to be used in a majority of n-i-p perovskite devices and has been shown to enable power-conversion efficiencies of up to 20.8% [249]. Another hole-transporting material with which efficiencies exceeding 20% have been achieved is the polymer *poly(triaryl amine)*(PTAA)[64]. The third hole-transporter *poly(hexylthiophene)* (P3HT) is another polymer that has been employed in various studies, though it has not achieved comparable performances [250, 246].

The three hole-transporting materials were deposited onto perovskite with similar parameters found in literature, so that they would form fully functioning devices lacking the hole-accepting cathode. These films were then subjected to thermal stressing by placing them on a hot plate at 80°C in ambient air at a relative humidity in the range of 40-60%.

Photographs of the evolution of these films in 24 hour intervals of a total time of 96 h are shown in Figure 6.3. The first signs of degradation are visible after 24 h for all three hole-transporting materials. After 96 h, the degradation has progressed significantly, where all perovskites films have become predominantly yellow. The corresponding absorption spectra and X-ray diffraction patterns confirm the degradation of the perovskite. The breakdown of the perovskite structure is clearly visible in the absorption spectra of all devices (Figure 6.4 a). Before heat exposure, the samples exhibit a strong absorption in the visible range from 750 to 450 nm characteristic of $CH_3NH_3PbI_3$. In the spectra taken after heat exposure, this absorption feature disappears with time, which correlates with a visible color change of the films (Figure 6.3), which become almost transparent in the red region of the spectrum.

The rate at which this happens is different for all three hole-transporting materials and correlated with their ability to prevent both moisture ingress and molecule egress from the

perovskite i.e. most likely methylammonium iodide. This in turn depends on molecular and structural properties of the films the materials form, as well as the layer thickness and the dopants of the material. These parameters have been optimized exclusively with the aim to maximize device performance rather than to minimize absorber degradation.

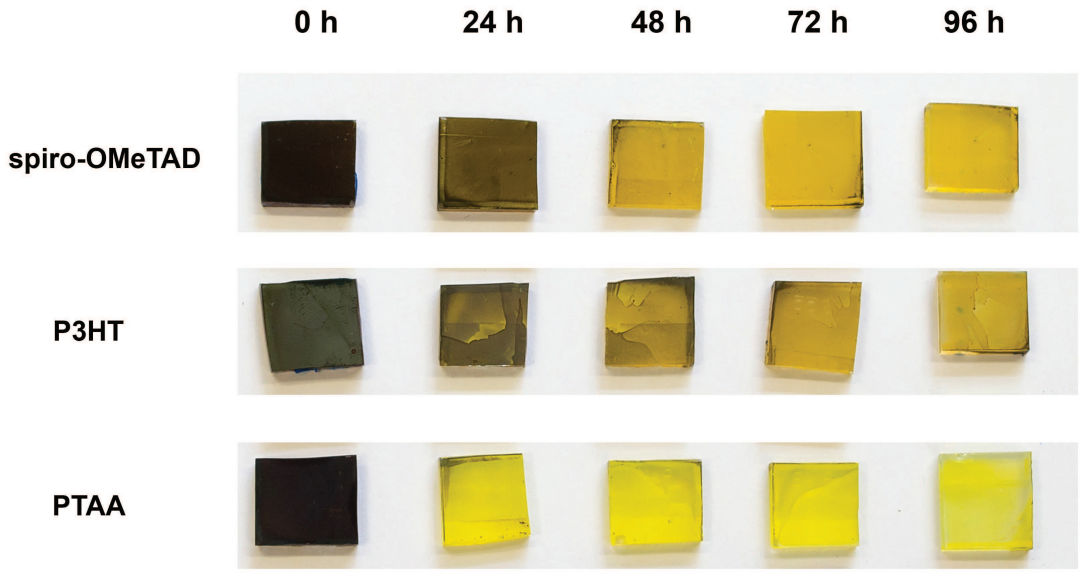

Figure 6.3: Photo illustrating the visible degradation of the perovskite layer. The color shifts from almost black to yellow for all organic HTLs indicating a similar degradation process of the perovskite without a protective hole-transporter as shown in figure 6.1.

The X-ray diffractograms taken before and after heat exposure (Figure 6.4) confirm that the discoloration of the perovskite films, which are characterized by their strongest diffraction peaks at 14.28°and 28.57°, correlates with a breakdown of the perovskite crystal structure. The residual film exhibits an XRD pattern similar to that of neat lead iodide, with its characteristic diffraction peak at 12.80°, which is in accordance with the disintegration of the perovskite into its starting materials and the removal of methylammonium iodide.

For spiro-OMeTAD and P3HT, the perosvkite absorber retains some of its characteristic absorption edge at around 750 nm after 24 hours of thermal stressing. However, after 48 h, this absorption is fully bleached, correlated with a strong yellow coloration of the perovskite absorber (figure 6.3).

The fastest degradation rate is observed for the device with PTAA. The device color has completely changed from dark brown to yellow after 24 h, losing completely the absorption onset at around 750 nm. One of the reason could be that the polymer layer is comparatively thin when prepared according to literature [64, 251].

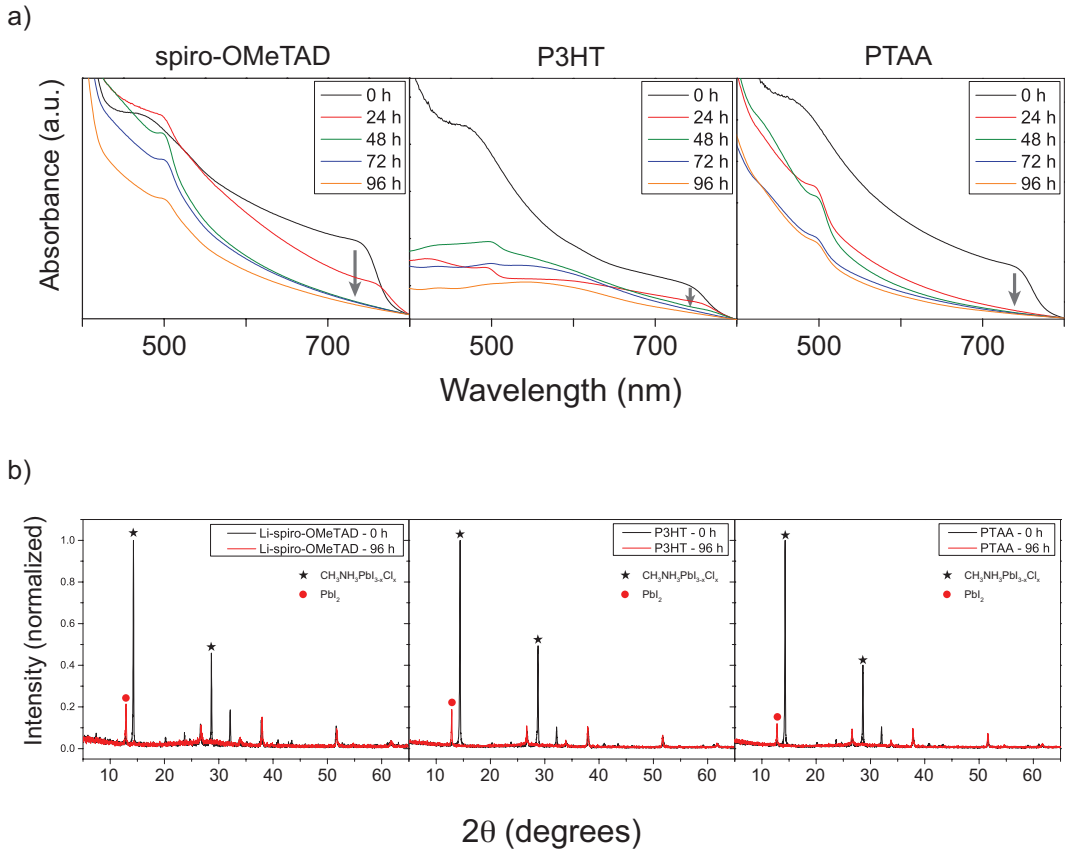

Figure 6.4: (a) Photo illustrating the visible degradation of the perovskite layer. b) The spectral changes from the diffraction features characteristic for the $CH_3NH_3PbI_3$ at 14.28°and 28.57°(black star) to a new diffraction feature at 12.80°associated with PbI_2 indicate degradation of the perovskite crystal structure.

An additional factor which may have an impact on the moisture-barrier properties of these materials is the use of dopants. The intrinsically low hole mobility of the amorphous spiro-OMeTAD can be overcome to a certain extent by increasing the carrier density by oxidative doping [252, 253, 254]. Lithium salts are most commonly used as effective p-dopants in the presence of oxygen [254]. Despite higher intrinsic hole mobilities compared to their amorphous counterpart, polymeric hole-conductors generally still need to be *p*-doped in order to achieve comparably high photocurrents [251, 255].

An aspect, which was not relevant when Lithium was introduced as additive to solid-state dye-sensitized solar cells [237], is its intrinsically hygroscopic nature. It is conceivable that the property of Li-TFSI to attract moisture could accelerate the degradation process of the perovskite absorber. In order to evaluate the impact of lithium doping on the degradation process perovskite films with doped and undoped spiro-OMeTAD were subjected to the same thermal stressing conditions as before. The heat induced degradation progressed in fact

noticeably faster for the spiro-OMeTAD layer which had been doped with Li-TFSI (figure 6.5 a)). In the absence of a dopant, the degradation proceeds more slowly, nevertheless already after 24 h, a reduction of absorption indicates that the perovskite structure begins to break down (figure 6.5 b)). The diffraction pattern after 96 h exhibits some remaining features characteristic for the perovskite structure, however, the feature dominating the spectrum can be attributed to lead iodide which is indicative of the overall breakdown of the perovskite. This suggests that the highly hygroscopic nature of the lithium-based dopant may have a significant role in introducing moisture into the perovskite structure, thus accelerating its degradation. Nevertheless, even in the absence of the hygroscopic dopant, the structural integrity of the perovskite absorber cannot be retained under thermal stressing with spiro-OMeTAD.

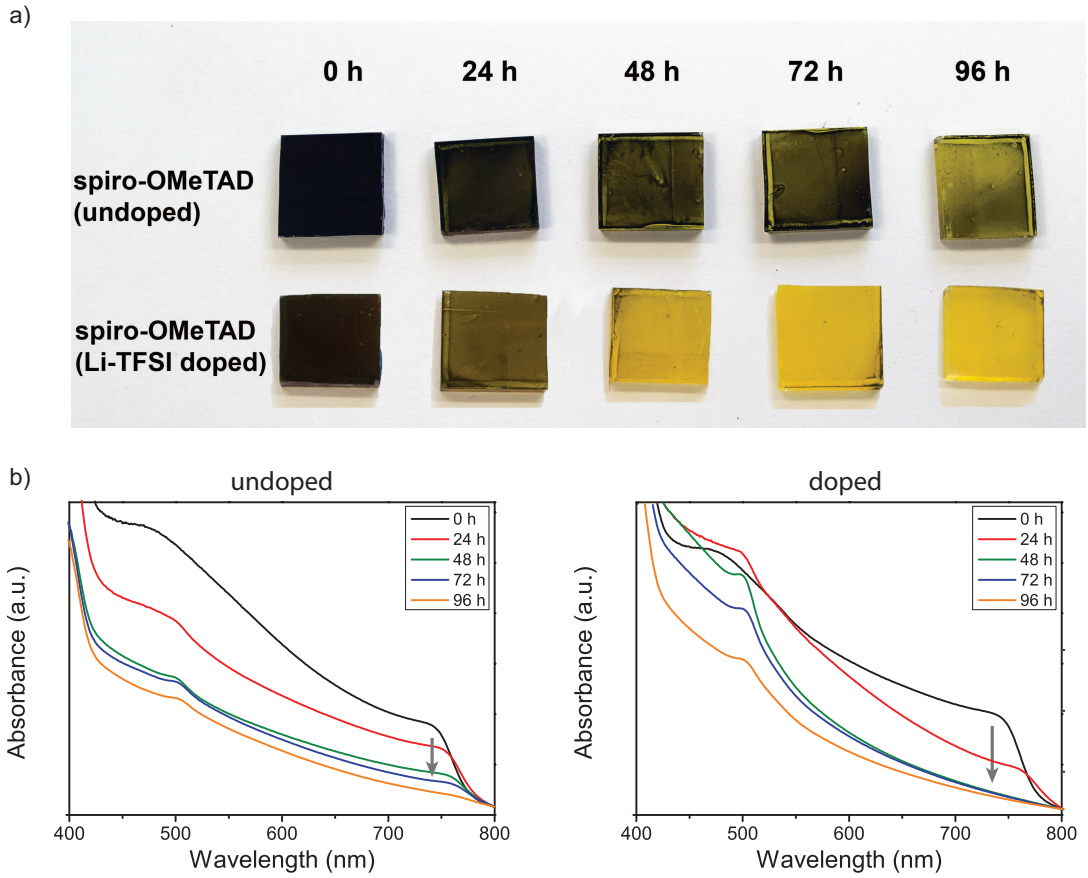

Figure 6.5: (a) Photos of two perovskite devices with undoped and doped spiro-OMeTAD as hole transporting layer exposed to 80°C, comparing their respective degradation rates. b) Concomitantly, the absorption spectra show that in the absence of Li-TFSI the degradation process proceed upmuch more slowly, allowing the perovskite absorber to retain its absorption onset upmuch longer (> 48 h), though decreasing in strength with time.

6.2 SWNT-based hole-transporting structure

Clearly, none of these typically employed hole transporters are effective barriers against thermally induced degradation of methylammonium lead triiodide in ambient atmosphere. To counteract this degradation process, the insulating polymer poly(methyl methacrylate) (PMMA) is employed, which has a fairly low moisture vapor transmission rate of < 60 g/m^2 and should therefore be capable of inhibiting the intrusion of moisture into the perovskite structure while siupmultaneously inhibiting the evaporation of the methylammonium iodide. In fact, the effectiveness of a 300 nm thick layer PMMA as a protective layer is shown in Figure 6.6. Even after 96 h of continuous heat exposure at 80°C in air, no significant difference in color, absorption, or crystal structure of the perovskite layer can be observed. Within a time frame of 96 h, PMMA can thus fully inhibit the degradation process.

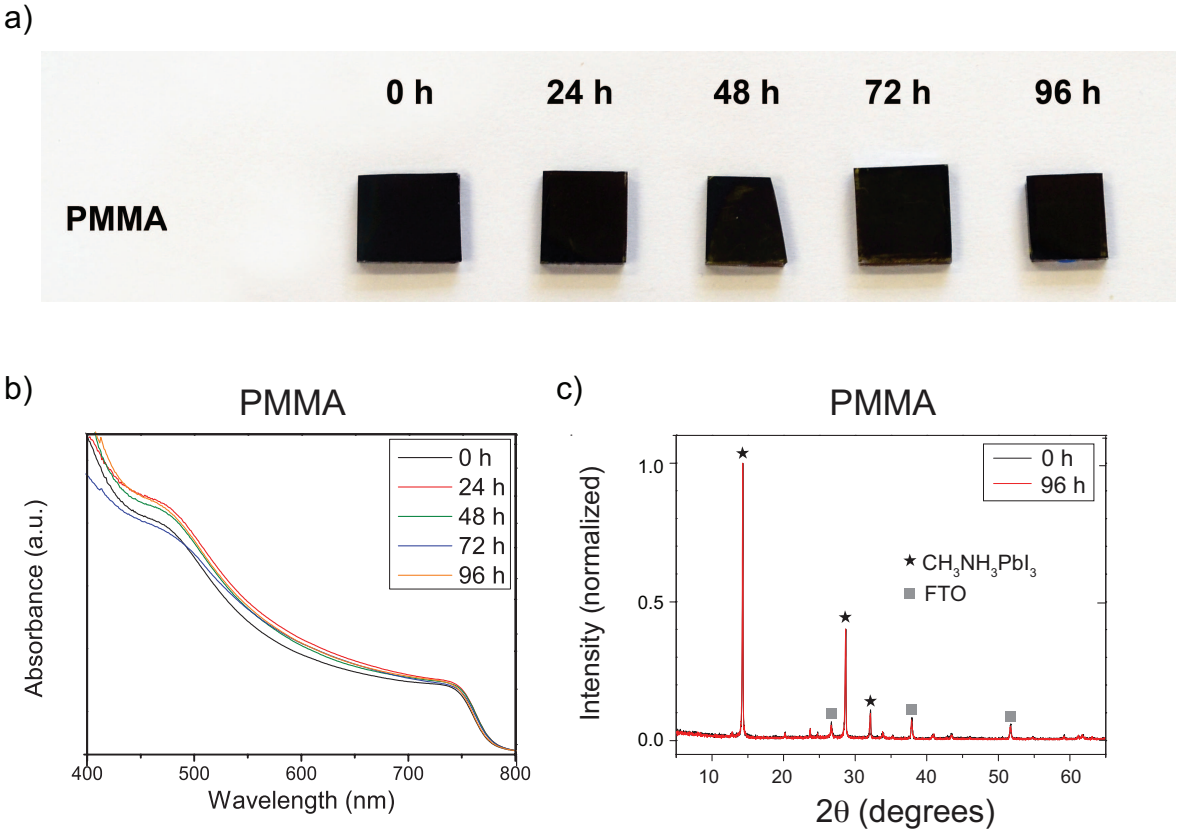

Figure 6.6: (a) Photos of a perovskite absorber covered with 300 nm of PMMA exposed to 80C for up to 96 h. b) The absorption shows no significant changes over the induced by the thermal stressing. c) Comparison of X-ray diffraction pattern before and after 96 h of thermal stressing reveals that the perovskite crystal structure is fully preserved due to the protective PMMA top layer.

Lacking π-conjugation, PMMA is not capable of transporting charge on its own and acts as an insulator. However, by combining PMMA with a highly conductive component, this insulator/hole-conductor composite may be able to retain the protective properties of PMMA while possessing selective charge collection properties similar to the organic hole-transporters.

In the previous chapter a two-layer approach was introduced in which SWNTs are used to enhance the charge transporting properties of a host matrix, in that case spiro-OMeTAD. In this approach a dense layer of P3HT-wrapped SWNTs is deposited directly onto the perovskite absorber and then - by subsequent deposition - embedded in the hole-transporter matrix. Photoinduced absorption spectroscopy suggested that photogenerated holes are directly transferred from the perovskite to the SWNTs (figure 5.9). With an aspect ratio $>$ 1000 i.e. a length exceeding 1 μm, the nanotubes should be able to fully penetrate a polymer matrix with a thickness of 300 nm.

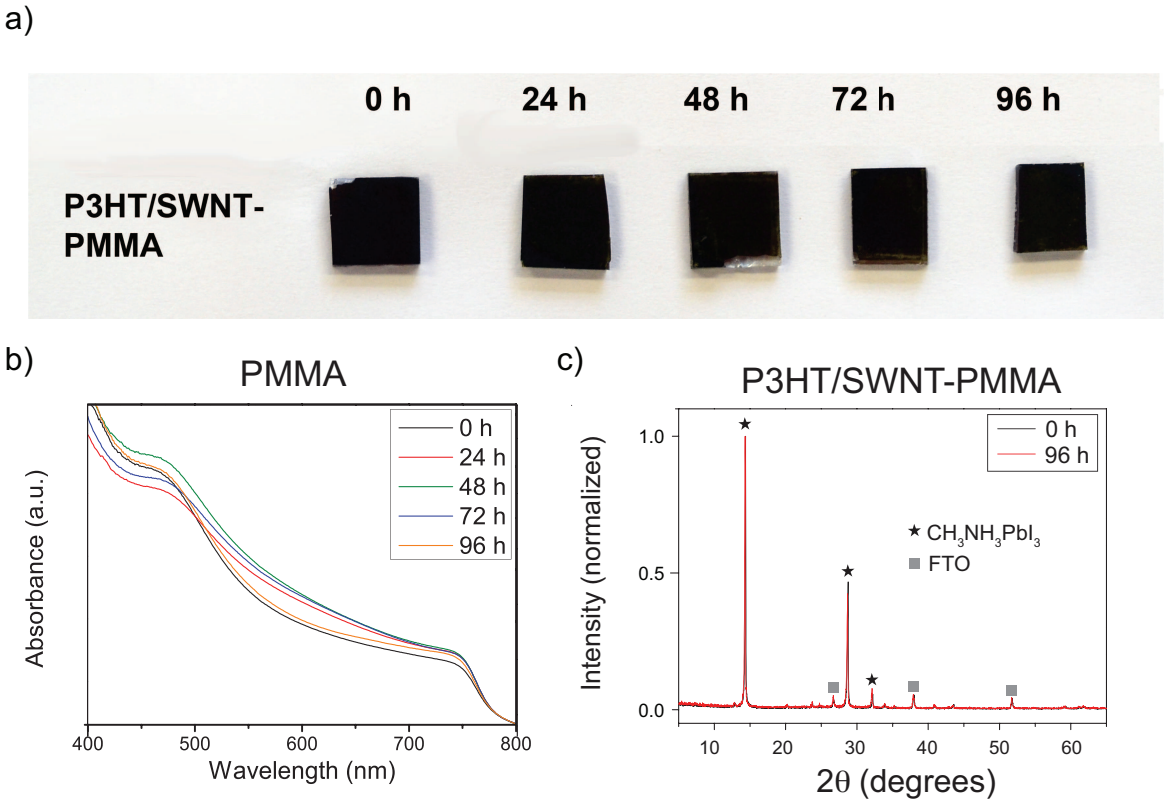

Figure 6.7: (a) Photos in 24 h intervals of a perovskite absorber covered with the double-layer structure composed of a layer of P3HT-wrapped SWNTs underneath a 300 nm layer of PMMA which was exposed to 80deg C for up to 96 h. b) The absorption shows no significant changes over the induced by the thermal stressing. c) Comparison of X-ray diffraction pattern before and after 96 h of thermal stressing reveals that the perovskite crystal structure is completely undegraded showing that the protective properties of PMMA are fully retained in the presence of the SWNT underlayer.

In order to be an effective hole-transporting composite, this two-layer structure needs to extract charges effectively and selectively while at the same time retaining the protective qualities of a neat PMMA film at the same thickness. Repeating thermal stressing experiments on the composite structure analogous to the ones performed on the other hole-transporting materials and neat PMMA, allowed a direct comparison of the stability properties of the various different layers. In fact, as shown in figure 6.7, the perovskite absorber does not experience any kind of noticeable degradation within a time frame of 96 h, as both absorption spectra and X-ray diffraction pattern remain more or less unchanged. That means that the presence of SWNTs underneath the PMMA layer does not impair the protective properties of PMMA.

However, the merit of this structure is only given provided the SWNTs can extract p-type charges selectively and efficiently in absence of a dedicated hole-transporter such as spiro-OMeTAD.

Prior to the fabrication of fully integrated perovskite devices, the ability of the SWNT network to make contact was tested by lateral conductivity measurements. Although the obtained resistivity values were comparatively high (> 50 k$\Omega/\square$), these measurements showed that the SWNTs penetrate the PMMA capping layer, on the one hand, and form an interconnected network which is able to conduct charge laterally over macroscopic distances of several centimeters, on the other hand.

In perovskite devices, the P3HT-wrapped SWNTs were deposited the same way as described in chapter 5 at the interface with the perovskite absorber (figure 6.8 a). The complete device structure has fluorine doped tin oxide as transparent anode, collecting the photogenerated electrons. A thin compact layer acts as hole-blocking electron collection layer. The $CH_3NH_3PbI_3$ absorber is then coated onto a 400 nm layer of meso-structured alumina. Because the perovskite is deposited onto heated substrates, it forms a thick capping layer on top of the alumina layer. The SWNT-PMMA composite structure is then deposited onto the perovskite capping layer. In the cross section (figure 6.8 d)), P3HT/SWNTs can be seen dangling from the interface between the HTM and the perovskite.

6.2.1 PMMA layer thickness

Because of the non-conductive nature of PMMA, the two-layer structure requires fine optimization with respect to the relative thicknesses of the conductive SWNT layer underneath

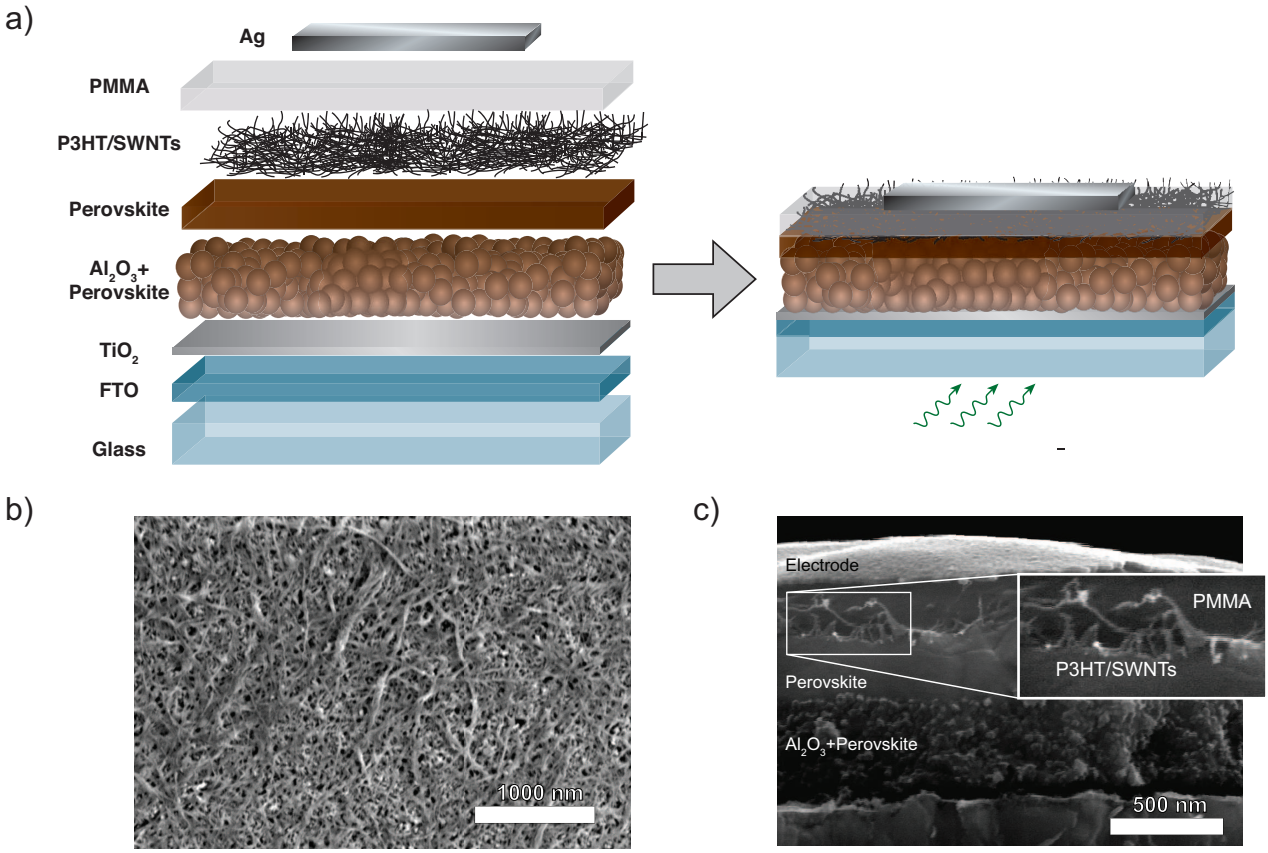

Figure 6.8: Schematic illustration of the solar cell with a carbon nanotube/polymer composite as hole-transporting structure. Schematic architecture of the investigated device consisting of sequential layers of FTO as transparent electrode, a TiO_2 compact layer, a mesostructured layer of Al_2O_3 coated with $CH_3NH_3PbI_3$ and the hole transporting structure composed of a P3HT/SWNT layer in-filled with a PMMA matrix

the inert polymer layer. Two interdependent constraints dictate the optimization procedure. For stability, the thickness of the PMMA layer has to be as thick as possible in order to minimize moisture ingress. For performance, however, when the PMMA layer is too thick, charge extraction will be hampered which will result in an increase in series resistance. Additionally, even when optimizing the two-layer structure just for effective charge extraction, reducing the layer thickness of PMMA does not automatically result in better performance, because when the PMMA layer falls below the optimum thickness, shunt paths can open up through which the metal electrode can directly contact the perovskite absorber, which will lead to non-radiative recombination losses. The reason for this behavior is the mesh-like structure of the SWNT film (figure 6.8 b)), which will allow the metal of the cathode to reach the perovskite through the openings in the network. These openings and holes need to be completely filled and covered by the PMMA layer. The optimum thickness for performance is therefore achieved when a balance between minimized series resistance and

a maximized shunt resistance is found. The thickness of the PMMA layer, in turn, is dependent on the thickness of the SWNT network and on the infiltration depth necessary to maximize the shunt resistance. At a fixed SWNT layer thickness, based on the experiments in the previous chapter, a PMMA thickness range from 35-550 nm was investigated. An an optimum concentration of PMMA in toluene was found to be around 50 mg/ml, which yields a film of a thickness of around 300 nm. The performance of the best performing device is shown in figure 6.12 a). This device has a PMMA top layer of 300 nm and yields a scanned power-conversion efficiency of 14.2%.

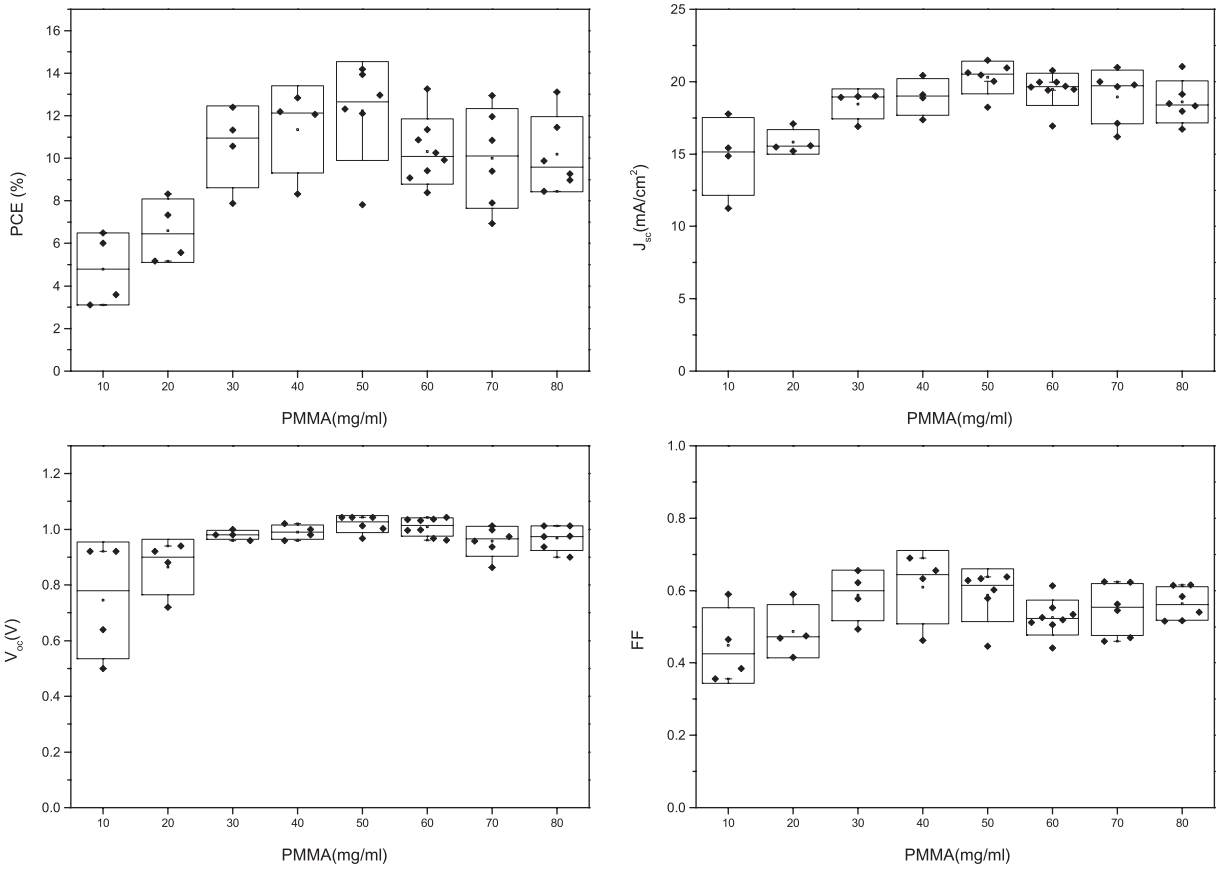

Figure 6.9: Performance parameters of devices with PMMA layers ranging in thickness from 35 nm (10 mg/ml) to 550 nm (80 mg/ml). The best performing devices were achieved at a thickness of around 300 nm (50 mg/ml). At this thickness a balance is reached between maximizing shunt resistance and minimizing series resistance.

6.2.2 SWNT type

The initial optimization of device performance with respect to the PMMA thickness was done using a purified distribution of SWNTs which had been produced with the HiPco process (see section 3.1). These commercially purchased SWNTs have a synthetic distribution of

2:1 of semiconducting to metallic SWNTs and a diameter range of 0.8 - 1.2 nm. In the next step of the performance optimization a range of SWNT types were screened for improved performance. Figure 6.10 shows the first screening of SWNT types, in which the purified HiPco SWNTs were compared to their raw counterparts which contain up to 35% of residual Fe catalyst as opposed to less than 15%; and to two types of CoMoCAT SWNTs, SG 7,6, which have a diameter in the range 0.7 - 1.1 nm and SG 6,5i, which have a diameter in the range of 0.7-0.9 nm, and are to 95% of semiconducting character.

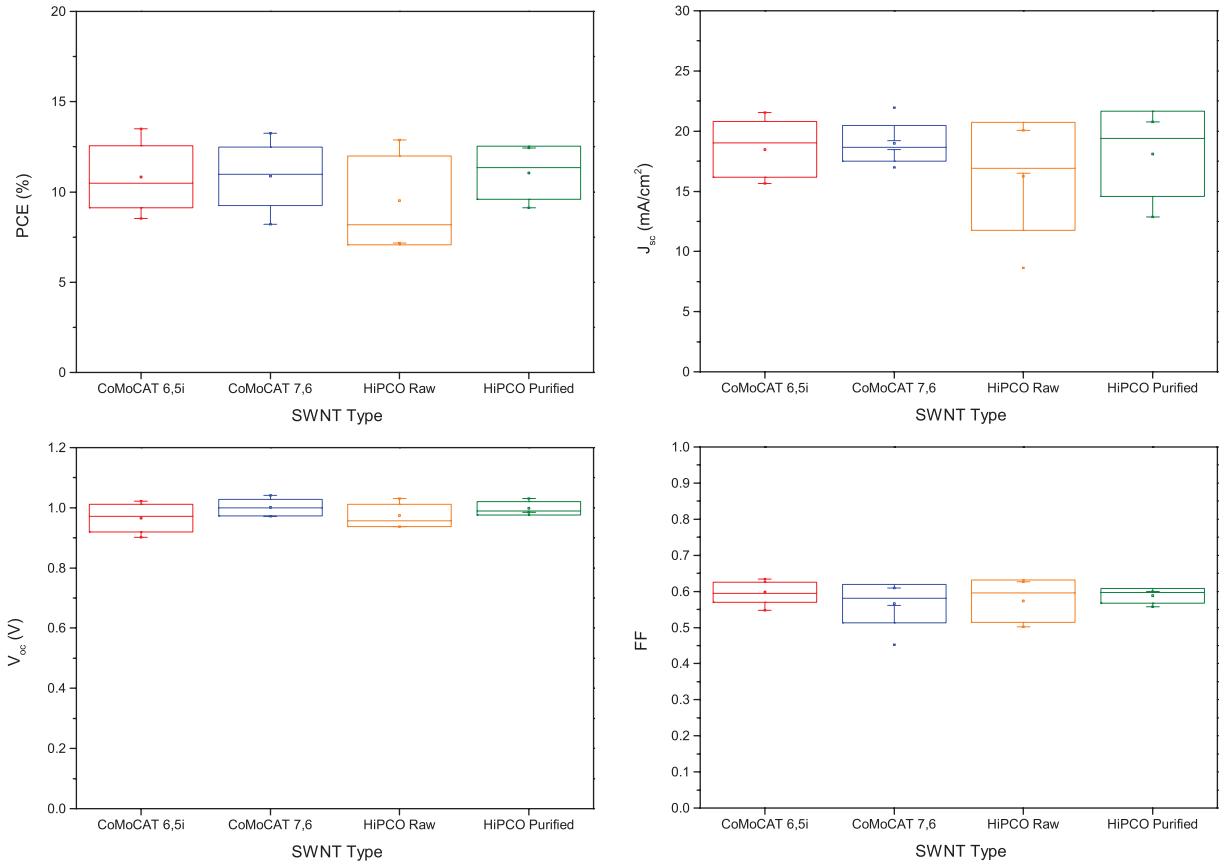

Figure 6.10: Performance parameters of devices with different SWNT types at a fixed concentration and a fixed PMMA layer of 300 nm. The compared SWNT types include raw and purified HiPco SWNTs (diameter 0.8-1.2 nm, 33% metallic SWNTs), CoMoCAT SG 7,6 (diameter 0.7-1.1- nm, 33% metallic) and CoMoCAT SG 6,5i (diameter 0.7-0.9 nm, $<$ 5% metallic).

Except for the unpurified (raw) HiPco SWNTs, the device performances of all SWNT types are highly comparable. A decrease in SWNT diameter does not seem to have a significant effect on device performance. More importantly, decreasing the concentration of metallic-type SWNTs does not result in an improvement of the device performance. In organic solar cells, the presence of metallic SWNTs usually results in increased recombination and has therefore an deleterious effect on the device performance [189, 171]. However, even

though any charge transport can only occur through the polymer-wrapped SWNTs, a reduction of the metallic content in the SWNT distribution does not lead to an observable improvement in device performance. It is conceivable that the polymer-wrapping leads to preferential charge kinetics for holes over electrons thus suppressing an increase in recombination in metallic SWNTs. If this holds to be true, an increase in metallic SWNTs in the distribution should not have a detrimental effect on the device performance. This was confirmed in a second SWNT screening experiment. In this experiment, the compared HTLs were comprised of purified HiPco SWNTs, arc discharge SWNTs with a wider diameter range of 1.2-1.7 nm and CG200, a CoMoCAT SWNT type, which has a diameter range of 0.7-1.4 nm, and an increased metallic tube content .

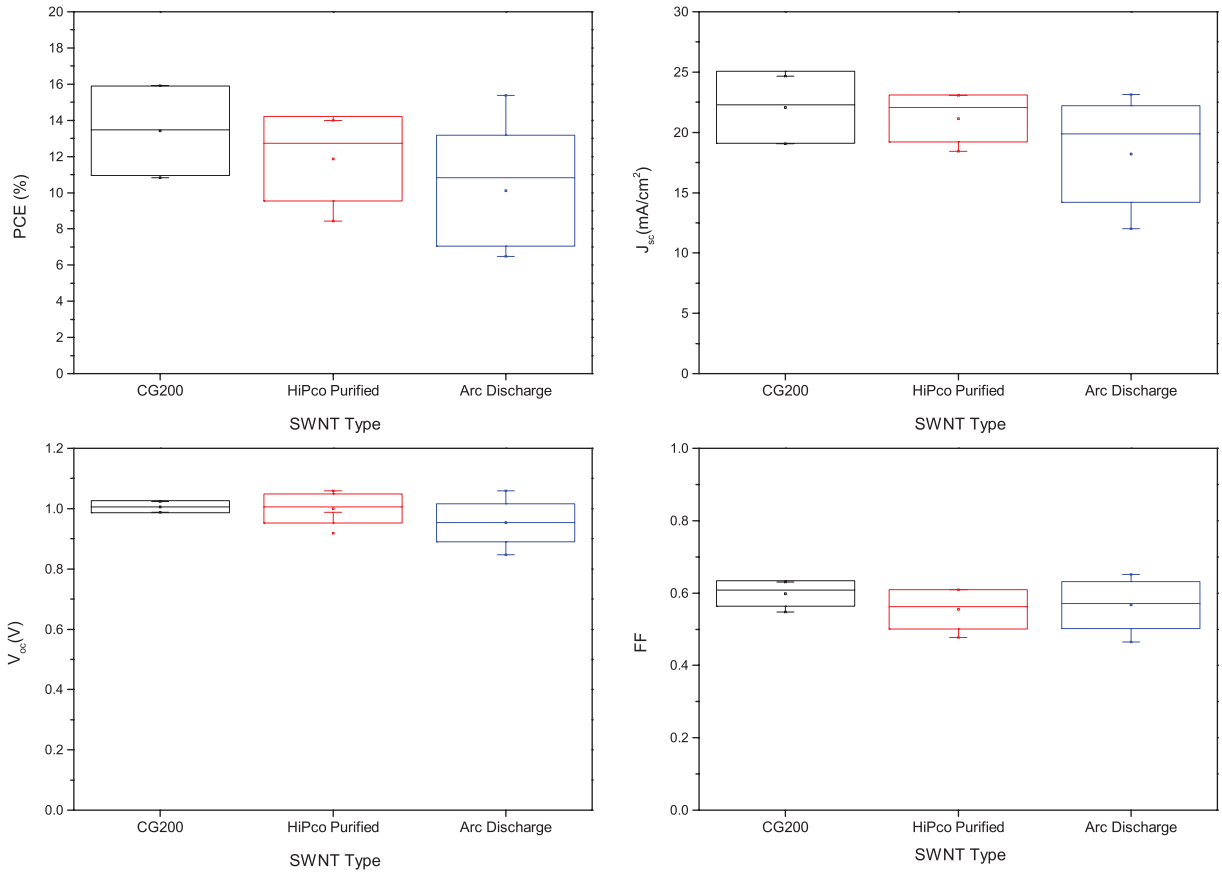

Figure 6.11: Second screening of different SWNT types. The performance parameters of devices are shown at a fixed concentration and a fixed PMMA layer of 300 nm. The compared SWNT types include the standard purified HiPco SWNTs, wide-diameter arc discharge SWNTs (diameter 1.1 - 1.4 nm, 1/3 metallic) and CoMoCAT CG20 SWNTs (diameter 0.7-1.4 nm, 40-50% metallic). The CG200 SWNTs appear to yield the best device performance due to improved charge extraction.

In figure 6.11 the performance parameters of devices are shown which have HTLs comprised of the aforementioned SWNT types. Most notably, CG200 SWNTs outperform the

purified HiPco SWNTs, yielding a higher scanned power-conversion efficiency which can largely be ascribed to a better charge extraction, in form of a higher short-circuit current and slightly better fill factor. This is further illustrated in figure 6.12 a), in which the current-voltage curves of the best-performing devices with HiPco and CG200 SWNTs are shown. Despite the significantly higher content of metallic SWNTs, the shunt resistance of the CG200 containing device appears to be the same as the one of the HiPco device. However, as in the initial screening, the short-circuit current is higher as is the fill factor, which can be attributed to the reduction in series resistance due to the higher conductivity of the CG200 SWNTs (table 6.3).

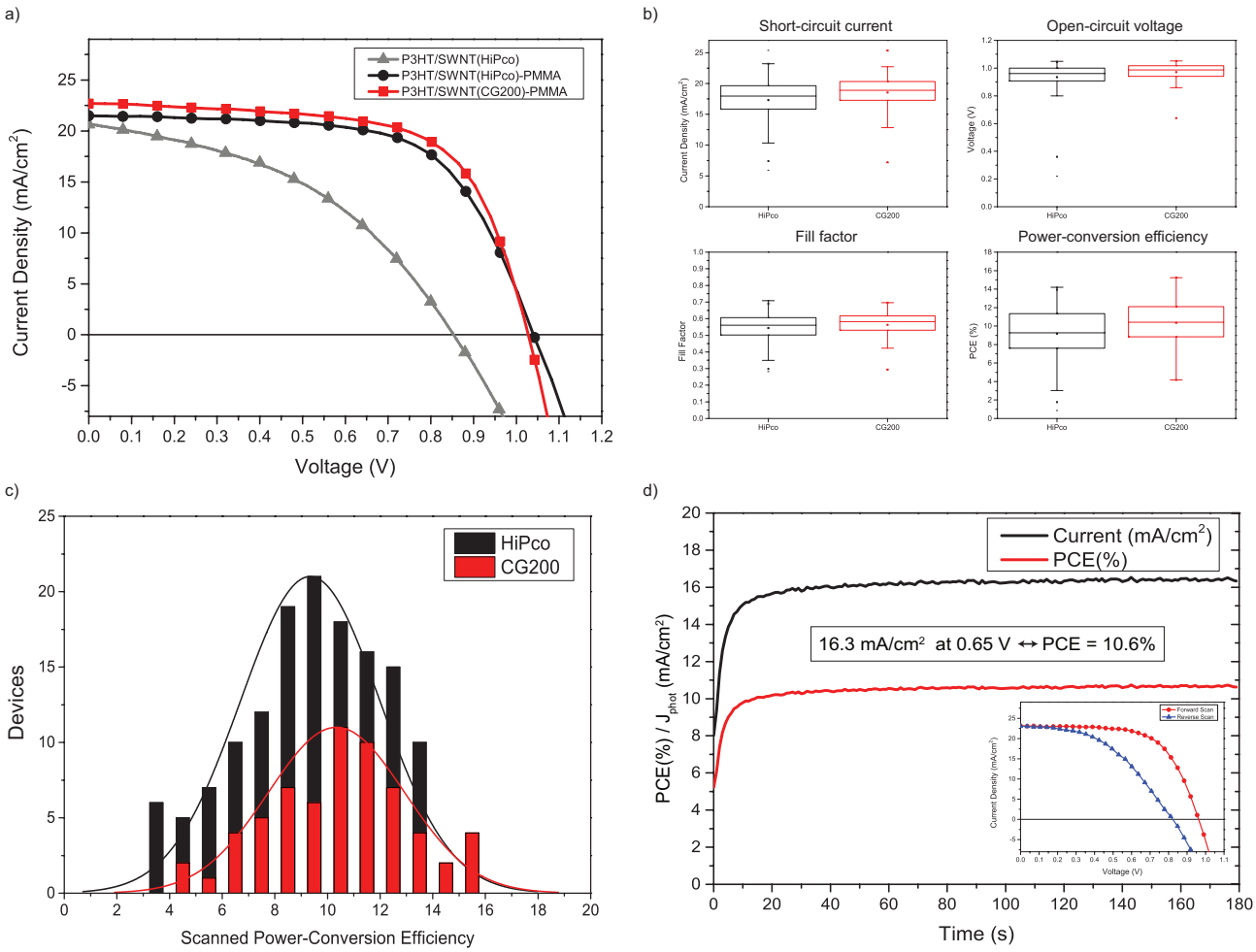

Figure 6.12: In a) the current-voltage curves of the champion devices are shown. The three devices have different HTL structures, P3HT/HiPco SWNTs without the PMMA layer, P3HT/HiPco SWNTs with a top-layer of 300 nm of PMMA and P3HT/CG200 SWNTs also with a top-layer of 300 nm of PMMA.

The current-voltage characteristics of the champion devices in which the HTL is composed of the SWNT-PMMA double-layer structure are shown in figure 6.12 a) together with a

device without the PMMA capping layer. In the absence of the PMMA layer charge can still be extracted, however, the performance of the device is strongly limited by the reduced shunt resistance and an early onset of recombination which results in a comparatively low open-circuit voltage. This illustrates the previously described effect of PMMA, to block shunt paths between the metal cathode and the perovskite absorber by infilling the holes and gaps in the SWNT mesh.

In b) and c) of figure 6.12 the statical distribution of performance parameters and PCE of 145 HiPco and CG200 based devices are shown (precise figures given in table 6.3). This comparison reveals that CG200 devices are systematically performing better than their counterparts containing purified HiPco SWNTs. In figure 6.12, the best steady-state efficiency for a device with CG200 SWNTs is shown. The stabilized power-output for this device was 10.6%, which is 75% of the scanned PCE (shown as inset).

Because of its superior performance, any subsequent experiments were done with P3HT-wrapped CG200 SWNTs rather than with purified HiPco SWNTs.

HTL structure	J_{sc}[mA cm^{-2}]	V_{oc}[V]	FF	PCE[%]	R_s[Ω cm^{-2}]
P3HT/HiPco	20.65	0.85	0.42	7.37	9.9
P3HT/HiPco-PMMA	21.49	1.04	0.63	14.15	3.8
P3HT/CG200-PMMA	22.71	1.02	0.66	15.29	3.0
P3HT/HiPco-PMMA (mean)	17.99	0.96	0.56	9.29	x
P3HT/CG200-PMMA (mean)	18.85	0.99	0.58	10.43	x

Table 6.1: Performance parameters of the best-performing devices shown in figure 6.12 a). As well as the statistical average of a total of 145 individual devices.

6.3 Different protective matrices

PMMA is a convenient material as inert polymer matrix to provide a certain degree of protection for the perovskite absorber because it can be relatively easily dissolved in organic solvents such as toluene or chlorobenzene. Because all the charges are conducted through the SWNTs, the function of PMMA is merely passive. That means that other materials, with similar properties such as forming dense, pin-hole free films and being relatively water-resistant, should be able to replace PMMA, making the SWNT-polymer double-layer structure highly flexible for the choice of materials.

The two materials that were chosen for comparison were *polystyrene* (PS) and *polycarbonate* (PC). Both polymers can be dissolved in chlorobenzene making them both compatible with perovskite. In particular PC requires vigorous ultrasound treatment with a sonication probe in order to be dissolved. The concentration of the polymers was optimized such that the resulting layer would have a thickness of roughly 300 nm (±20 nm). The polymer layers were then deposited - same as PMMA - by spincoating.

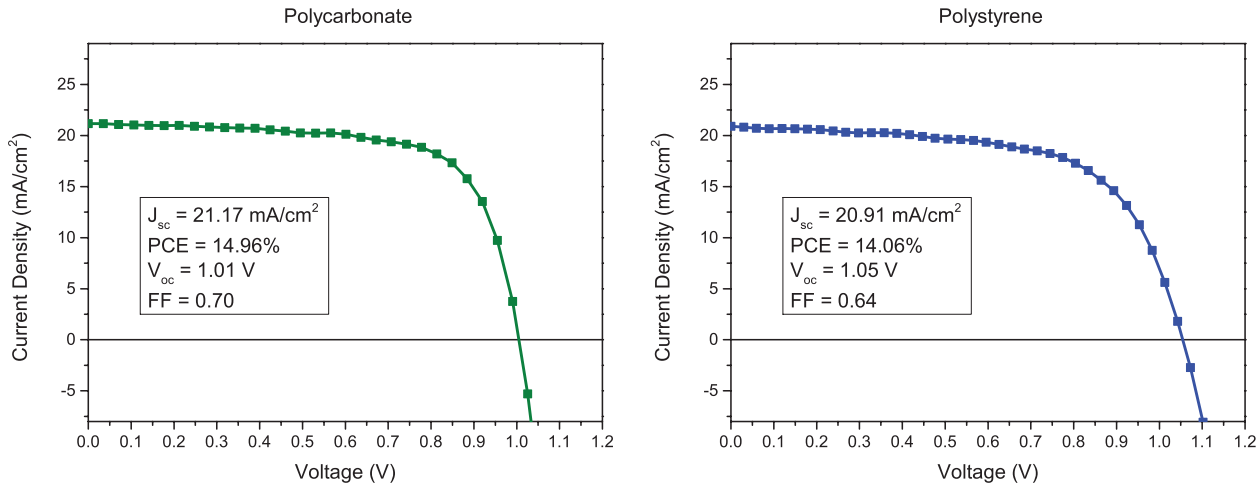

Figure 6.13: Current-voltage characteristics of representative devices with polystyrene and polycarbonate as inert polymer matrix covering P3HT/CG200 SWNTs. At a layer thickness of around 300 nm, both devices yield comparable efficiencies in the 14-15% range.

With respect to stability an important metric to consider for the protective polymer layer is the water vapor transmission rate (WVTR), which is an inherent physical property of a material which describes how upmuch water vapor can permeate through the material over a given time period. The units are usually grams of water per square meter of material per 24 hour at a fixed thickness [256].

HTL structure	J_{sc}[mA cm^{-2}]	V_{oc}[V]	FF	PCE[%]	WVTR [gm^{-2} per 24h]	T_g[°C]
PMMA	22.71	1.02	0.66	15.29	55	105
PC	21.17	1.01	0.70	14.96	115	154
PS	20.91	1.05	0.63	14.06	1220 - 6102	74 - 110

Table 6.2: Performance parameters of the best-performing devices with different polymer matrices as shown in figure 6.13. Beside the device data, there are also important physical properties of the polymers given, namely the water vapor transmission rate (WVTR) and the glass transition temperature (T_g)

In the context of stability tests for solar cells, thermal cycling in the range of 60-80°C is an essential part in order to assess the stability of the devices under elevated temperatures as they would encounter under real-life operating conditions. For polymers to withstand temperatures temperatures in this range, their glass transition temperature T_g - the temperature when a polymer properties change from being hard and glassy to being a soft and rubbery - has to be above that. The values for PMMA, PC and PS are shown in table 6.2. The T_g of PS falls directly into the relevant range, making it therefore not an ideal material. Additionally, its WVTR is one to two orders of magnitude higher than for PMMA and PC. While the WVTR of PC is not as good as for PMMA, it is an interesting material for thermal stability tests as its T_g with 154°C is significantly above the relevant testing range.

6.4 Thermal stressing

Thermal stressing experiments were carried out with P3HT/CG200 SWNTs as conductive elements and PMMA and PC protective top-layers. The thermal stressing was done analogously to the stability testing of the other polymer HTMs in section 7.3. The devices were exposed to 80°C on a hotplate under ambient humidity conditions (RH $\sim 50 - 80\%$) and under ambient light.

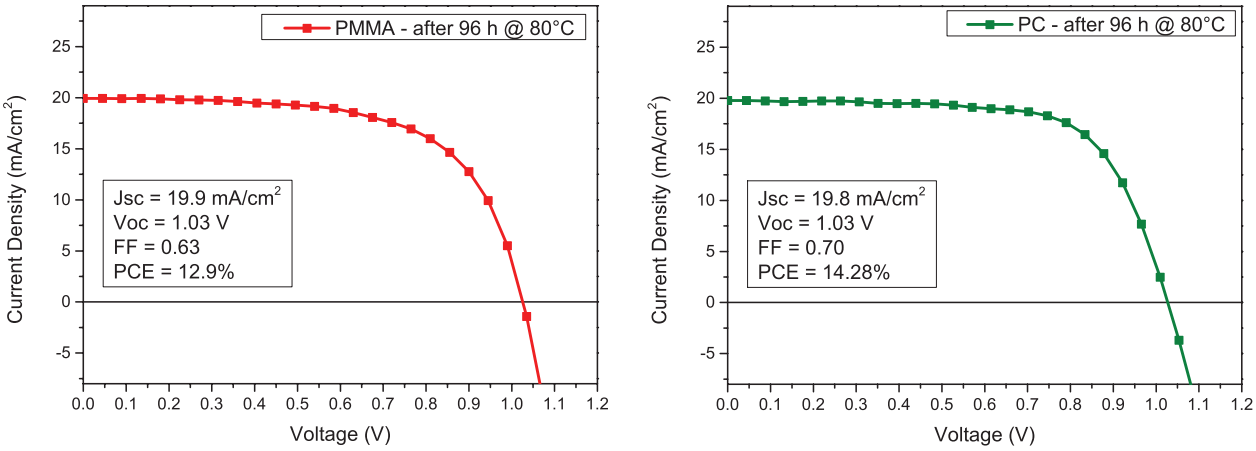

Figure 6.14: Current-voltage characteristics of two devices with PMMA and PC as inert polymer matrix covering P3HT/CG200 SWNTs after 96 h of thermal stressing at 80°C. The device with PC does not appear to be affected by the temperature exposure, in contrast, the low fill factor of the PMMA device indicates structural changes to the PMMA matrix.

In figure 6.14 the JV curves of the two best-performing devices with PMMA and PC after 96 h at 80°C are shown. While the device with PC shows undiminished good performance, the device with PMMA exhibits a relatively low fill factor which indicates structural damage to the device, most plausibly due to changes of the PMMA matrix. Considering the glass transition temperature of PMMA is relatively close to the thermal stressing temperature, it is conceivable that the PMMA has started to change in a way that impacts the fill factor negatively. The glass transition temperature of PC is, however, high enough that it remained unchanged. Both polymers appear, however, to effectively prevent degradation of the perovskite absorber while retaining the charge extraction ability of the SWNTs.

The other hole-transporting materials (spiro-OMeTAD, P3HT and PTAA) did not protect the perovskite absorber sufficiently to remain operational solar cells. Accordingly, devices with these HTMs did not yield any power-output.

6.5 Operation at elevated temperatures

To further illustrate the improved thermal stability of the hole-transporting SWNT-polymer double-layer structure, device operation was tested under elevated temperatures up to 100°C. The compared HTMs included PMMA and PC for the SWNT-composites, and lithium-doped spiro-OMeTAD (Li-spiro-OMeTAD), P3HT and PTAA. The thermal dependence of the device performance was tested with a custom-built sample chamber, which was externally heated. The temperature was controlled with an IR thermometer. Before measuring the photovoltaic performance of the devices, they were held at each temperature point for 20 minutes in order to let them equilibrate. The performance of the devices was measured in the temperature range between 25°C and 100°C. The performance parameters of all devices with the spiro-OMeTAD, the two polymer hole-transporters, PTAA and P3HT, as well as the nanotube-polymer composite structures measured at each temperature point are given in figure 6.15.

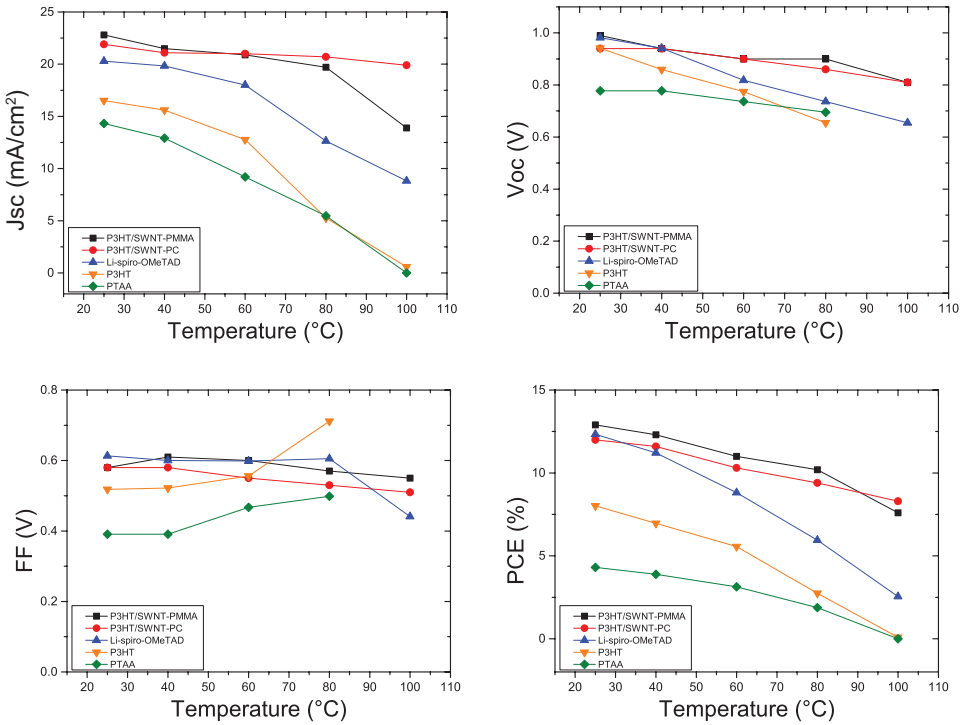

Figure 6.15: Performance parameters of devices under thermal stressing comparing the performance of several different HTLs. PMMA and PC were used as inert polymer matrices covering P3HT/CG200 nanohybrids; the conventional HTMs used in this experiment included spiro-OMeTAD, P3HT and PTAA. The respective JV-scans were taken after 20 minutes of equilibration at each temperature point. The decrease in efficiency is governed mainly by a strongly decreasing photocurrent. The voltage decreases most notably for P3HT. For the two polymers the fill factor tends to increase with temperature. However, at 100°C both polymer-based HTLs were not able to extract any photocurrent.

As can be seen in figure 6.15 with temperature the performance of all HTMs declines, mainly due to decreasing current and voltage. In fact, for the two polymeric hole-transporters, P3HT and PTAA, the fill factor increases significantly with temperature. However, for the last data point at 100°C, these devices did not generate any measurable photocurrent, hence there are no data for voltage and fill factor. In order to directly compare the relative decline in performance with temperature of the different hole-transporters, the efficiencies were normalized to the initial PCE value, shown in figure 6.16.

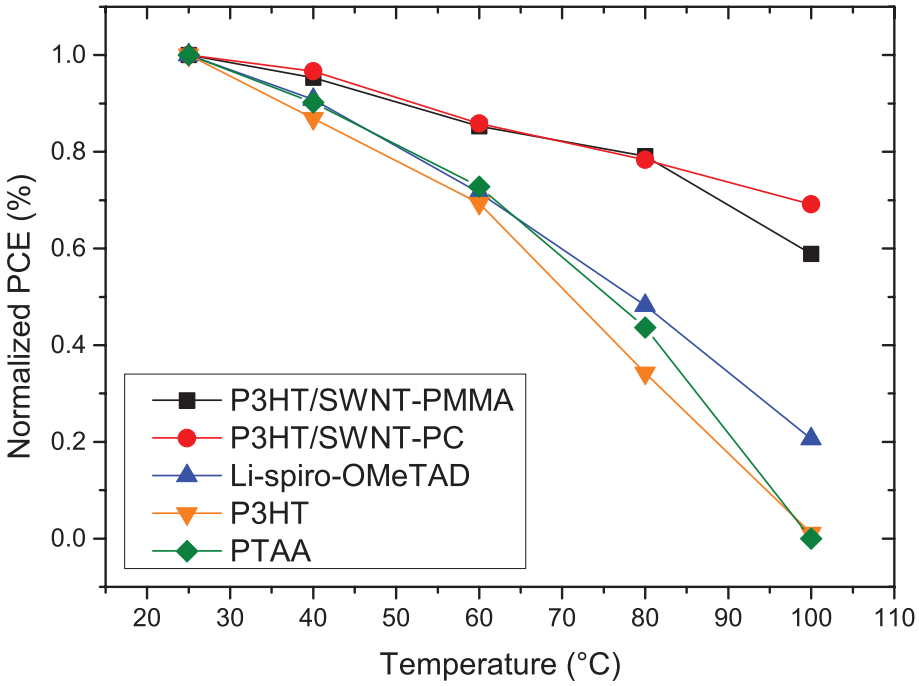

Figure 6.16: Normalized PCE values of devices with all investigated hole-transporters are plotted against temperature. The conventional hole-transporters exhibit a similar decrease in performance. Li-spiro-OMeTAD is the only one of the three that is still operational at 100°C. The performance decrease of the SWNT-based HTLs also shows the same trend. Only the last data point at 100°C, shows a more significant drop in performance for the device with PMMA as top-layer polymer, which makes sense considering that 100°C is approaching the T_g of PMMA.

The normalized PCE values plotted against temperature in figure 6.16 illustrate a trend for the conventional hole-transporting materials as well as for the SWNT-based composites. While devices with both types of HTL decrease in performance, the decrease for the conventional HTMs is much more severe, leading to irreparable physical damage from which none of the devices recovered after having cooled down to room temperature (figure 6.17). It is likely that there are two mechanisms in play that damage the structural integrity of those devices. The water permeability of the HTLs, which has been demonstrated in the previ-

ous experiments, is likely to allow moisture ingress and methylamine egress, thus leading to physical degradation of the perovskite absorber. At the same time, the hole-transporters themselves might undergo structural changes, which could impede charge extraction. The latter mechanism has to be considered since the degradation process of the perovskite absorber results in the loss of the organic methylamonium, the inorganic lead iodide, however, remains and as a semiconductor with a bandgap of 2.55 eV [257], should conceivably still act as a photodiode. However, after thermal stressing, the devices were allowed to cool down to room temperature. They were then tested again. The devices with the conventional hole-transporters do not exhibit any rectifying behavior (figure 6.17).

The drop in performance for both protective polymer matrices in the SWNT-based HTM is significantly less than for the other HTMs. The strikingly similar performance trend with temperature in the range up to 80°C suggests that this decrease in efficiency may occur independent of the material properties of the polymer matrices and could represent the coefficient of the perovskite cells, which from this data being $\sim -0.33\%/°C$, is similar to that of the thin film photovoltaics based on copper indium gallium (di)selenied (CIGS) [258].

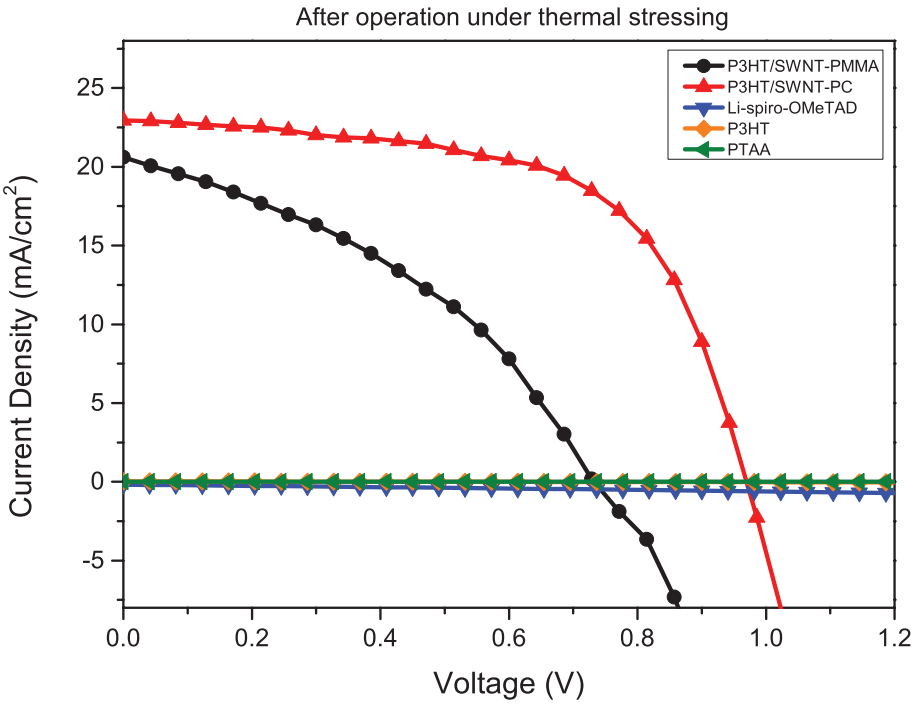

Figure 6.17: Normalized PCE values of devices with all investigated hole-transporters are plotted against temperature. The conventional hole-transporters exhibit a similar decrease in performance. Li-spiro-OMeTAD is the only one of the three that is still operational at 100°C. The performance decrease of the SWNT-based HTLs also shows the same trend. Only the last data point at 100°C, shows a more significant drop in performance for the device with PMMA as top-layer polymer, which makes sense considering that 100°C is approaching the T_g of PMMA.

Protective polymer	J_{sc}[mA cm^{-2}]	V_{oc}[V]	FF	PCE[%]
PMMA	20.61	0.73	0.38	5.71
PC	22.95	0.97	0.60	13.36

Table 6.3: Performance parameters of the devices with hole-transport structures based on the SWNT-polymer composites after the thermal stressing cycle, measured at room temperature. The corresponding JV-curves are shown in figure 6.17. Presumably due to irreversible structural damages to the PMMA matrix, the device does not recover. The device with the PC matrix, however, fully recovers and performs even better than before the thermal stressing cycle.

In the range above 80°C a significant drop in the efficiency of the device with the PMMA matrix can be observed which is likely to be caused by approaching the glass transition temperature of the polymer. Structural damage to the protective matrix may hence be responsible for increased shunting and recombination due to direct contact between the electrode and the perovskite. This consequence can be seen in figure 6.17, which shows the current-voltage characteristics of the thermally stressed devices after having cooled down to room temperature. The JV-curve of the PMMA-based device shows that the device is operational, however, the structural integrity of the polymer top-layer has clearly been compromised resulting in a significant impairment of the shunt resistance which results in a very low fill factor. Additionally, the increase in non-radiative recombination becomes apparent in the reduction of the photovoltage to around 75% of its initial value before thermal stressing.

The comparison with the device in which PC forms the top-layer shows that the most drastic changes in the performance characteristics occur most likely due to chances to the polymer matrix. Since PC is upmuch more thermally stable, the device recovers fully from being exposed to elevated temperatures and operates at an even slightly higher efficiency than before the heating cycle. This is further evidence that the decrease in performance is related to the perovskite absorber rather than to the hole transporter.

6.6 Direct water exposure

The reasoning for the improved stability of the devices containing the protective polymer matrix is that in particular moisture ingress is minimized. As many studies in literature have reported [58, 59, 60], moisture initiates the decomposition of the perovskite. Even at very low molecular concentrations, water can structurally degrade the perovskite [259].

Direct evidence for the water resistance of the SWNT-based composite structures can be demonstrated by exposing device with PC to a running stream of water for 60 s. To show that this is a good demonstration of the ability of the PC-structure to withstand water, a similar device with Li-spiro-OMeTAD was also exposed to water.

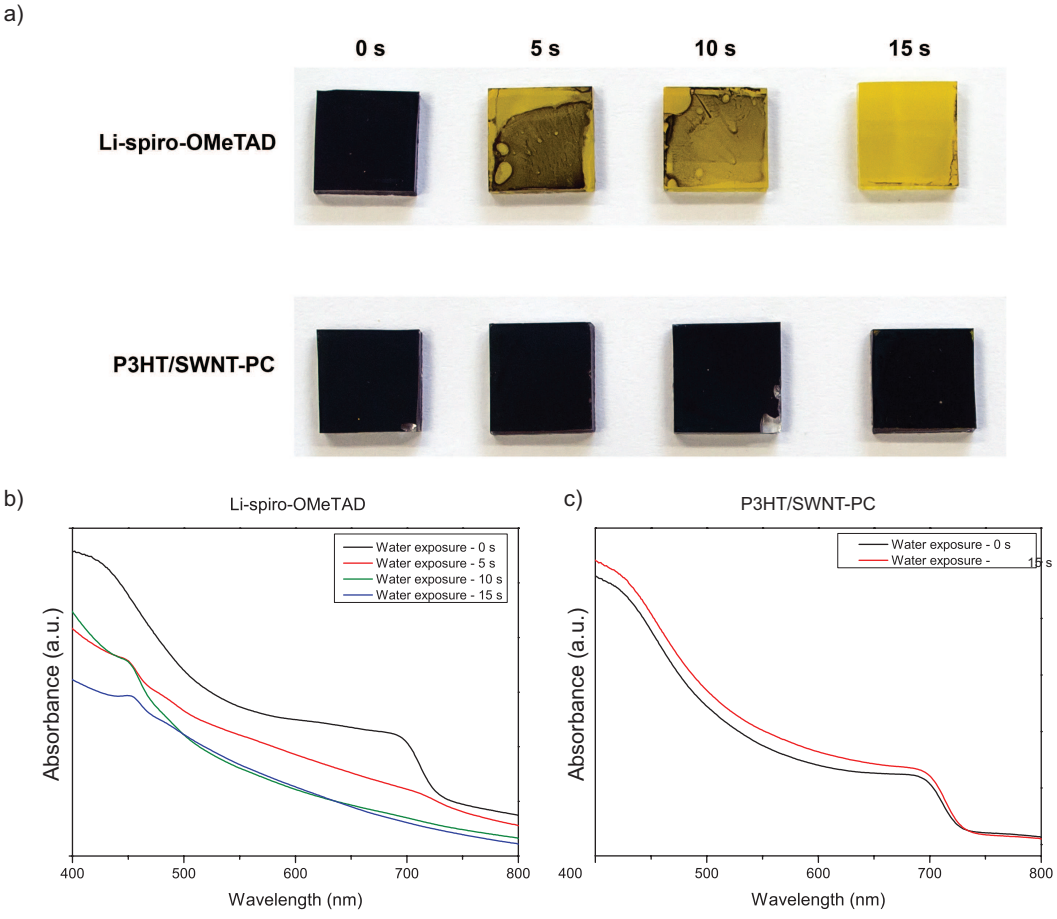

Figure 6.18: Devices with two types of HTLs were directly exposed to a stream of running water: devices with Li-spiro-OMeTAD and with P3HT/SWNT-PC. In a) photos of devices at 5 s intervals under water exposure are shown. Even after 5 s, the device with Li-spiro-OMeTAD shows severe signs of degradation. The devices with PC as protective matrix, in contrast, do not exhibit any visible signs of degradation. In b) and c) the respective absorption spectra are shown. Corresponding to the visible degradation and decoloration of the Li-spiro-OMeTAD devices, the perovskite characteristic absorption step has completely disappeared. In contrast, the devices with the SWNT-polymer still show the perovskite typical absorbance in c)

The devices with Li-spiro-OMeTAD show almost instantly first signs of degradation when they come into contact with water. As evident from merely five seconds of water exposure in figure 6.18 a), the perovskite already shows signs of severe degradation. The severity of the degradation becomes apparent from the absorption spectrum in figure 6.18 b), which shows that the characteristics absorption onset has already almost fully disappeared at this point. This illustrates that water easily penetrates the Li-spiro-OMeTAD layer, and instantly dissolves and removes the organic component of the perovskite. In stark contrast, the devices with the nanotube-polymer composite exhibit no signs of degradation - even when the water exposure is extended up to several minutes. Accordingly, the absorption spectrum still shows the perovskite specific absorbance.

To test whether the structural integrity of the perovskite is preserved together with its optoelectronic properties, a full device SWNT-PC HTL was exposed to the running stream of water (figure 6.19).

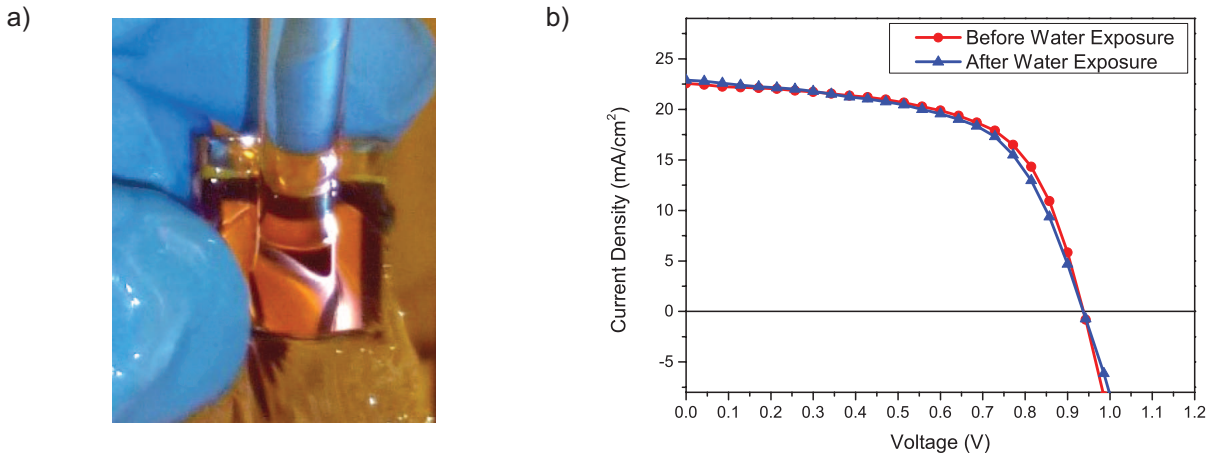

Figure 6.19: a) shows a photo of a device being exposed to a stream of running water. In b) the JV-curves of the device before and after water exposure are shown. They barely show any difference indicating that that SWNT-PC composite protected the perovskite sufficiently so it remains fully functional.

As the films had not shown any signs of degradation of the perovskite, the current-voltage curves, shown in figure 6.19 b), before and after demonstrate that the device operates after water exposure at almost exactly the same efficiency as before. This is a further illustration that the SWNT-PC composite effectively protects the highly water-sensitive perovskite from moisture induced degradation.

6.7 Summary

In summary, this study has addressed the issues of thermal and moisture instability of n-i-p perovskite solar cells. Exposing the perovskite absorber to 80°C in ambient atmosphere, rapid degradation of the perovskite structure was observed. Within 24 h, the material has largely transformed to lead iodide, which was shown by absorption spectroscopy and X-ray diffraction. This degradation is likely induced by moisture since keeping the perovskite at 80°C for 96 h in a completely dry atmosphere does not lead to degradation. However, the parameter that was not fully controlled in this study was the exposure to light. It can therefore not be ruled out that light-induced degradation processes in conjunction with ambient oxygen could have contributed to the observed degradation [260].

Using thermal stressing as a method to investigate the protective properties of a range of conventional hole-transporting materials, it was shown that - in particular when a lithium-based dopant is employed - that neither the small-molecule material spiro-OMeTAD, nor the polymers PTAA or P3HT, can sufficiently prevent moisture ingress and is therefore unable to protect the perovskite from degradation. When moisture ingress is blocked for example by deposition of a water-resilient polymer such as PMMA, the degradation during thermal stressing can be prevented.

Based on the discovery in the previous chapter that, when SWNTs and neat spiro-OMeTAD are employed in a double-layer structure, most of the charges are extracted through the nanotubes, a double-layer structure was used where the top layer is an inert polymer such as PMMA, PC or PS. The polymer-wrapped nanotubes can clearly extract charge sufficiently selective that no additional p-type material is required. The polymer matrix which forms the top-layer encapsulating the SWNT layer serves a merely passive role for charge extraction by preventing the formation of direct shunt paths between the metal cathode and the perovskite, since the SWNT network will not have perfect coverage and direct contact is possible in the holes and gaps of the mesh like SWNT-layer. The second function of the polymer matrix is to prevent moisture ingress.

In thermal stressing experiments, devices with the SWNT-polymer composite do not suffer from degradation of the perovskite absorber while remaining fully operational. While PMMA shows some onset of some structural instability, the performance of the PC-based device remains the same after 96 h. The superior stability of PC compared to PMMA is likely related to the upmuch higher glass transition temperature of PC which is 154°C as

compared to 105°C for PMMA.

Furthermore, devices with three conventional organic HTMs, spiro-OMeTAD, P3HT and PTAA were compared to SWNT-PMMA and SWNT-PC based HTLs, when operated under elevated temperatures of up to 100°C. The performance of the devices with the organic HTMs rapidly declined and resulted in all cases to complete irreparable device failure. In contrast, while the efficiency decreased for the SWNT-based hole-transporting composites as well, the decrease was upmuch slower and can possibly be attributed to thermally induced reversible changes to the perovskite absorber rather than degradation of the perovskite or the hole-transporter. This corroborated by the device with the PC-matrix which fully recovers after the thermal cycle and performs even better than prior to heating. The temperature coefficient for $CH_3NH_3PbI_3$ can therefore be estimated to be approximately $\sim -0.33\%/°C$.

Finally, the water-stability of the composite structures is shown to be good enough to expose devices to a running stream of water without compromising the perovskite absorber and retaining its optoelectronic properties. A device which was directly exposed to the water stream is still fully operational at about the same efficiency as before the water exposure.

Composite structures of sequentially deposited polymer-wrapped SWNTs and an inert polymer matrix can efficiently extract charges and effectively protect the perovskite absorber from moisture-induced degradation throughout the typical operational temperature range.

Chapter 7

Investigating the role of 4-*tert* butylpyridine in perovskite solar cells

7.1 The steady-state performance challenge

In the previous chapters, it was shown that polymer-wrapped SWNTs efficiently and selectively extract charge from the perovskite-SWNT interface. The efficiency of those devices was determined from current-voltage curves which were obtained from voltage sweeps from forward bias to short-circuit. In contrast to most other photovoltaic technologies, when the scan direction of the voltage sweep is changed, now starting at short-circuit and going to forward bias, the current-voltage curve changes as well. This behavior is referred to as "hysteresis" [245, 261]. Since the power-conversion efficiency is the product of the performance parameters which are extracted from the current-voltage characteristics, a change in the curve entails a change in efficiency, thus introducing ambiguity in determining the operational efficiency of devices. Several parameters were shown to affect this hysteretic behavior such as scan direction, pre-biasing, light soaking and the scan rate [245]. The latter had been shown to have the most significant impact, aside from the scan direction, on the magnitude of the hysteresis [261, 262]. Current-voltage sweeps are therefore to be considered an insufficiently unequivocal metric for determining the operational performance because slow transient processes inside the device alter its intrinsic efficiency depending on extrinsic conditions. This ambiguity in determining the power-conversion efficiency of a perovskite solar cell can be avoided by using a steady-state measurement, which lets the system reach its steady state before determining the performance. There are two measurements which have been shown to unambiguously quantify the steady-state performance of a device. The first one allows the system to reach its steady state at each measurement point along the current-

voltage curve [261]. The drawback of this method is that the time-scales of the transient processes are on the order of tens of seconds, meaning that scanning a device at such a slow scan-rate makes this measurement very time-intensive and may allow degradation processes to set in. The second method tracks the photocurrent of a device when it is held at constant bias around its maximum power-point. The value at which the photocurrent does not have a slope any more i.e. when it is stable, is referred to as "stabilized power output" (SPO).

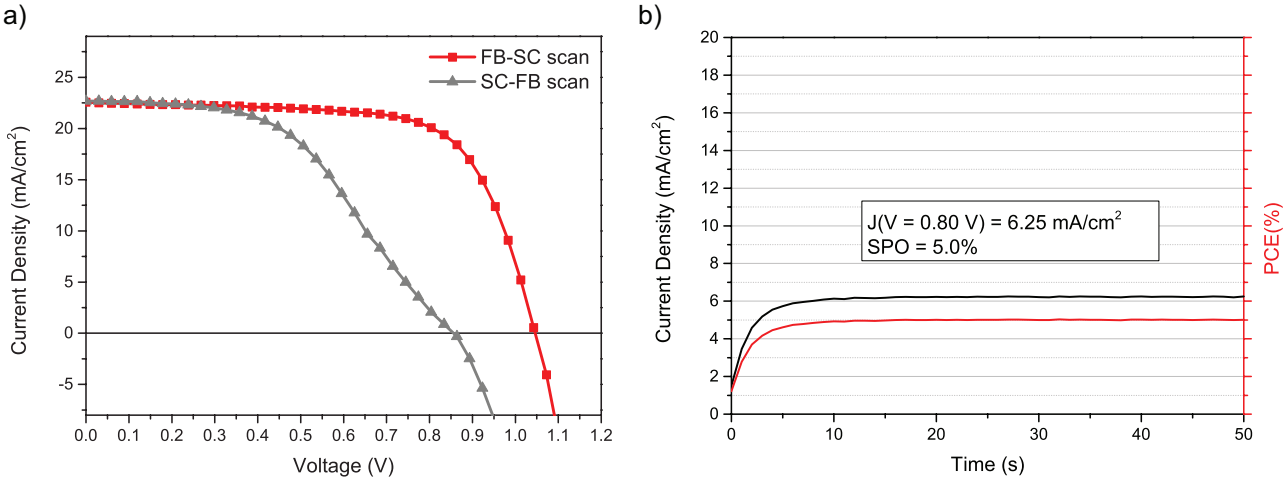

Figure 7.1: a) Illustration of the scan-dependent hysteresis. The current-voltage scans of both directions of a device with the P3HT/CG200-PMMA composite as HTL are shown. In b) the stabilized-power output of the same device is shown, which has been determined by holding the device at the maximum power-point as determined from the FB-SC scan in a).

Scan	J_{sc}[mA cm^{-2}]	V_{oc}[V]	FF	PCE[%]]
FB-SC	22.56	1.05	0.69	16.34
SC-FB	22.68	0.86	0.47	9.17

Table 7.1: Performance parameters of a device with a P3HT/CG200-PMMA composite HTL. The parameters for scans as shown in figure 7.1 a) for both direction are given, showing a significant difference in PCE depending on the scan direction.

In figure 7.1 a) the hysteretic current-voltage behavior of a perovskite device with the P3HT/CG200-PMMA composite HTL is illustrated by the forward-bias to short-circuit scan (FB-SC scan, red) and the short-circuit to forward-bias scan (SC-FB scan, gray). While the FB-SC scan exhibits very good performance parameters (table 7.1), the SC-FB scan in the other direction yields a much lower voltage and a very low fill factor, resulting in a PCE which is merely ~ 0.56 of the initial reverse scan. However, at a scan speed of ~ 0.3 V/s even the SC-FB scan still yields an overestimation of the operational efficiency of the device, as the stabilized power-output (shown in figure 7.1 b)) gives a power-conversion efficiency of merely 5.00%. This means that even the forward scan is distorted by the internal processes of

the perovskite, since the the steady-state efficiency is much lower than the scanned efficiency, in fact compared to the reverse scan, it's merely 31% of the scanned performance. The origin of this discrepancy is only partially related to the inherent hysteresis in the perovskite, which can be demonstrated using a doped spiro-OMeTAD as hole-transporter in a device with the same architecture.

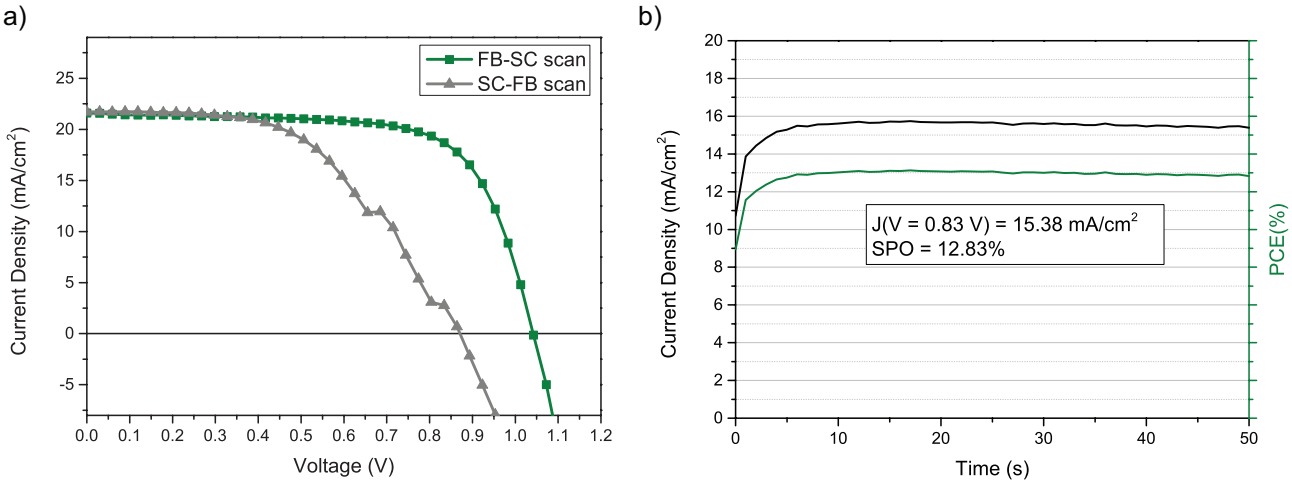

Figure 7.2: a) Comparison with a standard fully doped spiro-OMeTAD device. The current-voltage scans of both directions are shown. In b) the stabilized-power output of the same device is shown, which has been determined by holding the device at the maximum power-point as determined from the FB-SC scan in a).

Scan	J_{sc}[mA cm^{-2}]	V_{oc}[V]	FF	PCE[%]]
FB-SC	21.60	1.04	0.69	15.55
SC-FB	21.70	0.87	0.52	9.82

Table 7.2: Performance parameters of a device with doped spiro-OMeTAD as HTL. The parameters for scans as shown in figure 7.1 a) for both direction are given.

While not evident from the scans in figure 7.3 a), which exhibit a similar hysteresis as the SWNT-PMMA device, it becomes clear from the stabilized power-output in figure 7.3 b) that the steady-state performance of this device is much better than that of the device with the SWNT based HTL. In fact, the SPO of the spiro-OMeTAD device achieves an efficiency of around 12.8%, showing that this device performs under steady-state conditions at around 82% of its scanned efficiency. This is evidence that the discrepancy between scanned efficiency and steady-state performance can to some degree be mitigated by the charge selective contact to the perovskite.

Comparing the two hole-transporter systems it is not obvious why spiro-OMeTAD yields a so much higher stabilized-power output and experiences a much lower discrepancy be-

tween scanned and steady-state performance. Many approaches were investigated to improve the stabilized power-output for the SWNT-based system, however, the best SPO that was achieved at 10.6% (figure 6.12) was still much lower than the one delivered by spiro-OMeTAD.

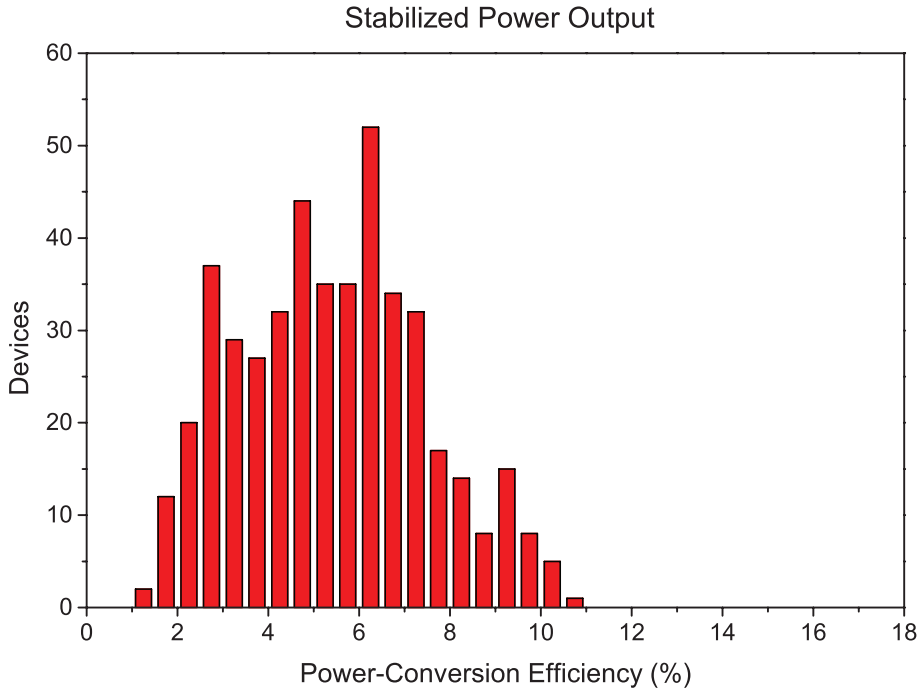

Figure 7.3: Distribution of stabilized power output for 460 devices with the P3HT/CG200-PMMA hole collection layer, with an average of 5.33%.

One interesting aspect of spiro-OMeTAD is the necessity for the additive 4-*tert*-butylpyridine (tBP). It is added alongside Li-TFSI, which is responsible for doping the spiro-OMeTAD layer making the amorphous hole-conductor sufficiently conductive [220]. While tBP is crucial for the film formation of spiro-OMeTAD when it has been doped with Li-TFSI, it is unclear whether it may play any active role in the process of charge extraction.

7.2 4-*tert*-butylpyridine (tBP)

4-*tert*-butylpyridine made its first appearance in a liquid-phase dye-sensitized solar cell (DSSC), where the sensitized TiO_2 electrode was dipped in tBP prior to the dye sensitization. As a result, a substantial efficiency improvement was achieved mainly due to an increase in the open-circuit voltage [263]. The initial explanation was that tBP adsorbs to the TiO_2 surface where it blocks states which are active as intermediates in the heterogeneous charge transfer thus reducing the dark current [263]. In follow-up studies it was shown that the treatment of the TiO_2 electrode with tBP or the addition of tBP to the electrolyte shifts the conduction band edge thus yielding an increased V_{oc} [264, 265, 266]. This negative shift in the energy bands of TiO_2 results in the reduction of available states for electron injection thus delaying the onset of charge recombination [267]. A reduction of the recombination rate results in a longer charge carrier lifetime which in turn results in an increase in open-circuit voltage [268]. Dürr et al. conclude in their study that tBP preferentially adsorbs to defect states on the TiO_2 surface which induce electronic states inside the TiO_2 bandgap and thus are responsible for an increased charge carrier recombination [269]. The adsorption of tBP effectively passivates these recombination centers. As a result, the recombination rate decreases despite a shift of the conduction band toward more negative potentials [269]. In summary, tBP affects the electronic properties of TiO_2 by both shifting its conduction band edge and by passivating recombination centers.

A major evolutionary leap for the dye-sensitized solar cell was achieved by Bach et al. who demonstrated that the liquid electrolyte can be replaced by a solid-state organic hole transport material, namely spiro-OMeTAD [23]. In a follow-up study it was shown that employing tBP in the solid-state configuration also has a beneficial effect on the solar cell performance [270]. In this case, the addition of tBP to spiro-OMeTAD led, as in the liquid-state configuration, to a reduction of the charge recombination rate at the interface [270].

Shortly after, the first incarnations of a perovskite solar cell were published which were both still liquid-state configurations, however, the perovskite absorber dissolved within minutes in the electrolyte [24]. The eventual breakthrough for perovskite solar cells came therefore when the perovskite absorber was employed in a solid-state configuration using spiro-OMeTAD reaching an efficiency of more than 10% (as elaborated in more detail in chapter 2) exceeding anything previously achieved with a solid-state DSSC [25, 50]. Both reports were based on an n-i-p architecture with spiro-OMeTAD as the p-type layer containing Li-

TFSI and tBP, which had become indispensible additives to spiro-OMeTAD for solid-state DSSCs. Since then, the best performing n-i-p devices have all employed at least those two additives in their hole-transporting materials [271, 249]. Nguyen et al. show that instead of doping spiro-OMeTAD with Li-TFSI, it can also be partially pre-oxidized to obtain a high conductivity; however, for good solar cell performance tBP was found to be indispensable [92]. This finding is interesting in the light of tBP being a crucial additive to spiro-OMeTAD when it is doped in order to aid film formation. In the absence of tBP, the film formation suffers from dewetting and poor homogeneity. As a result, the overall device performance suffers (figure 7.4). It has been argued that tBP increases the polarity of the spiro-OMeTAD solution and thus improves its wetting behavior when spincoated [270].

7.3 Effect on hole-transporting materials

The comparison of devices containing lithium-doped spiro-OMeTAD with and without tBP as HTL illustrates why it is difficult to disentangle the effect tBP might have on steady-state device performance from its effect on film formation. The poor film quality of the doped spiro-OMeTAD layer without tBP leads to a significantly lower performance of the devices in their current-voltage scans compared to their counterparts which contain tBP (figure 7.4).

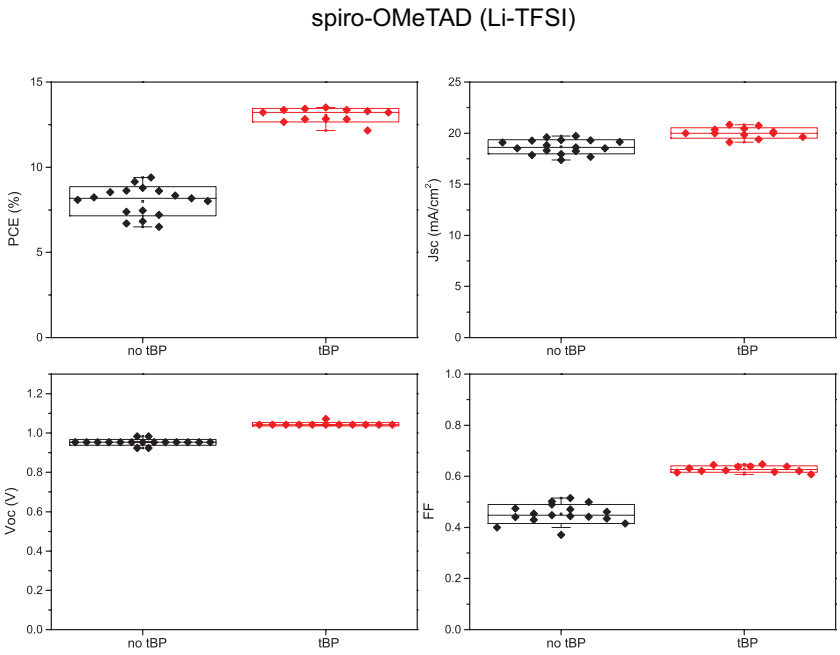

Figure 7.4: Scanned performance parameters of devices with a spiro-OMeTAD hole-transporting layer, with and without tBP

While the difference in the film quality and thus the significantly different scanned efficiencies may obscure any effect tBP may have on the steady-state efficiency (figure 7.5 a)), the fact that the SPO/PCE ratio, which is a metric for the discrepancy between scanned and steady-state efficiency, shows an improvement with the addition of tBP (figure 7.5 b)), indicates that tBP might in fact have an electronic effect.

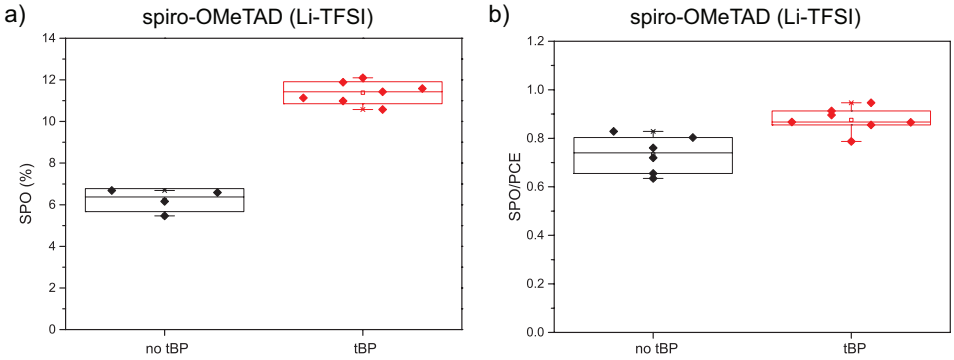

Figure 7.5: Steady-state performance of devices with a spiro-OMeTAD hole-transporting layer, with and without tBP

In the previous chapter, the detrimental effect of Li-TFSI has been demonstrated. Other studies have also pointed out that Li-TFSI could have a deleterious impact on the long-term stability [220, 92, 254]. Therefore, other strategies are pursued to enhance the hole conductivity, such as using protic ionic liquids to intrinsically oxidize spiro-OMeTAD [254] or pre-oxidizing a fraction of hole-transporter before mixing it into the undoped host matrix [92, 233].

One of the advantages of replacing Li-TFSI as a dopant, aside from removing a hygroscopic and destabilizing element from the hole-transporter, is that film formation is not impeded by the dopant. This is therefore a system, with which the effect of tBP can be investigated without introducing ambiguity in the results due to structural effects.

The first such system that was investigated was spiro-OMeTAD(preox). The procedure for the pre-oxidation of spiro-OMeTAD has been described in detail by Nguyen et al.[92]. Of the typical concentration of 96 mg/ml of spiro-OMeTAD 10wt% had been pre-oxidized. The direct comparison of devices with and without tBP shows that the presence of tBP affects the current-voltage characteristics in two ways (figure 7.6). The short-circuit current is slightly reduced whereas the voltage is increased. As a net result, the scanned power-conversion efficiency is slightly better for devices with tBP. A much more significant effect can be observed in the steady-state efficiency (figure 7.7). The stabilized power-output is

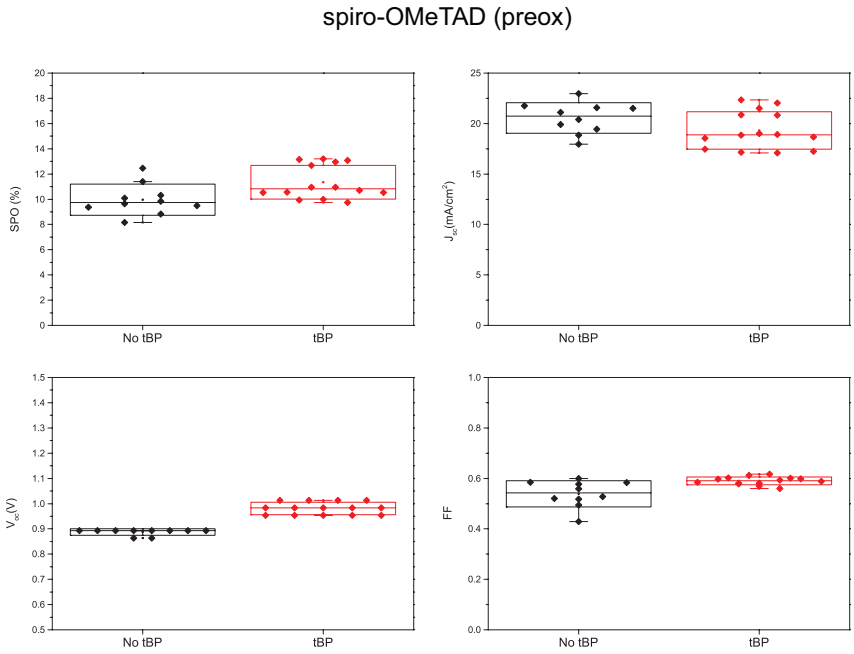

Figure 7.6: Scanned performance parameters of devices with a partially pre-oxidized spiro-OMeTAD hole-transporting layer, with and without tBP

about twice as high for devices with tBP. The ratio of scanned to steady-state performance reflects this improvement (figure 7.7 b)).

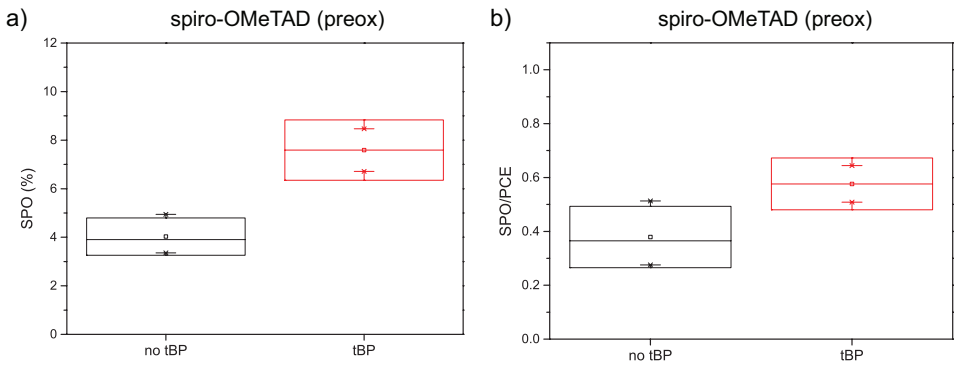

Figure 7.7: Steady-state performance parameters of devices with a partially pre-oxdidized spiro-OMeTAD hole-transporting layer, with and without tBP

In both cases, for the conventionally lithium-doped spiro-OMeTAD and for the pre-oxidized spiro-OMeTAD, the device data indicates that the addition of tBP to the hole-transporter improves the steady-state performance. This improvement manifests both in absolute values and in terms of relative performance under steady-state conditions compared to the transient current-voltage sweeps. It is therefore reasonable to conclude that one of the factors why conventional devices show a dramatically better steady-state performance than the SWNT-PMMA system might be the presence of tBP.

7.4 Effect on the SWNT-PMMA system

A straightforward way to implement tBP into the SWNT-PMMA system would be adding it to the SWNT solution prior to deposition. However, adding tBP to the SWNT solution results in poor film formation of the SWNTs because it leads to clustering. This is most likely due to the comparatively high boiling point of tBP ($T_B \sim 196°C$). The drop-wise spincoating deposition of the SWNT-nanohybrids out of chloroform relies on the rapid evaporation of the solvent on the spinning substrate. Because of the relatively low boiling point of chloroform ($T_B \sim 61°C$) and the rapid spinspeed, this happens within 3 seconds, which is how a sequence of drops can be deposited without removing the previously deposited SWNTs. It is conceivable that tBP delays the solvent evaporation such that the SWNTs can be moved by every subsequent droplet leading to cluster formation on the substrate.

Instead, a small amount of tBP, equivalent to what is commonly contained in spiro-OMeTAD, was added to the PMMA matrix. Compared to devices without tBP, a significant improvement of the steady-state performance could be noted. A concentration dependence study of the tBP in the PMMA matrix yielded the following results.

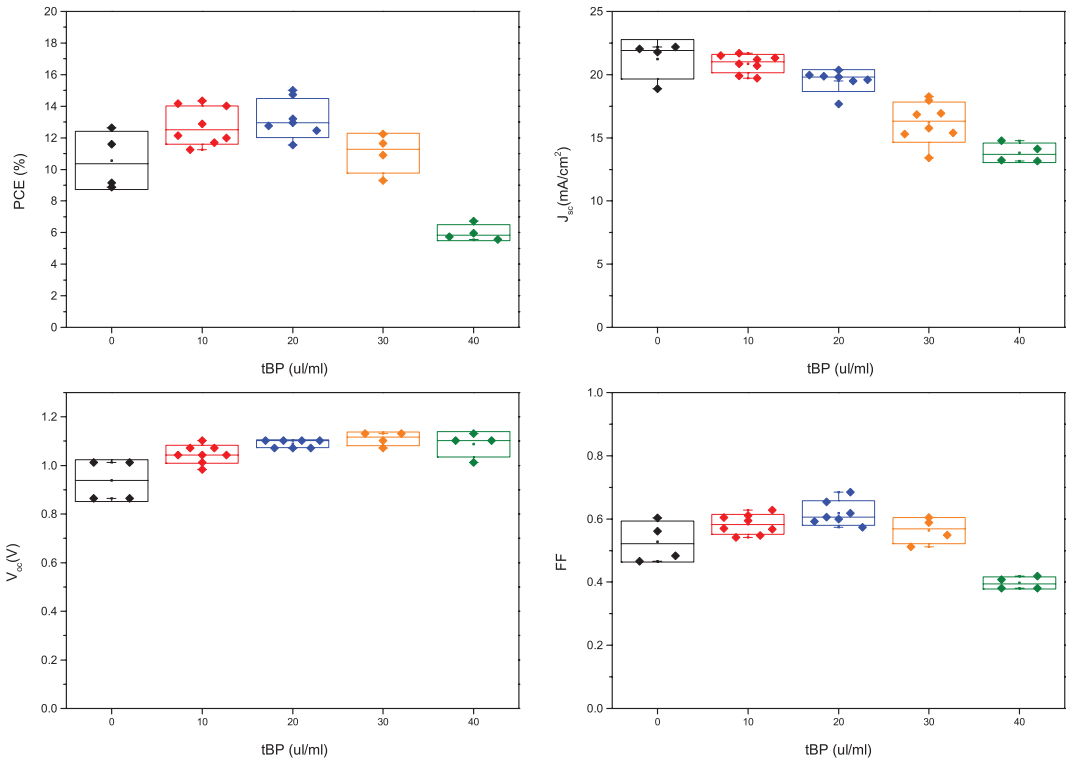

Figure 7.8: Scanned performance parameters of a concentration dependence study of tBP added to the PMMA matrix encapsulating P3HT-wrapped CG200 SWNTs.

The scanned performance parameters in figure 7.8 already indicate a significant trend. Similar to what could be observed in spiro-OMeTAD, the addition of tBP leads to an incremental increase in voltage with the concentration of tBP. Simultaneously, the current is inversely correlated with the tBP concentration. For the fill factor, there appears to be an optimum concentration which therefore coincides with the optimum concentration for the efficiency at 20 µl/ml, at which the product of current and voltage is maximized.

The effect on the steady-state efficiency in figure 7.9 a) is even more striking. The trend follows the one observed for the scanned efficiency, reaching the highest values for a tBP concentration of 20 µl/ml. At this concentration, the stabilized power-output yields values above 13%, more importantly even, the ratio of steady-state performance to the scanned efficiency reaches values in the range of 80-90%.

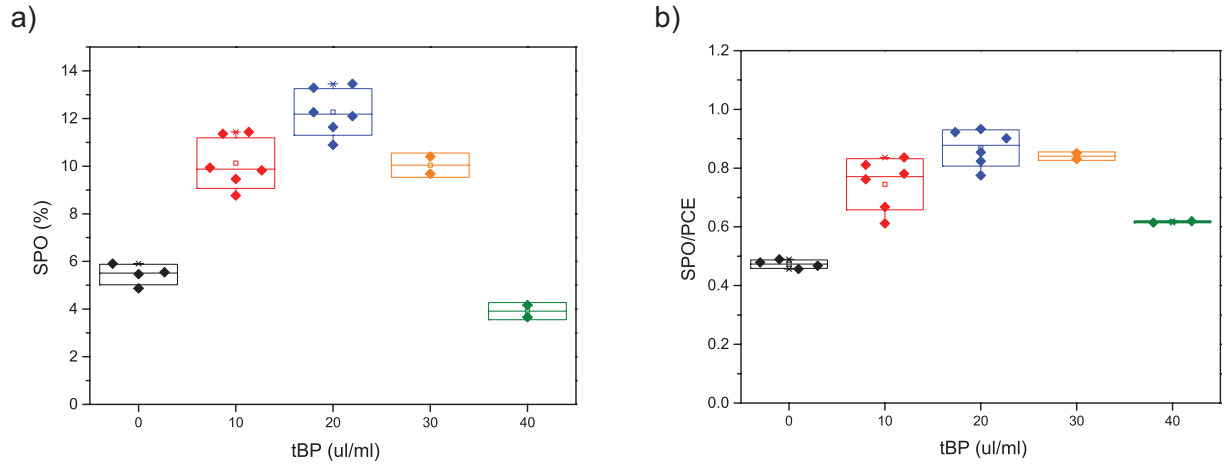

Figure 7.9: Steady-state performance of SWNT-based devices with increasing tBP concentration in the range from 0 to 40 µl/ml added to the PMMA solution. a) shows the stabilized power output, which peaks at a concentration of 20 µ/l/ml and reaches values above 13%. b) shows the corresponding ratios of steady-state efficiency to scanned efficiency from figure 7.8. At the optimal concentration, at the highest steady-state efficiency these values are in the range of 80-90%.

In figures 7.10 a) and b) the device statistics for scanned and steady-state performance for 146 devices are shown, in which devices without any tBP and devices with 20 µl/ml of tBP in the PMMA solution are compared. The current-voltage sweeps show that the addition of tBP improves most notably the fill factor and the voltage, and leads to a slight decrease in current. The net effect of adding tBP to PMMA is an overall improvement in scanned power-conversion efficiency.

The even more important improvement, however, can be observed in the values of the stabilized power-output (shown in figure 7.10 b)), which shifts from a distribution around

5% to above 12%. Adding tBP to the polymer matrix which encapsulates the layer of the charge transporting SWNTs has strong enhancing effects on both scanned and steady-state performance of the devices.

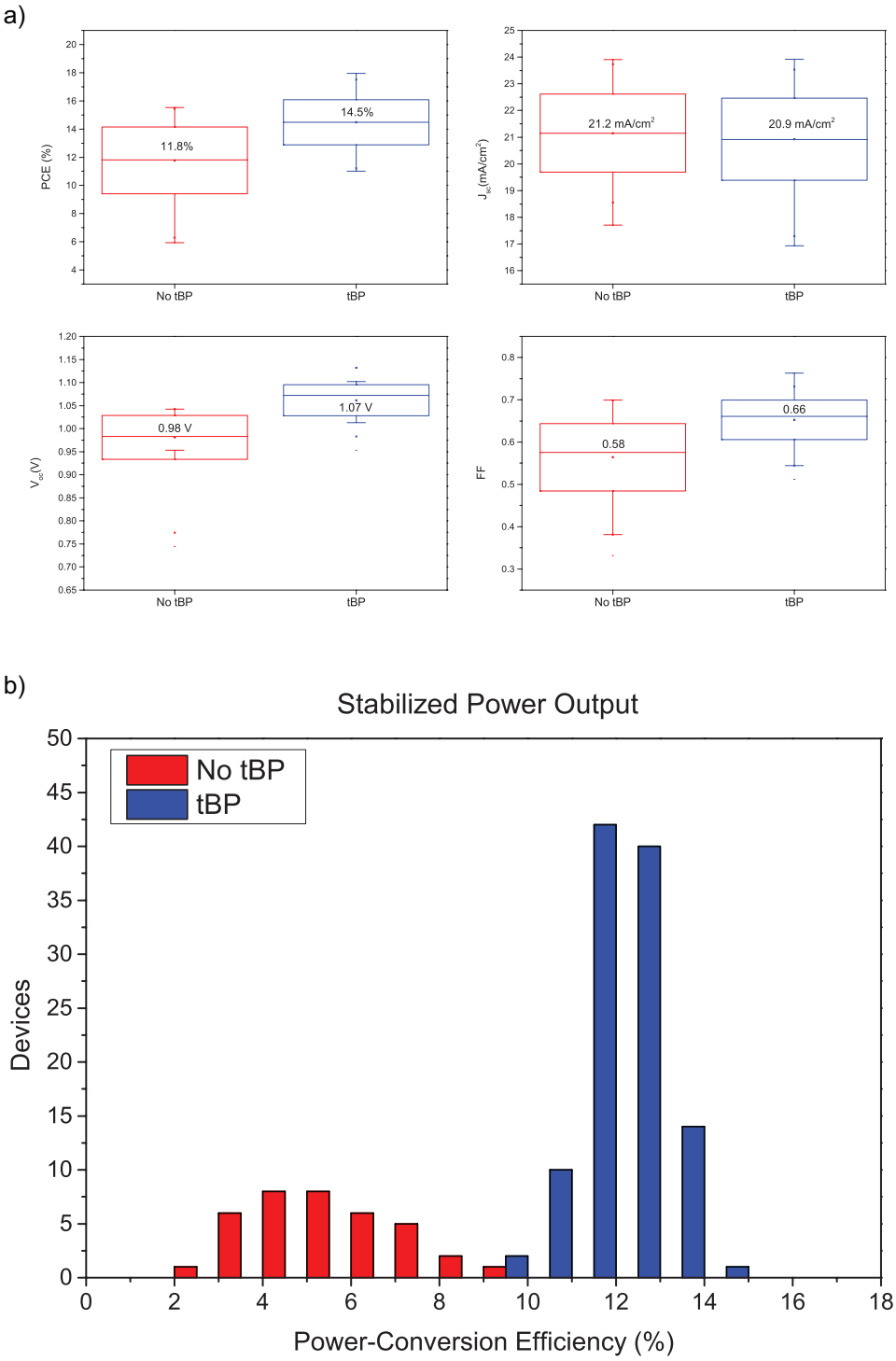

Figure 7.10: Steady-state performance of SWNT-based devices with increasing tBP concentration added to the PMMA matrix

Further device optimization at a fixed tBP concentration, yielded the highest achieved stabilized power-output to date for the P3HT/CG200-PMMA system, at scanned PCE of 17.3% and a an SPO of 14.2% which corresponds to a ratio of steady-state to scanned efficiency of 82%.

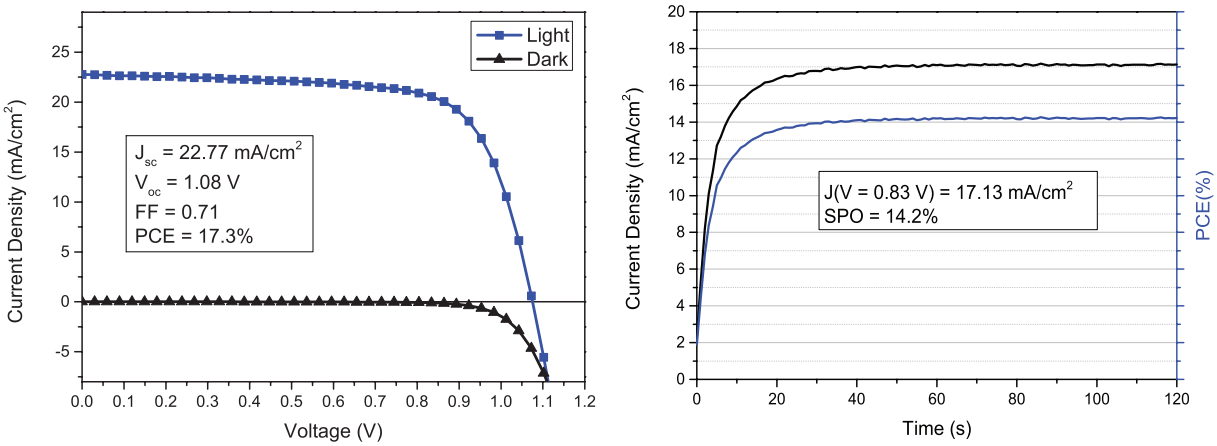

Figure 7.11: Steady-state performance of SWNT-based devices with increasing tBP concentration added to the PMMA matrix

The improvements in both scanned and steady-state efficiency are apparent, however, the interface which tBP acts upon and which mechanism underlies this interaction is not. In the following, this question is elucidated by deconstructing a device layer by layer in order to identify the mechanism of how tBP improves the device performance so significantly.

7.5 Identifying the tBP interaction interface

The mechanism by which tBP can affect the steady-state performance of a perovskite solar cell is not obvious and has not previously been described in literature. Before being able to address questions regarding the mechanism, all possible interactions of tBP with components of the solar cell need to be inspected. One can identify four layers and interfaces with which tBP can plausibly interact. Interactions could occur between tBP and the PMMA layer, the SWNT layer, the perovskite absorber and the electron-selective TiO_2 layer.

7.5.1 tBP and the inert polymer matrix

The PMMA polymer matrix capping the device does not directly contribute to the charge extraction. Its main role is to minimize shunting paths caused by direct contact between the perovskite absorber and the metal electrode. It thus affects charge extraction only passively. To makes sure that the beneficial effect of tBP is not based on a PMMA specific interaction, this question was investigated. Changes in the PMMA layer thickness can be excluded, as the change in thickness due to the addition of tBP at a concentration of around 2vol% is minimal, which does not result in an observable change in performance. In fact, the correlation between deliberate, controlled thickness variation and its effect on performance has been studied in detail. In order to induce significant changes to the performance the PMMA matrix has to change by 20-25% thickness which corresponds to comparable changes in PMMA concentration. Furthermore, the PMMA layer thickness correlates in a very specific way with the device performance, as first shown in the previous chapter (figure 6.9): the optimum thickness is around 300 nm, thicker layers increase series resistance and reduce the charge collection efficiency, whereas thinner layers lead to increased recombination and reduced shunt resistance. This characteristic behavior becomes apparent by direct comparison of current-voltage characteristics of devices with different PMMA thicknesses (figure 7.12).

PMMA[nm]	J_{sc}[mA cm^{-2}]	V_{oc}[V]	FF	PCE[%]	R_s[Ω cm^{-2}]
100	22.96	0.97	0.62	13.81	2.31
200	22.39	1.04	0.71	16.53	2.32
300	22.36	1.11	0.72	17.75	2.41
400	20.83	1.04	0.55	11.91	10.60

Table 7.3: Performance parameters of the best-performing device with PMMA layer thicknesses ranging from 100 to 400 nm.

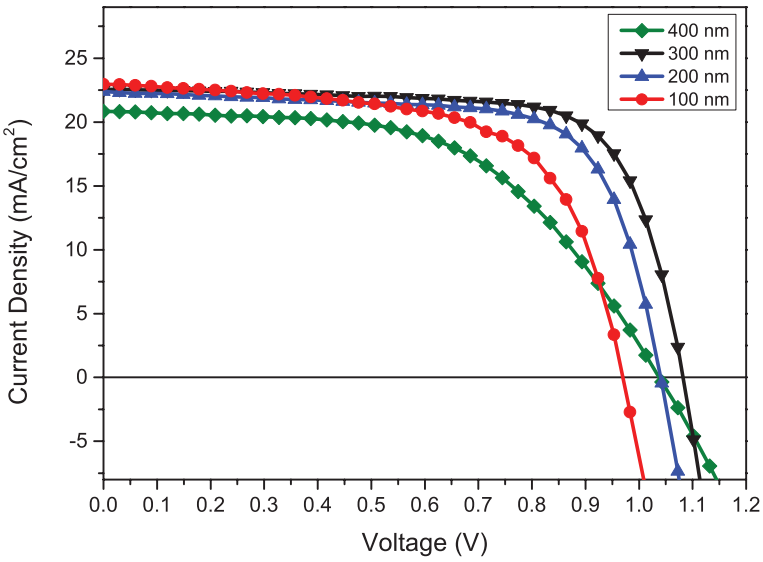

Figure 7.12: Current-voltage characteristics of devices with different PMMA layer thicknesses, demonstrating how the performance correlates with the layer thickness.

As has been shown in the previous chapter, polycarbonate (PC) is a good and viable alternative to PMMA as inert polymer matrix. If tBP were to have an effect which is structure-specific to PMMA, it should not necessarily have the same effect on PC. However, when added at the same concentration to PC, the same effect can be observed in figures 7.13 and 7.14.

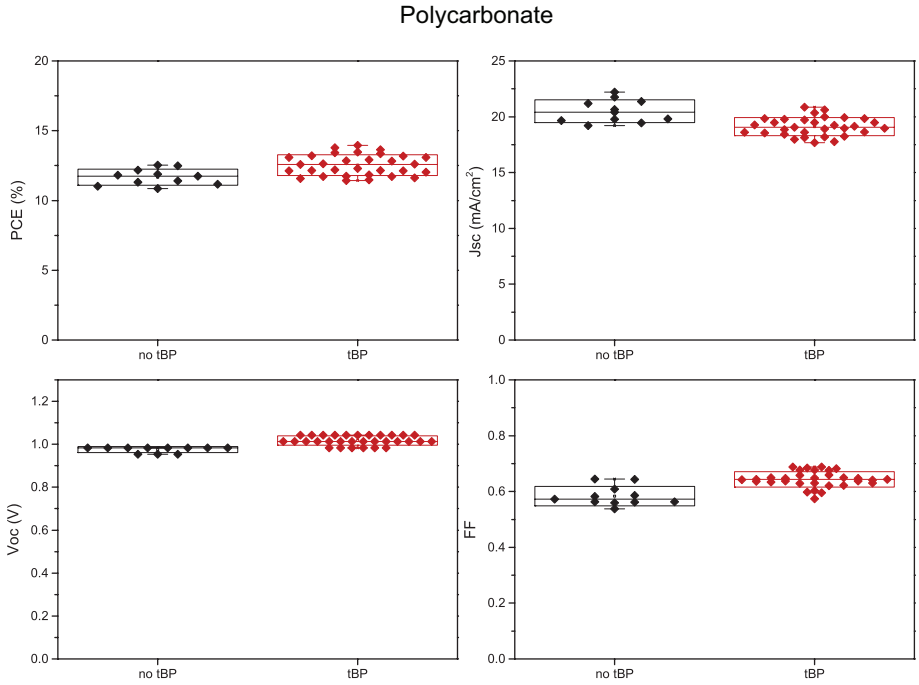

Figure 7.13: Scanned performance parameters of devices with PC as inert matrix on top of P3HT/CG200 SWNTs, with and without tBP.

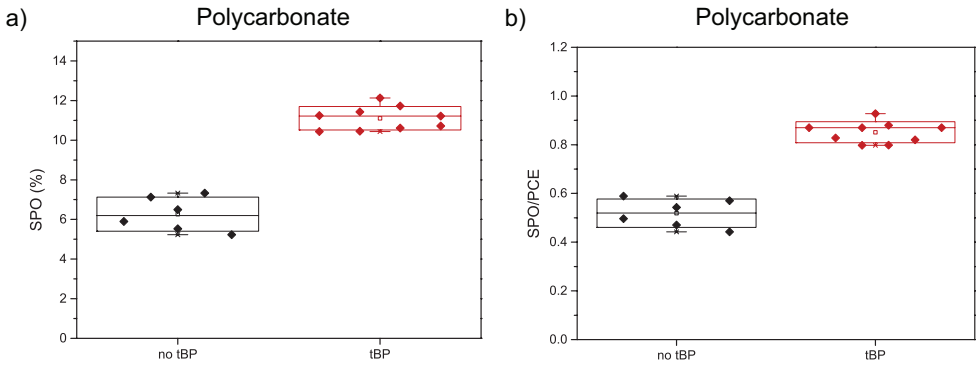

Figure 7.14: Steady-state performance parameters of devices with PC as inert matrix on top of P3HT/CG200 SWNTs, with and without tBP.

The effect of adding tBP to the PC matrix is exactly the same as for PMMA, both for the scanned performance parameters as well as for the steady-state performance. A relatively low stabilized power-output of less than 8% increased to up to 12%, shifting the ratio of steady-state to scanned performance into the range of 80-90%. These results are evidence that the beneficial effect of tBP occurs independent of the independent polymer matrix.

As mentioned above, tBP could not directly mixed into the SWNT solution, because it negatively impacts the film formation of the SWNTs. Additionally, at a comparable concentration to the one added to PMMA, the individual droplets start to degrade the perovskite. It is therefore difficult to assess whether tBP has a direct effect on the SWNT layer. Comparing the changes in performance between the SWNT-based system with the ones observed for spiro-OMeTAD in section 7.3, the trends in performance are practically identical which indicates that the beneficial effect of tBP occurs independent of the hole-transporter system. Instead, this would suggest that tBP interacts with another interface in the device.

7.5.2 tBP and TiO_2

The prime candidate for positive interactions with tBP is actually the TiO_2 layer. All the observed effects are consistent with previous observations in DSSCs, where the interaction between tBP and TiO_2 surface states results in an increase in voltage and decrease in current [270, 272].

However, the TiO_2 surface is deeply buried in this solar cell structure. The perovskite absorber is coated onto a 400 nm thick alumina scaffold, which it fully infiltrates. Addition-

ally, it forms a thick capping layer, which gives the active layer a total thickness of around 1000 nm (figure 7.15). Being an additive to the hole-transporting layer, tBP would need to penetrate the entire active layer in order to reach the TiO_2 compact layer.

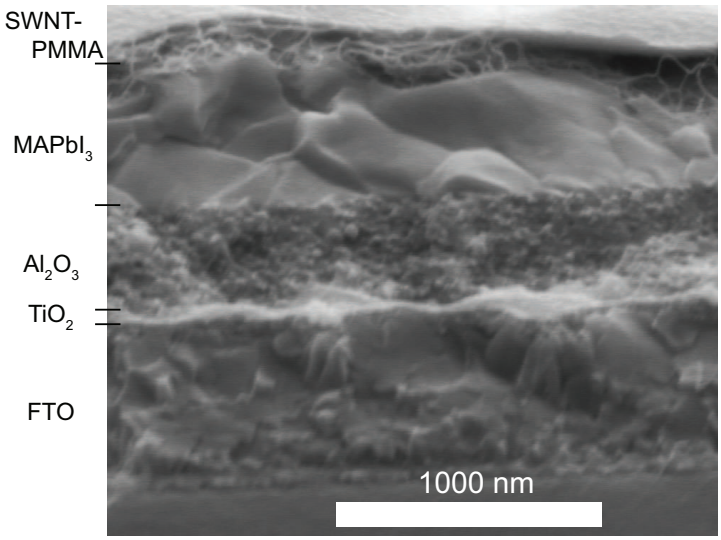

Figure 7.15: Cross section of a typical n-i-p device, with FTO as transparent anode at the bottom, a thin TiO_2 compact layer blocks holes and selectively collects electrons, 400 nm of mesoporous Al_2O_3 form a scaffold which is coated with $MAPbI_3$ perovskite, on top of the scaffold sit another 600 nm of perovskite capping layer, which is contacted by the SWNT-PMMA composite, which contains the tBP.

Nevertheless, if the observed effect stems from the interaction between the electron-selective TiO_2 compact layer and tBP, treating it directly with tBP should presumably yield a similar positive impact on the steady-state efficiency. To test this, the compact layer was pre-modified by dipping it in undiluted tBP, similarly to what has been reported for dye-sensitized solar cells in the past [263, 270].

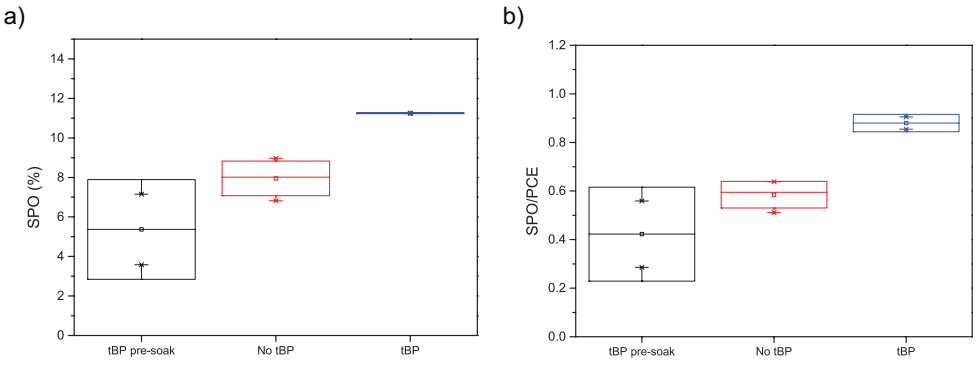

Figure 7.16: Steady-state performance of devices whose TiO_2 had been pre-modified with tBP, compared to devices without any tBP and devices with tBP added to the PMMA layer.

However, the results of the premodification of the TiO_2 compact layer with tBP are shown in figure 7.16 a) and b), and they show that the premodification does not improve the steady-state performance, neither in absolute values (figure 7.16 a)) nor relative to the scanned performance (figure 7.16 b)).

It is possible, however, that the subsequent deposition of the active layer could remove the adsorbed tBP from the TiO_2 surface. Assuming that the observed changes in device performance rely crucially on the interaction between tBP and TiO_2, the absence of the latter should result in tBP being ineffective. Based on this reasoning, devices without the TiO_2 compact layer were fabricated.

Consistent with previous results [262, 273], after being held at forward bias, the devices without the charge-selective n-type TiO_2 layer still exhibit the rectifying current-voltage behavior of a working solar cell, although with significantly reduced shunt resistance. Under steady-state conditions, however, the performance drops very rapidly to a very low PCE. In contrast, it can still be observed that the addition of tBP to the PMMA layer has an effect on the scanned and, in particular, on the stabilized performance despite the absence of TiO_2. In addition, its effect is analogous to what can be observed in full devices, which contain the charge-selective n-type contact. In terms of scanned efficiency, voltage and fill factor increase while the photocurrent decreases. The most visible effect is, once again, the much higher stabilized power-output which increases more than six-fold to around 6.5%.

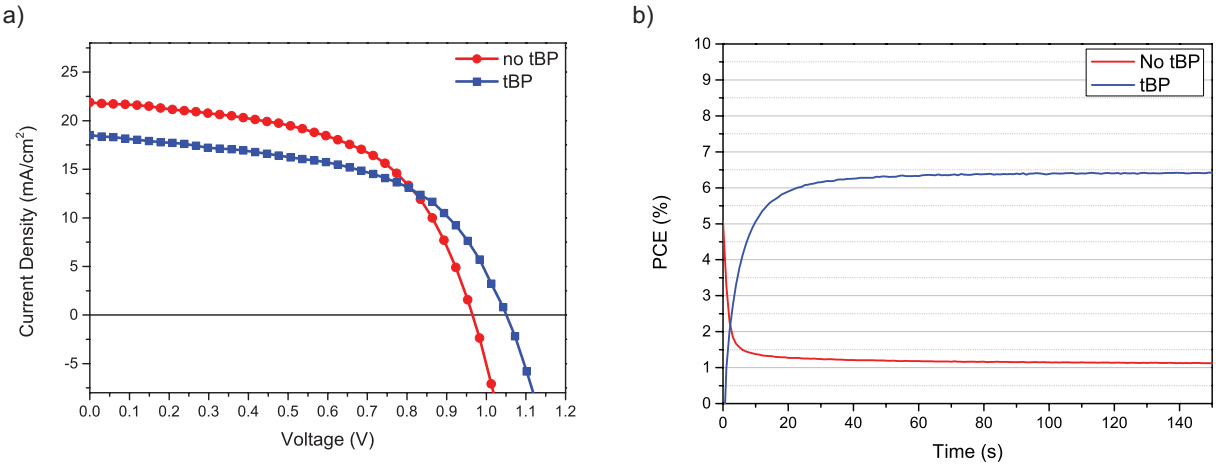

Figure 7.17: a) shows the scanned performance of a ETL-free device with and without tBP. The changes in the current-voltage charateristics are analogous to devices with an electron-selective TiO_2 compact layer. b) shows the corresponding stabilized power-output for the two devices, which reveals a much better performance by the device containing tBP.

This finding suggests that the beneficial effect of tBP on the steady-state performance is not the result of its specific interaction with TiO_2. The only remaining interface is therefore the one between the perovskite and the HTL. By ruling out interactions at the other interfaces, it appears that tBP affects the charge collection efficiency at this interface, especially under steady-state conditions. Considering the observation that the effect of tBP occurs independent of the hole-transporting material, this leads to the conclusion that tBP interacts specifically with the surface of the perovskite. The following experiments were therefore designed with the aim to elucidate in what way tBP could interact with the perovskite surface such that it improves the steady-state performance.

7.6 Probing the mechanism

The mechanism which could underlie a reduction in the disparity between the transient scans and the steady-state performance of perovskite solar cells, will inevitably be connected to the root cause of this disparity i.e. the origin of the hysteresis. The time scales of the observed transient processes suggest that the movement of ionic species are the cause of a change in the charge extraction efficiency [262, 273, 274, 275]. Direct observations of moving ions have been shown by Huang et al.[276, 277]. A numerical drift-diffusion model by van Reenen et al. suggests that moving ions would produce the experimental results previously described by Tress et al. only in the presence of traps [278]. This result confirms previous findings of trap passivation reducing hysteretic behavior [274, 279, 280].

In order to assess the impact of tBP on charge extraction independent of the effectiveness of the commonly used charge-selective contacts, quasi-symmetric devices were fabricated without those selective contacts, in which the perovskite absorber is directly sandwiched between FTO and gold. In order for the perovskite absorber to be similar in its structure to the one used in devices, it was also coated onto an alumina scaffold. The latter has been shown to directly affect the Fermi level of perovskite, effectively n-doping it, making these devices not fully symmetric [281]. The effect of tBP was investigated by spincoating tBP in chlorobenzene - at the same concentration as was used in PMMA - onto the perovskite prior to evaporating the gold electrode. The devices were both forward and reverse biased for 10 seconds before taking the current-voltage characteristics under one sun illumination and in the dark.

The current-voltage curves of the two devices are shown in figure 7.18. The tBP-treated device, in contrast to the untreated device, shows a much more pronounced rectifying behavior after being forward biased. The difference is most pronounced in the dark. In the absence of charge-selective layers, the untreated device behaves like an ohmic resistor with practically no rectification. The tBP-treated device, however, still shows typical diode behavior. This fundamental change in the current-voltage characteristics of the device in the absence of photogenerated charges cannot be explained by the mere passivation of trap states. Even without charge selective layers, after forward biasing, there remains a driving force for charges to be extracted at their respective electrodes.

To gain further insight into the nature of this driving force, Kelvin probe measurements were performed on a bare perovskite sample and a sample that had been treated with a

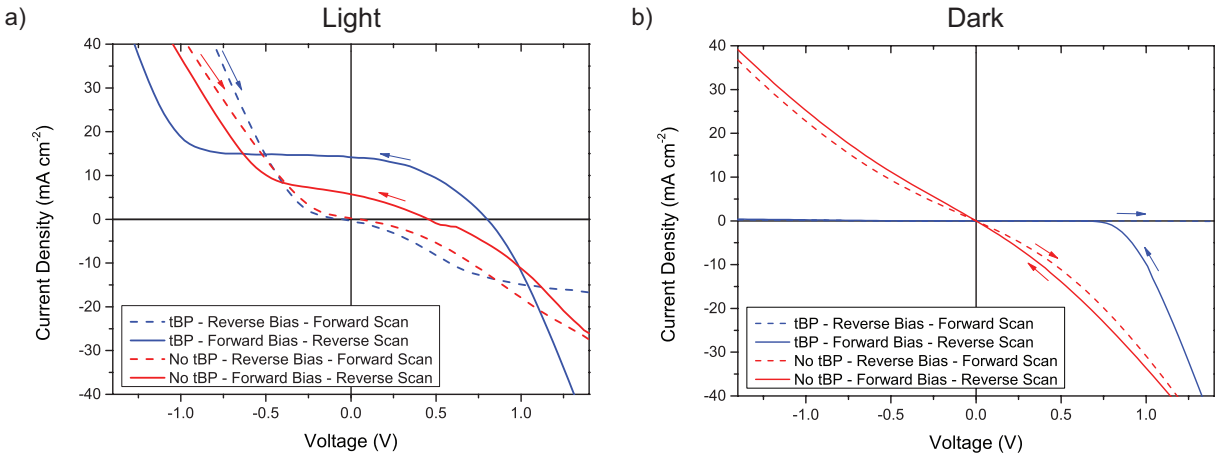

Figure 7.18: Comparison of tBP-treated and untreated perovskite devices without charge selective contacts. a) shows the current-voltage characteristics for both devices under light when positively biased and when negatively biased. b) shows the current-voltage scans of the same two devices under the same conditions, revealing rectifying behavior for the device with tBP-treatment whereas the device without tBP behaves like a resistor.

dilute tBP solution at the same concentration as is present in PMMA. In this measurement the workfunction of the perovskite was measured using a Kelvin probe. Measuring the workfunction of the surface before and after tBP-treatment reveals a significant shift of the workfunction from 4.32 eV to 4.93 eV (figure 7.19). This shift would imply that the bands are bent upward in this region, suggesting improved charge extraction for holes rather than for electrons (figure A.2).

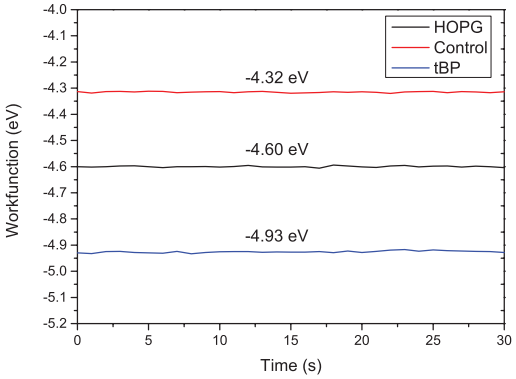

Figure 7.19: Workfunctions determined by Kelvin Probe measurements of a perovskite film before and after treated with tBP in chlorobenzene. To control for solvent washing effects, neat chlorobenzene was spincoated on the control film. As reference highly-oriented pyrolytic graphite (HOPG) is used, with a known workfunction of $\phi_{\mathrm{HOPG}} = 4.60$eV. The workfunction values for the untreated and the tBP treated film can be determined relative to that of HOPG. For the untreated perovskite film a workfunction $\phi_{\mathrm{control}} = 4.32$ eV is measured. The tBP treatment leads to a significant shift to $\phi_{\mathrm{tBP}} = 4.93$. This change in workfunction towards larger values indicates an effective "p-doping" of this interface, and holes dominating the charge carrier distribution in this region.

A plausible interaction which causes this band bending would be an acid-base reaction between tBP and the perovskite. tBP is polar and can be considered as a moderately strong base. It is therefore conceivable that it would deprotonate methylammonium at the interface creating a localized negative ionic charge. These immobile, negatively charged ions at the interface would attract mobile holes to compensate for the negative charge in order to maintain the charge neutrality of the crystal. The increase in positive charge carriers in this region would effectively p-dope the perovskite at this interface, resulting in a slight upwards band bending which in turn can facilitate hole extraction, and impede electron transfer (illustrated schematically in Figure 7.19). This possible mechanism would be consistent with both our poling measurements, which show rectification in the absence of charge-selective contacts (Figure 7.18), and the Kelvin probe measurements, which show a shift in work function of the perovskite surface towards larger values. The mechanism proposed would additionally be consistent with the observation that the photocurrent decreases with increasing tBP concentration (Figure 7.9), as this can be explained by the presence of an increasingly strong ionic charge-barrier impairing the charge extraction at this interface.

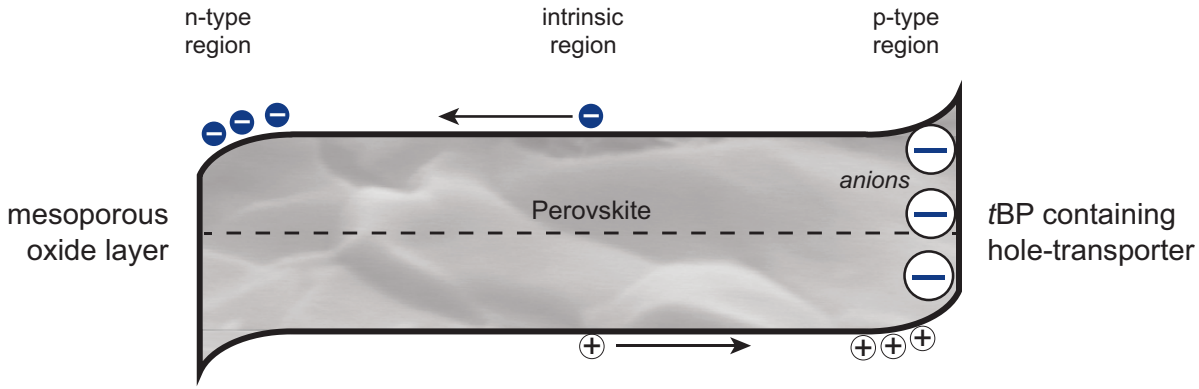

Figure 7.20: Schematic illustration of the tBP-perovskite interaction resulting in a bending of the perovskite bands. In previous publications it has been shown that a metal oxide effectively n-dopes the perovskite absorber (on the lefthand side) [281]. Complementarily, the interaction of tBP with the perovskite appears to result in effective p-doping on the righthand side. The posited mechanism is based on an interaction of tBP with methylammonium at the interface, which creates negative ionic charge. These immobile charges are compensated by mobile positively charged holes in order to preserve the charge neutrality of the crystal. The accumulation of holes at this interface results in effective p-doping and consequential upwards bending of the bands in this region. This effect is evidenced by the shift in the work-function from 4.32 eV to 4.93 eV. This configuration would make this interface more charge selective by preventing the transfer of photogenerated electrons whilst facilitating the transfer of holes. The enhanced charge separation would explain the improvement in open-circuit voltage and, in particular, in steady-state efficiency.

7.7 Summary

In summary, this study shows that the role of tBP as an additive to the hole-transporting material, independent of the material itself, affects the steady-state charge-collection efficiency of a perovskite solar cell by making the interface between the hole transporter and the perovskite intrinsically more selective for holes. This demonstrates that the charge-selective interfaces play a crucial role for efficient steady-state charge extraction.

In the initial findings it was observed that tBP has a highly beneficial effect on the steady-state performance of spiro-OMeTAD, but even more strikingly, of the previously discussed SWNT-PMMA structure. In order to elucidate the governing mechanism for this observation, each layer of a typical device was evaluated with regards to its interaction with tBP and the resulting effect on device performance.

Starting with the encapsulating PMMA matrix, which contains the tBP, it was shown that the effect can also be observed with different inert polymers as top layer, leading to the conclusion that tBP does not specifically interact with PMMA.

In the next step, the interaction with TiO_2 was investigated. Since the effect is still observable even in the absence of TiO_2, is evidence that the mechanism of improved performance due to tBP cannot be based on a specific interaction between tBP and TiO_2.

Poling experiments of quasi-symmetric devices, which do no contain any charge selective layer, show that tBP must directly interact with the perovskite making the side of the perovskite which had been treated with tBP more charge selective for holes thus creating an asymmetry in the device, which will make it exhibit rectifying behavior characteristic of a diode. The latter result in combination with previous findings, which exclude each other layer as origin for the previously noted effect of tBP on the device performance, indicates that tBP directly interacts with the perovskite. An acid-base reaction is proposed as mechanism which could be responsible for this effect.

This finding is important for the development of new hole-transporting materials in general, which must be shown to efficiently extract charge under steady-state conditions rather than merely in transient scans. The effect of tBP has to be taken into consideration when comparing the new materials to the established standard materials of the field such as spiro-OMeTAD, in particular, when it contains both Li-TFSI and tBP.

Chapter 8

Conclusion and Outlook

8.1 Key findings

In this thesis, the application of single-walled carbon nanotubes (SWNTs) wrapped in a conjugated polymer as charge-transporting layer for perovskite solar cells was investigated. In three development phases, a highly efficient hole-transporting layer was developed which contains polymer-wrapped SWNTs as conducting element and an inert polymer matrix to stabilize the perovskite absorber by preventing moisture ingress.

In the first development phase, the functionalized SWNTs were examined with respect to their charge selectiveness and charge transport properties by employing them as additive to spiro-OMeTAD in place of the commonly used lithium dopant. The crucial development was the finding that the SWNTs can be used most effectively when they are deposited as a separate layer instead of being dispersed in the solution of the hole transporter. Devices with such a sequentially deposited double-layer structure were shown to yield efficiencies on par with those of control devices containing the lithium salt. Transient decay measurements revealed that the charge extraction time increased by around one order of magnitude in the presence of SWNTs, which would explain the significant increase in efficiency compared to devices with pristine spiro-OMeTAD. Trying to further elucidate the mechanism of charge extraction of the double-layer structure, photoinduced absorption measurements were carried out. The results of those measurements indicate that a large fraction of photogenerated hole transfer from the perovskite absorber to the SWNTs rather than to the spiro-OMeTAD.

In the second development phase, the finding of photogenerated holes being injected from the perovskite into the SWNTs was explored further. By replacing the dedicated hole-transporter spiro-OMeTAD with an inert polymer poly(methylmethacrylate) (PMMA)

and maintaining device operation, it was demonstrated that the SWNTs can act as hole-transporters in their own right. Interestingly, it was found that metallic SWNTs do not have a detrimental effect on the device performance, despite potentially providing recombination pathways. In fact, a distribution of SWNTs with a slightly higher metallic to semiconducing SWNT ratio was found to perform slightly better.

In this composite structure the SWNTs are embedded in a 300 nm thick PMMA matrix. This can be exploited as a functional encapsulation layer, which can inhibit the ingress of moisture and thus can prevent the degradation of the perovskite absorber. This was demonstrated by thermal stressing experiments, in which perovskite solar cells were exposed to 80°C in ambient humidity conditions. The double-layer composed of SWNTs and PMMA was shown to be vastly superior compared to standard hole-transporting materials including spiro-OMeTAD, P3HT and PTAA. The enhanced resilience against degradation was further demonstrated by operating devices at increased temperatures of up to 100°C. While other hole-transporting materials could not sustain solar cell operation at higher temperatures, composite structures of SWNTs embedded in PMMA and polycarbonate (PC) were shown to be capable of operating even at 100°C. In particular, the thermally more stable polycarbonate showed no signs of structural damage to the device after the heating cycle.

The fundamental issue of hysteresis was addressed in the third development phase. The issue arises, probably due to moving ionic species in the perovskite and manifests itself in a dependence of the current-voltage scan on the scanning conditions which include the scan direction, scan speed, pre-bias, and light-soaking. The lack of unambiguity of the current-voltage scans for determining the power-conversion efficiency of perovskite solar cells, prompted the use of stabilized power-output (SPO) as a steady-state performance metric, which would avoid ambiguous efficiency caused by transient processes. The SPO of the SWNT-PMMA devices, however, tended to be only a fraction of the initial current-voltage scans, yielding around 40-50% of the scanned efficiency. This as significantly lower compared to the doped spiro-OMeTAD hole-transporter.

A rigorous comparison of the SWNT-based hole-transporting layer with the doped spiro-OMeTAD hole-transporter gave rise to the idea that the additive 4-*tert*-butylpyridine (tBP) could be responsible for the better steady-state performance. This suspicion was subsequently confirmed by mixing tBP into the PMMA matrix thus improving the steady-state performance of devices with the SWNT-PMMA composite structure.

In order to elucidate the mechanism by which tBP improves the steady-state performance, its possible interaction with all relevant interfaces was investigated. This elimination process revealed that tBP most likely interacts directly with the perovskite. The interaction is posited to be an acid-base reaction of tBP with the perovskite making the interface intrinsically more p-type, resulting in band bending which favors hole over electron transfer thus improving the selective charge extraction under steady-state conditions.

8.2 Outlook

The work presented in this thesis provides a lot of scope for further exploration. This work has demonstrated that P3HT-wrapped SWNTs embedded in an inert polymer matrix makes an excellent hole-transporting layer for the prototypical methylammonium lead iodide perovskite. This perovskite, however, is particularly vulnerable to degradation due to the volatility of the methylammonium cation. As stability is the key development necessary for commercialisation of perovskite solar cells, increasing effort will be focused on developing more intrinsically stable perovskite absorbers. The most promising material is currently the mixed A-site cation, mixed halide perovskite, $FA_xCs_{1-x}Pb(I_yBr_{1-y})_3$ [66, 282]. To perform under harsh real-world condition this perovskite requires a resilient hole-transporter such as the SWNT-polymer composite. The use of the SWNT based composite on this perovskite absorber would therefore merit investigating.

The encapsulating polymer PMMA has a range of advantages such as being highly economical and easy to process. However, it's not necessarily the most resilient considering that its glass transition temperature is with 105°C relatively close to the operating regime of a solar cell and with a water vapor transmission rate of 55.2 g m^{-2} is only in the medium-range of water resistant plastics [256]. For more stringent and intensive stability tests it would seem advisable to explore even more impermeable materials such as poly(vinyl chloride) (PVC) or poly(tetrafluoroethylene) (PTFE) with WVTR of 15.0 g m^{-2} and 4.0 g m^{-2}, respectively.

Another aspect that is worth exploring further is the impact of the electronic property of the SWNTs on the charge extraction. Surprisingly, the presence of metallic species does not have a detrimental effect on the performance, even though they ostensibly constitute an additional recombination path. Yet, no such increase in recombination was observed. The polymer wrapping could plausibly hamper electron transfer from the perovskite to the SWNTs and thus prevent charge-carrier recombination. It would certainly be of great

interest to explore the transfer kinetics of mixed distributions of SWNTs and of different wrapping polymers. To date the two studies by Schulz and Ihly which have closely examined the perovskite-SWNT interface with respect to the energy level alignment and the resulting charge carrier transfer kinetics have focused on purified semiconducting SWNTs wrapped in a polyfluorene derivative [231, 232]. Similar studies with mixed distributions and P3HT as wrapping polymer could give insights into possible limitations and avenues for tailoring the hole-transporting layer more precisely to the perovskite absorber.

Another aspect that make the composite charge-transport layer of SWNTs and PMMA very attractive with respect to industrial scaling, is the fact that it is significant less costly than most other hole-transporter systems. This can be attributed in large part to the comparatively small amounts of SWNTs necessary for good conduction. As an example, using the cheapest commercially available spiro-OMeTAD (Sigma-Aldrich, 257.00 £/g) would amount to $\sim$ 1580 £/m^2, in contrast, the P3HT-wrapped SWNTs (CG200, SWeNT, 880 £/g) would cost merely $\sim$ 152.00 £/m^2, being ten times cheaper than spiro-OMeTAD.

The work of this thesis has exclusively focused on the n-i-p architecture of the perovskite solar cell, in which SWNTs as hole-transporter can be deposited onto the perovskite absorber. Having shown that SWNTs form an efficient p-type contact should encourage further exploration of the use of SWNTs in p-i-n architectures [230]. That SWNT films have enormous potential to be employed as transparent electrode has been demonstrated in the past [140]. In particular, the mechanical flexibility of SWNTs compared to other electrode materials such as ITO, which are comparatively brittle, could been an enormous advantage for developing perovskite solar cells on flexible substrates [52, 101, 283]. This could be in fact one of the most promising avenues for a wide-spread industrial scale application of perovskite solar cells, because this can largely eliminate the costs of the relatively expensive glass based substrates and, above all, of the prohibitively costly installation, which can amount to almost half the cost of a photovoltaic system [284].

Perovskite based photovoltaic solar cells have the potential to revolutionize the energy market by reducing the cost of solar power to a point where it can outcompete fossil fuels. To achieve that goal the devices need to be both highly efficient and highly stable and resilient. The pioneering work presented in this thesis shows that single-walled carbon nanotube have the potential to contribute towards the development of such an efficient and stable perovskite solar cell. This could be an important step towards bringing perovskite devices into the real world, where it could have an enormous contribution towards the generation of green energy.

Appendix A

Poster presentations

This appendix includes posters relating to the work described in this thesis that have been presented at international conferences

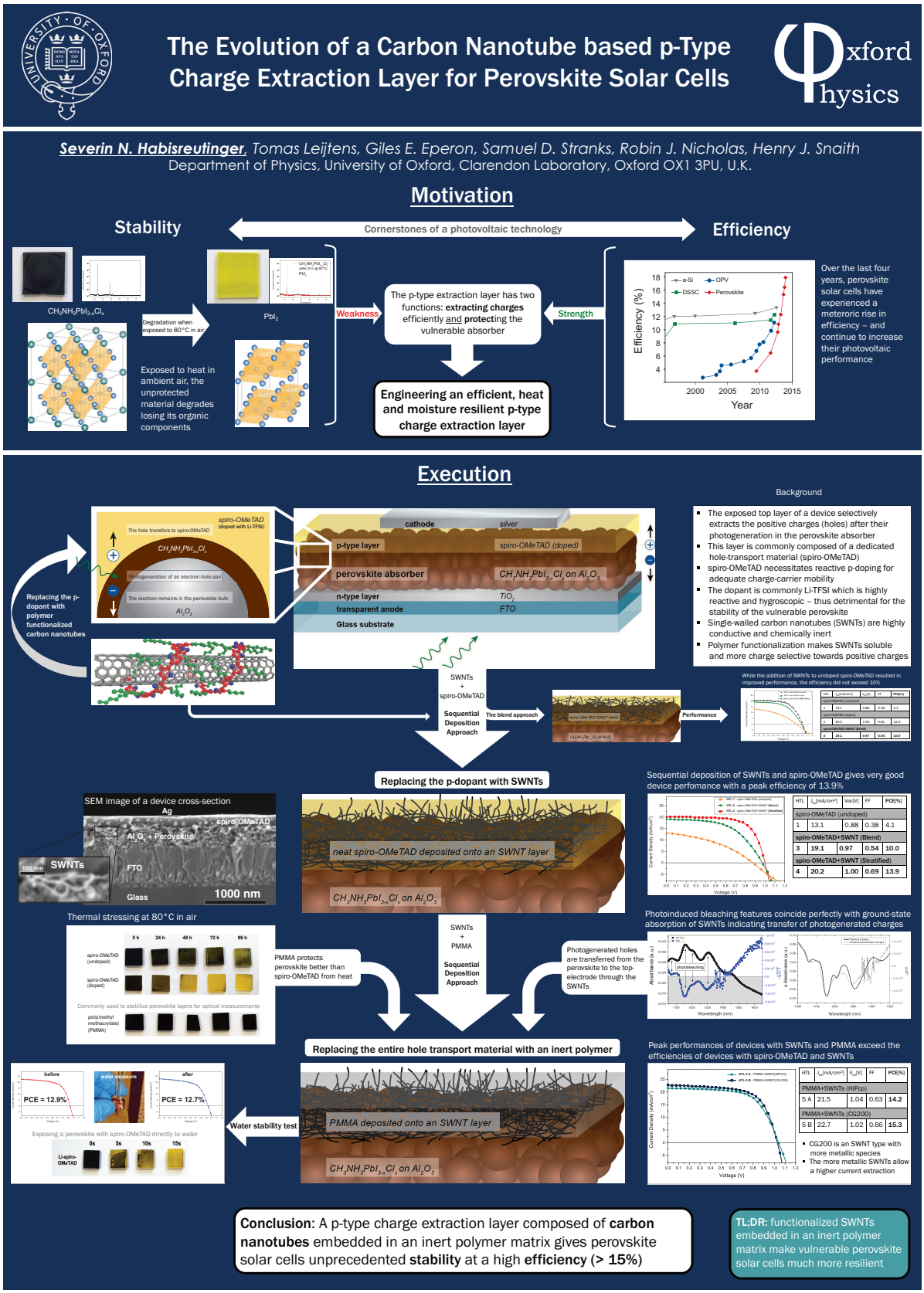

Figure A.1: Poster based on work described in chapters 5 and 6. Presented at the international conference for Solution processed Semiconductor Solar Cells (SSC14), 2014, Oxford, United Kingdom.

Interfacial vulnerabilities of perovskite solar cells

Oxford Physics

Severin N. Habisreutinger, Tomas Leijtens, Robin J. Nicholas, Henry J. Snaith
Department of Physics, University of Oxford, Clarendon Laboratory, Oxford OX1 3PU, U.K.

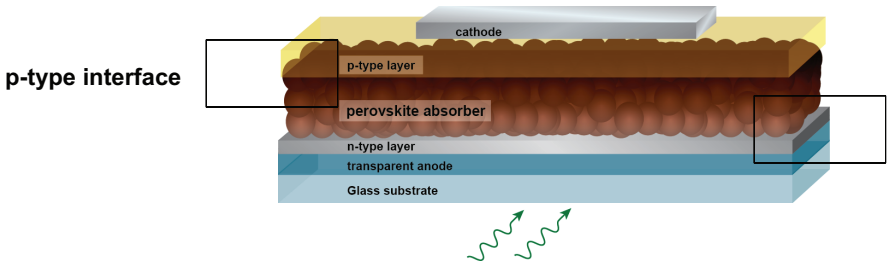

p-type interface

Perovskite degradation due to moisture

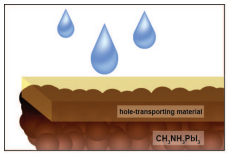

- Organic-inorganic metal halide perovskites such as methylammonium lead iodide are prone to rapid degradation in the presence of moisture
- Cause for this degradation is mainly the hygroscopic nature of the organic cation
- This leads to rapid hydrolization and degradation of the material in the presence of water

$CH_3NH_3PbI_3 \Leftrightarrow PbI_2 + CH_3NH_3I$

Thermal stressing of various hole transporters in ambient air

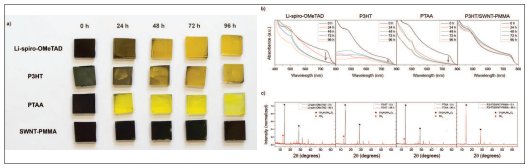

Common organic hole-transporters are poor moisture barriers at 80 °C, being unable to prevent rapid perovskite degradation

n-type interface

Trap mediated recombination losses in TiO_2

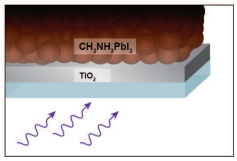

- TiO_2 commonly used as electron selective compact layer or sensitizer scaffold
- Thermal annealing of TiO_2 commonly generates O_2 surface vacancies which can be filled by adsorbed ambient O_2
- Upon UV irradiation generated holes lead to desorption of adsorbed O_2 species
- O_2 vacancy sites are associated with electron trapping sites ~1eV below the conduction band edge

Generation of recombination sites on TiO_2(110) due to oxygen desorption

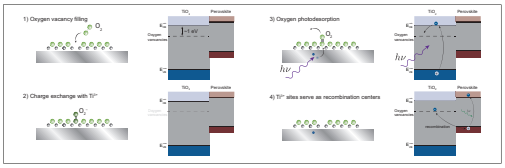

UV Irradiation can generate of recombination sites by initiating the photodesorption of adsorbed oxygen species thus creating recombination centers

Hole-transporter composite structure of carbon nanotubes and an inert polymer matrix

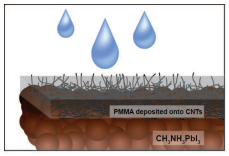

- A two-layered composite of functionalized single-walled carbon nanotubes and poly(methyl methacrylate) (PMMA) is capable of preventing moisture ingress
- Even direct exposure to running water is possible without a significant decrease in performance
- The PMMA layer can also block ambient oxygen
- Tests with respect to stable performance were all done using the CNT-PMMA composite

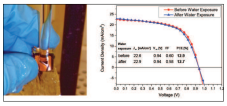

Performance of the champion device employing the CNT-PMMA structure

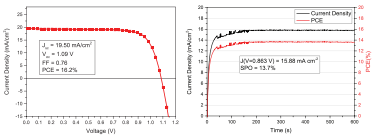

- Discrepancy between scanned and stabilized performance due to hysteretic current-voltage characteristics
- Underlining the importance of the stabilized power output as a reliable performance metric

UV-induced performance decrease of mp-TiO_2 devices due to absence of ambient oxygen

Comparing a mesoporous TiO_2 with an Al_2O_3 scaffold

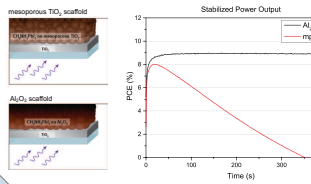

- *Stabilized power output (SPO)*: product of stabilized photocurrent at a constant bias at the maximum power point
- The device with a TiO_2 scaffold does give a stabilized power output
- We ascribe this to UV induced trap-site generation

Encapsulating HTL acts as oxygen barrier

Measuring SPO with and without UV-Filter on the same mp-TiO_2 device

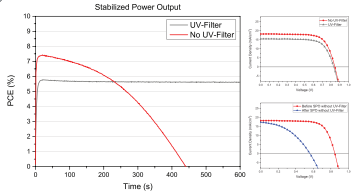

- Removing the UV range from the AM1.5 spectrum with a longpass filter, the device yields a stabilized efficiency
- This corroborates the proposed loss mechanism associated with UV-induced creation of recombination sites due to photodesorption of oxygen
- UV-cutoff leads to a relative performance decrease by ~15%

The moisture vulnerability of perovskite will require sophisticated encapsulation for long-term stability ⇔ in absence of passivating ambient oxygen, UV irradiation leads to a rapid decrease in performance by creating oxygen vacancies on the TiO_2 surface

Figure A.2: Poster based on work described in chapters 6 and 7. Presented at the international conference on Hybrid and Organic Photovoltaics, 2015, Rome, Italy.

Bibliography

[1] Paul B. MacCready. "The Case for Battery Electric Vehicles". In Daniel Sperling & James S. Cannon, editors, "The Hydrogen Energy Transition", pages 227–233. Elsevier (2004). Cited on page 1

[2] R.K. Pachauri & L.A. Meyer. "IPCC, 2014: Climate Change 2014: Synthesis Report. Contribution of Working Groups I, II and III to the Fifth Assessment Report of the Intergovernmental Panel on Climate Change" (2014). ISBN 9789291691432. Cited on page 1, 2

[3] "Population Prospects: The 2015 Revision, Key Findings and Advance Tables" (2015). Cited on page 1

[4] British Petroleum. "BP Statistical Review of World Energy 2015" (2015). Cited on page 1, 3

[5] GISTEMP-Team. "GISS Surface Temperature Analysis (GISTEMP)" (2016). Cited on page 1

[6] J. Hansen, R. Ruedy, M. Sato & K. Lo. *Reviews of Geophysics*, **48**, 4 (2010) RG4004. ISSN 8755-1209. Cited on page 1

[7] Esteban Ortiz-Ospina & Max Roser. "World Population Growth" (2016). Cited on page 2

[8] Max Roser. "Energy Production & Changing Energy Sources - OurWorldInData.org" (2015). Cited on page 2

[9] Max Roser. "CO2 and other Greenhouse Gas Emissions" (2015). Cited on page 2

[10] O. Edenhofer, R. Pichs-Madruga, Y. Sokona, E. Farahani, S. Kadner, K. Seyboth, A. Adler, I. Baum, S. Brunner, P. Eickemeier, B. Kriemann, J. Savolainen, S. Schlomer, C. von Stechow, T. Zwickel & J.C. Minx. "IPCC, 2014: Climate Change 2014: Mitigation of Climate Change. Contribution of Working Group III to the Fifth Assessment Report of the Intergovernmental Panel on Climate Change" (2014). Cited on page 2

[11] Todd Foley, Kane Thornton, Rainer Hinrichs-rahlwes, Steve Sawyer, Marietta Sander, Richard Taylor, Sven Teske, Harry Lehmann, Marcel Alers & David Hales. "Renewables 2015 Global Status Report" (2015). Cited on page 3

[12] Nathan S. Lewis, George Crabtree, Arthur J Nozik, Michael R Wasielewski & Paul Alivisatos. *Basic Energy Sciences Workshop on Solar Energy Utilization*, page 276. Cited on page 3

[13] Gabriele Centi & Siglinda Perathoner. *ChemSusChem*, **3**, 2 (2010) 195–208. ISSN 1864-564X. Cited on page 4

[14] SolarPower Europe. *Global Market Outlook*, page 32. Cited on page 4

[15] U.S. Energy Information Administration. , June (2015) 1–12. Cited on page 4

[16] B. Jones-Albertus, D. Feldman, R. Fu, K. Horowitz & M. Woodhouse. *Progress in Photovoltaics: Research and Applications*, page Submitted. Cited on page 4

[17] T.E. Graedel. *Annual Review of Materials Research*, **41**, 1 (2011) 323–335. ISSN 1531-7331. Cited on page 4

[18] Rolf Frischknecht, R. Itten, P. Sinha, M. de Wild-Scholten, J. Zhang, V. Fthenakis, H. C. Kim, M. Raugei & M. Stucki. "Life Cycle Inventories and Life Cycle Assessments of Photovoltaic Systems". INTERNATIONAL ENERGY AGENCY PHOTOVOLTAIC POWER SYSTEMS PROGRAMME (2015). ISBN 9783906042282. Cited on page 4

[19] W. Moomaw, P. Burgherr, G. Heath, M. Lenzen, J. Nyboer & A. Verbruggen. "Annex II: Methodology. In IPCC Special Report on Renewable Energy Sources and Climate Change Mitigation" (2011). Cited on page 5

[20] C. W. Tang. *Applied Physics Letters*, **48**, 2 (1986) 183–185. ISSN 00036951. Cited on page 5

[21] K. W J Barnham & G. Duggan. *Journal of Applied Physics*, **67**, 7 (1990) 3490–3493. ISSN 00218979. Cited on page 5

[22] Brian O'Regan & Michael Gratzel. *Nature*, **353**, 6346 (1991) 737–740. Cited on page 5

[23] U Bach, D Lupo, P Comte & JE Moser. *Nature*, **395**, October (1998) 583–585. Cited on page 5, 29, 98, 144

[24] Akihiro Kojima, Kenjiro Teshima, Yasuo Shirai & Tsutomu Miyasaka. *Journal of the American Chemical Society*, **131**, 17 (2009) 6050–6051. ISSN 0002-7863. Cited on page 5, 34, 40, 98, 144

[25] Michael M Lee, Joël Teuscher, Tsutomu Miyasaka, Takurou N Murakami & Henry J Snaith. *Science*, **338**, 6107 (2012) 643–7. ISSN 1095-9203. Cited on page 5, 34, 35, 41, 42, 79, 144

[26] Jian Gong, Seth Darling & Fengqi You. *Energy & Environmental Science*, **8**, 7 (2015) 1953–1968. ISSN 1754-5692. Cited on page 5

[27] Editors M S Dresselhaus, G Dresselhaus & Ph Avouris. "Carbon Nanotubes", volume 4216 (2003). ISBN 3540410864. Cited on page 6

[28] Jenny Nelson. "The Physics of Solar Cells". Imperial College Press (2003). ISBN 978-1-86094-340-9. Cited on page 9

[29] P Würfel. "Physics of Solar Cells", volume 7. Wiley-VCH Verlag GmbH, Weinheim, Germany (2005). ISBN 9783527618545. Cited on page 9, 75

[30] Mahbube Khoda Siddiki, Jing Li, David Galipeau & Qiquan Qiao. *Energy & Environmental Science*, **3**, 7 (2010) 867. ISSN 1754-5692. Cited on page 12

[31] L M Peter. *Philosophical transactions. Series A, Mathematical, physical, and engineering sciences*, **369**, 1942 (2011) 1840–1856. ISSN 1364-503X. Cited on page 12

[32] William Shockley & Hans J. Queisser. *Journal of Applied Physics*, **32**, 3 (1961) 510–519. ISSN 00218979. Cited on page 13

[33] National Renewable Energy Laboratory. "NREL Efficiency Chart" (2016). Cited on page 13, 28, 43

[34] Raymond T. Tung. *Applied Physics Reviews*, **1**, 1. ISSN 19319401. Cited on page 23

[35] John Bardeen. *Physical Review*, **71**, 10 (1947) 717–727. ISSN 0031899X. Cited on page 23

[36] Martin A. Green. *AIP Advances*, **3**, 11. ISSN 21583226. Cited on page 25

[37] Barry C. Thompson & Jean M. J. Fréchet. *Angewandte Chemie International Edition*, **47**, 1 (2008) 58–77. ISSN 14337851. Cited on page 25, 72

[38] Simon Gélinas, Olivier Paré-Labrosse, Colin Nadeau Brosseau, Sebastian Albert-Seifried, Christopher R. McNeill, Kiril R. Kirov, Ian A. Howard, Richard Leonelli, Richard H. Friend & Carlos Silva. *Journal of Physical Chemistry C*, **115**, 14 (2011) 7114–7119. ISSN 19327447. Cited on page 25

[39] Gang Li, Rui Zhu & Yang Yang. *Nature Photonics*, **6**, 3 (2012) 153–161. ISSN 1749-4885. Cited on page 25, 26, 71, 72, 73

[40] H Hoppe & N S Sariciftci. *Journal of Material Research*, **19**, 7 (2004) 1924–1946. Cited on page 25, 71

[41] Anders Hagfeldt, Gerrit Boschloo, Licheng Sun, Lars Kloo & Henrik Pettersson. *Chemical Reviews*, **110**, 11 (2010) 6595–6663. Cited on page 27

[42] Brian O'Regan & Michael Grätzel. *Nature*, **353** (1991) 737–740. ISSN 0028-0836. Cited on page 28

[43] David B. Mitzi. **48** (2005) 510. Cited on page 33

[44] Giles E Eperon, Samuel D. Stranks, Christopher Menelaou, Michael B Johnston, Laura M. Herz & Henry J. Snaith. *Energy & Environmental Science*, **7**, 3 (2014) 982. ISSN 1754-5692. Cited on page 34, 35, 37

[45] David B Mitzi. "Synthesis, Structure, and Properties of Organic-Inorganic Perovskites and Related Materials". In "Progress in Inorganic Chemistry", pages 1–121. John Wiley & Sons, Inc. (2007). ISBN 9780470166499. Cited on page 34

[46] C. R. Kagan. *Science*, **286**, 5441 (1999) 945–947. ISSN 00368075. Cited on page 34

[47] Constantinos C. Stoumpos, Christos D. Malliakas & Mercouri G. Kanatzidis. *Inorganic Chemistry*, **52**, 15 (2013) 9019–9038. ISSN 0020-1669. Cited on page 34, 37

[48] Pablo P. Boix, Shweta Agarwala, Teck Ming Koh, Nripan Mathews & Subodh G. Mhaisalkar. *The Journal of Physical Chemistry Letters*, **6**, 5 (2015) 898–907. ISSN 1948-7185. Cited on page 34

[49] Regan Arndt & R Puto. *TUV America*, , 978 (2010) 1–15. Cited on page 34

[50] Hui-Seon Kim, Chang-Ryul Lee, Jeong-Hyeok Im, Ki-Beom Lee, Thomas Moehl, Arianna Marchioro, Soo-Jin Moon, Robin Humphry-Baker, Jun-Ho Yum, Jacques E Moser, Michael Grätzel & Nam-Gyu Park. *Scientific reports*, **2** (2012) 591. ISSN 2045-2322. Cited on page 34, 35, 41, 42, 144

[51] Mingzhen Liu, Michael B Johnston & Henry J Snaith. *Nature*, **501**, 7467 (2013) 395–8. ISSN 1476-4687. Cited on page 34, 42

[52] Olga Malinkiewicz, Aswani Yella, Yong Hui Lee, Guillermo Mínguez Espallargas, Michael Graetzel, Mohammad K. Nazeeruddin & Henk J. Bolink. *Nature Photonics*, **8**, 2 (2013) 128–132. ISSN 1749-4885. Cited on page 34, 42, 165

[53] Julian Burschka, Norman Pellet, Soo-Jin Moon, Robin Humphry-Baker, Peng Gao, Mohammad K. Nazeeruddin & Michael Grätzel. *Nature*, **499**, 7458 (2013) 316–9. ISSN 1476-4687. Cited on page 34, 42

[54] Constantinos C. Stoumpos, Christos D. Malliakas & Mercouri G. Kanatzidis. *Inorganic Chemistry*, **52**, 15 (2013) 9019–9038. ISSN 00201669. Cited on page 35

[55] Yixin Zhao & Kai Zhu. *Chemical communications (Cambridge, England)*, **50**, 13 (2014) 1605–7. ISSN 1364-548X. Cited on page 35, 113

[56] Christian Müller, Tobias Glaser, Marcel Plogmeyer, Michael Sendner, Sebastian Döring, Artem A. Bakulin, Carlo Brzuska, Roland Scheer, Maxim S. Pshenichnikov, Wolfgang Kowalsky, Annemarie Pucci & Robert Lovrinčić. *Chemistry of Materials*, **27**, 22 (2015) 7835–7841. ISSN 0897-4756. Cited on page 35

[57] Giles E Eperon, Severin N Habisreutinger, Tomas Leijtens, Bardo J Bruijnaers, Jacobus J van Franeker, Dane W. DeQuilettes, Sandeep Pathak, Rebecca J Sutton, Giulia Grancini, David S Ginger, Rene A J Janssen, Annamaria Petrozza & Henry J Snaith. *ACS Nano*, **9**, 9 (2015) 9380–9393. ISSN 1936-0851. Cited on page 35

[58] Aurélien M. A. Leguy, Yinghong Hu, Mariano Campoy-Quiles, M. Isabel Alonso, Oliver J. Weber, Pooya Azarhoosh, Mark van Schilfgaarde, Mark T. Weller, Thomas Bein, Jenny Nelson, Pablo Docampo & Piers R. F. Barnes. *Chemistry of Materials*, **27**, 9 (2015) 3397–3407. ISSN 0897-4756. Cited on page 35, 36, 37, 115, 136

[59] Jeffrey A. Christians, Pierre A. Miranda Herrera & Prashant V. Kamat. *Journal of the American Chemical Society*, **137**, 4 (2015) 1530–1538. ISSN 0002-7863. Cited on page 35, 36, 37, 115, 136

[60] Jinli Yang, Braden D Siempelkamp, Dianyi Liu & Timothy L Kelly. *ACS Nano*, **9**, 2 (2015) 1955–1963. ISSN 1936-0851. Cited on page 37, 39, 115, 136

[61] Jun Hong Noh, Sang Hyuk Im, Jin Hyuck Heo, Tarak N Mandal & Sang Il Seok. Cited on page 37

[62] Teck Ming Koh, Kunwu Fu, Yanan Fang, Shi Chen, T. C. Sum, Nripan Mathews, Subodh G. Mhaisalkar, Pablo P. Boix & Tom Baikie. *Journal of Physical Chemistry C*, **118**, 30 (2014) 16458–16462. ISSN 19327455. Cited on page 37

[63] Andreas Binek, Fabian C. Hanusch, Pablo Docampo & Thomas Bein. *The Journal of Physical Chemistry Letters*, **6**, 7 (2015) 150316103833007. ISSN 1948-7185. Cited on page 38

[64] Nam Joong Jeon, Jun Hong Noh, Woon Seok Yang, Young Chan Kim, Seungchan Ryu, Jangwon Seo & Sang Il Seok. *Nature*, **517**, 7535 (2015) 476–480. ISSN 0028-0836. Cited on page 38, 116, 117

[65] Michael Saliba, Taisuke Matsui, Ji-Youn Seo, Konrad Domanski, Juan-Pablo Correa-Baena, Mohammad Khaja Nazeeruddin, Shaik M Zakeeruddin, Wolfgang Tress, Antonio Abate, Anders Hagfeldt & Michael Grätzel. *Energy Environ. Sci.*, **9**, 6 (2016) 1989–1997. ISSN 1754-5692. Cited on page 38

[66] David P McMeekin, Golnaz Sadoughi, Waqaas Rehman, Giles E Eperon, Michael Saliba, M. T. Horantner, Amir Haghighirad, Nobuya Sakai, Lars Korte, Bernd Rech, Michael B Johnston, Laura M Herz & Henry J Snaith. *Science*, **351**, 6269 (2016) 151–155. ISSN 0036-8075. Cited on page 38, 164

[67] Xu Dong, Xiang Fang, Minghang Lv, Bencai Lin, Shuai Zhang, Jianning Ding & Ningyi Yuan. *J. Mater. Chem. A*, **3** (2015) 5360–5367. ISSN 2050-7488. Cited on page 38

[68] Simone Guarnera, Antonio Abate, Wei Zhang, Jamie M. Foster, Giles Richardson, Annamaria Petrozza & Henry J. Snaith. *The Journal of Physical Chemistry Letters*, **6**, 3 (2015) 432–437. ISSN 1948-7185. Cited on page 38, 39

[69] Wenzhe Li, Haopeng Dong, Liduo Wang, Nan Li, Xudong Guo, Jiangwei Li & Yong Qiu. *Journal of Materials Chemistry A*, **2** (2014) 13587–13592. ISSN 2050-7488. Cited on page 38

[70] Guangda Niu, Wenzhe Li, Fanqi Meng, Liduo Wang, Haopeng Dong & Yong Qiu. *Journal of Materials Chemistry A*, **2**, 3 (2014) 705. ISSN 2050-7488. Cited on page 38

[71] Young Soo Kwon, Jongchul Lim, Hui-Jun Yun, Yun-Hi Kim & Taiho Park. *Energy & Environmental Science*, **7**, 4 (2014) 1454. ISSN 1754-5692. Cited on page 38, 39

[72] Jian Liu, Yongzhen Wu, Chuanjiang Qin, Xudong Yang, Takeshi Yasuda, Ashraful Islam, Kun Zhang, Wenqin Peng, Wei Chen & Liyuan Han. *Energy & Environmental Science*, **7**, 9 (2014) 2963–2967. ISSN 1754-5692. Cited on page 38, 39

[73] Lingling Zheng, Yao-Hsien Chung, Yingzhuang Ma, Lipei Zhang, Lixin Xiao, Zhijian Chen, Shufeng Wang, Bo Qu & Qihuang Gong. *Chemical Communications*, **50**, 76 (2014) 11196. ISSN 1359-7345. Cited on page 38, 39

[74] Weiwei Li, W S Christian Roelofs, Mathieu Turbiez, Martijn M Wienk & René a J Janssen. *Advanced materials (Deerfield Beach, Fla.)*, **26**, 20 (2014) 3304–9. ISSN 1521-4095. Cited on page 38

[75] Kwangseok Do, Hyeju Choi, Kimin Lim, Hyunjun Jo, Jin Woo Cho, Mohammad K Nazeeruddin & Jaejung Ko. *Chemical Communications*, **1** (2014) 10–13. ISSN 1364-548X. Cited on page 38

[76] Hyeju Choi, Sojin Park, Sanghyun Paek, Piyasiri Ekanayake, Mohammad Khaja Nazeeruddin & Jaejung Ko. *J. Mater. Chem. A*, **2**, 45 (2014) 19136–19140. ISSN 2050-7488. Cited on page 38

[77] Jiewei Liu, Sandeep Pathak, Thomas Stergiopoulos, Tomas Leijtens, Konrad Wojciechowski, Stefan Schumann, Nina Kausch-Busies & Henry J. Snaith. *The Journal of Physical Chemistry Letters*, pages 1666–1673. ISSN 1948-7185. Cited on page 38, 39

[78] Yingzhuang Ma, Yao-Hsien Chung, Lingling Zheng, Danfei Zhang, Xiao Yu, Lixin Xiao, Zhijian Chen, Shufeng Wang, Bo Qu, Qihuang Gong & Dechun Zou. *ACS Applied Materials & Interfaces*, **7**, 12 (2015) 6406–6411. ISSN 1944-8244. Cited on page 38

[79] Jie Min, Zhi-guo Zhang, Yi Hou, Cesar Omar, Ramirez Quiroz, Thomas Przybilla, Carina Bronnbauer, Fei Guo, Karen Forberich, Hamed Azimi, Tayebeh Ameri, Erdmann Spiecker, Yongfang Li & Christoph J Brabec. Cited on page 38

[80] Hyeju Choi, Jin Woo Cho, Moon-Sung Kang & Jaejung Ko. *Chem. Commun.*. ISSN 1359-7345. Cited on page 38

[81] Meng Zhang, Miaoqiang Lyu, Hua Yu, Jung-Ho Yun, Qiong Wang & Lianzhou Wang. *Chemistry - A European Journal*, **21**, 1 (2015) 434–439. ISSN 09476539. Cited on page 38

[82] Junyan Xiao, Jiangjian Shi, Huibiao Liu, Yuzhuan Xu, Songtao Lv, Yanhong Luo, Dongmei Li, Qingbo Meng & Yuliang Li. *Advanced Energy Materials*, **5**, 8 (2015) 1401943. ISSN 16146832. Cited on page 38, 39

[83] Jing Zhang, Zhelu Hu, Like Huang, Guoqiang Yue, Jinwang Liu, Xingwei Lu, Ziyang Hu, Minghui Shang, Liyuan Han & Yuejin Zhu. *Chem. Commun.*, **51**, 32 (2015) 7047–7050. ISSN 1359-7345. Cited on page 38

[84] Jing Cao, Jun Yin, Shangfu Yuan, Yun Zhao, Jing Li & Nanfeng Zheng. *Nanoscale*, **7**, 21 (2015) 9443–9447. ISSN 2040-3364. Cited on page 38

[85] Yongsheng Liu, Ziruo Hong, Qi Chen, Huajun Chen, Wei-Hsuan Chang, Yang Michael Yang, Tze-Bin Song & Yang Yang. *Advanced Materials*, **28**, 3 (2016) 440–446. ISSN 09359648. Cited on page 38, 39

[86] Anyi Mei, Xiong Li, Linfeng Liu, Zhiliang Ku, Tongfa Liu, Yaoguang Rong, Mi Xu, Min Hu, Jiangzhao Chen, Ying Yang, Michael Grätzel & Hongwei Han. *Science*, **345**, 6194 (2014) 295–298. ISSN 0036-8075. Cited on page 38, 39, 81

[87] Yaoguang Rong, Zhiliang Ku, Anyi Mei, Tongfa Liu, Mi Xu, Songguk Ko, Xiong Li & Hongwei Han. *Journal of Physical Chemistry Letters*, **5**, 12 (2014) 2160–2164. ISSN 19487185. Cited on page 38, 39

[88] Huawei Zhou, Yantao Shi, Kai Wang, Qingshun Dong, Xiaogong Bai, Yujin Xing, Yi Du & Tingli Ma. *The Journal of Physical Chemistry C*, , 15 mL (2015) 150216032236005. ISSN 1932-7447. Cited on page 38, 39

[89] Xiaobao Xu, Zonghao Liu, Zhixiang Zuo, Meng Zhang, Zhixin Zhao, Yan Shen, Huanping Zhou, Qi Chen, Yang Yang & Mingkui Wang. *Nano Letters*, **15**, 4 (2015) 2402–2408. ISSN 1530-6984. Cited on page 38, 39

[90] Xiong Li, Manuel Tschumi, Hongwei Han, Saeed Salem Babkair, Raysah Ali Alzubaydi, Azhar Ahmad Ansari, Sami S. Habib, Mohammad Khaja Nazeeruddin, Shaik M. Zakeeruddin & Michael Grätzel. *Energy Technology*, **3**, 6 (2015) 551–555. ISSN 21944288. Cited on page 38, 39

[91] Jixian Xu, Oleksandr Voznyy, Riccardo Comin, Xiwen Gong, Grant Walters, Min Liu, Pongsakorn Kanjanaboos, Xinzheng Lan & Edward H. Sargent. *Advanced Materials*, **28**, 14 (2016) 2807–2815. ISSN 09359648. Cited on page 38, 39

[92] William H. Nguyen, Colin D. Bailie, Eva L. Unger & Michael D. McGehee. *Journal of the American Chemical Society*, **136**, 31 (2014) 10996–11001. ISSN 15205126. Cited on page 39, 99, 145, 146

[93] Yongsheng Liu, Qi Chen, Hsin-Sheng Duan, Huanping Zhou, Yang (Michael) Yang, Huajun Chen, Song Luo, Tze-Bin Song, Letian Dou, Ziruo Hong & Yang Yang. *J. Mater. Chem. A*, **3**, 22 (2015) 11940–11947. ISSN 2050-7488. Cited on page 39

[94] Juan Dong, Yanhong Zhao, Jiangjian Shi, Huiyun Wei, Junyan Xiao, Xin Xu, Jianheng Luo, Jing Xu, Dongmei Li, Yanhong Luo & Qingbo Meng. *Chem. Commun.*, **50**, 87 (2014) 13381–13384. ISSN 1359-7345. Cited on page 39

[95] Zhengguo Xiao, Cheng Bi, Yuchuan Shao, Qingfeng Dong, Qi Wang, Yongbo Yuan, Chenggong Wang, Yongli Gao & Jinsong Huang. *Energy & Environmental Science*, **7**, 8 (2014) 2619. ISSN 1754-5692. Cited on page 39, 42

[96] Jeong-Hyeok Im, Chang-Ryul Lee, Jin-Wook Lee, Sang-Won Park & Nam-Gyu Park. *Nanoscale*, **3**, 10 (2011) 4088–93. ISSN 2040-3372. Cited on page 41, 98

[97] James M. Ball, Michael M Lee, Andrew Hey & Henry J. Snaith. *Energy & Environmental Science*, **6**, 6 (2013) 1739. ISSN 1754-5692. Cited on page 41, 89

[98] Samuel D Stranks, Giles E Eperon, Giulia Grancini, Christopher Menelaou, Marcelo J P Alcocer, Tomas Leijtens, Laura M Herz, Annamaria Petrozza & Henry J Snaith. *Science*, **342**, 6156 (2013) 341–344. ISSN 1095-9203. Cited on page 41

[99] Atsuhiko Miyata, Anatolie Mitioglu, Paulina Plochocka, Oliver Portugall, Jacob Tse-Wei Wang, Samuel D. Stranks, Henry J. Snaith & Robin J. Nicholas. *Nature Physics*, **11**, 7 (2015) 582–587. ISSN 1745-2473. Cited on page 42

[100] Giles E. Eperon, Victor M. Burlakov, Pablo Docampo, Alain Goriely & Henry J. Snaith. *Advanced Functional Materials*, **24**, 1 (2014) 151–157. ISSN 1616301X. Cited on page 42

[101] Pablo Docampo, James M Ball, Mariam Darwich, Giles E Eperon & Henry J Snaith. *Nature communications*, **4** (2013) 2761. ISSN 2041-1723. Cited on page 42, 98, 165

[102] Qi Chen, Huanping Zhou, Ziruo Hong, Song Luo, Hsin-Sheng Duan, Hsin-Hua Wang, Yongsheng Liu, Gang Li & Yang Yang. *Journal of the American Chemical Society*, **136**, 2 (2014) 622–5. ISSN 1520-5126. Cited on page 42

[103] Yanbo Li, Jason K. Cooper, Raffaella Buonsanti, Cinzia Giannini, Yi Liu, Francesca M. Toma & Ian D. Sharp. *Journal of Physical Chemistry Letters*, **6**, 3 (2015) 493–499. ISSN 19487185. Cited on page 42

[104] Pavel Nikolaev, Michael J Bronikowski, R.Kelley Bradley, Frank Rohmund, Daniel T Colbert, K.A Smith & Richard E Smalley. *Chemical Physics Letters*, **313**, 1-2 (1999) 91–97. ISSN 00092614. Cited on page 45

[105] Nanointegris. "Technical Data Sheet - HiPco SWCNTs" (2015). Cited on page 45

[106] B. Kitiyanan, W.E. Alvarez, J.H. Harwell & D.E. Resasco. *Chemical Physics Letters*, **317**, 3-5 (2000) 497–503. ISSN 00092614. Cited on page 45, 46

[107] Anton V Naumov, Oleg a Kuznetsov, Avetik R Harutyunyan, Alexander a Green, Mark C Hersam, Daniel E Resasco, Pavel N Nikolaev & R Bruce Weisman. *Nano letters*, **9**, 9 (2009) 3203–8. ISSN 1530-6992. Cited on page 46

[108] Robert A. Bell. "Conduction in Carbon Nanotube Networks". Springer Theses. Springer International Publishing, Cham (2015). ISBN 978-3-319-19964-1. Cited on page 53, 56

[109] Jeroen W G Wildöer, Liesbeth C Venema, Andrew G Rinzler, Richard E Smalley & Cees Dekker. *Nature*, **391**, 6662 (1998) 59–62. ISSN 00280836. Cited on page 56

[110] Jean-Christophe Charlier & Stephan Roche. *Reviews of Modern Physics*, **79**, 2 (2007) 677–732. ISSN 0034-6861. Cited on page 58, 63

[111] R. Saito, G. Dresselhaus & M. Dresselhaus. *Physical Review B*, **61**, 4 (2000) 2981–2990. ISSN 0163-1829. Cited on page 59

[112] Noriaki Hamada, Shin-ichi Sawada & Atsushi Oshiyama. *Physical Review Letters*, **68**, 10 (1992) 1579–1581. ISSN 0031-9007. Cited on page 60

[113] Riichiro Saito, Mitsutaka Fujita, G. Dresselhaus & M. S. Dresselhaus. *Physical Review B*, **46**, 3 (1992) 1804–1811. ISSN 0163-1829. Cited on page 60

[114] T. W. Ebbesen, H. J. Lezec, H. Hiura, J. W. Bennett, H. F. Ghaemi & T. Thio. *Nature*, **382**, 6586 (1996) 54–56. ISSN 0028-0836. Cited on page 60, 63

[115] T.W. Odom, J.L. Huang, P. Kim & C.M. Lieber. *Nature*, **391**, January (1998) 62–64. ISSN 0028-0836. Cited on page 60

[116] J. Mintmire & C. White. *Physical Review Letters*, **81**, 12 (1998) 2506–2509. ISSN 0031-9007. Cited on page 61

[117] Cees Dekker. *Physics Today*, **52**, 5 (1999) 22–28. ISSN 00319228. Cited on page 63

[118] R. Saito, M. Fujita, G. Dresselhaus & M S Dresselhaus. *Applied Physics Letters*, **60**, 18 (1992) 2204. ISSN 00036951. Cited on page 63

[119] C T White & T N Todorov. *Nature*, **393**, 6682 (1998) 240–242. Cited on page 63

[120] Paul McEuen, Marc Bockrath, David Cobden, Young-Gui Yoon & Steven Louie. *Physical Review Letters*, **83**, 24 (1999) 5098–5101. ISSN 0031-9007. Cited on page 63

[121] W Liang, M Bockrath, D Bozovic, J H Hafner, M Tinkham & H Park. *Nature*, **411**, 6838 (2001) 665–669. ISSN 0028-0836. Cited on page 63

[122] J Kong, E Yenilmez, T W Tombler, W Kim, H Dai, R B Laughlin, L Liu, C S Jayanthi & S Y Wu. *Physical review letters*, **87**, 10 (2001) 106801. ISSN 0031-9007. Cited on page 63

[123] Paul L McEuen. *Physics World*. ISSN 1098-0121. Cited on page 63

[124] Ali Javey, Jing Guo, Qian Wang, Mark Lundstrom & Hongjie Dai. *Nature*, **424**, 6949 (2003) 654–7. ISSN 1476-4687. Cited on page 63, 72

[125] T. Dürkop, S. A. Getty, Enrique Cobas & M. S. Fuhrer. *Nano Letters*, **4**, 1 (2004) 35–39. ISSN 1530-6984. Cited on page 63, 71

[126] Zhuangchun Wu, Zhihong Chen, Xu Du, Jonathan M Logan, Jennifer Sippel, Maria Nikolou, Katalin Kamaras, John R Reynolds, David B Tanner, Arthur F Hebard & Andrew G Rinzler. *Science (New York, N.Y.)*, **305**, 5688 (2004) 1273–6. ISSN 1095-9203. Cited on page 64

[127] E. S. Snow, J. P. Novak, P. M. Campbell & D. Park. *Applied Physics Letters*, **82**, 13 (2003) 2145. ISSN 00036951. Cited on page 64

[128] Dong-ming Sun, Marina Y. Timmermans, Ying Tian, Albert G. Nasibulin, Esko I. Kauppinen, Shigeru Kishimoto, Takashi Mizutani & Yutaka Ohno. *Nature Nanotechnology*, **6**, 3 (2011) 156–161. ISSN 1748-3387. Cited on page 64

[129] M S Fuhrer, J Nygård, L Shih, M Forero, Young-Gui Yoon, Hyoung Joon Choi, Jisoon Ihm, Steven G Louie, A Zettl & Paul L McEuen. *Science*, **288**, 5465 (2000) 494–497. ISSN 0036-8075. Cited on page 64, 65

[130] M. Stadermann, S. J. Papadakis, M. R. Falvo, J. Novak, E. Snow, Q. Fu, J. Liu, Y. Fridman, J. J. Boland, R. Superfine & S. Washburn. *Physical Review B - Condensed Matter and Materials Physics*, **69**, 20 (2004) 10–12. ISSN 01631829. Cited on page 64

[131] L. Hu, D. S. Hecht & G. Grüner. *Nano Letters*, **4**, 12 (2004) 2513–2517. ISSN 1530-6984. Cited on page 64

[132] M A Alam, N Pimparkar, S Kumar & J Murthy. *MRS Bulletin*, **31**, 06 (2006) 466–470. ISSN 1938-1425. Cited on page 64

[133] Peter N Nirmalraj, Philip E Lyons, Sukanta De, Jonathan N Coleman & John J Boland. *Nano letters*, **9**, 11 (2009) 3890–5. ISSN 1530-6992. Cited on page 64

[134] Jae-Won Do, David Estrada, Xu Xie, Noel N. Chang, Justin Mallek, Gregory S. Girolami, John A Rogers, Eric Pop & Joseph W Lyding. *Nano Letters*, **13**, 12 (2013) 5844–5850. ISSN 1530-6984. Cited on page 64

[135] Andriy V Kyrylyuk, Marie Claire Hermant, Tanja Schilling, Bert Klumperman, Cor E Koning & Paul van der Schoot. *Nature Nanotechnology*, **6**, 6 (2011) 364–9. ISSN 1748-3395. Cited on page 64, 72

[136] Zhen Yao, Cees Dekker, Henk W. Ch. Postma & Leon Balents. *Nature*, **402**, 6759 (1999) 273–276. ISSN 00280836. Cited on page 64

[137] Shengdong Li, Zhen Yu, Christopher Rutherglen & Peter J Burke. *Nano*, pages 0–4. ISSN 1530-6984. Cited on page 64

[138] David Hecht, Liangbing Hu & George Grüner. *Applied Physics Letters*, **89**, 13 (2006) 2004–2007. ISSN 00036951. Cited on page 64

[139] I. Balberg & N. Binenbaum. *Physical Review B*, **28**, 7 (1983) 3799–3812. ISSN 01631829. Cited on page 64

[140] David S. Hecht, Liangbing Hu & Glen Irvin. *Advanced Materials*, **23**, 13 (2011) 1482–1513. ISSN 09359648. Cited on page 64, 165

[141] Dong Hun Shin, Hyung Cheoul Shim, Jin Won Song, Soohyun Kim & Chang Soo Han. *Scripta Materialia*, **60**, 8 (2009) 607–610. ISSN 13596462. Cited on page 65

[142] Hong-Zhang Geng, Ki Kang Kim, Kyu Lee, Gil Yong Kim, Ha Kyu Choi, Dae Sik Lee, Kay Hyeok An, Young Hee Lee, Youngkyu Chang, Young Sil Lee, Byeongyeol Kim & Young Jun Lee. *Nano*, **02**, 03 (2007) 157–167. ISSN 1793-2920. Cited on page 65

[143] Mark C Hersam. *Nature Nanotechnology*, **3**, 7 (2008) 387–94. ISSN 1748-3395. Cited on page 66

[144] Sarbajit Banerjee, Tirandai Hemraj-Benny & Stanislaus S. Wong. *Advanced Materials*, **17**, 1 (2005) 17–29. ISSN 09359648. Cited on page 66

[145] Richard Martel. *ACS Nano*, **2**, 11 (2008) 2195–2199. ISSN 19360851. Cited on page 66

[146] M. J. O'Connell. *Science*, **297**, 5581 (2002) 593–596. ISSN 00368075. Cited on page 66

[147] Ming Zheng, Anand Jagota, Ellen D Semke, Bruce A Diner, Robert S McLean, Steve R Lustig, Raymond E Richardson & Nancy G Tassi. *Nature Materials*, **2**, 5 (2003) 338–42. ISSN 1476-1122. Cited on page 66

[148] Basudeb Maji, Suman K Samanta & Santanu Bhattacharya. *Nanoscale*, **6**, 7 (2014) 3721. ISSN 2040-3364. Cited on page 66

[149] Xiaomin Tu, Suresh Manohar, Anand Jagota & Ming Zheng. *Nature*, **460**, 7252 (2009) 250–253. ISSN 0028-0836. Cited on page 66

[150] Suman Kalyan Samanta, Martin Fritsch, Ullrich Scherf, Widianta Gomulya, Satria Zulkarnaen Bisri & Maria Antonietta Loi. *Accounts of chemical research*, **47**, 8 (2014) 2446–56. ISSN 1520-4898. Cited on page 67

[151] S M Keogh, T G Hedderman, E Gregan, G Farrell, G Chambers & H J Byrne. *The journal of physical chemistry. B*, **108**, 20 (2004) 6233–41. ISSN 1520-6106. Cited on page 67

[152] Shuai Liang, Guang Chen, Jessica Peddle & Yuming Zhao. *Chemical Communications*, **48** (2012) 3100. ISSN 1359-7345. Cited on page 67

[153] Fabien A. Lemasson, Timo Strunk, Peter Gerstel, Frank Hennrich, Sergei Lebedkin, Christopher Barner-Kowollik, Wolfgang Wenzel, Manfred M. Kappes & Marcel Mayor. *Journal of the American Chemical Society*, **133**, 4 (2011) 652–655. ISSN 00027863. Cited on page 67

[154] Adrian Nish, Jeong-Yuan Hwang, James Doig & Robin J Nicholas. *Nature Nanotechnology*, **2**, 10 (2007) 640–6. ISSN 1748-3395. Cited on page 67

[155] Jia Gao, Maria Antonietta Loi, Elton José Figueiredo de Carvalho & Maria Cristina dos Santos. *Acs Nano*, **5**, 5 (2011) 3993–3999. Cited on page 67

[156] Widianta Gomulya, Guadalupe Diaz Costanzo, Elton J Figueiredo De Carvalho, Satria Zulkarnaen Bisri, Vladimir Derenskyi, Martin Fritsch, Nils Fr??hlich, Sybille Allard, Pavlo Gordiichuk, Andreas Herrmann, Siewert Jan Marrink, Maria Cristina Dos Santos, Ulrich Scherf & Maria Antonietta Loi. *Advanced Materials*, **25**, 21 (2013) 2948–2956. ISSN 09359648. Cited on page 67

[157] Huiliang Wang, Bing Hsieh, Gonzalo Jiménez-Osés, Peng Liu, Christopher J Tassone, Ying Diao, Ting Lei, Kendall N Houk & Zhenan Bao. *Small (Weinheim an der Bergstrasse, Germany)*, pages 1–8. ISSN 1613-6829. Cited on page 67

[158] Tsuyohiko Fujigaya & Naotoshi Nakashima. *Science and Technology of Advanced Materials*, **16**, 2 (2015) 024802. ISSN 1468-6996. Cited on page 67

[159] Hang Woo Lee, Yeohoon Yoon, Steve Park, Joon Hak Oh, Sanghyun Hong, Luckshitha S Liyanage, Huiliang Wang, Satoshi Morishita, Nishant Patil, Young Jun Park, Jong Jin Park, Andrew Spakowitz, Giulia Galli, Francois Gygi, Philip H-S S Wong, Jeffrey B-H H Tok, Jong Min Kim & Zhenan Bao. *Nature Communications*, **2** (2011) 541. ISSN 2041-1723. Cited on page 67

[160] Huiliang Wang, Ghada I Koleilat, Peng Liu, Gonzalo Jiménez-Osés, Ying-Chih Lai, Michael Vosgueritchian, Ya Fang, Steve Park, Kendall N Houk & Zhenan Bao. *ACS nano*, **8**, 3 (2014) 2609–17. ISSN 1936-086X. Cited on page 67

[161] Atsushi Ikeda, Kazuyuki Nobusawa, Tomoe Hamano & Jun Ichi Kikuchi. *Organic Letters*, **8**, 24 (2006) 5489–5492. ISSN 15237060. Cited on page 67, 72

[162] Wei-Chao Chen, Hsiang-Ting Lien, Tzu-Wei Cheng, Chaochin Su, Cheong-Wei Chong, Abhijit Ganguly, Kuei-Hsien Chen & Li-Chyong Chen. *ACS Applied Materials & Interfaces*, **7**, 8 (2015) 4616–4622. ISSN 1944-8244. Cited on page 67

[163] Hongwei Gu & Timothy M. Swager. *Advanced Materials*, **20**, 23 (2008) 4433–4437. ISSN 09359648. Cited on page 68

[164] T Schuettfort, H J Snaith, A Nish & R J Nicholas. *Nanotechnology*, **21**, 2 (2010) 25201. ISSN 1361-6528. Cited on page 68, 72, 89, 100, 101

[165] Samuel D Stranks, Christian Weisspfennig, Patrick Parkinson, Michael B Johnston, Laura M Herz & Robin J Nicholas. *Nano Letters*, **11**, 1 (2010) 66–72. ISSN 1530-6992. Cited on page 68, 72, 73

[166] Nanditha M Dissanayake & Zhaohui Zhong. *Nano Letters*, **11**, 1 (2011) 286–90. ISSN 1530-6992. Cited on page 68, 69, 70, 73, 79, 100

[167] Jianxin Geng, Byung Seon Kong, Seung Bo Yang, Sang Cheon Youn, Sohyun Park, Taiha Joo & Hee Tae Jung. *Advanced Functional Materials*, **18**, 18 (2008) 2659–2665. ISSN 1616301X. Cited on page 68

[168] Emmanuel Kymakis, Nikolaos Kornilios & Emmanuel Koudoumas. *Journal of Physics D: Applied Physics*, **41**, 16 (2008) 165110. ISSN 0022-3727. Cited on page 68

[169] Run Long & Oleg V Prezhdo. *Nano letters*. ISSN 1530-6992. Cited on page 68, 73

[170] Fei Lan & Guangyong Li. *Nano Letters*, **13**, 5 (2013) 2086–91. ISSN 1530-6992. Cited on page 68, 69, 73, 74

[171] Yosuke Kanai & Jeffrey C Grossman. *Nano Letters*, **8**, 3 (2008) 908–12. ISSN 1530-6984. Cited on page 70, 125

[172] M. C. Scharber & N. S. Sariciftci. *Progress in Polymer Science*, **38**, 12 (2013) 1929–1940. ISSN 00796700. Cited on page 71

[173] M. Knupfer. *Applied Physics A: Materials Science & Processing*, **77**, 5 (2003) 623–626. ISSN 0947-8396. Cited on page 71

[174] Oleksandr V. Mikhnenko, Hamed Azimi, Markus Scharber, Mauro Morana, Paul W. M. Blom & Maria Antonietta Loi. *Energy & Environmental Science*, **5**, 5 (2012) 6960. ISSN 1754-5692. Cited on page 71

[175] Xinjian Zhou, J-y Ji-Yong Park, Shaoming Huang, Jie Liu & Paul P.L. McEuen. *Physical Review Letters*, **95**, 14 (2005) 146805. ISSN 0031-9007. Cited on page 71

[176] Sebastiano Cataldo, Patrizio Salice, Enzo Menna & Bruno Pignataro. *Energy & Environmental Science*, **5**, 3 (2012) 5919–5940. ISSN 1754-5692. Cited on page 71, 73

[177] Robert C. Tenent, Teresa M. Barnes, Jeremy D. Bergeson, Andrew J. Ferguson, Bobby To, Lynn M. Gedvilas, Michael J. Heben & Jeffrey L. Blackburn. *Advanced Materials*, **21**, 31 (2009) 3210–3216. ISSN 09359648. Cited on page 72

[178] Wojciech J. Grzegorczyk, Tom J. Savenije, Tieneke E. Dykstra, Jorge Piris, Juleon M. Schins & Laurens D.A. Siebbeles. *The Journal of Physical Chemistry C*, **114**, 11 (2010) 5182–5186. ISSN 1932-7447. Cited on page 72

[179] Ji Luo, L. M. Peng, Z. Q. Xue & J. L. Wu. *Journal of Chemical Physics*, **120**, 17 (2004) 7998–8001. ISSN 00219606. Cited on page 72

[180] Jianxin Geng & Tingying Zeng. *Journal of the American Chemical Society*, **128**, 51 (2006) 16827–33. ISSN 0002-7863. Cited on page 72, 73

[181] Emmanouil Lioudakis, Andreas Othonos & Ioannis Alexandrou. **3** (2008) 278–283. Cited on page 72

[182] Yosuke Kanai & Jeffrey C Grossman. *Nano Letters*, **8**, 3 (2008) 908–12. ISSN 1530-6984. Cited on page 72, 73

[183] Torben Schuettfort, Adrian Nish & Robin J Nicholas. *Nano Letters*, **9**, 11 (2009) 3871–3876. ISSN 1530-6992. Cited on page 72

[184] Andrew J. Ferguson, Jeffrey L. Blackburn, Josh M. Holt, Nikos Kopidakis, Robert C. Tenent, Teresa M. Barnes, Michael J. Heben & Garry Rumbles. *The Journal of Physical Chemistry Letters*, **1**, 15 (2010) 2406–2411. ISSN 1948-7185. Cited on page 73

[185] E. Kymakis & G. a. J. Amaratunga. *Applied Physics Letters*, **80**, 1 (2002) 112. ISSN 00036951. Cited on page 73

[186] E. Kymakis, I. Alexandrou & G. a. J. Amaratunga. *Journal of Applied Physics*, **93**, 3 (2003) 1764. ISSN 00218979. Cited on page 73

[187] Brian J. Landi, Ryne P. Raffaelle, Stephanie L. Castro & Sheila G. Bailey. *Progress in Photovoltaics: Research and Applications*, **13**, 2 (2005) 165–172. ISSN 10627995. Cited on page 73

[188] Emmanuel Kymakis & Gehan A J Amaratunga. *Reviews on advanced materials science*, **10** (2005) 300–305. Cited on page 73

[189] E Kymakis, E Koudoumas, I Franghiadakis & G A J Amaratunga. *Journal of Physics D: Applied Physics*, **39**, 6 (2006) 1058–1062. ISSN 0022-3727. Cited on page 73, 125

[190] Rodolfo L. Patyk, Bruno S. Lomba, Ana Flávia Nogueira, Clascídia A. Furtado, Adelina Pinheiro Santos, Regina M Q Mello, Liliana Micaroni & Ivo A. Hümmelgen. *Physica Status Solidi - Rapid Research Letters*, **1**, 1 (2007) 43–45. ISSN 18626270. Cited on page 73, 74

[191] Marisol Reyes-Reyes, Kyungkon Kim & David L. Carroll. *Applied Physics Letters*, **87**, 8 (2005) 3–6. ISSN 00036951. Cited on page 73

[192] Liming Liu, William E. Stanchina & Guangyong Li. *Applied Physics Letters*, **94**, 23 (2009) 50–53. ISSN 00036951. Cited on page 73

[193] Shenqiang Ren, Marco Bernardi, Richard R Lunt, Vladimir Bulovic, Jeffrey C Grossman & Silvija Gradečak. *Nano Letters*, **11**, 12 (2011) 5316–5321. ISSN 1530-6992. Cited on page 73, 81

[194] Sumit Chaudhary, Haiwei Lu, Astrid M Müller, Christopher J Bardeen & Mihrimah Ozkan. *Nano Letters*, **7**, 7 (2007) 1973–9. ISSN 1530-6984. Cited on page 74

[195] G Dinesha M R Dabera, K D G Imalka Jayawardena, M R Ranga Prabhath, Iskandar Yahya, Y Yuan Tan, N Aamina Nismy, Hidetsugu Shiozawa, Markus Sauer, G Ruiz-Soria, Paola Ayala, Vlad Stolojan, a a Damitha T Adikaari, Peter D Jarowski, Thomas Pichler & S Ravi P Silva. *ACS nano*, **7**, 1 (2013) 556–65. ISSN 1936-086X. Cited on page 74, 75, 79, 100

[196] Martin A. Green. *Nature Energy*, **1**, 1 (2016) 15015. ISSN 2058-7546. Cited on page 75

[197] Collins, Bradley, Ishigami & Zettl. *Science*, **287**, 5459 (2000) 1801–4. ISSN 1095-9203. Cited on page 75, 79

[198] Xinming Li, Zheng Lv & Hongwei Zhu. *Advanced Materials*, **27**, 42 (2015) 6549–6574. ISSN 15214095. Cited on page 75, 76

[199] J T Hu, O Y Min, P D Yang & C M Lieber. *Nature*, **399**, 6731 (1999) 48–51. Cited on page 76

[200] M. Tzolov, B. Chang, a. Yin, D. Straus, J. Xu & G. Brown. *Physical Review Letters*, **92**, 7 (2004) 075505. ISSN 0031-9007. Cited on page 76

[201] Marian B. Tzolov, Teng Fang Kuo, Daniel A. Straus, Aijun Yin & Jimmy Xu. *Journal of Physical Chemistry C*, **111**, 15 (2007) 5800–5804. ISSN 19327447. Cited on page 76

[202] Jinquan Wei, Yi Jia, Qinke Shu, Zhiyi Gu, Kunlin Wang, Darning Zhuang, Gong Zhang, Zhicheng Wang, Jianbin Luo, Anyuan Cao & Dehai Wu. *Nano Letters*, **7**, 8 (2007) 2317–2321. ISSN 15306984. Cited on page 76

[203] Zhongrui Li, Vasyl P Kunets, Viney Saini, Yang Xu, Enkeleda Dervishi, Gregory J Salamo, Alexandru R Biris & Alexandru S Biris. *ACS nano*, **3**, 6 (2009) 1407–14. ISSN 1936-086X. Cited on page 76

[204] Zhongrui Li, Viney Saini, Enkeleda Dervishi, Vasyl P. Kunets, Jianhui Zhang, Yang Xu, Alexandru R. Biris, Gregory J. Salamo & Alexandru S. Biris. *Applied Physics Letters*, **96**, 2010 (2010) 2008–2011. ISSN 00036951. Cited on page 76

[205] Yi Jia, Anyuan Cao, Xi Bai, Zhen Li, Luhui Zhang, Ning Guo, Jinquan Wei, Kunlin Wang, Hongwei Zhu, Dehai Wu & P. M. Ajayan. *Nano letters*, **11**, 5 (2011) 1901–5. ISSN 1530-6992. Cited on page 77, 78

[206] Yi Jia, Peixu Li, Xuchun Gui, Jinquan Wei, Kunlin Wang, Hongwei Zhu, Dehai Wu, Luhui Zhang, Anyuan Cao & Ying Xu. *Applied Physics Letters*, **98**, 13 (2011) 98–101. ISSN 00036951. Cited on page 77

[207] Yi Jia, Anyuan Cao, Feiyu Kang, Peixu Li, Xuchun Gui, Luhui Zhang, Enzheng Shi, Jinquan Wei, Kunlin Wang, Hongwei Zhu & Dehai Wu. *Physical chemistry chemical physics : PCCP*, **14**, 23 (2012) 8391–6. ISSN 1463-9084. Cited on page 77

[208] Enzheng Shi, Luhui Zhang, Zhen Li, Peixu Li, Yuanyuan Shang, Yi Jia, Jinquan Wei, Kunlin Wang, Hongwei Zhu, Dehai Wu, Sen Zhang & Anyuan Cao. *Scientific reports*, **2** (2012) 884. ISSN 2045-2322. Cited on page 77, 78

[209] Kehang Cui, Anton S. Anisimov, Takaaki Chiba, Shunjiro Fujii, Hiromichi Kataura, Albert G. Nasibulin, Shohei Chiashi, Esko I. Kauppinen & Shigeo Maruyama. *Journal of Materials Chemistry A*, **2**, 29 (2014) 11311. ISSN 2050-7488. Cited on page 77

[210] Feijiu Wang, Daichi Kozawa, Yuhei Miyauchi, Kazushi Hiraoka, Shinichiro Mouri, Yutaka Ohno & Kazunari Matsuda. *Nature Communications*, **6** (2015) 6305. ISSN 2041-1723. Cited on page 77, 78

[211] Yeonwoong Jung, Xiaokai Li, Nitin K Rajan, André D Taylor & Mark a Reed. *Nano Letters*, **13**, 1 (2013) 95–9. ISSN 1530-6992. Cited on page 77, 79

[212] Jiangtao Di, Zhenzhong Yong, Xinhe Zheng, Baoquan Sun & Qingwen Li. *Small*, **9**, 8 (2013) 1367–1372. ISSN 16136810. Cited on page 77

[213] Ru Li, Hongfang Li, Jingyun Zou, Xiaohua Zhang & Qingwen Li. *Nanoscale*, **1** (2014) 1–4. ISSN 2040-3364. Cited on page 77

[214] Ru Li, Jiangtao Di, Zhenzhong Yong, Baoquan Sun & Qingwen Li. *Journal of Materials Chemistry A*, **2**, 12 (2014) 4140. ISSN 2050-7488. Cited on page 77, 78

[215] Masashi Shiraishi & Masafumi Ata. *Carbon*, **39**, 12 (2001) 1913–1917. ISSN 00086223. Cited on page 79

[216] Peng Liu, Qin Sun, Feng Zhu, Kai Liu, Kaili Jiang, Liang Liu, Qunqing Li & Shoushan Fan. *Nano Letters*, **8**, 2 (2008) 647–651. ISSN 15306984. Cited on page 79

[217] Zhen Li, Sneha a Kulkarni, Pablo P Boix, Enzheng Shi, Anyuan Cao, Kunwu Fu, Sudip K Batabyal, Jun Zhang, Qihua Xiong, Lydia Helena Wong, Nripan Mathews & Subodh G. Mhaisalkar. *ACS Nano*, **8**, 7 (2014) 6797–6804. ISSN 1936-0851. Cited on page 79

[218] Jiyong Lee, Mini Mol Menamparambath, Jae-Yeol Hwang & Seunghyun Baik. *ChemSusChem*, **8**, 14 (2015) 2358–2362. ISSN 18645631. Cited on page 79

[219] Severin N. Habisreutinger, Tomas Leijtens, Giles E. Eperon, Samuel David Stranks, Robin J. Nicholas & Henry J. Snaith. *The Journal of Physical Chemistry Letters*, **5** (2014) 4207–4212. ISSN 1948-7185. Cited on page 79, 80, 98, 100

[220] Antonio Abate, Tomas Leijtens, Sandeep Pathak, Joël Teuscher, Roberto Avolio, Maria E Errico, James Kirkpatrik, James M Ball, Pablo Docampo, Ian McPherson & Henry J Snaith. *Physical chemistry chemical physics : PCCP*, **15**, 7 (2013) 2572–9. ISSN 1463-9084. Cited on page 79, 99, 143, 146

[221] Severin N Habisreutinger, Tomas Leijtens, Giles E Eperon, Samuel David Stranks, Robin J Nicholas & Henry J Snaith. *Nano Letters*, **14**, 10 (2014) 5561–5568. ISSN 1530-6984. Cited on page 80, 113

[222] Molang Cai, Vincent Tiing Tiong, Tubuxin Hreid, John Bell & Hongxia Wang. *Journal of Materials Chemistry A: Materials for energy and sustainability*, **00** (2014) 1–10. ISSN 2050-7488. Cited on page 81

[223] Anthony W. Musumeci, Glaura G. Silva, Jiang Wen Liu, Wayde N. Martens & Eric R. Waclawik. *Polymer*, **48**, 6 (2007) 1667–1678. ISSN 00323861. Cited on page 81

[224] Haiwei Chen, Xu Pan, Weiqing Liu, Molang Cai, Dongxing Kou, Zhipeng Huo, Xiaqin Fang & Songyuan Dai. *Chemical communications (Cambridge, England)*, **49**, 66 (2013) 7277–9. ISSN 1364-548X. Cited on page 81

[225] Xiaoli Zheng, Haining Chen, Zhanhua Wei, Yinglong Yang, He Lin & Shihe Yang. *Frontiers of Optoelectronics*, pages 1–10. ISSN 2095-2759. Cited on page 81

[226] Zhanhua Wei, Haining Chen, Keyou Yan, Xiaoli Zheng & Shihe Yang. *J. Mater. Chem. A*, **3**, 48 (2015) 24226–24231. ISSN 2050-7488. Cited on page 81

[227] Hao Li, Kun Cao, Jin Cui, Shuangshuang Liu, Xianfeng Qiao, Yan Shen & Mingkui Wang. *Nanoscale*. ISSN 2040-3364. Cited on page 81

[228] Qiang Luo, He Ma, Ye Zhang, Xuewen Yin, Zhibo Yao, Ning Wang, Jianbao Li, Shoushan Fan, Kaili Jiang & Hong Lin. *J. Mater. Chem. A*. ISSN 2050-7488. Cited on page 82

[229] Kerttu Aitola, Kari Sveinbjornsson, Juan Pablo Correa Baena, Antti Kaskela, Antonio Abate, Ying Tian, Erik M. J. Johansson, Michael Grätzel, Esko Kauppinen, Anders Hagfeldt & Gerrit Boschloo. *Energy Environ. Sci.*, pages 461–466. ISSN 1754-5692. Cited on page 82

[230] Il Jeon, Takaaki Chiba, Clement Delacou, Yunlong Guo, Antti Kaskela, Olivier Reynaud, Esko I. Kauppinen, Shigeo Maruyama & Yutaka Matsuo. *Nano Letters*, **15**, 10 (2015) 6665–6671. ISSN 15306992. Cited on page 82, 165

[231] Philip Schulz, Anne-Marie Dowgiallo, Mengjin Yang, Kai Zhu, Jeffrey L Blackburn & Joseph J. Berry. *The Journal of Physical Chemistry Letters*, **7**, 3 (2016) 418–425. ISSN 1948-7185. Cited on page 82, 83, 165

[232] Rachelle Ihly, Anne-Marie Dowgiallo, Mengjin Yang, Philip Schulz, Noah Stanton, Obadiah G. Reid, Andrew Ferguson, Kai Zhu, Joseph J. Berry & Jeffrey Blackburn. *Energy Environ. Sci.*. ISSN 1754-5692. Cited on page 82, 83, 84, 165

[233] Tomas Leijtens, Tommaso Giovenzana, Severin N. Habisreutinger, Jonathan S. Tinkham, Nakita K. Noel, Brett A Kamino, Golnaz Sadoughi, Alan Sellinger & Henry J. Snaith. *ACS Applied Materials & Interfaces*, **8**, 9 (2016) 5981–5989. ISSN 1944-8244. Cited on page 90, 146

[234] Brian C. O'Regan & Frank Lenzmann. *The Journal of Physical Chemistry B*, **108**, 14 (2004) 4342–4350. ISSN 1520-6106. Cited on page 93

[235] Gerrit Boschloo, Anders Hagfeldt & C O N Spectus. *Accounts of Chemical Research*, **42**, 11 (2009) 1819–1826. Cited on page 98

[236] Henry J. Snaith. *Advanced Functional Materials*, **20**, 1 (2010) 13–19. ISSN 1616301X. Cited on page 98

[237] Henry J. Snaith & Michael Gratzel. *Applied Physics Letters*, **89**, 26 (2006) 262114. ISSN 00036951. Cited on page 98, 103, 118

[238] Andrew J. Pearson, Giles E. Eperon, Paul E. Hopkinson, Severin N. Habisreutinger, Jacob Tse-Wei Wang, Henry J. Snaith & Neil C. Greenham. *Advanced Energy Materials*, **6**, 13 (2016) 1600014. ISSN 16146832. Cited on page 99

[239] Samuel D Stranks, Johannes K Sprafke, Harry L Anderson & Robin J Nicholas. *ACS Nano*, **5**, 3 (2011) 2307–2315. ISSN 1936-086X. Cited on page 101

[240] Lioz Etgar, Peng Gao, Zhaosheng Xue, Qin Peng, Aravind Kumar Chandiran, Bin Liu, Md K Nazeeruddin & Michael Grätzel. *Journal of the American Chemical Society*, **134**, 42 (2012) 17396–9. ISSN 1520-5126. Cited on page 102

[241] Arianna Marchioro, Joël Teuscher, Dennis Friedrich, Marinus Kunst, Roel van de Krol, Thomas Moehl, Michael Grätzel & Jacques-E. Moser. *Nature Photonics*, **8**, 3 (2014) 250–255. ISSN 1749-4885. Cited on page 102

[242] Tomas Leijtens, Jongchul Lim, Joël Teuscher, Taiho Park & Henry J Snaith. *Advanced Materials*, **25**, 23 (2013) 3227–33. ISSN 1521-4095. Cited on page 102, 111

[243] Wolfgang Bauhofer & Josef Z. Kovacs. *Composites Science and Technology*, **69**, 10 (2009) 1486–1498. ISSN 02663538. Cited on page 103

[244] Pablo Docampo, Andrew Hey, Stefan Guldin, Robert Gunning, Ullrich Steiner & Henry J. Snaith. *Advanced Functional Materials*, **22**, 23 (2012) 5010–5019. ISSN 1616301X. Cited on page 106

[245] Henry J. Snaith, Antonio Abate, James M. Ball, Giles E. Eperon, Tomas Leijtens, Nakita K. Noel, Samuel D. Stranks, Jacob Tse-Wei Wang, Konrad Wojciechowski & Wei Zhang. *The Journal of Physical Chemistry Letters*, **5**, 9 (2014) 1511–1515. ISSN 1948-7185. Cited on page 107, 140

[246] Dongqin Bi, Lei Yang, Gerrit Boschloo, Anders Hagfeldt & Erik M J Johansson. *The Journal of Physical Chemistry Letters*, **4**, 9 (2013) 1532–1536. ISSN 1948-7185. Cited on page 108, 116

[247] R Bruce Weisman & Sergei M Bachilo. *Nano Letters*, **3**, 9 (2003) 1235–1238. Cited on page 109

[248] Yoshio Kimoto, Makoto Okano & Yoshihiko Kanemitsu. *Physical Review B*, **87**, 19 (2013) 195416. ISSN 1098-0121. Cited on page 110

[249] D. Bi, W. Tress, M. I. Dar, P. Gao, J. Luo, C. Renevier, K. Schenk, A. Abate, F. Giordano, J.-P. Correa Baena, J.-D. Decoppet, S. M. Zakeeruddin, M. K. Nazeeruddin, M. Gra tzel & A. Hagfeldt. *Science Advances*, **2**, 1 (2016) e1501170–e1501170. ISSN 2375-2548. Cited on page 116, 145

[250] Hisham A. Abbas, Ranjith Kottokkaran, Balaji Ganapathy, Mehran Samiee, Liang Zhang, Andrew Kitahara, Max Noack & Vikram L. Dalal. *APL Materials*, **3**, 2015 (2015) 016105. ISSN 2166-532X. Cited on page 116

[251] Jun Hong Noh, Sang Hyuk Im, Jin Hyuck Heo, Tarak N Mandal & Sang Il Seok. *Nano Letters*, **13**, 4 (2013) 1764–9. ISSN 1530-6992. Cited on page 117, 118

[252] Julian Burschka, Amalie Dualeh, Florian Kessler, Etienne Baranoff, Ngoc-Lê Cevey-Ha, Chenyi Yi, Mohammad K Nazeeruddin & Michael Grätzel. *Journal of the American Chemical Society*, **133**, 45 (2011) 18042–18045. ISSN 1520-5126. Cited on page 118

[253] Amalie Dualeh, Thomas Moehl, Mohammad Khaja Nazeeruddin & Michael Grätzel. *ACS nano*, **7**, 3 (2013) 2292–301. ISSN 1936-086X. Cited on page 118

[254] Antonio Abate, Derek J Hollman, Joël Teuscher, Sandeep Pathak, Roberto Avolio, Gerardino D'Errico, Giuseppe Vitiello, Simona Fantacci & Henry J Snaith. *Journal of the American Chemical Society*, **135**, 36 (2013) 13538–48. ISSN 1520-5126. Cited on page 118, 146

[255] Francesco Di Giacomo, Stefano Razza, Fabio Matteocci, Alessandra D'Epifanio, Silvia Licoccia, Thomas M. Brown & Aldo Di Carlo. *Journal of Power Sources*, **251** (2014) 152–156. ISSN 03787753. Cited on page 118

[256] Thermo Scientific. "Physical Properties Table". Cited on page 129, 164

[257] C E Finlayson & P J A Sazio. *Journal of Physics D: Applied Physics*, **39**, 8 (2006) 1477–1480. ISSN 0022-3727. Cited on page 134

[258] A Virtuani, D Pavanello & G Friesen. *Proceedings of the 25th European Photovoltaic Solar Energy Conference*, pages 4248–4252. Cited on page 134

[259] Jarvist M Frost, Keith T Butler, Federico Brivio, Christopher H Hendon, Mark van Schilfgaarde & Aron Walsh. *Nano letters*, **14**, 5 (2014) 2584–90. ISSN 1530-6992. Cited on page 136

[260] Daniel Bryant, Nicholas Aristidou, Sebastian Pont, Irene Sanchez-Molina, Thana Chotchunangatchaval, Scot Wheeler, James R. Durrant & Saif A. Haque. *Energy Environ. Sci.*, **9**, 5 (2016) 1655–1660. ISSN 1754-5692. Cited on page 138

[261] Eva Lisa Unger, Eric T Hoke, Colin D Bailie, William H Nguyen, Andrea Ruth Bowring, Thomas Heumuller, Mark Greyson Christoforo & Michael D. McGehee. *Energy & Environmental Science*, **7** (2014) 3690–3698. ISSN 1754-5692. Cited on page 140, 141

[262] W. Tress, N. Marinova, T. Moehl, S. M. Zakeeruddin, Mohammad Khaja Nazeeruddin & M. Grätzel. *Energy Environ. Sci.*, **8**, 3 (2015) 995–1004. ISSN 1754-5692. Cited on page 140, 156, 158

[263] M K Nazeeruddin, A Kay, I. Rodicio, R. Humphry-Baker, E. Mueller, P Liska, N Vlachopoulos & M. Graetzel. *Journal of the American Chemical Society*, **115**, 14 (1993) 6382–6390. ISSN 0002-7863. Cited on page 144, 155

[264] G Schlichthörl, S Y Huang, J Sprague & a J Frank. *The Journal of Physical Chemistry B*, **101**, 41 (1997) 8141–8155. ISSN 1520-6106. Cited on page 144

[265] Saif a Haque, Yasuhiro Tachibana, Richard L Willis, Jacques E Moser, Michael Grätzel, David R Klug & James R Durrant. *The Journal of Physical Chemistry B*, **104**, 3 (2000) 538–547. ISSN 1520-6106. Cited on page 144

[266] Gerrit Boschloo, Leif Häggman & Anders Hagfeldt. *Journal of Physical Chemistry B*, **110**, 26 (2006) 13144–13150. ISSN 15206106. Cited on page 144

[267] Saif a. Haque, Emilio Palomares, Byung M. Cho, Alex N M Green, Narukuni Hirata, David R. Klug & James R. Durrant. *Journal of the American Chemical Society*, **127**, 10 (2005) 3456–3462. ISSN 00027863. Cited on page 144

[268] R. Kern, R. Sastrawan, J. Ferber, R. Stangl & J. Luther. *Electrochimica Acta*, **47**, 26 (2002) 4213–4225. ISSN 00134686. Cited on page 144

[269] M. Durr, a. Yasuda & G. Nelles. *Applied Physics Letters*, **89**, 6 (2006) 061110. ISSN 00036951. Cited on page 144

[270] Jessica Krüger, Robert Plass, Le Cevey, Marco Piccirelli, Michael Grätzel & Udo Bach. *Applied Physics Letters*, **79**, 13 (2001) 2085–2087. ISSN 00036951. Cited on page 144, 145, 154, 155

[271] W. S. Yang, J. H. Noh, N. J. Jeon, Y. C. Kim, S. Ryu, J. Seo & S. I. Seok. *Science*, **348**, 6240 (2015) 1234–1237. ISSN 0036-8075. Cited on page 145

[272] Shun Yu, Sareh Ahmadi, Chenghua Sun, Pal Palmgren, Franz Hennies, Marcelo Zuleta & Mats Gothelid. *The Journal of Physical Chemistry C*, **114**, 5 (2010) 2315–2320. ISSN 1932-7447. Cited on page 154

[273] Ye Zhang, Mingzhen Liu, Giles E. Eperon, Tomas C. Leijtens, David McMeekin, Michael Saliba, Wei Zhang, Michele de Bastiani, Annamaria Petrozza, Laura M. Herz, Michael B. Johnston, Hong Lin & Henry J. Snaith. *Mater. Horiz.*, **2** (2015) 315–322. ISSN 2051-6347. Cited on page 156, 158

[274] Nakita K. Noel, Samuel D. Stranks, Antonio Abate, Christian Wehrenfennig, Simone Guarnera, Amir Haghighirad, Aditya Sadhanala, Giles E Eperon, Sandeep K. Pathak, Michael B Johnston, Annamaria Petrozza, Laura Herz & Henry Snaith. *Energy & Environmental Science*, **7** (2014) 3061–3068. ISSN 1754-5692. Cited on page 158

[275] Yuchuan Shao, Zhengguo Xiao, Cheng Bi, Yongbo Yuan & Jinsong Huang. *Nature Communications*, **5** (2014) 5784. ISSN 2041-1723. Cited on page 158

[276] Zhengguo Xiao, Yongbo Yuan, Yuchuan Shao, Qi Wang, Qingfeng Dong, Cheng Bi, Pankaj Sharma, Alexei Gruverman & Jinsong Huang. *Nature Materials*, **14**, 2 (2014) 193–198. ISSN 1476-1122. Cited on page 158

[277] Yongbo Yuan, Jungseok Chae, Yuchuan Shao, Qi Wang, Zhengguo Xiao, Andrea Centrone & Jinsong Huang. *Advanced Energy Materials*, **5**, 15 (2015) 1500615. ISSN 16146832. Cited on page 158

[278] Stephan van Reenen, Martijn Kemerink & Henry J Snaith. *The Journal of Physical Chemistry Letters*, **6**, 19 (2015) 3808–3814. ISSN 1948-7185. Cited on page 158

[279] Antonio Abate, Michael Saliba, Derek J Hollman, Samuel D Stranks, Konrad Wojciechowski, Roberto Avolio, Giulia Grancini, Annamaria Petrozza & Henry J Snaith. *Nano letters*, **14**, 6 (2014) 3247–54. ISSN 1530-6992. Cited on page 158

[280] Konrad Wojciechowski, Samuel D Stranks, Antonio Abate, Golnaz Sadoughi, Aditya Sadhanala, Nikos Kopidakis, Garry Rumbles, Chang-zhi Li, Richard H Friend, Alex K.-Y. Jen & Henry J Snaith. *ACS Nano*, **8**, 12 (2014) 12701–12709. ISSN 1936-0851. Cited on page 158

[281] Tomas Leijtens, Samuel D. Stranks, Giles E. Eperon, Rebecka Lindblad, Erik M J Johansson, Ian J. McPherson, Håkan Rensmo, James M. Ball, Michael M. Lee & Henry J. Snaith. *ACS Nano*, **8**, 7 (2014) 7147–7155. ISSN 1936086X. Cited on page 158, 160

[282] Michael Saliba, Taisuke Matsui, Ji-Youn Seo, Konrad Domanski, Juan-Pablo Correa-Baena, Mohammad K. Nazeeruddin, Shaik M Zakeeruddin, Wolfgang Tress, Antonio Abate, Anders Hagfeldt & Michael Grätzel. *Energy Environ. Sci.*. ISSN 1754-5692. Cited on page 164

[283] Dianyi Liu & Timothy L. Kelly. *Nature Photonics*, **8**, 2 (2013) 133–138. ISSN 1749-4885. Cited on page 165

[284] Alan J. Sangster. "RENEWABLE ENERGY TECHNOLOGIES: COST ANALYSIS SERIES". In "Green Energy and Technology", volume 194, pages 145–172 (2014). ISBN 9783319085111. Cited on page 165

Abbreviations

CO_2 Carbon dioxide

IPCC Intergovernmental Panel on Climate Change

BOS Balance of systems

LCOE Levelized cost of electricity

EPBT Energy payback time

GHG Greenhouse gas

g_{CO_2eq} Gram of CO_2 equivalent

E_g Bandgap energy

k_B Boltzmann constant: 1.381×10^{-23} m^2 $kg \cdot s^{-2}$ K^{-2}

J_{sc} Short-circuit current

V_{oc} Open-circuit voltage

FF Fill factor

PCE Power-conversion efficiency

CNT Carbon nanotube

SWNT Single-walled carbon nanotube

MWNT Multi-walled carbon nanotube

P3HT Poly(3-hexylthiophene)

PMMA Poly(methyl methacrylate)

PC Polycarbonate

spiro-OMeTAD 2,2,7,7-tetrakis-(N,N-di-p-methoxyphenylamine)9,9-spirobifluorene

PTAA Poly(triarylamine)

tBP 4-*tert*-Butylpyridine

Li-TFSI Bis(trifluoromethane)sulfonimide lithium

FTO Fluorine-doped tin oxide

AM 1.5 Air mass 1.5

DOS Density of states

PIA Photoinduced absorption

F_4TCNQ 2,3,5,6-Tetrafluoro-7,7,8,8-tetracyanoquinodimethane